

Ministry of Science and Higher Education of the Russian Federation  
ITMO University

ISSN 2220-8054

***NANOSYSTEMS:***  
***PHYSICS, CHEMISTRY, MATHEMATICS***

**2025, volume 16(3)**

**Наносистемы: физика, химия, математика**

**2025, том 16, № 3**



# **NANOSYSTEMS:**

## **PHYSICS, CHEMISTRY, MATHEMATICS**

### **ADVISORY BOARD MEMBERS**

**Chairman:** V.N. Vasiliev (*St. Petersburg, Russia*),  
V.M. Buznik (*Moscow, Russia*); V.M. Ievlev (*Voronezh, Russia*), P.S. Kop'ev (*St. Petersburg, Russia*), V.N. Parmon (*Novosibirsk, Russia*), A.I. Rusanov (*St. Petersburg, Russia*),

### **EDITORIAL BOARD**

**Editor-in-Chief:** I.Yu. Popov (*St. Petersburg, Russia*)

#### **Section Co-Editors:**

Physics – V.M. Uzdin (*St. Petersburg, Russia*),

Material science – V.V. Gusarov (*St. Petersburg, Russia*); O.V. Al'myasheva (*St. Petersburg, Russia*);

Chemistry – V.K. Ivanov (*Moscow, Russia*),

Mathematics – I.Yu. Popov (*St. Petersburg, Russia*).

#### **Editorial Board Members:**

V.M. Adamyan (*Odessa, Ukraine*); A.P. Alodjants (*St. Petersburg, Russia*); S. Bechta (*Stockholm, Sweden*); J. Behrndt (*Graz, Austria*); A. Chatterjee (*Hyderabad, India*); A.V. Chizhov (*Dubna, Russia*); A.N. Enyashin (*Ekaterinburg, Russia*), E.A. Gudilin (*Moscow, Russia*); H. Jónsson (*Reykjavik, Iceland*); A.R. Kaul (*Moscow, Russia*); A.A. Kiselev (*Durham, USA*); Yu.S. Kivshar (*Canberra, Australia*); S.A. Kozlov (*St. Petersburg, Russia*); P.A. Kurasov (*Stockholm, Sweden*); A.V. Lukashin (*Moscow, Russia*); G.P. Miroshnichenko (*St. Petersburg, Russia*); I.Ya. Mittova (*Voronezh, Russia*); H. Najjar (*Monastir, Tunisia*), Nguyen Anh Tien (*Ho Chi Minh, Vietnam*); V.V. Pankov (*Minsk, Belarus*); K. Pankrashkin (*Oldenburg, Germany*); A.V. Ragulya (*Kiev, Ukraine*); V. Rajendran (*Tamil Nadu, India*); A.A. Rempel (*Ekaterinburg, Russia*); A.A. Rogachev (*Minsk, Belarus*); V.Ya. Rudyak (*Novosibirsk, Russia*); H.M. Sedighi (*Ahvaz, Iran*); D. Shoikhet (*Karmiel, Israel*); M.N. Smirnova (*Moscow, Russia*); P. Stovicek (*Prague, Czech Republic*); V.M. Talanov (*Novocherkassk, Russia*); A.Ya. Vul' (*St. Petersburg, Russia*); A.V. Yakimansky (*St. Petersburg, Russia*), V.A. Zagrebnov (*Marseille, France*).

#### **Editors:**

I.V. Blinova; A.I. Popov; E.S. Trifanova (*St. Petersburg, Russia*),

R. Simoneaux (*Philadelphia, Pennsylvania, USA*).

**Address:** ITMO University, Kronverkskiy pr., 49, St. Petersburg 197101, Russia.

**Phone:** +7(812)607-02-54, **Journal site:** <http://nanojournal.ifmo.ru/>,

**E-mail:** [nanojournal.ifmo@gmail.com](mailto:nanojournal.ifmo@gmail.com)

### **AIM AND SCOPE**

The scope of the journal includes all areas of nano-sciences. Papers devoted to basic problems of physics, chemistry, material science and mathematics inspired by nanosystems investigations are welcomed. Both theoretical and experimental works concerning the properties and behavior of nanosystems, problems of its creation and application, mathematical methods of nanosystem studies are considered.

The journal publishes scientific reviews (up to 30 journal pages), research papers (up to 15 pages) and letters (up to 5 pages). All manuscripts are peer-reviewed. Authors are informed about the referee opinion and the Editorial decision.

# CONTENT

## MATHEMATICS

M.M. Rahmatullaev, Z.A. Burxonova

**Free energy and entropy for the constructive Gibbs measures of the Ising model on the Cayley tree of order three** 261

## PHYSICS

Mohammad Elsaid, Diana Dahliah, Ayham Shaer, Mahmoud Ali  
**Theoretical study of the effective g-factor of Cd<sub>1-x</sub>Mn<sub>x</sub>Te quantum wire under the combined effects of the applied magnetic field, spin-orbit coupling, and exchange effects** 274

O.B. Chukanova, K.A. Tsarik

**Influence of SiC MOSFET design on on-resistance and breakdown voltage** 282

O.I. Sabirov, A.E. Rajabov, A.R. Matnazarov,

B.Kh. Eshchanov, Sh. Otajanov, U.K. Sapaev

**Study of femtosecond laser amplification in MgO:LiTaO<sub>3</sub> crystals with periodic nonlinear properties** 291

I. Setiawan, R. Ekawita, R. Sugihakim, B.E. Gunara

**Fast forward of adiabatic quantum dynamics: an application to planar Dirac systems** 298

Soma Mukhopadhyay, Ch. Vidyullatha, Pooja Saini, Zahid Malik

**Effect of electron-phonon interaction on the first excited energy level of a Gaussian GaAs quantum dot** 306

M.S. Guselnikov, A.A. Gaidash, G.P. Miroshnichenko, A.V. Kozubov

**Properties of multi-moded phase-randomized coherent states** 311

M.N. Potkina, I.S. Lobanov

**Optimality of linear vacancy defect for skyrmion nucleation** 317

K.A. Chichay, I.S. Lobanov, V.M. Uzdin

**Magnetic structure of domain walls in stressed cylindrical wires** 325

I. Stepanov, R. Goncharov, A.D. Kiselev

**Sub-Poissonian light in fluctuating thermal-loss bosonic channels** 333

## **CHEMISTRY AND MATERIAL SCIENCE**

O.M. Gajtko, S.V. Golodukhina, S.Yu. Kottsov, A.G. Son, T.O. Kozlova, A.E. Baranchikov <b>Epoxide-mediated synthesis of germania aerogels in acetic acid</b>	<b>343</b>
V.A. Grinberg, V.V. Emets, A.V. Shapagin, A.A. Averin, A.A. Shiryayev <b>TiO<sub>2</sub> nanotubes modified with cadmium oxide for photoelectrocatalytic oxidation of alcohols</b>	<b>352</b>
M.G. Mikhaleva, S.V. Usachev, A.S. Vedenkin, M.I. Ikim, G.G. Politenkova, S.M. Lomakin <b>Investigation of morphological features and thermal stability of regenerated wood cellulose from solutions in [BMIm]Cl</b>	<b>364</b>
A.R. El Zanin, S.V. Boroznin, I.V. Zaporotskova <b>Boron doped small fullerenes C<sub>20</sub>, C<sub>24</sub>, C<sub>28</sub> as a basis for the formation of heterostructures</b>	<b>374</b>
<b>Paper abstracts in Russian</b>	<b>386</b>
<b>Information for authors</b>	<b>392</b>

# Congratulations

The Editorial Board of the Journal congratulates

**Vladimir Konstantinovich Ivanov**, Deputy Editor-in-Chief for the Chemistry section, on his election as an Academician of the Russian Academy of Sciences

and

**Oksana Vladimirovna Almyasheva**, Deputy Editor-in-Chief for the Materials Sciences section, on her election as a Corresponding Member of the Russian Academy of Sciences.

We wish our colleagues new scientific achievements!

Editor-in-Chief of the Journal Nanosystems: Physics, Chemistry, Mathematics  
Popov I.Yu.

## Free energy and entropy for the constructive Gibbs measures of the Ising model on the Cayley tree of order three

Muzaffar M. Rahmatullaev<sup>1,2,a</sup>, Zulxumor A. Burxonova<sup>3,4,b</sup>

<sup>1</sup>V. I. Romanovskiy Institute of Mathematics, Uzbekistan Academy of Sciences, Tashkent, Uzbekistan

<sup>2</sup>New Uzbekistan University, Tashkent, Uzbekistan

<sup>3</sup>Namangan State University, Namangan, Uzbekistan

<sup>4</sup>Namangan State Technical University, Namangan, Uzbekistan

<sup>a</sup>[mrahmatullaev@rambler.ru](mailto:mrahmatullaev@rambler.ru), <sup>b</sup>[zulxumorburxonova4@gmail.com](mailto:zulxumorburxonova4@gmail.com)

Corresponding author: M. M. Rahmatullaev, [mrahmatullaev@rambler.ru](mailto:mrahmatullaev@rambler.ru)

PACS 82B23, 82B26, 60G70

**ABSTRACT** In this paper, we identify non-translation-invariant constructive Gibbs measures for the Ising model on a third-order Cayley tree, which differ from known ones. We provide the conditions for the existence of at least two distinct Gibbs measures, which implies that a phase transition occurs. The free energies and entropies corresponding to the identified measures are calculated. These free energies and entropies are then compared with the known ones and shown to differ from them.

**KEYWORDS** Cayley tree, Ising model, Gibbs measure, free energy, entropy.

**ACKNOWLEDGEMENTS** The authors thank Obid Sh. Karshiboev for valuable advice and an anonymous referee for helpful suggestions that improved the paper.

**FOR CITATION** Rahmatullaev M.M., Burxonova Z.A. Free energy and entropy for the constructive Gibbs measures of the Ising model on the Cayley tree of order three. *Nanosystems: Phys. Chem. Math.*, 2025, **16** (3), 261–273.

### 1. Introduction

One of the main problems for the Ising model is to describe all limiting Gibbs measures corresponding to the model. It is well known that for the Ising model such measures form a nonempty, convex, and compact subset in the set of all probability measures. The problem of completely describing the element of this set is far from being completely solved. Some translation-invariant (see, e.g., [1–3]), periodic [4, 5], and continuum sets of non-periodic Gibbs measures for the Ising model on a Cayley tree have already been described (see, e.g., [2, 3, 6, 7]).

In [8, 9], the notion of weakly periodic Gibbs measure is introduced. This notion generalizes the notion of periodic Gibbs measures and such a measure is non-periodic. In [10], the author constructs new sets of non-periodic Gibbs measures for the Ising model on the Cayley tree of order  $k$ , which called  $(k_0)$ -translation-invariant,  $(k_0)$ -periodic and  $(k_0)$ -non-translation-invariant, respectively. In [11], authors investigate  $p$ -adic Gibbs measures for the  $q$ -state Potts model with an external field and establish the conditions for the existence of a phase transition. In  $p$ -adic case, such kind of constructed measures for the Ising model were studied in [12–14]. In [15], the authors construct a very wide class of Gibbs measures. The existence of the Gibbs measures for a given model defines the occurrence of a phase transition [16, 17].

Entropy and free energy are fundamental concepts in thermodynamics that provide a powerful framework for understanding the behavior of systems. By considering both the energy content and the disorder of a system, these concepts allow us to predict the direction and extent of spontaneous processes, making them invaluable tools in various fields of science and engineering [18].

The progress in nanoscience and nanotechnology has spurred considerable research into adapting the principle of thermodynamics and statistical mechanics for small systems with a limited number of particles, moving beyond traditional large-scale applications [5].

Nanoscale systems are characterized by their dynamic structures, unlike the static equilibrium of macroscopic phases. Phase coexistence in these small systems shifts from sharp points to ranges of temperature and pressure. This behavior invalidates the Gibbs phase rule and allows for the formation of metastable phases that are unique to the nanoscale [19, 36–39].

Working with nanoscale materials presents difficulties in accurately describing how their properties and phase changes behave. To overcome these hurdles, we need to formulate new thermodynamic and statistical models specifically designed for small-scale systems. This is particularly crucial for understanding molecular self-assembly, a core

process in bottom-up nanotechnology, which is fundamentally governed by phase transition phenomena as emphasized by Feynman [20].

In [21], the authors present, for the Ising model on the Cayley tree, some explicit formulae of the free energies (and entropies) according to boundary conditions. They include translation-invariant, periodic as well as those corresponding to (recently discovered) weakly periodic Gibbs states. It is proved that the free energies for the translation-invariant and periodic boundary conditions are equal.

In [22], the authors consider the calculation of the entropy of an Ising ferromagnet with nonmagnetic impurities distributed at random over the lattice sites or bonds. In [23], the authors found the exact free energy of such a chain as a function of the impurity concentration, temperature, and the external magnetic field. In [24], the authors studied Ising-Vannimenus model on a Cayley tree for order two with competing nearest-neighbor and prolonged next-nearest-neighbor interactions. Moreover, the free energies and entropies, associated with translation invariant Gibbs measures, are calculated.

In [25], the author considers the Ising-Vannimenus model on a Cayley tree of order three. In [26], the authors generalized the Ising-Vannimenus model's Gibbs measures on a Cayley tree of any order using the Kolmogorov consistency condition and classified the fixed points. They obtained a new formula to calculate the free energy of the model on the Cayley tree of any order under given boundary conditions. In [27], the author studied thermodynamic properties of mixed-spin (2, 1/2) Ising and Blum-Capel models on the Cayley tree.

In [28], the author constructs the partition function and then calculate the free energy of the Ising model having the prolonged next nearest and nearest neighbor interactions and external field on a two-order Cayley tree using the self-similarity of the semi-infinite Cayley tree. In [29], the author calculated the free energy and entropy for (1,1/2)-MSIM. In [30], the author identified regions where the disordered phases are extreme by means of the tree-indexed Markov chain and satisfied the Kesten-Stigum condition for non-extremality of the disordered phase according to the fixed point.

Recently, in [31], we constructed new Gibbs measures for the Ising model on the Cayley tree of order two and calculated free energies of these measures. We noticed that these free energies are equal to the free energies of the translation-invariant boundary conditions.

In this paper, we construct Gibbs measures for the Ising model on a third-order Cayley tree, which differ from those mentioned above, and calculate the free energies and entropies. Also, we prove that the free energies and entropies corresponding to the obtained measures (which are constructed on the Cayley tree of order three) differ from the free energies of the translation-invariant boundary conditions.

This paper is organized as follows. In Section 2, we present necessary main definitions and formulas. In the next two sections, we construct new Gibbs measures. In Section 5, we calculate the free energy corresponding to these measures. In Section 6, we calculate the entropy corresponding to the measures.

## 2. Preliminaries

Let  $\Gamma^k = (V, L), k \geq 1$  be the Cayley tree of order  $k$ , where  $V$  and  $L$  are the set of vertices and the set of all edges of the tree  $\Gamma^k$ , respectively.  $\Gamma^k$  can be represented as a group  $G_k$ , which is the free product of  $k + 1$  cyclic groups of the second order (see, e.g. [2, 7]).

Two vertices  $x$  and  $y$  are called nearest neighbors if there exists an edge  $l \in L$  connecting them  $l = \langle x, y \rangle$ . A collection of nearest neighbor pairs  $\langle x, x_1 \rangle, \langle x_1, x_2 \rangle, \dots, \langle x_m, y \rangle$  is called the path from  $x$  to  $y$ . By the path, one can define distance  $d$  on the tree. The distance between vertices  $x$  and  $y$  is the number of edges of the shortest path from  $x$  to  $y$ . Let us fix a vertex  $x^0 \in V$  and call it as a root of the tree. Then for any natural number  $n$ , we introduce the following set:

$$W_n = \{x \in V \mid d(x, x^0) = n\}, \quad V_n = \bigcup_{m=0}^n W_m, \quad L_n = \{\langle x, y \rangle \in L : x, y \in V_n\},$$

The sets  $W_n$  and  $V_n$  are called a sphere and a ball with radius  $n$ , respectively.

For a given  $x \in W_n$ , we introduce

$$S(x) = \{y \in W_{n+1} : d(x, y) = 1\}, \quad x \in W_n,$$

which is called a set of direct successors of  $x$ .

For  $A \subseteq V$ , a spin configuration on  $A$  is defined as a function

$$x \in A \rightarrow \sigma_A(x) \in \Phi = \{-1, 1\}.$$

The set of all configurations coincides with  $\Omega_A = \Phi^A$ . We denote  $\Omega = \Omega_V$  and  $\sigma = \sigma_V$ .

We consider the Hamiltonian of the Ising model

$$H(\sigma) = -J \sum_{\langle x, y \rangle \in L} \sigma(x)\sigma(y), \tag{1}$$

where  $J \in R, \sigma(x) \in \Phi$  and  $\langle x, y \rangle$  are the nearest neighbors.

For every  $n$ , we then define a measure  $\mu_n$  on  $\Omega_{V_n}$  by

$$\mu_n(\sigma_n) = Z_n^{-1} \exp\{-\beta H(\sigma_n) + \sum_{x \in W_n} h_x \sigma(x)\}, \tag{2}$$

where  $\beta = \frac{1}{T}$  ( $T$  is a temperature,  $T > 0$ ),  $\sigma_n = \{\sigma(x), x \in V_n\} \in \Omega_{V_n}$ ,  $Z_n^{-1}$  is the normalizing factor, and

$$H(\sigma_n) = -J \sum_{\langle x,y \rangle \in L_n} \sigma(x)\sigma(y).$$

The compatibility condition for the measures  $\mu_n, n > 1$  is

$$\sum_{\sigma^{(n)}} \mu_n(\sigma_{n-1}, \sigma^{(n)}) = \mu_{n-1}(\sigma_{n-1}), \tag{3}$$

where  $\sigma^{(n)} = \{\sigma(x), x \in W_n\}$ .

Let  $\mu_n, n \geq 1$  be a sequence of measures on the sets  $\Omega_{V_n}$  that satisfy compatibility condition (3). By the Kolmogorov theorem, we then have a unique limit measure  $\mu$  on  $\Omega$  such that

$$\mu(\{\sigma \mid_{V_n} = \sigma_n\}) = \mu_n(\sigma_n),$$

for every  $n = 1, 2, \dots$  and  $\sigma_n \in \Phi^{V_n}$ . Such a measure is called a splitting Gibbs measure corresponding to the Hamiltonian (1) and function  $h_x, x \in V$ .

**Theorem 2.1** [1–3] The measures  $\mu_n(\sigma_n), n = 1, 2, \dots$ , in (2) are compatible iff for any  $x \in V$ , the following equation holds:

$$h_x = \sum_{y \in S(x)} f(h_y, \theta), \tag{4}$$

where  $f(x, \theta) = \arctan h(\theta \tanh x), \theta = \tanh(J\beta)$ .

**Definition 2.1** Let  $K$  be a subgroup of  $G_k, k \geq 1$ . We say that a function  $h = \{h_x \in R : x \in G_k\}$  is  $K$ -periodic if  $h_{yx} = h_x$  for all  $x \in G_k$  and  $y \in K$ . A  $G_k$ -periodic function  $h$  is called the translation-invariant one.

**Definition 2.2** A Gibbs measure is called  $K$ -periodic if it corresponds to  $K$ -periodic function  $h$ .

**Definition 2.3** A set of quantities  $h = \{h_x, x \in G_k\}$  is called  $K$ -weakly periodic, if  $h_x = h_{ij}$ , for any  $x \in H_i, x_\downarrow \in H_j$ , where  $x_\downarrow$ -ancestor of  $x$ .

Theorem 2.1 establishes a one-to-one correspondence: a boundary condition solving the functional equation (4) uniquely determines a Gibbs measure and conversely. This means that finding all Gibbs measures is equivalent to finding all solutions to equation (4).

We aim to investigate the relationship between the boundary condition and the resulting free energy, specifically when the free energy exists:

$$F(\beta, h) = - \lim_{n \rightarrow \infty} \frac{1}{\beta |V_n|} \ln Z_n(\beta, h). \tag{5}$$

The authors of [15] define a large variety of Gibbs measures. Studying the Gibbs measures on a  $k$ -order Cayley tree is equivalent to solving a system of equations

$$\begin{cases} h = (a_1 - a_2)f(h, \theta) + (a_3 - a_4)f(l, \theta), \\ l = (b_1 - b_2)f(h, \theta) + (b_3 - b_4)f(l, \theta), \end{cases} \tag{6}$$

where  $a_i, b_i, i = 1, 2, 3, 4$  are non-negative integers and

$$a_1 + a_2 + a_3 + a_4 = k, \quad b_1 + b_2 + b_3 + b_4 = k. \tag{7}$$

**Theorem 2.2** [15] Independently of the parameters, there is one Gibbs measure which corresponding to the solution  $(0, 0)$  of the system of equations (6), and if

$$|((a_3 - a_4)(b_1 - b_2) - (a_1 - a_2)(b_3 - b_4))\theta^2 + (a_1 - a_2 + b_3 - b_4)\theta| > 1$$

then there are at least three distinct Gibbs measures corresponding to the solutions  $(0, 0), (\pm h_*, \pm l_*)$ , of system of equations (6), where  $h_* > 0, l_* > 0$ .

If an arbitrary edge  $\langle x, y \rangle = l \in L$  is deleted from the Cayley tree  $\Gamma^k$ , it splits into two components, i.e., two identical semi-infinite trees  $\Gamma_0^k$  and  $\Gamma_1^k$  (see Fig. 1). In this paper, we consider semi-infinite Cayley tree  $\Gamma_0^k = (V^0, L^0)$ . The vertex  $x_0$  is considered as a root of tree, the root has  $k$  nearest neighbors and all other vertices of  $\Gamma_0^k$  has  $k + 1$  nearest neighbors.

This work identifies new families of Gibbs measures that differ from those described in the previous studies [5,31–34], as well as those presented in Theorem 2.2.

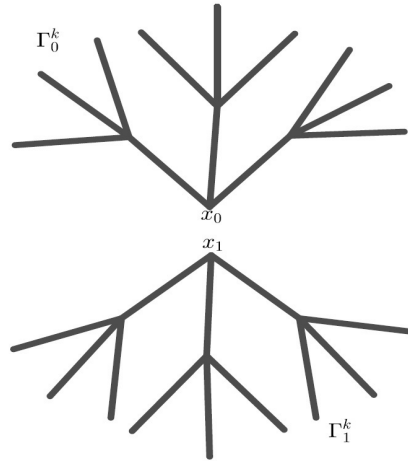


FIG. 1. The Cayley tree of order  $k = 3$ , separated to two semi-infinite sub-trees  $\Gamma_0^k$  and  $\Gamma_1^k$

### 3. Constructive Gibbs measures with rule A

This section will detail the construction of Gibbs measures for the Ising model on a Cayley tree of order three. The following definition specifies the set of quantities  $h = \{h_x, x \in V\}$ :

(A) If  $h_x = h_2$ , then we put  $h_1$  on all direct successors of  $x$ .

If  $h_x = h_1$ , then we put  $h_2$  and 0 on an arbitrary vertex and the other two vertices of direct successors of  $x$ , respectively.

If  $h_x = 0$ , then we put 0 on all direct successors of  $x$  (see Fig. 2).

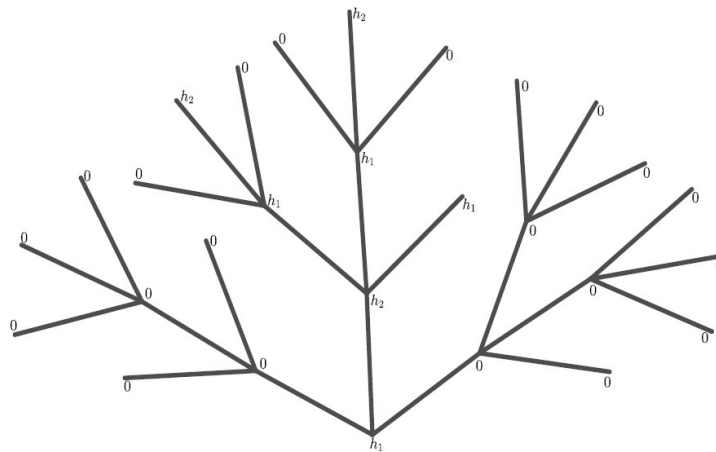


FIG. 2. Set of quantities  $h = \{h_x, x \in V\}$  corresponding to the rule (A)

The set of the boundary condition  $\{0, h_1, h_2\}$  defined by the rule (A) must satisfy the boundary condition (4):

$$\begin{cases} h_1 = f(h_2, \theta), \\ h_2 = 3f(h_1, \theta). \end{cases} \tag{8}$$

It is clear that  $h_1 = h_2 = 0$  is a solution of (8).

Using the formula  $f(x, \theta) = \arctan h(\theta \tanh x) = \frac{1}{2} \ln \frac{(1 + \theta)e^{2h} + (1 - \theta)}{(1 - \theta)e^{2h} + (1 + \theta)}$ , and introducing the notations  $\alpha = \frac{1 - \theta}{1 + \theta}$ ,  $z_i = e^{2h_i}$ ,  $i = 1, 2$ , we have  $\alpha \in (0, 1) \cup (1, +\infty)$ . By the last notations, (8) yields the following system of

equations:

$$\begin{cases} z_1 = \frac{z_2 + \alpha}{\alpha z_2 + 1}, \\ z_2 = \left( \frac{z_1 + \alpha}{\alpha z_1 + 1} \right)^3. \end{cases} \tag{9}$$

The following lemma defines the number of positive solutions of (9).

**Lemma 3.1** Let  $\mathcal{N}$  be a number of the positive solutions (9). Then the following assertions hold:

$$\mathcal{N} = \begin{cases} 3, & \text{if } \alpha \in (0; 2 - \sqrt{3}) \cup (2 + \sqrt{3}; \infty), \\ 1, & \text{if } \alpha \in \cup(2 - \sqrt{3}; 1) \cup (1; 2 + \sqrt{3}). \end{cases} \tag{10}$$

**Proof:** See Appendix 1.

Using Lemma 3.1, we obtain the following theorem:

**Theorem 3.1** For the Gibbs measures for the Ising model corresponding to  $h = \{h_x, x \in V\}$  which defined by rule (A) on the Cayley tree of order three the following statements hold:

- (1) if  $\alpha \in (0; 2 - \sqrt{3}) \cup (2 + \sqrt{3}; \infty)$ , then there are three Gibbs measures, moreover, two of them are non-translation-invariant Gibbs measures;
- (2) if  $\alpha \in (2 - \sqrt{3}; 1) \cup (1; 2 + \sqrt{3})$ , then there exists a unique translation-invariant Gibbs measure.

**Remark 3.1** The translation-invariant measure corresponding to  $(z_1, z_2) = (1, 1)$  found in Theorem 3.1 was studied [1, 8, 19].

#### 4. Constructive Gibbs measures with rule B

The values for the set  $h = \{h_x, x \in V\}$  are assigned according to the following rules.

**(B)** If  $h_x = h_2$ , then we put  $h_1$  on all direct successors of  $x$ .

If  $h_x = h_1$ , then we put 0 and  $h_2$  on an arbitrary vertex and the other two vertices of direct successors of  $x$ , respectively.

If  $h_x = 0$ , then we put 0 on all direct successors of  $x$  (see Fig. 3).

The set of quantities  $\{0, h_1, h_2\}$  as determined by the constructive rule (B) is constrained by the boundary condition specified in equation (4):

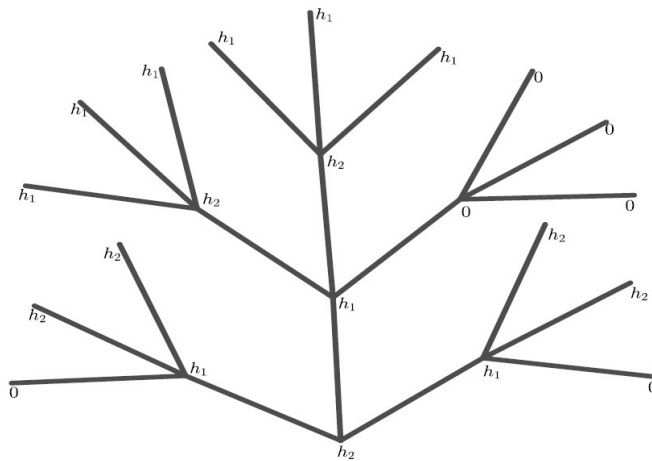


FIG. 3. Set of quantities  $h = \{h_x, x \in V\}$ , which corresponding to the rule (B)

$$\begin{cases} h_1 = 2f(h_2, \theta), \\ h_2 = 3f(h_1, \theta). \end{cases} \tag{11}$$

From (11), we write the following:

$$\begin{cases} z_1 = \left( \frac{z_2 + \alpha}{\alpha z_2 + 1} \right)^2, \\ z_2 = \left( \frac{z_1 + \alpha}{\alpha z_1 + 1} \right)^3. \end{cases} \tag{12}$$

According to the calculation in based on graphical analysis and the Descartes' theorem we have the following result:

**Lemma 4.1** Let  $\mathcal{K}$  be a number of the positive solutions of (12). Then the following assertions hold:

$$\mathcal{K} = \begin{cases} 3, & \text{if } \alpha \in (0; \alpha_{c_1}] \cup [\alpha_{c_2}; \infty), \\ 1, & \text{if } \alpha \in (\alpha_{c_1}; \alpha_{c_2}). \end{cases} \tag{13}$$

where  $\alpha_{c_1} \approx 0.44, \alpha_{c_2} \approx 2.3$ .

**Proof:** See Appendix 2.

Using Lemma 4.1 we obtain the following theorem:

**Theorem 4.1** Let  $k = 3$ . For the Ising model constructed with rule (B) on the Cayley tree, the following holds true:

- (1) if  $\alpha \in (0; \alpha_{c_1}] \cup [\alpha_{c_2}; \infty)$ , then there are three Gibbs measures, moreover, two of them are non-translation-invariant Gibbs measures;
- (2) if  $\alpha \in (\alpha_{c_1}; \alpha_{c_2})$ , then there exists unique translation-invariant Gibbs measure.

**Remark 4.1** The translation-invariant measure corresponding to  $(z_1, z_2) = (1, 1)$  found in Theorem 4.1 was studied [1, 8, 19].

**Remark 4.2** The measures found by rules (A) and (B) are neither periodic nor weakly periodic, they are new Gibbs measures (see in [5, 31–35]).

### 5. Free energy for the Gibbs measures constructed by rules (A) and (B)

In the section, we calculate the free energy for the measures found in the previous sections. Free energy plays an important role in the fields of chemistry and physics, being used to determine the occurrence of processes and reactions, energy transfer between systems, and their energetic stability.

The following theorem gives a formula of the free energy.

**Theorem 5.1** [21] For boundary conditions satisfying (4), the free energy is given by the formula

$$F(\beta, h) = - \lim_{n \rightarrow \infty} \frac{1}{|V_n|} \sum_{x \in V_n} a(x), \tag{14}$$

where

$$a(x) = \frac{1}{2\beta} \ln [4 \cosh(h_x - \beta J) \cdot \cosh(h_x + \beta J)].$$

**Theorem 5.2** The free energy of the Gibbs measures which are defined by rule (A) for the Ising model on the Cayley tree of order three is defined the following formula:

$$F_A(\beta, h_A) = -\frac{3}{4\beta} \ln(2 \cosh(\beta J)), \tag{15}$$

where  $h_A$  are constructed according to the rule (A).

**Proof** Let  $\mathcal{A} \subset V$ . Denote by  $|\mathcal{A}(h_{A_i})|$  the number of  $h_{A_i}$  in the set  $\mathcal{A}$ , where  $i = 0, 1, 2$  and  $h_{A_i}$  is defined by rule (A). Firstly, we calculate  $|W_{A_n}(h_{A_0})|, |W_{A_n}(h_{A_1})|, |W_{A_n}(h_{A_2})|$  (see Fig. 1).  $W_{A_n}$  are constructed according to the rule (A). After some calculations, we have

$$\begin{aligned} |W_{A_n}(h_{A_0})| &= \begin{cases} 3^n - 3^{\frac{n}{2}}, & \text{if } n \text{ is even,} \\ 3^n - 3^{\frac{n+1}{2}}, & \text{if } n \text{ is odd,} \end{cases} \\ |W_{A_n}(h_{A_1})| &= \begin{cases} 0, & \text{if } n \text{ is even,} \\ 3^{\frac{n+1}{2}}, & \text{if } n \text{ is odd,} \end{cases} \\ |W_{A_n}(h_{A_2})| &= \begin{cases} 3^{\frac{n}{2}}, & \text{if } n \text{ is even,} \\ 0, & \text{if } n \text{ is odd,} \end{cases} \end{aligned}$$

It is clear that

$$|V_{A_n}(h_{A_i})| = \sum_{k=0}^n |W_{A_k}(h_{A_i})|, \quad i = 1, 2. \tag{16}$$

Using (16) we find the following:

$$\begin{aligned} |V_{A_n}(h_{A_0})| &= \begin{cases} A_n, & n \text{ is even,} \\ B_n, & n \text{ is odd,} \end{cases} \\ |V_{A_n}(h_{A_1})| &= \begin{cases} C_n, & \text{if } n \text{ is even,} \\ D_n, & \text{if } n \text{ is odd,} \end{cases} \\ |V_{A_n}(h_{A_2})| &= \begin{cases} E_n, & \text{if } n \text{ is even,} \\ F_n, & \text{if } n \text{ is odd,} \end{cases} \end{aligned}$$

where

$$\begin{aligned} A_n &= \frac{9^{\frac{n+2}{2}} - 1}{8} - \frac{3^{\frac{n+2}{2}} - 1}{2}, \\ B_n &= \frac{3 \cdot (9^{\frac{n+1}{2}} - 1)}{8} - \frac{3^{\frac{n+1}{2}} - 1}{2}, \\ C_n &= \frac{3}{2}(3^{\frac{n}{2}} - 1) + 1, D_n = 0, E_n = 0, \\ F_n &= \frac{1}{2} \cdot (3^{\frac{n+1}{2}} - 1). \end{aligned}$$

According to (14), we have

$$\begin{aligned} F_A(\beta, h_A) &= \\ &= -\frac{1}{2\beta} \lim_{n \rightarrow \infty} \frac{2}{3^{n+1} - 1} \begin{cases} A_n \ln[4 \cosh(-\beta J) \cdot \cosh(\beta J)], & \text{if } n \text{ is even} \\ B_n \ln[4 \cosh(-\beta J) \cdot \cosh(\beta J)], & \text{if } n \text{ is odd} \end{cases} \\ &\quad - \frac{1}{2\beta} \lim_{n \rightarrow \infty} \frac{2}{3^{n+1} - 1} \begin{cases} C_n \ln[4 \cosh(h_{A_1} - \beta J) \cdot \cosh(h_{A_1} + \beta J)], & \text{if } n \text{ is even} \\ D_n \ln[4 \cosh(h_{A_1} - \beta J) \cdot \cosh(h_{A_1} + \beta J)], & \text{if } n \text{ is odd} \end{cases} \\ &\quad - \frac{1}{2\beta} \lim_{n \rightarrow \infty} \frac{2}{3^{n+1} - 1} \begin{cases} E_n \ln[4 \cosh(h_{A_2} - \beta J) \cdot \cosh(h_{A_2} + \beta J)], & \text{if } n \text{ is even} \\ F_n \ln[4 \cosh(h_{A_2} - \beta J) \cdot \cosh(h_{A_2} + \beta J)], & \text{if } n \text{ is odd} \end{cases} \\ &= -\frac{1}{2\beta} \cdot \frac{3}{4} \ln[4 \cosh(-\beta J) \cdot \cosh(\beta J)] = -\frac{3}{4\beta} \ln[2 \cosh(\beta J)]. \end{aligned}$$

Similarly, we can prove the following theorem for the Gibbs measures which are defined by rule **(B)**.

**Theorem 5.3** The free energy of the Gibbs measures for the Ising model, defined by rule **(B)** on the Cayley tree of order three, equals

$$F_B(\beta, h_B) = -\frac{3}{4\beta} \ln(2 \cosh(\beta J)), \tag{17}$$

where  $h_B$  is constructed according to the rule **(B)**.

**Remark 5.1** a) Due to Theorems 5.2 and 5.3, we have

$$F_A(\beta, h_A) = F_B(\beta, h_B).$$

Moreover, we also show that

$$F_A(\beta, h_A) = F_B(\beta, h_B) \neq F_{TI}(\beta, 0),$$

where  $F_{TI}(\beta, 0) = -\frac{1}{\beta} \ln(2 \cosh(\beta J))$  is the free energy of the translation-invariant (TI) boundary condition [21].

b) In [21] it is shown that

$$F_{WP}(\beta, h) < F_{TI}(\beta, 0).$$

In the present paper, we show that

$$F_{TI}(\beta, 0) < F_A(\beta, h_A) = F_B(\beta, h_B).$$

It implies that the free energy corresponding to the rule **(A)** differs from the free energy corresponding to the weakly periodic b.c., more precisely,

$$F_{WP}(\beta, h) < F_{TI}(\beta, 0) < F_A(\beta, h_A) = F_B(\beta, h_B).$$

**Corollary 5.1** The free energy of the Gibbs measures which are defined by rules **(A)** and **(B)** for the Ising model on the Cayley tree of order three is defined as follows::

$$F_A(\beta, h_A) = F_B(\beta, h_B) = \frac{3}{4} F_{TI}(\beta, 0).$$

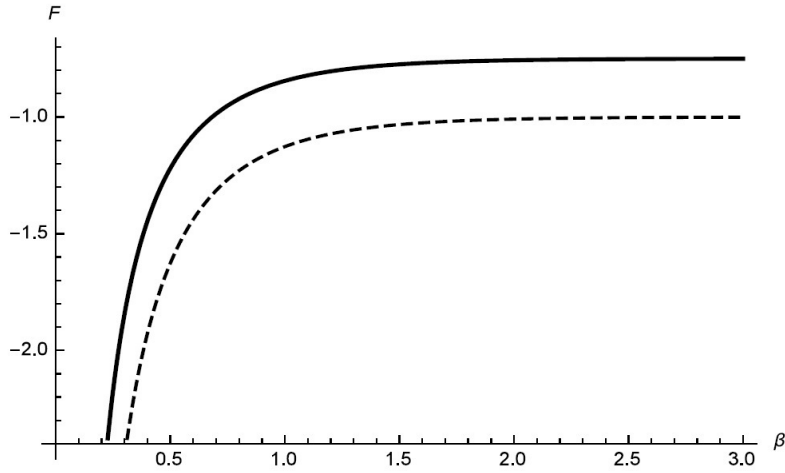


FIG. 4. Free energy  $F_{TI}(\beta, 0)$  (dotted line) and free energy built according to rules (A) and (B) i.e  $F_A(\beta, h_A) = F_B(\beta, h_B)$ (solid line). Here  $J = 1$  and  $k = 3$

**6. Entropy for the Gibbs measures constructed by rules (A) and (B)**

In this section, we calculate the entropy for rules (A) and (B). The concept of entropy is crucial to understanding processes in both physics and chemistry. In physics, it expresses the energetic state and disorder of systems, while in chemistry, it is used to determine whether reactions are spontaneous or non-spontaneous. The increase in entropy is the main trend observed in natural processes, indicating changes in energy and the efficiency of movements between systems.

The entropy is found by the following expression (see in [21]):

$$S(\beta, h) = - \frac{dF(\beta, h)}{dT}. \tag{18}$$

**Theorem 6.1** The entropy of the Gibbs measures which are given by rule (A) for the Ising model on the Cayley tree of order three is defined the following formula:

$$S_A(\beta, h_A) = \frac{3}{4} \cdot (\ln(2 \cosh(J\beta)) - J\beta \tanh(J\beta)). \tag{19}$$

**Proof** We calculate the entropy for the Gibbs measures constructed according to rule (A)

$$\begin{aligned} S_A(\beta, h_A) &= - \frac{dF(\beta, h_A)}{dT} = - \frac{d(-\frac{3}{4} \ln 2 \cosh \beta J)}{dT} = \\ &= \frac{3}{4} \ln(e^{\frac{J}{T}} + e^{-\frac{J}{T}}) - \frac{3}{4} \cdot \frac{J}{T} \cdot \frac{e^{\frac{J}{T}} - e^{-\frac{J}{T}}}{e^{\frac{J}{T}} + e^{-\frac{J}{T}}} = \\ &= \frac{3}{4} \cdot (\ln(2 \cosh(J\beta)) - J\beta \tanh(J\beta)). \end{aligned} \tag{20}$$

**Remark 6.1** In [21], the entropy of the (TI) boundary comdishihe the following formula for  $h = 0$

$$S_{TI}(\beta, 0) = \ln(2 \cosh(J\beta)) - J\beta \tanh(J\beta). \tag{21}$$

We have the following expression according to Theorem 6.1

$$S_A(\beta, h_A) = \frac{3}{4} \cdot (\ln(2 \cosh(J\beta)) - J\beta \tanh(J\beta)),$$

i.e. the entropy of Gibbs measures constructed according to rule (A) differs from  $S_{TI}(\beta, 0)$ .

The entropy calculation for Gibbs measures associated with rule (B) follows the same procedure as for rule (A).

**Theorem 6.2** The entropy of the Gibbs measures for the Ising model defined by rule (B) on the Cayley tree of order three, equals

$$S_B(\beta, h_B) = \frac{3}{4} \cdot (\ln(2 \cosh(J\beta)) - J\beta \tanh(J\beta)). \tag{22}$$

**Remark 6.2** In [21] and according to Theorem 6.2, we get the following

$$S_B(\beta, h_B) = \frac{3}{4} \cdot (\ln(2 \cosh(J\beta)) - J\beta \tanh(J\beta)),$$

i.e. the entropy of the calculated according to the **(B)** is different from the Gibbs measures  $S_{TI}(\beta, 0)$ .

**Corollary 6.1** The following relation is valid between the entropy of the Gibbs measures constructed according to **(A)** and **(B)** and the entropy  $S_{TI}(\beta, 0)$  of the Gibbs measures:

$$S_A(\beta, h_A) = S_B(\beta, h_B) = \frac{3}{4}S_{TI}(\beta, 0).$$

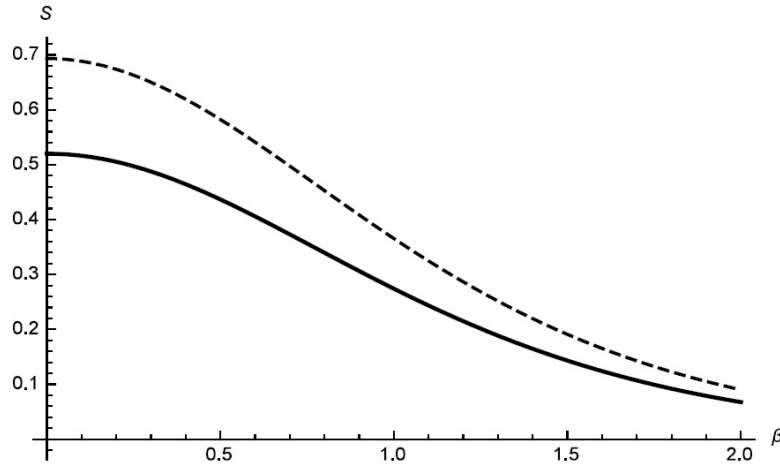


FIG. 5. Entropy  $S_{TI}(\beta, 0)$  (dotted line) and entropy built according to rules **(A)** and **(B)**, i.e.  $S_A(\beta, h_A) = S_B(\beta, h_B)$ (solid line). Here  $J = 1$  and  $k = 3$

**Appendix 1**

Let us now explain how to calculate the proof of Lemma 3.1.

**Proof** Solving system (9) reduces to analyzing the following equation

$$z_1 = \frac{\left(\frac{z_1 + \alpha}{\alpha \cdot z_1 + 1}\right)^3 + \alpha}{\alpha \cdot \left(\frac{z_1 + \alpha}{\alpha \cdot z_1 + 1}\right)^3 + 1}. \tag{23}$$

Simplifying (23), we have

$$(z_1 - 1) \cdot (z_1 + 1) \cdot ((\alpha^3 + \alpha) \cdot z_1^2 + (-\alpha^4 + 6 \cdot \alpha^2 - 1) \cdot z_1 + \alpha^3 + \alpha) = 0. \tag{24}$$

It follows  $z_1^{(0)} = 1$  or

$$(\alpha^3 + \alpha) \cdot z_1^2 + (-\alpha^4 + 6 \cdot \alpha^2 - 1) \cdot z_1 + \alpha^3 + \alpha = 0. \tag{25}$$

According to (9), every positive value of  $z_1$  corresponds to a positive value of  $z_2$ . Therefore, we only need to focus on the positive solutions of equation (25). Equation (25) can be rearranged as follows:

$$\alpha \cdot (\alpha^2 + 1)z_1^2 - (\alpha^4 - 6 \cdot \alpha^2 + 1)z_1 + \alpha \cdot (\alpha^2 + 1) = 0. \tag{26}$$

Denote by  $D$  the discriminant of the equation (26), i.e.

$$D = (\alpha^4 - 6 \cdot \alpha^2 + 1)^2 - 4 \cdot (\alpha^3 + \alpha)^2.$$

*Case I.* Equation (26) have two positive solutions, i.e.

$$\begin{cases} D > 0, \\ \alpha^4 - 6 \cdot \alpha^2 + 1 > 0. \end{cases} \tag{27}$$

After solving the inequalities, we find that

$$\alpha \in (0; 2 - \sqrt{3}) \cup (2 + \sqrt{3}; \infty),$$

the equation (26) has two positive solutions

$$z_1^{(1,2)} = \frac{\alpha^4 - 6 \cdot \alpha^2 + 1 \pm \sqrt{\alpha^8 - 16 \cdot \alpha^6 + 30 \cdot \alpha^4 - 16 \cdot \alpha^2 + 1}}{2 \cdot \alpha \cdot (\alpha^2 + 1)},$$

Inserting these solutions into system (9), we obtain two corresponding solutions

$$z_2^{(1,2)} = \left( \frac{3\alpha^4 - 4\alpha^2 + 1 \pm \sqrt{\alpha^8 - 16\alpha^6 + 30\alpha^4 - 16\alpha^2 + 1}}{\alpha(\alpha^4 - 4\alpha^2 + 3 \pm \sqrt{\alpha^8 - 16\alpha^6 + 30\alpha^4 - 16\alpha^2 + 1})} \right)^3.$$

It is clear that solutions  $z_1^{(1,2)}$  and  $z_2^{(1,2)}$  are positive.

Case 2. Equation (26) has a unique positive solution, i.e.

$$\begin{cases} D = 0, \\ \alpha^4 - 6 \cdot \alpha^2 + 1 > 0. \end{cases} \tag{28}$$

The equation  $D = 0$  yields that  $\alpha_{1,2} = \pm 1$ ,  $\alpha_{3,4} = 2 \pm \sqrt{3}$  and  $\alpha_{5,6} = -2 \pm \sqrt{3}$ . Since  $\alpha \in (0, 1) \cup (1, +\infty)$ , we consider the cases  $\alpha_{3,4} = 2 \pm \sqrt{3}$ . According to the inequality in (28), it is sufficient to consider the case  $\alpha_{3,4} = 2 \pm \sqrt{3}$ . If  $\alpha_{3,4} = 2 \pm \sqrt{3}$  then we get the translation-invariant solution  $(z_1, z_2) = (1, 1)$ .

Case 3. Let us assume that (26) does not have any positive solution, i.e.

$$D < 0, \tag{29}$$

or

$$\begin{cases} D \geq 0, \\ \alpha^4 - 6 \cdot \alpha^2 + 1 \leq 0. \end{cases} \tag{30}$$

It means that if  $\alpha \in (2 - \sqrt{3}; 1) \cup (1; 2 + \sqrt{3})$ , then the equation (26) does not have any positive solution.

**Appendix 2**

The proof of Lemma 4.1 is found using this basic idea using the following algebraic substitutions.

**Proof** Solving system (12) reduces to analyzing the following equation

$$z_2 = \left( \frac{\left( \frac{z_2 + \alpha}{\alpha \cdot z_2 + 1} \right)^2 + \alpha}{\alpha \cdot \left( \frac{z_2 + \alpha}{\alpha \cdot z_2 + 1} \right)^2 + 1} \right)^3. \tag{31}$$

Simplifying the last equation, we receive

$$\begin{aligned} & (z_2 - 1) \cdot (\alpha + 1)^3 \cdot (\alpha^3 \cdot z_2^6 - (\alpha^6 - 3 \cdot \alpha^5 + 6 \cdot \alpha^4 - 14 \cdot \alpha^3 + 6 \cdot \alpha^2 - 3 \cdot \alpha + 1) \cdot z_2^5 - \\ & - (\alpha^6 + 3 \cdot \alpha^5 - 9 \cdot \alpha^4 - 5 \cdot \alpha^3 - 9 \cdot \alpha^2 + 3 \cdot \alpha + 1) \cdot z_2^4 - \\ & - (\alpha^6 + 6 \cdot \alpha^5 - 15 \cdot \alpha^4 - 4 \cdot \alpha^3 - 15 \cdot \alpha^2 + 6 \cdot \alpha + 1) \cdot z_2^3 - \\ & - (\alpha^6 + 3 \cdot \alpha^5 - 9 \cdot \alpha^4 - 5 \cdot \alpha^3 - 9 \cdot \alpha^2 + 3 \cdot \alpha + 1) \cdot z_2^2 - \\ & - (\alpha^6 - 3 \cdot \alpha^5 + 6 \cdot \alpha^4 - 14 \cdot \alpha^3 + 6 \cdot \alpha^2 - 3 \cdot \alpha + 1) \cdot z_2 + \alpha^3) = 0. \end{aligned} \tag{32}$$

It follows that  $z_2^{(0)} = 1$  or

$$\begin{aligned} & \alpha^3 \cdot z_2^6 - (\alpha^6 - 3 \cdot \alpha^5 + 6 \cdot \alpha^4 - 14 \cdot \alpha^3 + 6 \cdot \alpha^2 - 3 \cdot \alpha + 1) \cdot z_2^5 - \\ & - (\alpha^6 + 3 \cdot \alpha^5 - 9 \cdot \alpha^4 - 5 \cdot \alpha^3 - 9 \cdot \alpha^2 + 3 \cdot \alpha + 1) \cdot z_2^4 - \\ & - (\alpha^6 + 6 \cdot \alpha^5 - 15 \cdot \alpha^4 - 4 \cdot \alpha^3 - 15 \cdot \alpha^2 + 6 \cdot \alpha + 1) \cdot z_2^3 - \\ & - (\alpha^6 + 3 \cdot \alpha^5 - 9 \cdot \alpha^4 - 5 \cdot \alpha^3 - 9 \cdot \alpha^2 + 3 \cdot \alpha + 1) \cdot z_2^2 - \\ & - (\alpha^6 - 3 \cdot \alpha^5 + 6 \cdot \alpha^4 - 14 \cdot \alpha^3 + 6 \cdot \alpha^2 - 3 \cdot \alpha + 1) \cdot z_2 + \alpha^3 = 0. \end{aligned} \tag{33}$$

Due to (12), each positive solution  $z_2$  defines a positive solution  $z_1$ . Thus, it is sufficient to consider positive solution of (33). We make a substitution  $\xi = z_2 + \frac{1}{z_2}$  and form the following equation

$$\begin{aligned} & \alpha^3 \cdot \xi^3 + (-\alpha^6 + 3 \cdot \alpha^5 - 6 \cdot \alpha^4 + 14 \cdot \alpha^3 - 6 \cdot \alpha^2 + 3 \cdot \alpha - 1) \cdot \xi^2 + \\ & + (-\alpha^6 - 3 \cdot \alpha^5 + 9 \cdot \alpha^4 + 2 \cdot \alpha^3 + 9 \cdot \alpha^2 - 3 \cdot \alpha + 1) \cdot \xi + \\ & + (\alpha^2 + 1) \cdot (\alpha^4 - 12 \cdot \alpha^3 + 26 \cdot \alpha^2 - 12 \cdot \alpha + 1) = 0. \end{aligned}$$

In the last cubic equation,  $D < 0$ , we know that when  $D < 0$ , the cubic equation has one real root. Let us find this real root. In order to simplify this solution, we make the following substitution

$$\begin{aligned} t = & (8 \cdot \alpha^{18} - 72 \cdot \alpha^{17} + 360 \cdot \alpha^{15} - 1380 \cdot \alpha^{15} + 4320 \cdot \alpha^{14} - \\ & - 11016 \cdot \alpha^{13} + 22944 \cdot \alpha^{12} - 39132 \cdot \alpha^{11} + 54288 \cdot \alpha^{10} - \\ & - 60712 \cdot \alpha^9 + 54504 \cdot \alpha^8 - 39564 \cdot \alpha^7 + 23952 \cdot \alpha^6 - 11448 \cdot \alpha^5 + \\ & + 12 \cdot (-15 \cdot \alpha^{24} + 252 \cdot \alpha^{23} - 2088 \cdot \alpha^{22} + 11568 \cdot \alpha^{21} - 48798 \cdot \alpha^{20} + \\ & + 167328 \cdot \alpha^{19} - 480252 \cdot \alpha^{18} + 1165176 \cdot \alpha^{17} - 2395593 \cdot \alpha^{16} + \\ & + 4179936 \cdot \alpha^{15} - 62049242 \cdot \alpha^{14} + 7861968 \cdot \alpha^{13} - 8527860 \cdot \alpha^{12} + \\ & + 7931520 \cdot \alpha^{11} - 6324768 \cdot \alpha^{10} + 4318848 \cdot \alpha^9 - 2521269 \cdot \alpha^8 + \\ & + 1254636 \cdot \alpha^7 - 527532 \cdot \alpha^6 + 187272 \cdot \alpha^5 - 54954 \cdot \alpha^4 + 13080 \cdot \alpha^3 - \\ & - 2412 \cdot \alpha^2 + 288 \cdot \alpha - 15)^{\frac{1}{2}} + 4536 \cdot \alpha^4 - 1452 \cdot \alpha^3 + 360 \cdot \alpha^2 - 72 \cdot \alpha + 8)^{\frac{1}{3}}. \end{aligned}$$

The result is the following expression:

$$\begin{aligned} \xi = & (t + 4 \cdot \alpha^3 \cdot (\alpha^{12} - 6 \cdot \alpha^{11} + 21 \cdot \alpha^{10} - 61 \cdot \alpha^9 + 141 \cdot \alpha^8 - 237 \cdot \alpha^7 + \\ & + 282 \cdot \alpha^6 - 237 \cdot \alpha^5 + 141 \cdot \alpha^4 - 67 \cdot \alpha^3 + 21 \cdot \alpha^2 - 6 \cdot \alpha + 1))/ \\ & (6 \cdot \alpha^6 \cdot t + 2 \cdot (\alpha^6 - 3 \cdot \alpha^5 + 6 \cdot \alpha^4 - 14 \cdot \alpha^3 + 6 \cdot \alpha^2 - 3 \cdot \alpha + 1)). \end{aligned}$$

By the substitution, we take

$$\begin{aligned} z_2 + \frac{1}{z_2} = & (t + 4 \cdot \alpha^3 \cdot (\alpha^{12} - 6 \cdot \alpha^{11} + 21 \cdot \alpha^{10} - 61 \cdot \alpha^9 + 141 \cdot \alpha^8 - 237 \cdot \alpha^7 + \\ & + 282 \cdot \alpha^6 - 237 \cdot \alpha^5 + 141 \cdot \alpha^4 - 67 \cdot \alpha^3 + 21 \cdot \alpha^2 - 6 \cdot \alpha + 1))/ \\ & (6 \cdot \alpha^6 \cdot t + 2 \cdot (\alpha^6 - 3 \cdot \alpha^5 + 6 \cdot \alpha^4 - 14 \cdot \alpha^3 + 6 \cdot \alpha^2 - 3 \cdot \alpha + 1)). \end{aligned}$$

The last one yields that

$$\begin{aligned} z_2^2 + & ((-4 \cdot \alpha^{15} + 24 \cdot \alpha^{14} - 84 \cdot \alpha^{13} + 244 \cdot \alpha^{12} - 564 \cdot \alpha^{11} + \\ & + 948 \cdot \alpha^{10} - 1128 \cdot \alpha^9 + 948 \cdot \alpha^8 - 564 \cdot \alpha^7 + 268 \cdot \alpha^6 - \\ & - 84 \cdot \alpha^5 + 24 \cdot \alpha^4 - 4 \cdot \alpha^3 - t)/(2 \cdot \alpha^6 - 6 \cdot \alpha^5 + 12 \cdot \alpha^4 - 28 \cdot \alpha^3 + \\ & + 6 \cdot \alpha^2 \cdot t + 12 \cdot \alpha^2 - 6 \cdot \alpha + 2)) \cdot z_2 + 1 = 0. \end{aligned}$$

We find the discriminant of the last quadratic equation

$$\begin{aligned} D = & ((-4 \cdot \alpha^{15} + 24 \cdot \alpha^{14} - 84 \cdot \alpha^{13} + 244 \cdot \alpha^{12} - \\ & - 564 \cdot \alpha^{11} + 948 \cdot \alpha^{10} - 1128 \cdot \alpha^9 + 948 \cdot \alpha^8 - \\ & - 564 \cdot \alpha^7 + 268 \cdot \alpha^6 - 84 \cdot \alpha^5 + 24 \cdot \alpha^4 - 4 \cdot \alpha^3 - \\ & - t)/(2 \cdot \alpha^6 - 6 \cdot \alpha^5 + 12 \cdot \alpha^4 - 28 \cdot \alpha^3 + 6 \cdot \alpha^2 \cdot t + \\ & + 12 \cdot \alpha^2 - 6 \cdot \alpha + 2))^2 - 4. \end{aligned}$$

We introduce the notation

$$\begin{aligned} p = & (-4 \cdot \alpha^{15} + 24 \cdot \alpha^{14} - 84 \cdot \alpha^{13} + 244 \cdot \alpha^{12} - 564 \cdot \alpha^{11} + \\ & + 948 \cdot \alpha^{10} - 1128 \cdot \alpha^9 + 948 \cdot \alpha^8 - 564 \cdot \alpha^7 + 268 \cdot \alpha^6 - \\ & - 84 \cdot \alpha^5 + 24 \cdot \alpha^4 - 4 \cdot \alpha^3 - t)/(2 \cdot \alpha^6 - 6 \cdot \alpha^5 + 12 \cdot \alpha^4 - 28 \cdot \alpha^3 + \\ & + 6 \cdot \alpha^2 \cdot t + 12 \cdot \alpha^2 - 6 \cdot \alpha + 2). \end{aligned}$$

As a result

$$z_2^2 + p \cdot z_2 + 1 = 0. \quad (34)$$

The discriminant of (34) is as follows:

$$D = p^2 - 4.$$

Case 1. Let (34) have two positive solutions, i.e.

$$\begin{cases} D > 0, \\ p < 0. \end{cases} \quad (35)$$

Case 2. Let (34) have a unique positive solution, i.e.

$$\begin{cases} D = 0, \\ p < 0. \end{cases} \quad (36)$$

Case 3. Assume that (34) does not have any positive solution, i.e.

$$D < 0, \quad (37)$$

or

$$\begin{cases} D \geq 0, \\ p \geq 0. \end{cases} \quad (38)$$

## References

- [1] Bleher P.M. and Ganikhodjaev N.N. On pure phases of the Ising model on the Bethe lattice. *Theory Probab. Appl.*, 1990, **35**, P. 216–227.
- [2] Rozikov U.A. *Gibbs measures on Cayley trees*, (Singapore: World Scientific), 2013.
- [3] Zachary S. Countable state space Markov random fields and Markov chains on trees, *Ann.Prob.*, 1983, **11**, P. 894–903.
- [4] Ganikhodjaev N.N., Rozikov U.A. A description of periodic extremal Gibbs measures of some lattice models on the Cayley tree. *Theor. Math. Phys.*, 1997, **111**, P. 480–486.
- [5] Rozikov U.A. Partition structures of the group representation of the Cayley tree into cosets by finite-index normal subgroups and their applications to the description of periodic Gibbs distributions. *Theor. Math. Phys.*, 1997, **112**, P. 929–933.
- [6] Rozikov U.A. Description uncountable number of Gibbs measures for inhomogeneous Ising model. *Theor. Math. Phys.*, 1999, **118**, P. 95–104.
- [7] Bleher P.M., Ganikhodjaev N.N. On pure phases of the Ising model on the Bethe lattice. *Theory Probab.Appl.*, 1990, **35**, P. 216–227.
- [8] Rozikov U.A., Rahmatullaev M.M. Description of weakly periodic Gibbs measures of the Ising model on the Cayley tree. *Theor. Math. Phys.*, 2008, **156**, P. 1218–1227.
- [9] Rozikov U.A., Rahmatullaev M.M. On weak periodic Gibbs measures of the Ising model on a Cayley tree, Dokl. AN Uzbekistan, 2008, **4**, P. 12–15.
- [10] Rahmatullaev M.M. Ising model on trees:  $(k_0)$ - non translation-invariant Gibbs measures. *Journal of Physics: Conference Series*, 2017, **819**, P. 012019.
- [11] Rakhmatullaev M.M., Samijonova N.D. Translation-invariant  $p$ -adic quasi Gibbs Measures for the Potts Model with an external field on the Cayley Tree. *Nanosystems: Physics, Chemistry, Mathematics*, 2025, **16**(2), P. 164–175.
- [12] Rahmatullaev M.M., Khakimov O.N., Tukhtabaev A.M. A  $p$ -adic generalized Gibbs measure for the Ising model on a Cayley tree. *Theoretical and Mathematical Physics*, 2019, **201**(1), P. 1521–1530.
- [13] Rahmatullaev M.M., Tukhtabaev A.M. Non periodic  $p$ -adic generalized Gibbs measure for Ising model,  $p$ -Adic Numbers, Ultrametric Analysis and Applications, 2019, **11**(4), P. 319–327.
- [14] Rahmatullaev M.M., Tukhtabaev A.M. Some non-periodic  $p$ -adic generalized Gibbs measures for the Ising model on a Cayley tree of order  $k$ . *Mathematical Physics, Analysis and Geometry*, 2023, **26**(22).
- [15] Rozikov U.A., Rakhmatullaev M.M. Ising model on Cayley tree: a new class of Gibbs measures and their comparison with known ones. *J. Stat. Mech.*, 2017, P. 093205.
- [16] Mavlonov I.M., Sattarov A.M., Karimova S.A., Haydarov F.H. On solutions to nonlinear integral equation of the Hammerstein type and its applications to Gibbs measures for continuous spin systems. *Nanosystems: Physics, Chemistry, Mathematics*, 2024, **15**(1), P. 23–30.
- [17] Rahmatullaev M.M., Egamov D.O. Translation-invariant Gibbs measures for the mixed spin-1/2 and spin-1 Ising model with an external field on a Cayley tree. *Nanosystems: Physics, Chemistry, Mathematics*, 2024, **15**(5), P. 576–585.
- [18] Friedli S., Velenik Y. A Concrete Mathematical Introduction, Statistical Mechanics of Lattice Systems, Cambridge University Press, 2017.
- [19] Georgii H.O. *Gibbs Measures and Phase Transitions*. de Gruyter, Berlin (1998)
- [20] Feynman R.P. There's plenty of room at the bottom, *Engineering and Science*, 1960, **5**(23), P. 22–36.
- [21] Gandolfo D., Rahmatullaev M.M., Rozikov U.A. Ruiz J. On Free Energies of the Ising Model on the Cayley Tree. *J. Stat Phys*, 2013, **150**, P. 1201–1217.
- [22] Semkin S.V., Smagin V.P., Tarasov V.S. Frustrations in a Diluted Ising Magnet on the Bethe Lattice. *J. Exp. Theor. Phys.*, 2022, **134**, P. 713–719.
- [23] Semkin S.V., Smagin V.P. Free energy, entropy, and magnetization of a onedimensional Ising model of a diluted magnet. *Theor. Math. Phys.*, 2023, **217**, P. 17881794.
- [24] Mukhamedov F., Akin H., and Khakimov O. Gibbs measures and free energies of IsingVannimenus model on the Cayley tree. *Journal of Statistical Mechanics: Theory and Experiment*, 2017.
- [25] Akin H. A novel computational method of the free energy for the Ising model on Cayley tree of order three. *Chin. J. Phys.*, 2022, **77**, P. 2276–2287.
- [26] Akin H. Calculation of some thermodynamic quantities for the Ising model on a  $k$ th order Cayley tree. *Physica B*, 2023, **662**.
- [27] Akin H. Investigation of thermodynamic properties of mixed-spin  $(2,1/2)$  Ising and Blum-Capel models on a Cayley tree. *Chaos, Solitons, Fractals*, 2024, **184**, P. 114980.
- [28] Akin H. Calculation of the free energy of the Ising model on a Cayley tree via the self-similarity method. *Axioms*, 2022, **11**, P. 703.
- [29] Akin H. Quantitative behavior of  $(1,1/2)$ -MSIM on a Cayley tree. *Chin. J. Phys.*, 2023, **83**, P. 501–514.
- [30] Akin H. The classification of disordered phases of mixed spin  $(2,1/2)$  Ising model and the chaoticity of the corresponding dynamical system, *Chaos, Solitons, Fractals*, 2023, **167**.
- [31] Rahmatullaev M.M., Burxonova Z.A. Constructive Gibbs measures for the Ising model on the Cayley tree. *Reports of Mathematical Physics*, 2024, **93**(3), P. 361–370.

- [32] Rozikov U.A., Rahmatullaev M.M. Weakly periodic ground states and Gibbs measures for the Ising model with competing interactions on the Cayley tree. *Theor. Math. Phys.*, 2009, **160**, P. 1291–1299.
- [33] Rahmatullaev M.M., Dekhkanov J. Existence weakly periodic Gibbs measures for the Ising model on the Cayley tree of order two. *Vladikavkaz Mathematical Journal*, 2021, **23**(4), P. 77–88.
- [34] Rahmatullaev M.M. On weakly periodic states and Gibbs measures of the Ising model on the Cayley tree, Fan, Tashkent, 2024. (in Russian)
- [35] Preston C. Gibbs States on Countable Sets. Cambridge University Press, London, 1974.
- [36] Esfarjani K., Mansoori G.A. Statistical mechanical modeling and its application to nanosystems. *Handbook of Theoretical and Computational Nanotechnology*, 2006, II(14), P. 1-45.
- [37] Hill L. *Thermodynamics of Small Systems*, W. A. Benjamin, New York, 1963.
- [38] Hill T.L. A Different Approach to Nanothermodynamics. *Nano Letters*, **1**, 2001, P. 273–275.
- [39] Mansoori G.A. Proceedings of the first Conference on Nanotechnology-The Next Industrial Revolution, 2002, **2**, P. 345.

---

*Submitted 18 March 2025; revised 10 April 2025; accepted 15 April 2025*

*Information about the authors:*

*Muzaffar M. Rahmatullaev* – V.I. Romanovskiy Institute of Mathematics, Uzbekistan Academy of Sciences, 4-b, University str, 100174, Tashkent, Uzbekistan; New Uzbekistan University, 100000, Tashkent, Uzbekistan; ORCID 0000-0003-2987-7714; mrahmatullaev@rambler.ru

*Zulxumor A. Burxonova* – Namangan State University, 161, Boburshox str, 160107, Namangan, Uzbekistan; Namangan State Technical University, 12, Islom Karimov str, 160103, Namangan, Uzbekistan; ORCID 0009-0000-7212-1598; zulxumorburxonova4@gmail.com

*Conflict of interest:* the authors declare no conflict of interest.

## Theoretical study of the effective g-factor of Cd<sub>1-x</sub>Mn<sub>x</sub>Te quantum wire under the combined effects of the applied magnetic field, spin-orbit coupling, and exchange effects

Mohammad Elsaid, Diana Dahliah, Ayham Shaer, Mahmoud Ali

Department of Physics, An-Najah National University, Palestine

Corresponding author: Mohammad Elsaid, [mkelsaid@najah.edu](mailto:mkelsaid@najah.edu)

**ABSTRACT** In this paper, the energy formula for charge carrier ( $e$ ) confined in a diluted magnetic semiconductor (DMS) quantum well QW made from Cd<sub>1-x</sub>Mn<sub>x</sub>Te is generated and utilized to calculate the Density of States (DOS) and the Lande g-factor. The Landau levels in a quantum wire that is placed in uniform magnetic field along its axis, taking into account the presence of Rashba spin-orbit interaction and exchange effect, are explored. These effects have altered the DOS and the Landau levels. The electron g-factor for the lowest state is explored. Our results show that the g-factor is strongly affected by the combined effects of magnetic field and Rashba spin-orbit interaction strengths. The g-factor can vary in a wide range of expands for the bulk value of 2 up to 300, which makes it a good candidate for spintronic applications.

**KEYWORDS** Lande g-factor, Rashba effect, magnetic field, density of states

**ACKNOWLEDGEMENTS** This research receives funding from An-Najah National University Grant No. ANNU-2219-Sc0n1

**FOR CITATION** Elsaid M., Dahliah D., Shaer A., Ali M. Theoretical study of the effective g-factor of Cd<sub>1-x</sub>Mn<sub>x</sub>Te quantum wire under the combined effects of the applied magnetic field, spin-orbit coupling, and exchange effects. *Nanosystems: Phys. Chem. Math.*, 2025, **16** (3), 274–281.

### 1. Introduction

At the nanoscale, electrons in nanostructures behave differently compared to bulk materials. The two main reasons cause the properties of nanomaterials to significantly deviate from those of bulk materials are the effects of quantum confinement and the increase in the relative surface area to volume ratio. These factors can alter or enhance the properties such as reactivity, as well as the optical, and magnetic characteristics of nanomaterials [1–5]. The optical and electrical characteristics of low-dimensional semiconductor structures such as quantum wires have attracted considerable interest in recent years due to their potential technological applications [6, 7]. The spin-dependent phenomena in quantum wires (QW) have promoted the implementation of these nanowires as potential building blocks in spin electronic devices and future quantum devices [7–9]. Researchers have been exploring nanowires from various materials, well-developed material synthesis, and fabrication techniques have enabled the production of high-quality quantum wires with precise control over their dimensions and properties. For example, chemical precipitation, and laser ablation has been used to produce high-quality nanowires [10, 11].

It has been noticed that the electron spin plays a crucial role in influencing the electrical and optical properties of QW semiconductor structures. Numerous theoretical studies have offered deeper insights into the electrical, dynamical and thermal properties in one-dimensional systems. Kasapoglu et al. studied the combined effects of electric and magnetic fields on the optical absorption coefficients and refractive index changes in GaAs nanowires using the effective-mass approximation and the compact density-matrix approach [12]. A. Bouazra et al. investigated the stability of quantum wire with respect to its shape and size. They examined the optical properties, as well as the energy levels of electrons and holes, along with their corresponding wave functions in various shapes of InAs quantum wires [13]. R. Khordad studied the influence of the external magnetic field and the Rashba effect on the optical properties of 1D quantum wire [14]. Y. Khoshbakht investigated the thermodynamic properties of a nanowire under the presence of the Rashba spin-orbit interaction and external magnetic field. The study provided analytical expressions for the mean energy, the free energy, the specific heat, the entropy, and the magnetic susceptibility of nanowires in the presence of gate-controlled Rashba spin-orbit interaction and an in-plane magnetic field [15]. B. H. Mehdiyev investigated the effect of finite temperature on the electrical conductance of diluted magnetic semiconductor cylinders made of CdTe [16].

One of the essential material parameters of a QW is the effective Lande g-factor. This parameter represents the response of a material to a magnetic field. The study of the effective Lande g-factor in semiconductor nanowires has received great attention because of its importance in manipulating the spin splitting of carrier bands. Its effect on device

performance should be considered. In particular, exploring the g-factor provides a deeper understanding of the behavior of electrons in magnetic fields and helps scientists assist these findings in practical applications.

Many studies have been carried out on the effective Lande g-factor in low-dimensional structures. Several theoretical and experimental studies examine the effect of spin-orbit coupling and the magnetic field on the g-factor. The effects of the magnetic field and Rashba effect on the Lande g-factor in the InAs quantum wire have been examined [17]. In Ref. [18], the authors have explored the g-factor in diluted magnetic semiconductor (DMS) quantum well with parabolic potential in the presence of an external perpendicular magnetic field, the study shows that the g-factor increases with increasing the magnetic field due the increment in the strength of spin-orbit coupling [18]. The authors examined the electron g-factor for various sub-bands in quantum wire in Ref. [19], the effects of electric field, magnetic field, and Rashba spin-orbit interaction strength on g-factor have been explored.

Rogério de Sousa et. al found that the g-factor of a heterojunction quantum dot is very sensitive to its radius and magnetic field arising from the interplay between Rashba and Dresselhaus spin-orbit interactions [20]. Rodrigues et al. investigated the optical properties of CdMnTe/CdTe heterostructures grown on Si substrate, highlighting the effects of quantum confinement and structural roughness on emission spectrum [21].

In this work, we will study the g-factor in Cadmium Telluride material that doped with Manganese Cd<sub>1-x</sub>Mn<sub>x</sub>Te nanowires, where  $x$  is the fraction of moles of Mn ions. The spin splitting of the sub-bands can be enhanced by introducing magnetic ions (Mn). The strong s-d exchange interaction between the carriers and the local magnetic ions can be enhanced by an external magnetic field [22, 23]. The Lande g-factor in Cd<sub>1-x</sub>Mn<sub>x</sub>Te nanowires can be controlled by varying the magnetic field, the concentration of Mn, the radius of the wire and it's temperature. It has been recorded that the Lande g-factor in CdTe at zero magnetic field is  $-0.5$  while for Cd<sub>0.98</sub>Mn<sub>0.02</sub>Te, it goes to 100 at 4 K [24]. Afanasiev et al. explored the behavior of the electron g-factor due to the s-d exchange interaction between electrons and manganese ions in coupled quantum wells of CdTe and CdMnTe, where the dependence of electron g-factor on the barrier thickness and temperature is experimentally investigated [25].

This work aims to compute and investigate the dependence of energy spectra Density of States (DOS) and effective Lande g-factor of CdMnTe QW. A theoretical examination of the Lande g-factor in a CdMnTe QWs is carried out, considering the effects of an external magnetic field, with particular emphasis on the Rashba effect and the exchange interactions.

## 2. Theoretical model

The Hamiltonian of an electron in quantum wire (QW) of a given radius  $\rho$  under an external magnetic field ( $B$ ) in the  $z$ -direction that is parallel to the axis of the wire that represented the kinetic energy operator term and confinement potential term is given by [18]:

$$H = \frac{-\hbar^2}{2m^*} \left( \frac{1}{\rho^2} \frac{\partial^2}{\partial \varphi^2} + \frac{\partial^2}{\partial z^2} \right) - i\hbar \frac{eB}{2m^*} \frac{\partial}{\partial \varphi} + \frac{e^2 B^2 \rho^2}{8m^*} + \frac{1}{2} g^* \mu_B B \sigma_z + \frac{-1}{2} S_0 B_{5/2} \left( \frac{S g_{Mn} \mu_B B}{K_B (T + T_0)} \right) N_0 x J_{s-d} \sigma_z + \frac{\alpha}{\hbar} [\vec{\sigma} \times \vec{P}] \cdot \vec{n}. \quad (1)$$

Where, in this model, the vector potential induced by the magnetic field is defined as  $A = \left( \frac{-By}{2}, \frac{Bx}{2}, 0 \right)$ . The constants that are in the Hamiltonian are defined as  $g^*$  and  $m^*$  donated the electron effective g-factor and effective mass, respectively.  $\sigma_z$  denotes the Pauli spin matrix along the  $z$ -axis. The third term represents the Zeeman effect, that will lead to extra energy splitting in the spectrum. The fourth term indicates the exchange effect which describes the s-d exchange Heisenberg interaction between the conduction electrons and Mn ions. Where  $S_0$  is the effective spin,  $B_{5/2}$  is the Brillouin function,  $S$  is the spin of the localized electrons of Mn ions,  $g_{Mn}$  is the g-factor of Mn,  $k_B$  is the Boltzmann constant,  $N_0$  is the density of unit cells and  $J_{s-d}$  is constant which describe the exchange interaction according to the s-d exchange integral. The last term is the Rashba term which significantly influences the magnetic properties of Mn-doped CdTe wire. Here  $\vec{P}$  is the momentum operator,  $\alpha$  is the strength of the spin orbit coupling,  $\vec{\sigma} = (\sigma_x, \sigma_y, \sigma_z)$  denotes the Pauli spin matrices and  $\vec{n}$  is the unit normal to the surface.

After determining each term of the Hamiltonian, the full Hamiltonian is written in a matrix form as follows:

$$\begin{pmatrix} H_{11} - \varepsilon & \alpha e^{i\varphi} \frac{\partial}{\partial z} \\ -\alpha e^{i\varphi} \frac{\partial}{\partial z} & H_{22} - \varepsilon \end{pmatrix} \begin{pmatrix} \psi_1(\varphi, z) \\ \psi_2(\varphi, z) \end{pmatrix}, \quad (2)$$

where,

$$H_{11} = -\frac{\hbar}{2m^*} \left( \frac{1}{\rho^2} \frac{\partial^2}{\partial \varphi^2} + \frac{\partial^2}{\partial z^2} \right) - i\hbar \frac{eB}{2m^*} \frac{\partial}{\partial \varphi} + \frac{e^2 B^2 \rho^2}{8m^*} - \frac{i\alpha}{\rho} \frac{\partial}{\partial \varphi} + \frac{eB\rho}{2\hbar c} \alpha + \frac{1}{2} g^* \mu_B B + 3A,$$

$$H_{22} = -\frac{\hbar}{2m^*} \left( \frac{1}{\rho^2} \frac{\partial^2}{\partial \varphi^2} + \frac{\partial^2}{\partial z^2} \right) - i\hbar \frac{eB}{2m^*} \frac{\partial}{\partial \varphi} + \frac{e^2 B^2 \rho^2}{8m^*} + \frac{i\alpha}{\rho} \frac{\partial}{\partial \varphi} - \frac{eB\rho}{2\hbar c} \alpha - \frac{1}{2} g^* \mu_B B - 3A.$$

$A$  is given by  $\frac{1}{6} S_0 B_{5/2} \left( \frac{S g_{Mn} \mu_B B}{K_B (T + T_0)} \right) N_0 x J_{s-d}$ , and the wave function is  $\psi_n(\varphi, z) = e^{ik_z z} e^{in\varphi} f$  which is the product of plane wave with angular part.

By diagonalizing the Hamiltonian Matrix, the energy dispersion relation for confined electron of the two sub-bands of each index ( $n$ ) found to be:

$$E_{n\mp} = \frac{\hbar^2(2K^2 - \gamma_1 - \gamma_2 + \gamma_3 + \gamma_4)}{4m\rho^2} \mp \frac{1}{4m\rho} \sqrt{(4mK\alpha)^2 + \hbar^4(\gamma_1 - \gamma_2 - \gamma_3 + \gamma_4)^2}, \quad (3)$$

$$\gamma_3 = n \left( \rho^2 \frac{eB}{\hbar} + \frac{2m\alpha\rho}{\hbar^2} + n \right), \quad (4)$$

$$\gamma_4 = n \left( \rho^2 \frac{eB}{\hbar} - \frac{2m\alpha\rho}{\hbar^2} + n + 1 \right) \quad (5)$$

$$\gamma_1 = -\frac{mg\mu_B B \rho^2}{\hbar^3} - \frac{6Am\rho^2}{\hbar^2} + \left( -\frac{\alpha m \rho^3}{\hbar^2} - \frac{\rho^4}{4} \right) \frac{eB}{\hbar} \quad (6)$$

$$\gamma_2 = \frac{mg\mu_B B \rho^2}{\hbar^3} + \frac{6Am\rho^2}{\hbar^2} + \left( \frac{\alpha m \rho^3}{\hbar^2} - \frac{\rho^4}{4} \right) \frac{eB}{\hbar}. \quad (7)$$

The energy in Eq. (3) depends on the radius of the nanowire, the strength of the external magnetic field, the Rashba parameter, the magnetic ion concentrations and the temperature.

The energy dispersion relation is used to calculate the density of states DOS of the electrons in the CdTe QW. The DOS is defined mathematically as the delta function and it can be written in terms of Green's function as follows

$$\text{DOS}(E) = -\frac{1}{\pi} \sum_E \text{Im}(G(E, \epsilon)), \quad (8)$$

where  $E$  is the energy, and  $\epsilon$  is a very small parameter. Green's function is defined as:

$$G(E, \epsilon) = \frac{1}{H - E + i\epsilon}. \quad (9)$$

In addition to previous quantities, the effective Lande g-factor ( $g$ ) is computed for the low-lying state using the relation

$$g = \frac{E_0(\uparrow) - E_0(\downarrow)}{\mu_B B}. \quad (10)$$

### 3. Results and discussions

In this section, we present the computed results for Landau energies of an electron confined in a cylindrical quantum wire under the presence of an external magnetic field, for different ranges of physical parameters. In the following computations, the values of the parameters in the energy expression are as follows:  $S = 5/2$  corresponding to the spins of the localized electrons of Mn ions, the g-factor of Mn  $g_{Mn} = 2$ , the effective spin  $S_0 = 1.97$ ,  $T_0 = 3K$ ,  $m^* = 0.096m_e$ ,  $J_{s-d} = 220$  meV, and  $g^* = -1.47$ . These values are taken from the literature [26].

In Fig. 1, the eigenenergies of different states range from  $n = -2$  to  $n = 2$  are plotted against the applied magnetic field for (a) in the presence of Rashba effect and (b) in the presence of Rashba and exchange effects for the two sublevels of each state: (spin up: solid line, and spin down: dotted line). The plot shows that the magnitude of the energy increases with increasing the external magnetic field, this can be explained as the increment of the magnetic field will enhance the confinement potential on the electron, so the energy splitting will be increased as it is expected.

The effect of the Rashba parameter ( $\alpha$ ) on the eigenenergies has been taken into account, Fig. 1(a) shows the enactment in the Rashba constant  $\alpha$  from 50 to 100 meV·nm changes the magnitude of the energy levels (red for  $\alpha = 50$  meV·nm and blue for 100 meV·nm), Rashba effect shifts the energy of the states with spin down to higher energy values, while shifting the energy of spin-up states to less positively energy under given value of the magnetic field. In Fig. 1(b), we show the exchange effect, in the presence of the Rashba effect, the exchange term has different influence on shifting the energy of the sublevels in the presence of the magnetic field compared to the Rashba term. By enhancing the exchange interaction through an increase in Mn ions, the spin-down states shift to lower energy levels, while the spin-up states move to higher energy levels. The energy change is due to the exchange term in the Hamiltonian being linearly proportional to the number of Mn ions in the CdTe nanowire. Furthermore, Fig. 1 demonstrates that the crossing point (degeneracy point) between the sublevels of the ground state shifts to higher magnetic field values as the molar concentration of Mn is increased. With increasing the magnetic field, energy levels corresponding to different quantum numbers (different sub bands). When such a crossing occurs, the ground state can switch to a different quantum number.

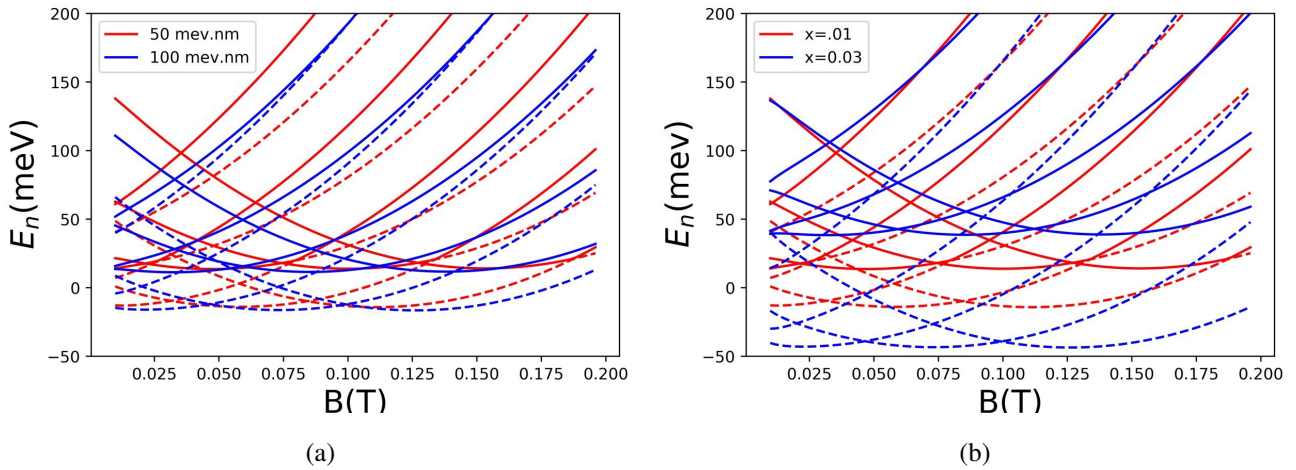


FIG. 1. The low-lying energy of states as a function of magnetic field (spin-up states in solid lines while spin-down in dashed lines) (a) in the presence of spin-orbit interaction only (red:  $\alpha = 50 \text{ meV}\cdot\text{nm}$ , blue:  $100=50 \text{ meV}\cdot\text{nm}$ ) (b) In the presence of the combined effect of RSOI and exchange effects (red:  $x = 0.01$ ,  $x = 0.03$ )

The density of states  $DOS(E)$ , which represents the number of states per unit of energy, is a fundamental property in solid-state physics and condensed matter. It is used to study electronic structure and carrier concentration, which, in turn, determine the type of matter and its conductivity. Therefore, we highlight the effects of Rashba and the exchange term on the density of the states of electrons.

Figure 2 displays the density of states  $DOS$  as a function of energy. Fig. 2(a) represents the density of states of spin up and spin down as a function of energy for  $Cd_{0.98}Mn_{0.02}Te$  of radius 10 nm in the presence of an external magnetic field of 1 T taken into account the Rashba effect of ( $\alpha = 50 \text{ meV}\cdot\text{nm}$ ). The presence of the Rashba spin orbit interaction lifts the degeneracy in the states, and as it can be noticed the number of states is more at low energy values. The Rashba spin orbit interaction reduces the difference in energy between the spin up and the spin down states as can be seen in Fig. 2(a). Also, it can be noticed at a given value of energy, it is more preferred to occupy the spin-up state compared to the spin-down state as the spin-up state has lower energy compared to the spin-down state. It's evident from the comparison between Fig. 2(a and b) after enhancing the exchange effect, by increasing  $x$  from 0.02 to 0.04, the degeneracy between the states are removed. By making a comparison between Fig. 2(a and b), it can be noticed that the separation in  $DOS$  peaks for the spin down levels is much larger compared to spin up.

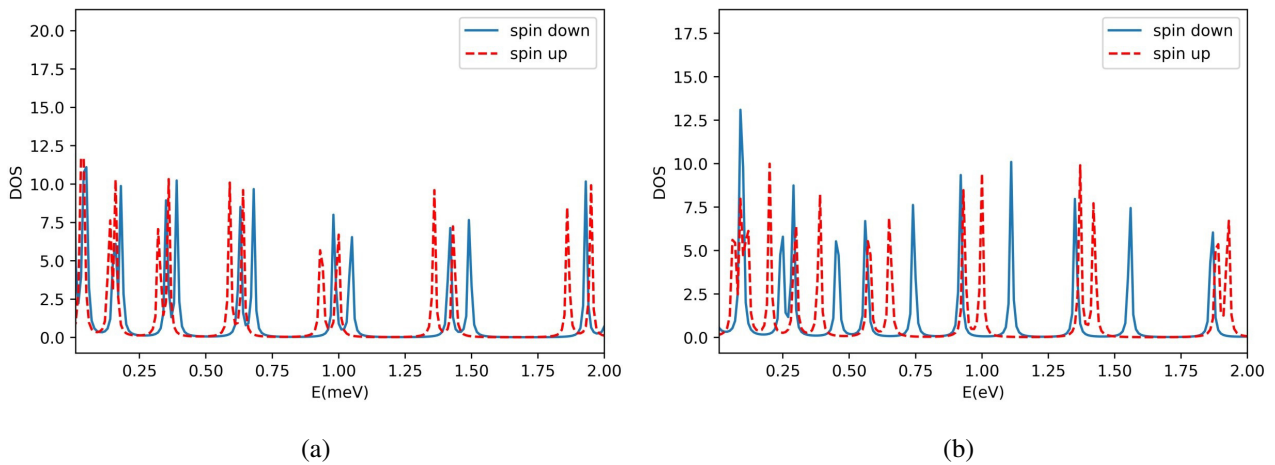


FIG. 2. The density of states of spin up and spin down as a function of energy for (a)  $Cd_{0.98}Mn_{0.02}Te$  (b)  $Cd_{0.96}Mn_{0.04}Te$  QW of radius 10nm in the presence of an external magnetic field of 1 T

The effective Lande  $g$ -factor of the electron in quantum wire made from CdMnTe (QW) under an external magnetic field ( $B$ ) in the  $z$ -direction that is parallel to the axis as a function of the radius of the confinement  $\rho$ , magnetic field ( $B$ ), the Rashba parameter ( $\alpha$ ), Mn ions concentration ( $x$ ), and temperature ( $T$ ) is examined.

In Fig. 3, the effective Lande  $g$ -factor has been plotted as a function of the QW radius for Cd<sub>0.99</sub>Mn<sub>0.01</sub>Te in the presence of an external magnetic field of 1 T taking into account the Rashba spin orbit interaction ( $\alpha = 50$  meV·nm). From Fig. 3, it is clear that as the radius of the confinement increases the  $g$ -factor decreases, and it reaches its bulk value for large values of  $\rho$ . It can be noticed that by modulating the radius of the QW, the  $g$ -factor can be tuned in a range from 2 to 200 which makes it a suitable for a wide range of applications. However, for experimental implementation, other factors should be considered, particularly, strain effects. Additional factors such as structural disorder, interfaces, and lattice strain can influence the effective  $g$ -factor. Disorder and impurity scattering may cause a modifying in the spin splitting effects induced by the Rashba spin-orbit interaction and exchange coupling. Similarly, strain in the crystal lattice can lift band degeneracies and alter the spin-orbit coupling strength, thereby affecting the  $g$ -factor. While these effects are beyond the scope of the present analytical model, they are crucial in realistic systems and should be taken into account when interpreting experimental data or designing spintronic devices based on Mn-doped CdTe nanostructures.

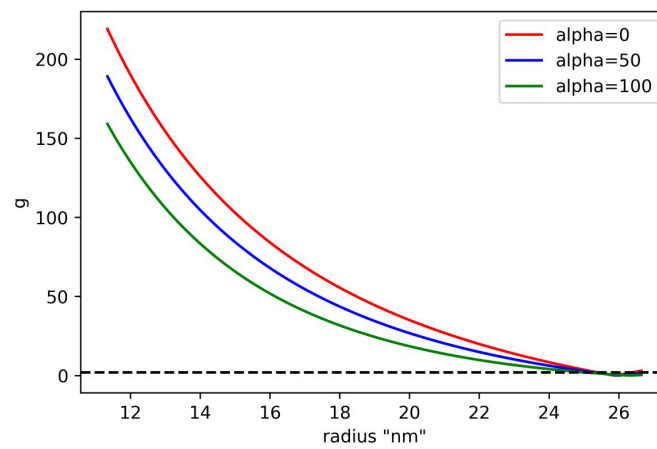


FIG. 3. The effective Lande  $g$ -factor vs. QW radius of for Cd<sub>0.99</sub>Mn<sub>0.01</sub>Te in the presence of an external magnetic field of 1 T

In Fig. 4, the effective Lande  $g$ -factor has been plotted as a function of the magnetic field ( $B$ ) for Cd<sub>0.98</sub>Mn<sub>0.02</sub>Te of radius 30nm in the presence of external magnetic field taken into account the Rashba effect ( $\alpha$  ranges from 50 up to 150 meV·nm). In CdTe QWs, in the absence of Rashba spin-orbit interaction, the effective  $g$ -factor increases with the applied magnetic field. This increase is attributed to the enhancement of the carrier confinement potential induced by the magnetic field. However, this confinement-induced enhancement of the  $g$ -factor saturates beyond a magnetic field strength of approximately 3 T. This trend is consistent with previous theoretical and experimental studies [23]. When the Rashba SOI is introduced, the  $g$ -factor exhibits a decreasing trend with increasing Rashba coupling strength ( $\alpha$ ), due to the reduced spin splitting, as illustrated in Fig. 1. The influence of Rashba SOI is particularly prominent at low magnetic fields. For instance, at  $\alpha = 50$  meV·nm, the SOI dominates for magnetic fields below 0.4 T, resulting in a decrease in the  $g$ -factor as the magnetic field increases. Above 0.4 T, the magnetic confinement becomes the dominant factor, leading to an increase in the  $g$ -factor. This behavior is clearly observed for  $\alpha = 50$  meV·nm and  $\alpha = 100$  meV·nm, as shown in Fig. 4.

For fixed parameters,  $\rho = 30$  nm,  $B = 1$  T, the SOI can be manipulated by changing the value of  $\alpha$ . The SOI strength effect on the Lande  $g$ -factor has been investigated in Fig. 5. In the first case, where the exchange interaction is neglected, a QW composed of CdTe is considered (represented by the red line). The effective  $g$ -factor decreases with increasing Rashba spin-orbit coupling strength ( $\alpha$ ). This behavior arises from the enhanced spin-orbit interaction, which reduces the energy splitting between the spin-up and spin-down states of the ground subband, thereby leading to a lower  $g$ -factor. However, when the exchange interaction is included the behavior of the  $g$ -factor changes. For small Mn concentrations, at low values of  $\alpha$ , the Rashba SOI and the exchange interaction act in opposition regarding the spin splitting of the ground state. As a result, increasing  $\alpha$  initially reduces the  $g$ -factor, reaching a minimum where the opposing effects remove the splitting and lead to a degenerate ground state, leading to an effective  $g$ -factor close to zero. Beyond this critical value of  $\alpha$ , the Rashba SOI becomes dominant, and both interactions contribute constructively to the spin splitting, resulting in an increase in the  $g$ -factor with further increases in  $\alpha$ , as illustrated in Fig. 5. In the case of stronger exchange interaction (e.g., higher Mn concentration, represented by the black line), the exchange term dominates. Here, the  $g$ -factor increases with increasing  $\alpha$ . This behavior is evident for Mn concentrations of  $x = 0.01$  and  $x = 0.05$ . The observed increase

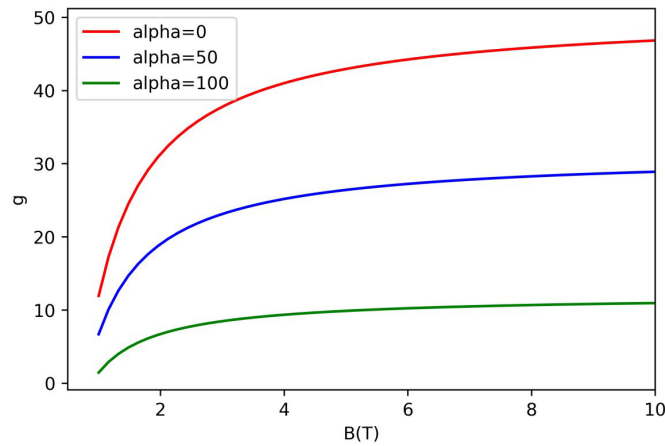


FIG. 4. Effective Lande g-factor vs. magnetic fields for CdTe QW at different values of the Rashba parameter ( $\alpha = (0.50 \text{ and } 100 \text{ meV}\cdot\text{nm})$ )

in g-factor can be explained by the exchange interaction, which enhances the energy splitting between spin-up and spin-down states in the ground subband as the Mn ion concentration increases. Since the g-factor is directly proportional to this energy splitting, it increases accordingly.

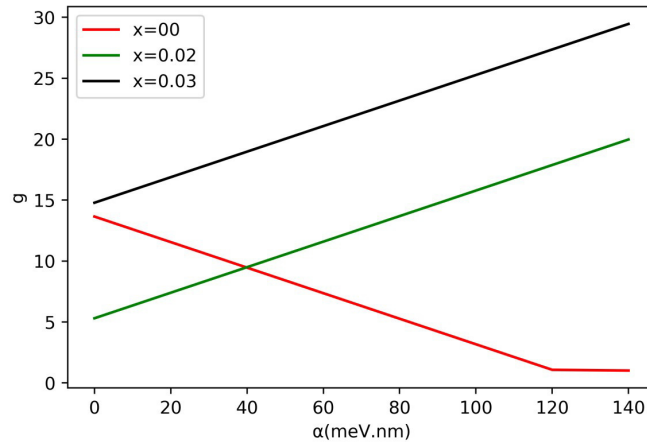


FIG. 5. Effective Lande g-factor vs. Rashba coefficient ( $\alpha$ )

The influence of exchange interaction is also investigated. Fig. 6 illustrates the dependence of the effective g-factor on the Mn ion concentration ( $x$ ) at various temperatures below 20 K. For a fixed temperature, the g-factor initially decreases with increasing Mn molar concentration in the low- $x$  regime. This decrease is attributed to the dominance of the Rashba SOI, which suppresses the spin splitting. As  $x$  increases further, the g-factor reaches a minimum (critical value) and subsequently increases approximately linearly with increasing  $x$ , due to the growing dominance of the exchange interaction, as discussed earlier.

As temperature increases, the g-factor decreases for a given Mn concentration. This reduction is due to the thermal fluctuations of magnetic moments, which weakens their alignment with the external magnetic field and thus diminishes the strength of the exchange interaction. As a consequence, the critical Mn concentration at which the g-factor begins to increase shifts to higher values with increasing temperature. This temperature dependence is further illustrated in Fig. 7. As shown, higher temperatures reduce the g-factor, and at elevated temperatures, the g-factor tends to approach its bulk semiconductor value. This behavior is consistent with the temperature dependence of the Brillouin function, which governs the magnetization of Mn ions and decreases with increasing temperature. As a result, the exchange-induced energy splitting between spin-up and spin-down states diminishes at higher temperatures, leading to a reduction in the effective g-factor.

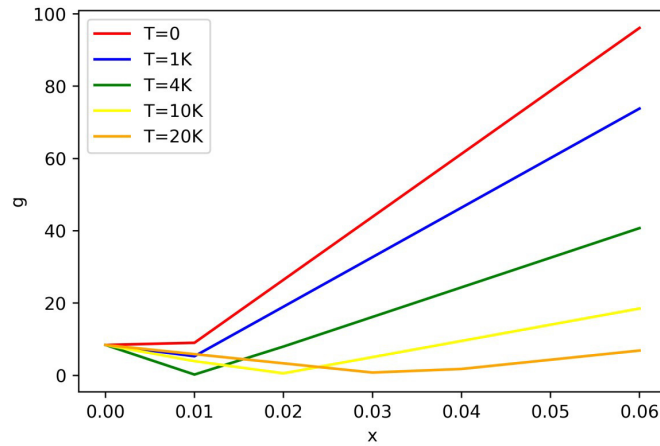


FIG. 6. Effective Lande g-factor vs. Mn molar concentration ( $x$ )

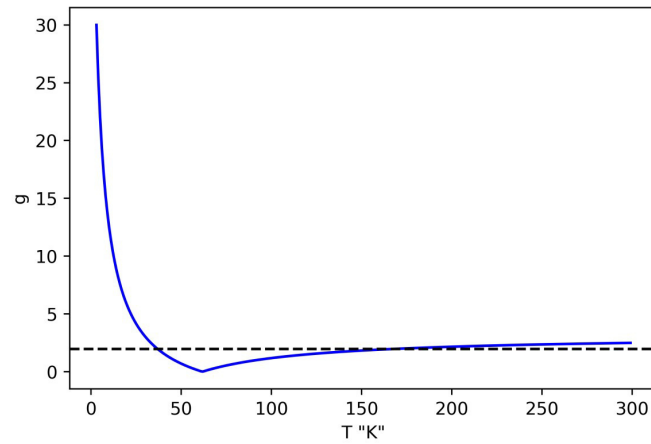


FIG. 7. The effective Lande g-factor vs. Temperature of for  $\text{Cd}_{0.99}\text{Mn}_{0.01}\text{Te}$  in the presence of an external magnetic field of 1 T

#### 4. Conclusion

In this work, we have analytically studied the energy spectrum of a cylindrical quantum wire (QW) composed of CdTe under an external magnetic field, incorporating both Rashba spin-orbit interaction (SOI) and exchange interaction effects. These interactions significantly influence the density of states (DOS) and modify the Landau level structure. We focused particularly on the behavior of the electron effective g-factor associated with the zeroth Landau level, demonstrating its strong dependence on both the magnetic field strength and the Rashba SOI parameter.

Our results reveal that, in Mn-doped CdTe quantum wires, the effective g-factor increases with the strength of the Rashba SOI, especially when the exchange interaction becomes significant. By tuning structural parameters of the QW and the Mn ion concentration, it is possible to engineer large, tunable g-factors. This tunability opens promising avenues for the use of such nanostructures in spintronic applications, where control over spin-dependent properties is essential.

#### References

- [1] Zarkevich N.A., Zverev V.I. Viable materials with a giant magnetocaloric effect. *Crystals*, 2020, **10** (9), 815.
- [2] Ali A.A., Shaer A., Elsaid M. Simultaneous effects of Rashba, magnetic field and impurity on the magnetization and magnetic susceptibility of a GaAs-semiconductor quantum ring. *J. of Magnetism and Magnetic Materials*, 2022, **556**, 169435.
- [3] Xiang G., Wang Y.G. Exploring electronic-level principles how size reduction enhances nanomaterial surface reactivity through experimental probing and mathematical modeling. *Nano Research*, 2022, **15**, P. 3812–3817.
- [4] Shaer A., Elsaid M.K. The Gaussian impurity effect on the electronic and magnetic properties of an electron confined in a lateral quantum dot. *Nanosystems: Phys., Chem., Math.*, 2022, **13** (3), P. 265–273.
- [5] Shaer A., Yücel M.B., Kasapoglu E. Hydrostatic pressure and temperature dependent optical properties of double inverse parabolic quantum well under the magnetic field. *Physica B: Condensed Matter*, 2024, **685**, 416057.

- [6] Tsolovikos A., Jariwala A., Suryanarayanan S., Bakolas E., Goldstein D. Separation delay in turbulent boundary layers via model predictive control of large-scale motions. *Physics of Fluids*, 2023, **35** (11), 115118.
- [7] Evseev S.S., Burmistrov I.S., Tikhonov K.S., Kachorovskii V.Y. Effect of elastic disorder on single-electron transport through a buckled nanotube. *Physical Review Research*, 2022, **4** (1), 013068.
- [8] Kim W.Y., Choi Y.C., Kim K.S. Understanding structures and electronic/spintronic properties of single molecules, nanowires, nanotubes, and nanoribbons towards the design of nanodevices. *J. of Materials Chemistry*, 2008, **18** (38), P. 4510–4521.
- [9] Zeng Z., Zhou C., Zhou H., et al. Spectral evidence for Dirac spinons in a kagome lattice antiferromagnet. *Nature Physics*, 2024, **20**, P. 1097–1102.
- [10] Xiao J., Liu P., Wang C.X., Yang G.W. External field-assisted laser ablation in liquid: An efficient strategy for nanocrystal synthesis and nanostructure assembly. *Progress in Materials Science*, 2017, **87**, P. 140–220.
- [11] Elsbahy M., Heo G.S., Lim S.M., Sun G., Wooley K.L. Polymeric nanostructures for imaging and therapy. *Chemical reviews*, 2015, **115** (19), P. 10967–11011.
- [12] Kasapoglu E., Urgan F., Duque C.A., Yesilgul U., Mora-Ramos M.E., Sar H., So I. The effects of the electric and magnetic fields on the nonlinear optical properties in the step-like asymmetric quantum well. *Physica E: Low-dimensional Systems and Nanostructures*, 2014, **61**, P. 107–110.
- [13] Bouazra A., Nasrallah S.A.B., Said M. Theory of electronic and optical properties for different shapes of InAs/InO. 52AlO. 48As quantum wires. *Physica E: Low-dimensional Systems and Nanostructures*, 2016, **75**, P. 272–279.
- [14] Khordad R. Optical properties of quantum wires: Rashba effect and external magnetic field. *J. of luminescence*, 2013, **134**, P. 201–207.
- [15] Khoshbakht Y., Khordad R., Rastegar Sedehi H.R. Magnetic and thermodynamic properties of a nanowire with Rashba spin–orbit interaction. *J. of Low Temperature Physics*, 2021, **202**, P. 59–70.
- [16] Mehdiyev B.H., Babayev A.M., Cakmak S., Artunc E. Rashba spin–orbit coupling effect on a diluted magnetic semiconductor cylinder surface and ballistic transport. *Superlattices and Microstructures*, 2009, **46** (4), P. 593–602.
- [17] Gharaati A., Khordad R. Electron g-factor in quantum wire in the presence of Rashba effect and magnetic field. *Superlattices and Microstructures*, 2012, **51** (1), P. 194–202.
- [18] Babanlı A.M., Artunç E., Kasalak T.F. Electron g-Factor in Diluted Magnetic Semiconductor Quantum Well with Parabolic Potential in the Presence of Rashba Effect and Magnetic Field. *Zeitschrift für Naturforschung A*, 2015, **70** (2), P. 109–114.
- [19] Kumar M., Lahon S., Jha P.K., Mohan M. Energy dispersion and electron g-factor of quantum wire in external electric and magnetic fields with Rashba spin orbit interaction. *Superlattices and Microstructures*, 2013, **57**, P. 11–18.
- [20] De Sousa R., Sarma S.D. Gate control of spin dynamics in III-V semiconductor quantum dots. *Physical Review B*, 2003, **68** (15), 155330.
- [21] Rodrigues L.N., Inoch W.F., Gomes M.L.F., Couto Jr.O.D.D., Archanjo B.S., Ferreira S.O. Localized-states quantum confinement induced by roughness in CdMnTe/CdTe heterostructures grown on Si(111) substrates. *J. of Semiconductors*, 2024, **45** (9), 092301.
- [22] Furdyna J.K. Diluted magnetic semiconductors. *J. of Applied Physics*, 1988, **64** (4), R29–R64.
- [23] Jin H., Livache C., Kim W.D., Diroll B.T., Schaller R.D., Klimov V.I. Spin-exchange carrier multiplication in manganese-doped colloidal quantum dots. *Nature materials*, 2023, **22** (8), P. 1013–1021.
- [24] Brandt N.B., Moshchalkov V.V. Semimagnetic semiconductors. *Advances in Physics*, 1984, **33** (3), P. 193–256.
- [25] Afanasiev M.M., Kozyrev N.V., Kirstein E., Kalevich V.K., Zhukov E.A., Mantsevich V.N., Krivenko I.S., Karczewski G., Yakovlev D.R., Kusraev Yu.G., Bayer M. Electron g-factor in coupled quantum wells CdTe and CdMnTe. *J. of Physics: Conference Series*, 2019, **1400** (6), 066023.
- [26] Kirstein E., Kozyrev N.V., Afanasiev M.M., Mantsevich V.N., Krivenko I.S., Kalevich V.K., Bayer M. Short range proximity effect induced by exchange interaction in tunnel-coupled CdTe and (Cd, Mn) Te quantum wells. *Physical Review B*, 2020, **101** (3), 035301.

---

Submitted 21 October 2024; revised 24 April 2025; accepted 8 May 2025

#### Information about the authors:

Mohammad Elsaid – Department of Physics, An-Najah National University, Palestine; ORCID 0000-0002-1392-3192; mkelsaid@najah.edu

Diana Dahliah – Department of Physics, An-Najah National University, Palestine; ORCID 0000-0002-6919-3539; diana.dahliah@najah.edu

Ayham Shaer – Department of Physics, An-Najah National University, Palestine; ORCID 0000-0002-6518-6470; ayham.shaer@najah.edu

Mahmoud Ali – Department of Physics, An-Najah National University, Palestine; ORCID 0000-0002-3738-5851; mahmoud.ali@najah.edu

*Conflict of interest:* the authors declare no conflict of interest.

## Influence of SiC MOSFET design on on-resistance and breakdown voltage

Olga B. Chukanova<sup>1,a</sup>, Konstantin A. Tsarik<sup>1,b</sup>

<sup>1</sup>National Research University of Electronic Technology, Moscow, Russia

<sup>a</sup>kukhtuaeva@mail.ru, <sup>b</sup>tsarik.kostya@mail.ru

Corresponding author: O. B. Chukanova, kukhtuaeva@mail.ru

PACS 85.30.De, 85.30.Tv

**ABSTRACT** To improve the efficiency of circuits including SiC MOSFET, it is necessary to increase their specific currents and reliability, respectively. One needs it to reduce the transistor on-resistance and to increase its breakdown voltage. To achieve these goals, the influences of the transistor's electrophysical characteristics on its design and technological features have been studied with Sentaurus TCAD. We showed that for increasing the transistor currents, it is necessary to reduce the channel length – the distance between the p-bases of the transistor sources, and to create a JFET region. For the increasing the breakdown voltage of the device, we proposed to increase the doping level of the drift region, and suggested a new transistor design that will allow one to obtain devices with a breakdown voltage up to 2500 V.

**KEYWORDS** SiC MOSFET, TCAD, JFET doping, breakdown voltage.

**ACKNOWLEDGEMENTS** The research was carried out within the state assignment of Ministry of Science and Higher Education of the Russian Federation (FSMR-2022-0004).

**FOR CITATION** Chukanova O.B., Tsarik K.A. Influence of SiC MOSFET design on on-resistance and breakdown voltage. *Nanosystems: Phys. Chem. Math.*, 2025, **16** (3), 282–290.

### 1. Introduction

Nowadays, many devices are formed on silicon wafers, particularly, devices for power applications. IGBT silicon transistor is the most applicable for power electronics since it has higher breakdown voltages and operating temperatures compared to other types of silicon devices. It is difficult to achieve a high power conversion factor using Si devices [1]. The most suitable devices for power applications are based on wide-bandgap materials [2], such as gallium nitride, silicon carbide or gallium oxide. SiC compared to Si has larger bandgap width – 3.26 eV, higher thermal conductivity – 4.9 W / cm·K, and higher value of the critical electric field strength of breakdown – 3 MV / cm.

Power MOSFETs can be lateral or horizontal. Power lateral devices must have a wide drift area to withstand high voltages, i.e. the cell size must be large. Vertical transistors don't require wide drift areas, that allows one to reduce the cell size and also solve the problem of large electric field on the surface.

Standard Si MOSFETs have breakdown voltages of less than 150 V [3] and there are many such offers from different companies. However, there is now a trend to increase the values of the device's operating voltages and breakdown voltages. Vertical silicon carbide devices have high breakdown voltages, high radiation resistance, low on-resistance and excellent switching frequencies compared to silicon-based devices therefore they are more attractive for power applications. The main researches in this area are aimed on improving their characteristics, namely, the breakdown voltage  $V_{bd}$ , the channel resistance  $R_{on,sp}$ , the gate charge  $Q_g$  and the maximum electric field in the gate dielectric  $E_{max,ox}$  [4–7].

Standard SiC MOSFETs have breakdown voltages in the range of 600 to 900 V and threshold voltages up to 10 V [8]. At breakdown voltages below 1000 V, the performance of SiC devices is strongly dependent on the on-resistance as well as the charge carrier mobility. If the charge carrier mobility is approximately 100 cm<sup>2</sup>/V·s, the on-resistance becomes almost equal to the ideal value when the breakdown voltage exceeds 5000 V. Even at high breakdown voltages, if the charge carrier mobility reaches values of 10 cm<sup>2</sup>/V·s, the performance of SiC devices deteriorates [9]. Therefore, it is necessary to create transistor designs with low on-resistance and high breakdown voltages.

Nowadays, a sufficient number of different designs of power SiC MOSFETs have been developed in order to improve the listed characteristics: SiC Power DI-MOSFET (Double-Implant Process) [10], Shielded SiC Planar Power MOSFET [11, 12], MOSFET with spreading layer or/and JFET region that solves the problem of low on-resistance [13], ACCUFET structure with epitaxial layer N-base region under the gate [14, 15], JBSFET with integrated JBS diode [16, 17], Bi-directional FET – 2 JBSFET with common drain [18, 19], trench-gate MOSFET or/and JFET region [20] etc. Shielded SiC Planar Power MOSFET has a shielded layer under source and base that solves a reachthrough problem, problem of a high gate oxide electric field and low channel mobility. But all the listed designs allowed obtaining devices with breakdown voltage in the range from 1000 to 1650 V. One work reflects the formation of an ACCUFET with a breakdown voltage of about 10 kV, but its threshold voltage was approximately zero.

In this paper, we study the design and technological features of a standard power MOSFET using physical simulation in the Sentaurus Technology Computer Aided Design (TCAD) and the transistor design to reduce channel resistance  $R_{on,sp}$  and increase the breakdown voltage  $V_{bd}$ .

## 2. Structure

Fig. 1 demonstrates a schematic image of the SiC MOSFET. The values of the layer thicknesses and their concentrations are standard for such structures [21–24]. When a bias is applied between the drain and source  $V_{ds}$ , and the gate-source voltage  $V_{gs}$  is greater than the threshold voltage  $V_{th}$ , the transistor opens and a vertical current exists between the drain and the source. If the gate-source voltage  $V_{gs}$  is less than the threshold  $V_{th}$ , and the bias  $V_{ds}$  is still applied between the drain and the source, then there is no current, the transistor is closed, the drift region is depleted, and an electric field begins to be induced. Breakdown occurs when the value of the induced electric field exceeds the critical value as the bias between the drain and the source increases.

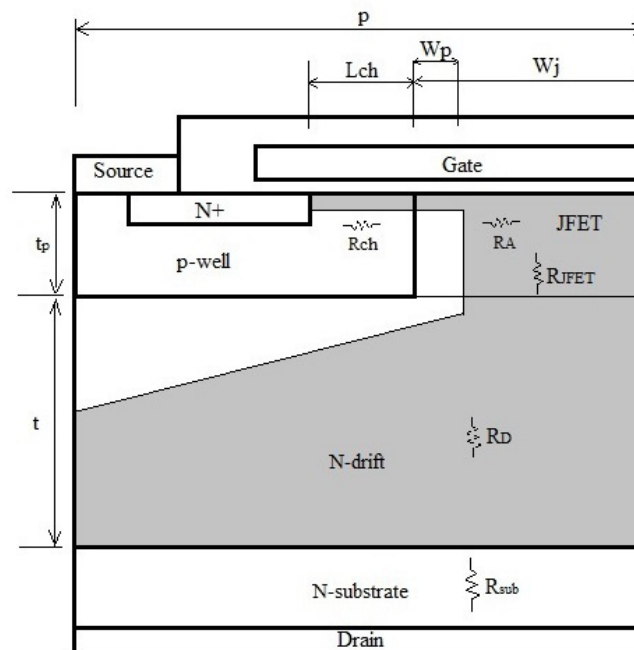


FIG. 1. Schematic image of SiC MOSFET,  $t_p$  – width of p-region,  $t$  – drift region width,  $p$  – half length of the structure,  $L_{ch}$  – channel length,  $W_p$  – width of p-n junction p-base/N-JFET,  $W_j$  – JFET region width

## 3. Simulation

The study of the design and technological features of SiC power MOSFETs has been carried out using the Sentaurus TCAD. Two-dimensional simulation of the structure has been carried out. To save time half of the structure was considered during simulation since the device is symmetrical relative to the vertical axis, therefore, to compare it with the real device the results of simulation drain currents, for example, should be increased twice.

The first step of the device simulation is to describe the structure, then you should form the device grid in the nodes of which such electrophysical characteristics of the device as electric field, voltage, current, etc. will be calculated using numerical calculations. The number of nodes in the grid affects the modeling process, namely, the accuracy of the results, as well as the convergence of the problem. If the number of nodes is small, i.e. a so-called “rough” grid has been generated, the result may be inaccurate. If the number of nodes is large and the grid is very “fine”, the problem may not converge or the simulation time will be too long. Therefore, it is important to select the optimal number of grid nodes. For the accuracy of the results, it is necessary to generate a “fine” grid only in the areas of heterojunctions, channel, concentration gradient, etc.

The key model in simulation of devices is the diffusion-drift model, which is based on the approximation of the Boltzmann charge transport equation in the diffusion-drift approximation. The current in the device flows due to the drift and diffusion of charge carriers simultaneously with their generation and recombination. The diffusion-drift model numerically solves the Poisson equations and calculates the concentrations of electrons and holes, and determines the electrostatic potential at each grid node. A thermodynamic model is often also included. The influence of temperature on

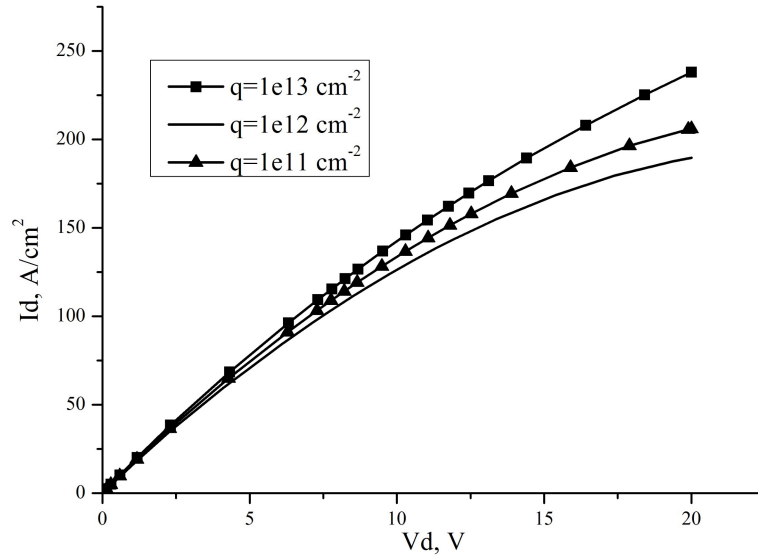


FIG. 2. The influence of positive charge density  $q$  at  $\text{SiO}_2/\text{SiC}$  heterojunction on MOSFET current-voltage characteristics at 20 V gate voltage

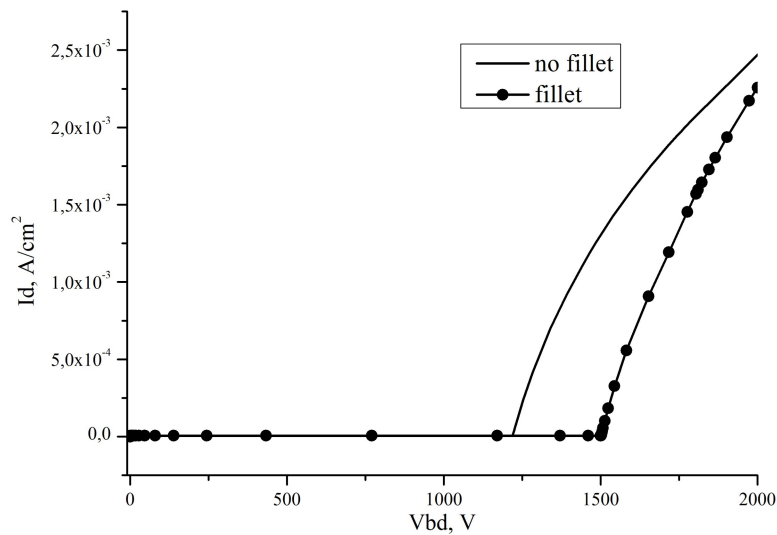


FIG. 3. Influence of drain p-region describing on SiC MOSFET breakdown voltage

the parameters of the device is taken into account. If it is included then the heat flow equations are additionally solved, i.e. the temperature gradient in the device is taken into account.

The physical model of the transistor should take into account the recombination and carrier generation. These are the processes of creation and destruction of an electron-hole pair by the transition of an electron from the valence band to the conduction band, thereby creating a hole in the valence band, and vice versa. The difference in energies between the final position of the electron and the initial one leads to different classifications of the recombination process. If the radiative recombination energy is released in the form of a photon and in the case of nonradiative recombination, it is transferred to one or more phonons.

The key model of recombination and generation is the Shockley-Read-Hall model. The Shockley-Read-Hall model describes the process of electrons and holes recombination through the trap levels in the forbidden band. An electron moves from the valence band to the trap level and then from this level to the conduction band. This process occurs in a semiconductor due to the presence of impurities and defects formed during the growth [22].

Auger recombination model should be included at simulation of power SiC MOSFETs that have high drain currents. Auger recombination is an interband transition of an electron or a hole. The energy released during such a transition is transferred to another electron or hole that affects the recombination rate [23].

Incomplete ionization models and band gap narrowing model should be also used since the dopant in 4H-SiC isn't completely ionized at room temperature. Doping dependence mobility and high field saturation mobility models have

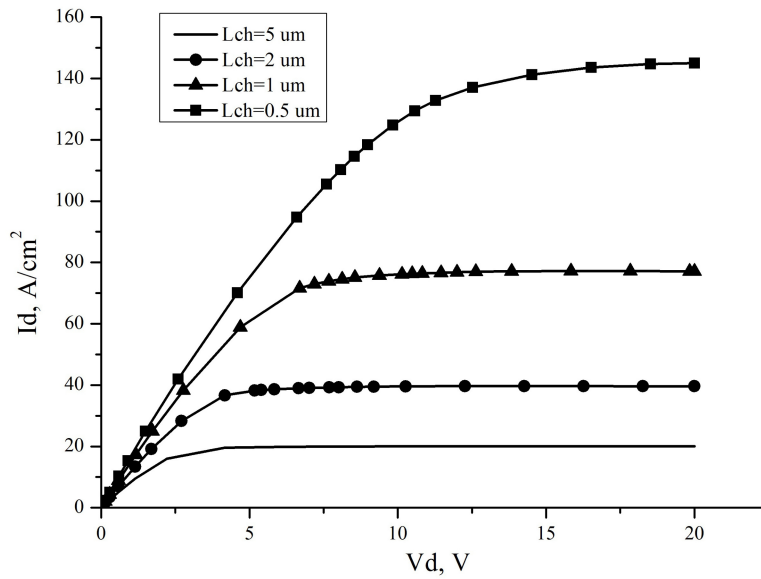


FIG. 4. Influence of length channel Lch on the transistor current-voltage characteristics at 15 V gate voltage

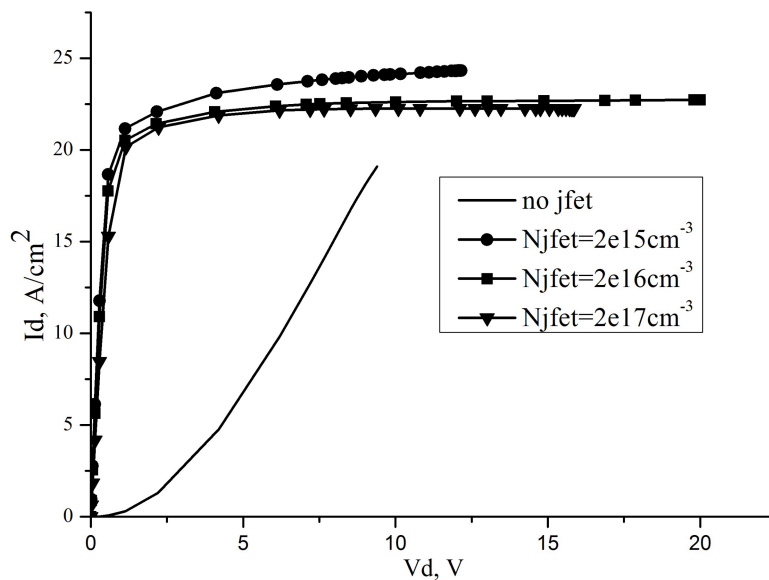


FIG. 5. Dependence of current-voltage characteristics on doping concentration of JFET region Njfet at 15 V gate voltage

been used to calculate the mobility. An avalanche model, i.e. impact ionization model, should also be used to simulate breakdown voltage.

One of the advantages of SiC for practical application is the formation of insulating silicon oxide layers SiO<sub>2</sub> on SiC by thermal oxidation. This effect is important for the fabrication of field-effect MOSFETs. There are two types of oxidation processes: dry and wet. The dry oxidation process of SiC is carried out in an O<sub>2</sub> atmosphere. The wet oxidation process is carried out in an O<sub>2</sub> and H<sub>2</sub>O atmosphere and it effectively reduces the influence of deep trap levels on the SiO<sub>2</sub>/SiC heterojunction, which improves the channel mobility of the MOSFET [24, 25]. Therefore, the effect of this charge on the transistor electrical characteristics has been studied (Fig. 2). Based on the literature data [26], the value of this charge is about 10<sup>11</sup> cm<sup>-2</sup>. The influence of this charge on the drain current at the same gate voltage is weak. Therefore, in our case a charge of 1·10<sup>11</sup> cm<sup>-2</sup> was set on the heterojunction.

It is necessary to describe the fillet of the p-doped region simulating such devices. If this is neglected the maximum electric field strength at breakdown voltage simulation will be concentrated at corner of the p-region. It will lead to incorrect results and a decrease in the breakdown voltage from 1500 V to 1200 V for the research structure heterostructure (Fig. 3).

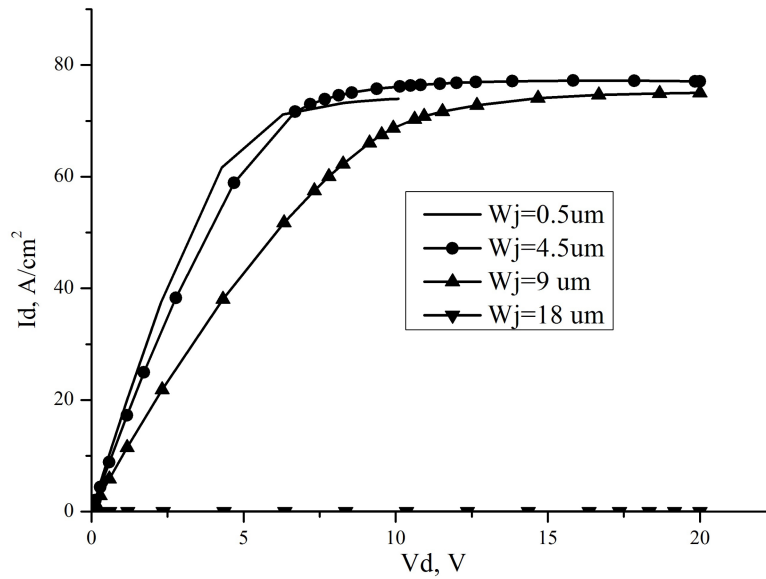


FIG. 6. Influence of JFET region width  $W_j$  on current-voltage characteristics at 15V gate voltage

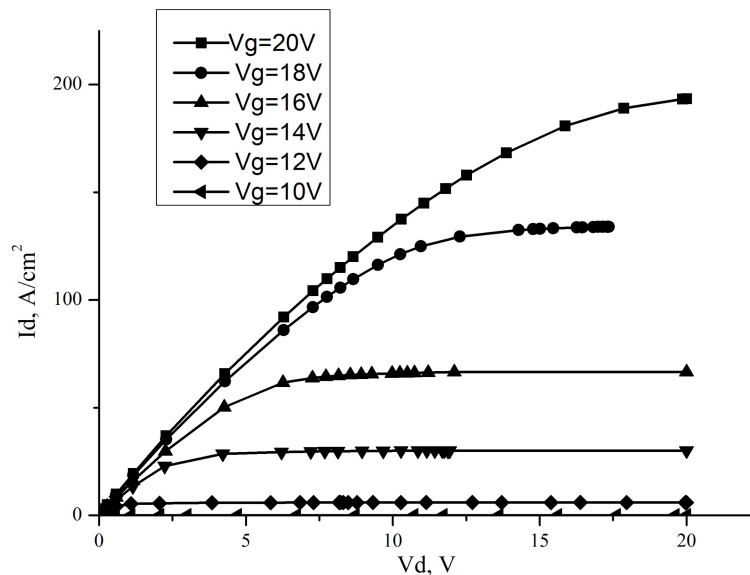


FIG. 7. Current-voltage characteristics of the SiC MOSFET

#### 4. On-resistance

One of such devices research directions is to reduce on-resistance. The most popular approach is to dope the region under the gate between the p-type regions [27]. This region is named as a JFET. JFETs are usually formed by implanting high-energy nitrogen ions with a concentration of about  $10^{17} \text{ cm}^{-3}$  [28]. In the open state, the current through the transistor begins to flow through the inversion layer, which is formed in the upper part of the p-type region due to the positive bias. This is so-called channel. The current then flows through the JFET region and then spreads into the drift region, in which the current flow region also extends under the p-type region at an angle of  $45^\circ$  (gray region in Fig. 1) [9]. The total on-state resistance of the transistor can be calculated using the following formula:

$$R_{on} = R_{ch} + R_A + R_{jfet} + R_{drift} + R_{subs},$$

where  $R_{ch}$  is the channel resistance,  $R_A$  is the resistance of the p-n junction,  $R_{jfet}$  is the resistance of the JFET region,  $R_{drift}$  is the resistance of the drift region and  $R_{subs}$  is the resistance of the N+ substrate.

The on-resistance depends on the channel length  $L_{ch}$  or the structure length  $p$ . The longer the channel length or the structure length, the greater the channel resistance. The influence of the channel length on the drain current was simulated

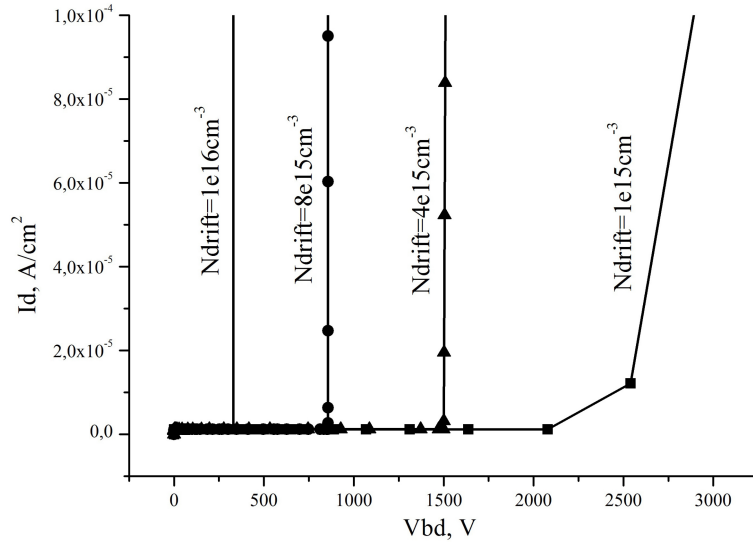


FIG. 8. Dependence of SiC MOSFET breakdown voltage on drift region doping concentration  $N_{drift}$

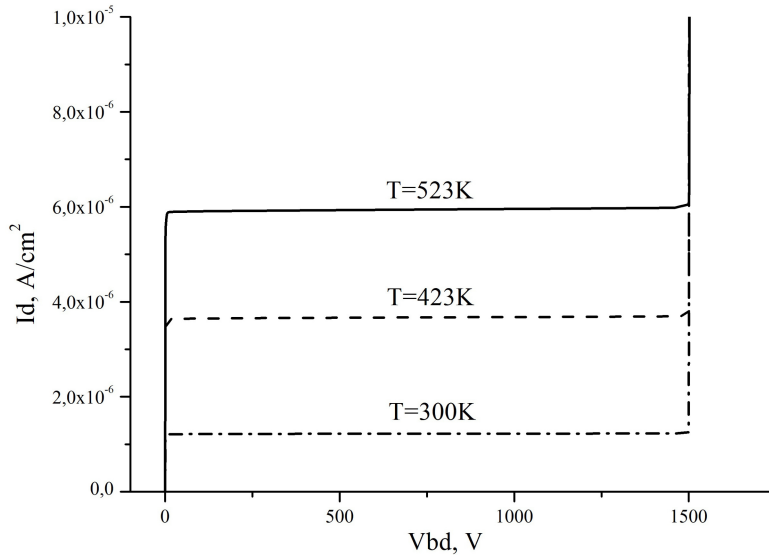


FIG. 9. SiC MOSFET breakdown voltage at different temperatures

(Fig. 4). Increasing the channel length, the resistance of the channel region also increases, which leads to a decrease of the drain current. Therefore, the optimal transistor channel length is about  $0.5-1 \mu\text{m}$ .

The p-n heterojunction resistance  $R_A$  depends on p-base/N-JFET junction width  $W_p$  at zero bias and on the JFET region width. In turn, the width  $W_p$  depends on the dopant concentration of the JFET region. The resistance of the JFET region is determined by the parameters of the p-base, the width of the JFET region and the width  $W_p$ . The resistance of the drift region also depends on the base parameters and the parameters of the JFET region. If the typical values of the resistance for 4H-SiC substrate are  $0.02 \Omega \cdot \text{cm}$  and  $350 \mu\text{m}$ , then the resistance is equal to  $7 \times 10^{-4} \Omega \cdot \text{cm}^2$  [29].

Obviously, the transistor resistance is greatly affected by the dopant concentration of the JFET region, as well as the length of the structure. Therefore, the dependences of the transistor drain current on the JFET region dopant concentration  $N_{JFET}$  and the width of this region  $L_S$  were investigated. Fig. 5 demonstrates that the JFET region doping reduces the transistor resistance, but the dopant concentration has small effect on the drain current value. The larger the width of the JFET region  $W_j$ , the lower the resistance and the higher the drain current (Fig. 6). Therefore, JFET region with a width of approximately in the range from  $0.5$  to  $9 \mu\text{m}$  should be created in the device to reduce the transistor resistance.

Thus, the following SiC MOSFET design was chosen: the distance between the p-regions  $W_j$  is about  $9 \mu\text{m}$ , the channel length  $L_{ch} - 1 \mu\text{m}$ , the thickness of the p-region  $t_p - 5 \mu\text{m}$ , the drift region width  $t - 25 \mu\text{m}$ , the doping concentration in the source region  $N^+$  is  $1.5 \times 10^{20} \text{ cm}^{-3}$ , the doping concentration in the p-region -  $4 \times 10^{17} \text{ cm}^{-3}$ , the doping concentration in the drift region  $N_{drift} = 4 \times 10^{15} \text{ cm}^{-3}$  and the JFET concentration is  $2 \times 10^{16} \text{ cm}^{-3}$ . For this transistor current-voltage

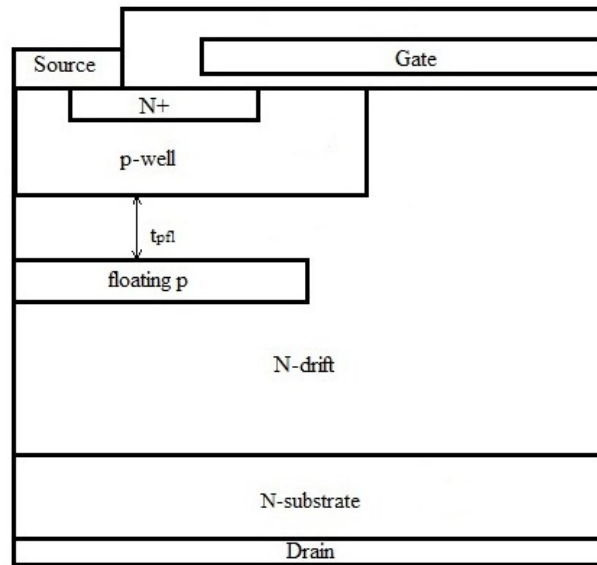


FIG. 10. Schematic image of SiC MOSFET with additional p-region in the drift region to increase the breakdown voltage

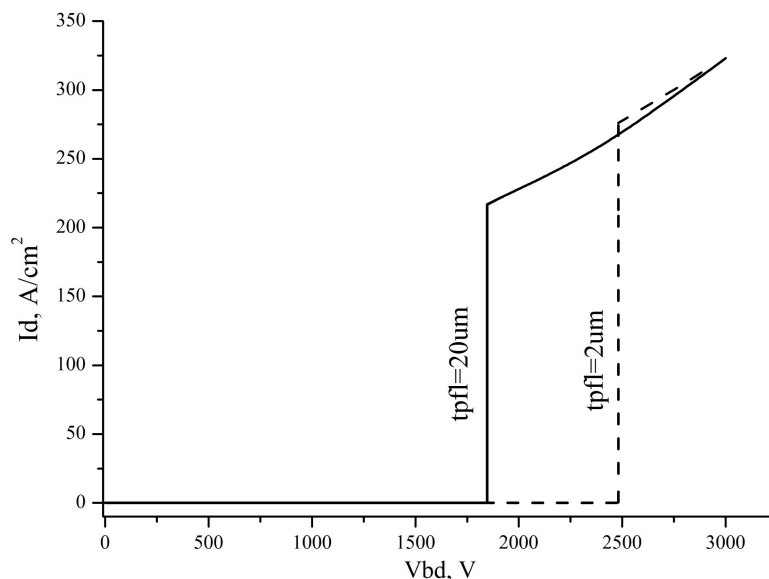


FIG. 11. Breakdown voltage of SiC MOSFET with additional p-region in drift region with different distances from p-base to additional p-region  $tp_{fl}$

characteristics were simulated (Fig. 7). The threshold voltage was 10 V, and the maximum drain current at 20 V on the gate was  $192 \text{ A/cm}^2$ . To obtain a higher transistor current the channel length or the distance between the p-regions should be reduced. The purpose of our work is to study the design and technological features of SiC MOSFET, so we consider the standard design and offer ways to improve the electrophysical characteristics of the device. Let us consider in more detail the methods for increasing the breakdown voltage of SiC MOSFET.

## 5. Breakdown voltage

The breakdown voltage of the research SiC power transistor depends on the doping concentration of drift region and on its width [30]. It was found that the value of the breakdown voltage weakly depends on the drift region width. SiC transistors with different drift region widths (20, 25, 30 and  $35 \mu\text{m}$ ) have been simulated. The breakdown voltages of the studied SiC transistors with different drift region widths were 1510 V, 1498 V, 1518 V and 1493 V accordingly. However, the doping concentration of the drift region has a strong effect on the breakdown voltage value. The lower the concentration, the higher the breakdown voltage takes place (Fig. 8).

The influence of temperature on the breakdown voltage was investigated (Fig. 9). The breakdown voltage of the device was 1500 V. The drain current increases at the same drain voltage values with increasing temperature, and the breakdown voltage doesn't change. This can be explained by the fact that holes have higher temperature coefficient in SiC [31], and accordingly, they have a higher ionization rate compared to electrons, so the breakdown voltage doesn't change. Despite the fact that there are many additional holes, electrons remain the main carriers.

As mentioned above, one of the key goal of SiC MOSFET study is to increase the breakdown voltage. One of the ways to solve this problem is to increase the doping level of the drift region. In this paper, we also propose a transistor design with an additional p-region in the drift region (Fig. 10). This p-region extends the peak of the breakdown electric field, which allows increasing the breakdown voltage. It is possible to obtain transistors with different breakdown voltages by changing the distance from the p-base to the additional p-region  $t_{pfl}$ : at 2  $\mu\text{m}$ , the transistor has a breakdown voltage of 2475 V, and at 20  $\mu\text{m}$  – 1845 V (Fig. 11).

## 6. Conclusion

In this article, the design and technological features of standard SiC MOSFET transistor are studied and the process of simulation such devices in the Sentaurus TCAD are described in detail. To reduce the on-resistance of such transistors, and, accordingly, to increase the drain currents, it is necessary to form the JFET region between the p-bases of the sources. Also, to increase the current, it is possible to reduce the channel length to 0.5–1  $\mu\text{m}$  or reduce the width of the JFET region. The distance between the p-bases of the sources should be less than 9  $\mu\text{m}$ . To increase the breakdown voltage of power SiC MOSFET, it is necessary to reduce the concentration of the dopant in the drift region: at the concentration of  $1e15\text{ cm}^{-3}$ , a breakdown voltage of 2500 V can be obtained. In order to increase the breakdown voltage, a new design of power SiC MOSFET with an additional p-region in the drift region is proposed. By varying the distance from this p-region to the p-base, it is possible to obtain transistors with the breakdown voltages of various values up to 2500 V.

## References

- [1] Shukla R.K., Srivastava A., Rani S., Singh N., Dwivedi V.K., Pandey S., Wadhvani N. Simulation and evaluation of perovskite solar cells utilizing various electron transport layers. *Nanosystems: Phys. Chem. Math.*, 2024, **15**(1), P. 135–146.
- [2] Pozdnyakov D.V., Borzdov A.V., Borzdov V.M. Simulation of a quasi-ballistic quantum-barrier field-effect transistor based on GaAs quantum wire. *Nanosystems: Phys. Chem. Math.*, 2025, **16**(2), P. 183–191.
- [3] Ryu S.-H. 3.7 mW-cm<sup>2</sup>, 1500 V 4H-SiC DMOSFETs for advanced high power, high frequency applications, IEEE International Symposium on Power Semiconductor Devices and ICs, 2011, P. 227–230.
- [4] Uchida K., Saitoh Y., Hiyoshi T., Masuda T., Wada K., Tamaso H., Hatayama T., Hiratsuka K., Tsuno T., Furumai M., Mikamura Y. The optimised design and characterization of 1200V/2.0 m cm<sup>2</sup> 4H-SiC V-groove trench MOSFETs. Proc. IEEE 27th Int. Symp. Power Semiconductor Devices IC's (ISPSD), Hong Kong, May 2015, P. 85–88.
- [5] Song Q., Yang S., Tang G., Han C., Zhang Y., Tang X., Zhang Y., Zhang Y. 4H-SiC trench MOSFET with L-shaped gate, *IEEE Electron Device Lett.*, 2016, **37**(4), P. 463–466.
- [6] Bharti D., Islam A. Optimization of SiC UMOSFET structure for improvement of breakdown voltage and on-resistance, *IEEE Trans. Electron Devices*, 2018, **65**(2), P. 615–621.
- [7] Wang Y., Ma Y., Hao Y. Simulation study of 4H-SiC UMOS-FET structure with pC-polySi/SiC shielded region, *IEEE Trans. Electron Devices*, 2017, **64**(9), P. 3719–3724.
- [8] Stevanovic L., Matocha K., Stum Z., Losee P.A., Gowda A., Glaser J., Beaupre R. Realizing the full potential of silicon carbide power devices. IEEE Workshop on Controls and Modelling of Power Electronics, 2010, P. 1–6.
- [9] Baliga B.J. *Fundamentals of Power Semiconductor Devices*. Springer-Science, Berlin. 2008.
- [10] Fujii Y., Suzuki A., Furukawa K. Silicon carbide semiconductor devices having buried silicon carbide conduction barrier layers therein: Patent US5170231A Osaka Japan, H01L29/78, issued 6 Aug 1996, 11 p.
- [11] Shenoy P.M., Baliga B.J. The planar 6H-SiC ACCUFET. *IEEE Electron Device Lett.*, 1997, **18**, P. 589–591.
- [12] Saha A., Cooper J.A. A 1-kV 4H-SiC power DMOSFET optimized for low on-resistance, *IEEE Trans. Electron Devices*, 2007, **55**, P. 2786–2791.
- [13] Shenoy P.M., Baliga B.J. Analysis and optimization of the planar 6H-SiC ACCUFET. *Solid State Electron.*, 1999, **43**, P. 213–220.
- [14] Miura N., Fujihira K., Nakao Y., Watanabe T., Tarui Y., Kinouchi S.-I., Imaizumi M., Oomori T. Successful development of 1.2 kV 4H-SiC MOSFETs with very low on-resistance of 5 m-cm<sup>2</sup>. IEEE International Symposium on Power Semiconductor Devices and ICs, 2006, P. 1–4.
- [15] Sung W., Baliga B.J. Monolithically integrated 4H-SiC MOSFET and JBS diode (JBSFET) using a single Ohmic/Schottky process scheme. *IEEE Electron Device Lett.*, 2016, **37**, P. 1605–1608.
- [16] Sung W., Baliga B.J. On developing one-chip integration of 1.2 kV SiC MOSFET and JBS diode (JBSFET). *IEEE Trans. Ind. Electron.*, 2017, **64**, P. 8206–8212.
- [17] Baliga B.J. Monolithically integrated AC switch having JBSFETs therein with commonly connected drain and cathode electrodes: Patent US0010804393 North Carolina State University H01L29/78, Baliga B.J., issued 28 Jun 2017.
- [18] Baliga B.J., Han K.: Monolithic SiC bi-directional field effect transistor (BiDFET): concept, implementation, and electrical characteristics. GO-MACTech 2018, 2018, Paper 3.2, P. 32–35.
- [19] Baliga B.J. Silicon carbide switching device with rectifying gate: Patent US5396085A North Carolina State University, Baliga B.J., issued 7 Mar 1995, 16 p.
- [20] Zhang Q., Gomez M., Bui C., Hanna E. 1600V 4H-SiC UMOSFETs with dual buffer layers, IEEE International Symposium on Power Semiconductor Devices and ICs, 2005, P. 159–162.
- [21] Yu H., Wang J., Liang S., Deng G., Liu H., Ji B., John Shen Z. 1.2-kV silicon carbide planar split-gate MOSFET with source field plate for superior figure-of-merits, *IET Power Electron.*, 2022, **15**, P. 1502–1510.
- [22] Shockley W., Read W.T. Statistics of the recombinations of holes and electrons. *Phys. Rev.*, 1952, **87**(5), P. 835–842.
- [23] Synopsys Sentaurus TCAD, Synopsys Inc., Sentaurus Device User Guide. 2015.

- [24] Yano H., Katafuchi F., Kimoto T. Effects of wet oxidation/anneal on interface properties of thermally oxidized SiO<sub>2</sub>/SiC MOS system and MOSFET's, *IEEE Trans. Electron Devices*, 1999, **46**(3), P. 504–510.
- [25] Okamoto M., Tanaka M., Yatsuo T., Fukuda K. Effect of oxidation process on the electrical characteristics of 4H-SiC p-channel metal-oxide-semiconductor field-effect transistors. *Appl. Phys. Lett.*, 2006, **89**, P. 023502
- [26] Bencherif H. Modeling and simulation of power MOSFETs based on 4H-SiC. 2020.
- [27] Chen X., Li X., Wang Y., Chen H., Zhou C., Zhang Ch., Li Ch., Deng X., Wu Y., Zhang B. Different JFET designs on conduction and short-circuit capability for 3.3 kV planar-gate silicon carbide MOSFETs. *IEEE J. of the Electron Devices Society*, 2020, **8**, P. 841–845.
- [28] Liu S., Huang M., Wang M., Zhang M., Wei J. Considerations for SiC super junction MOSFET: On-resistance, gate structure, and oxide shield. *Microelectronics Journal*, 2023, **137**, P. 105823.
- [29] Rudan M., Brunetti R., Reggiani S. *Springer Handbook of Semiconductor Devices*. Springer-Science, Berlin. 2021.
- [30] Luo H., Huang Y., Zheng K., Tan Ch., Wang L., Wang Sh., Ye H., Chen X. Reliability Investigation of 4H-SiC MOSFET Based on TCAD Simulation. 2018 19-th International Conference on Electronic Packaging Technology (ICEPT), United States, August 2018, P. 956–960.
- [31] Raghunathan R., Baliga B.J. Measurement of electron and hole impact ionization coefficients for SiC. Proceedings of 9-th International Symposium Power Semiconductor Devices and IC's", Germany, May 1997, P. 173–176.

---

*Submitted 11 November 2024; revised 30 May 2025; accepted 31 May 2025*

*Information about the authors:*

*Olga B. Chukanova* – National Research University of Electronic Technology, Shokin square, 1, Moscow, Zelenograd, 124498, Russia; ORCID 0000-0001-5726-630X; kukhtuaeva@mail.ru

*Konstantin A. Tsarik* – National Research University of Electronic Technology, Shokin square, 1, Moscow, Zelenograd, 124498, Russia; ORCID 0000-0002-8218-7774; tsarik\_kostya@mail.ru

*Conflict of interest:* the authors declare no conflict of interest.

## Study of femtosecond laser amplification in MgO:LiTaO<sub>3</sub> crystals with periodic nonlinear properties

Obid I. Sabirov<sup>1</sup>, Alisher E. Rajabov<sup>1</sup>, Anvar R. Matnazarov<sup>2</sup>, Bakhodir Kh. Eshchanov<sup>3</sup>, Shavkat Otajanov<sup>4</sup>, Usman K. Sapaev<sup>5</sup>

<sup>1</sup>Urgench State University, Urgench, Khorezm Region, Uzbekistan

<sup>2</sup>Urgench Innovative University, Urgench, Khorezm Region, Uzbekistan

<sup>3</sup>Chirchik State Pedagogical University, Chirchik, Tashkent Region, Uzbekistan

<sup>4</sup>National University of Uzbekistan named after Mirzo Ulugbek, Tashkent, Uzbekistan

<sup>5</sup>Tashkent Branch of the Russian Gubkin University, Tashkent, Uzbekistan

Corresponding author: Obid I. Sabirov, [obid7432505@gmail.com](mailto:obid7432505@gmail.com)

PACS 42.65.-k, 42.65.Yj

**ABSTRACT** This work presents a theoretical study of the parametric amplification process of optical radiation in crystals with periodic modulation of quadratic nonlinear susceptibility, using MgO:LiTaO<sub>3</sub> as an example. Special attention is given to analyzing the influence of basic factors such as linear absorption and dispersion on the process efficiency. It is found that in the infrared spectral range, linear absorption and dispersion effects significantly affect the signal wave amplification coefficient, determining the energy redistribution dynamics and spectral characteristics of the resulting radiation. The study introduces a novel approach to optimizing domain length relative to coherence length, achieving up to 18 % efficiency through precise tuning, which surpasses previously reported results for similar materials. The obtained results are important for optimizing nonlinear crystal parameters, developing efficient parametric amplification schemes, and creating promising optical devices operating in the infrared range.

**KEYWORDS** parametric amplification, nonlinear crystal MgO:LiTaO<sub>3</sub>, infrared range, laser technologies, nonlinear optics, quasi-phase matching

**FOR CITATION** Sabirov O.I., Rajabov A.E., Matnazarov A.R., Eshchanov B.Kh., Otajanov Sh., Sapaev U.K. Study of femtosecond laser amplification in MgO:LiTaO<sub>3</sub> crystals with periodic nonlinear properties. *Nanosystems: Phys. Chem. Math.*, 2025, **16** (3), 291–297.

### 1. Introduction

The parametric amplification process, first described within theoretical models of nonlinear optics, received experimental confirmation with the development of laser technologies that provide high-intensity radiation generation. The main reason for studying this phenomenon was the creation of lasers capable of inducing strong nonlinear effects in optical media [1, 2]. Since the first experimental demonstrations, parametric amplification has made significant progress, evolving from the use of traditional nonlinear crystals to modern nanostructured materials. Achievements in materials science, particularly in developing nonlinear photonic crystals and nanoscale structuring technologies, have greatly expanded the practical applications of this process, offering new possibilities for light control in optical systems [3].

The physical basis of parametric amplification lies in the coherent energy transfer from a strong pump wave to a weak signal wave in a medium with quadratic nonlinear susceptibility. The efficiency of this process depends on meeting the phase-matching condition, where three coherent waves form in the nonlinear medium: the pump wave, the signal wave, and the idler wave. However, strict phase matching can be disrupted by factors like linear absorption, group velocity dispersion, and thermal effects in the medium. In this work, we specifically investigate the impact of linear absorption, group velocity dispersion, and domain structure geometry on the efficiency of signal wave amplification in MgO:LiTaO<sub>3</sub> crystals, addressing challenges posed by the infrared spectral range where these effects are pronounced. To overcome these limitations, the quasi-phase matching mechanism is widely used, achieved through periodic modulation of the quadratic nonlinear susceptibility. This modulation is provided by the structural periodicity of the crystal's reciprocal lattice vector, typical for nonlinear photonic crystals [4, 5].

In recent years, studies of parametric amplification in nonlinear photonic crystals have become highly relevant due to their unique ability to tune across a wide range of laser radiation wavelengths. These materials are applied in generating high-intensity coherent radiation in the visible and infrared spectral ranges, where laser beam intensity is a key factor in nonlinear process efficiency. However, using powerful radiation sources comes with challenges, with linear absorption, dispersion, and related effects being the most significant limitations [6, 7]. Recent studies, such as those by Zhang et al. and

Li et al., have demonstrated improved efficiency in periodically poled lithium niobate (PPLN) crystals, but MgO:LiTaO<sub>3</sub> offers unique advantages due to its lower absorption in the mid-infrared range (1.5 – 3.5 μm) and higher damage threshold, making it a promising candidate for next-generation optical devices. Unlike previous works that primarily focused on nanosecond or picosecond pulses, this study explores the femtosecond regime, addressing the challenges of broad spectral widths and their impact on dispersion.

Visible and near-infrared (IR) tunable lasers provide a technology that supports numerous applications in spectroscopy, photochemistry, classical and quantum information processing, material structuring, optical imaging, and diagnostics in materials science and life sciences [8]. This work contributes to the field by providing a detailed numerical analysis of how linear absorption, dispersion, and domain geometry affect signal wave amplification efficiency in MgO:LiTaO<sub>3</sub>, offering insights into optimizing crystal parameters for enhanced performance in infrared applications. The novelty lies in the precise tuning of domain lengths to mitigate dispersion effects, achieving efficiencies up to 18 %, which is a significant improvement over previously reported values for similar materials [9, 10]. Numerical modeling showed that linear absorption and dispersion significantly influence the energy redistribution dynamics between waves, with specific impacts quantified in this study (e.g., efficiency drop from 6 to 4.7 % due to absorption).

This study employs numerical modeling to quantify how linear absorption, dispersion, and domain geometry influence signal wave amplification efficiency in MgO:LiTaO<sub>3</sub> crystals, focusing on the infrared range where these effects are pronounced. Using numerical modeling methods, it is shown that linear absorption and dispersion effects significantly change the energy redistribution dynamics between interacting waves and affect the spectral width and energy efficiency of the process. Special attention is given to the infrared range, where these effects are most noticeable, making the study results particularly relevant for developing modern optical systems.

## 2. Equations of parametric amplification under nonstationary conditions

Parametric amplification is a fundamental phenomenon in nonlinear optics, based on the coherent interaction of electromagnetic waves in media with quadratic nonlinear susceptibility. In this process, a high-frequency pump wave with frequency  $\omega_p$  and a weak signal wave with frequency  $\omega_s$  are introduced into a nonlinear crystal. Due to nonlinear interaction inside the crystal, two new coherent waves form: an amplified signal wave with frequency  $\omega_s$  and an idler wave with the frequency  $\omega_i$ . Energy and momentum are conserved in this process, expressed by the conditions of energy and phase matching:

$$\begin{aligned}\omega_p &= \omega_s + \omega_i, \\ k_p &= k_s + k_i + G,\end{aligned}$$

where  $k_p$ ,  $k_s$ , and  $k_i$  are the wave vectors of the pump, signal, and idler waves, respectively, and  $G$  is the reciprocal lattice vector arising in periodically poled crystals, such as nonlinear photonic crystals.

The efficiency of parametric amplification depends on several factors, including the crystal's optical properties like quadratic nonlinear susceptibility, linear absorption, group velocity dispersion, and thermal and photorefractive effects. This work focuses on the interplay of linear absorption, group velocity dispersion, and domain structure geometry, which are critical in the infrared spectral range due to the pronounced effects of material dispersion and absorption [11].

As a result of nonlinear interaction, energy exchange occurs between the waves, depending on the phase-matching condition. In real crystals, this condition can be violated due to dispersion, determined by the refractive index  $n(\omega)$  dependence on frequency. To compensate for phase mismatch, nonlinear photonic crystals use the quasi-phase matching mechanism, achieved by periodically modulating the sign of  $\chi^{(2)}$  with period  $\Lambda$ , corresponding to the reciprocal lattice vector  $G$ . The quasi-phase matching condition takes the form:

$$\Delta k = k_p - k_s - k_i - G = 0.$$

To describe the dynamics of parametric amplification in a nonlinear medium under nonstationary conditions, a system of coupled differential equations is used, accounting for the following physical effects:

- Linear absorption, which causes exponential decay of wave amplitudes and reduces process efficiency.
- Dispersion effects, including group velocity dispersion and higher-order dispersion, which affect phase matching and the temporal structure of pulses.
- Nonlinear interactions, determined by the effective nonlinear coupling coefficient.

The system of equations describing the evolution of complex amplitudes  $A_p$ ,  $A_s$ , and  $A_i$  (for pump, signal, and idler waves, respectively) is as follows [11]:

$$\begin{aligned}\frac{\partial A_p}{\partial z} + \frac{1}{v_p} \frac{\partial A_p}{\partial t} + \frac{\alpha_p}{2} A_p &= -i \frac{\omega_p}{2n_p c} \chi^{(2)} A_s A_i \exp(i\Delta k z), \\ \frac{\partial A_s}{\partial z} + \frac{1}{v_s} \frac{\partial A_s}{\partial t} + \frac{\alpha_s}{2} A_s &= -i \frac{\omega_s}{2n_s c} \chi^{(2)} A_p A_i^* \exp(-i\Delta k z), \\ \frac{\partial A_i}{\partial z} + \frac{1}{v_i} \frac{\partial A_i}{\partial t} + \frac{\alpha_i}{2} A_i &= -i \frac{\omega_i}{2n_i c} \chi^{(2)} A_p A_s^* \exp(-i\Delta k z),\end{aligned}$$

where:

- $A_p, A_s, A_i$  are the complex amplitudes of the pump, signal, and idler waves;
- $\omega_p, \omega_s, \omega_i$  are the frequencies of the pump, signal, and idler waves;
- $n_p, n_s, n_i$  are the refractive indices for the respective waves;
- $\chi^{(2)}$  is the effective second-order nonlinear coupling coefficient;
- $\alpha_p, \alpha_s, \alpha_i$  are the linear absorption coefficients [12, 13];
- Dispersion effects are modeled using the group velocity dispersion parameter  $\beta_2 = \frac{\partial^2 k}{\partial \omega^2}$ , incorporated into the equations via second-order temporal derivatives, ensuring accurate representation of pulse broadening in the infrared range [14, 15].

Boundary conditions for the system are chosen based on experimental setups typical for femtosecond laser systems:

$$\begin{aligned} A_p(z=0, t) &= A_{p0} \exp(-t^2/\tau_p^2), \\ A_s(z=0, t) &= 0.01 A_{p0}, \\ A_i(z=0, t) &= 0, \end{aligned}$$

where,  $A_{p0}$  is the maximum pump wave amplitude at the crystal input,  $\tau_p$  is the pump pulse duration (10, 50, or 100 fs), and  $A_s(z=0, t)$  is set to 1 % of  $A_{p0}$  to simulate a weak signal wave, consistent with experimental conditions.

### 3. Results and discussion

Figure 1 shows the dependence of the refractive index of this crystal on wavelength. Our calculations, based on the Sellmeier equations for the extraordinary wave (e–e–e interaction) as described in [12], agree with experimental data, confirming the reliability of our model. The refractive index was computed using the formula  $n^2(\lambda) = A + \frac{B}{\lambda^2 - C} + D\lambda^2$ , with coefficients  $A, B, C$ , and  $D$  derived from experimental data. The calculations were validated against measurements, showing a maximum deviation of less than 0.5 %. From the graph, it is clear that the refractive index decreases as wavelength increases, confirming theoretical predictions. The coherence length is calculated as  $L_c = \frac{\pi}{|k_p - k_s - k_i|} 16.2594 \mu\text{m}$ . Here, we considered only the extraordinary wave, i.e., e–e–e interaction. This result is crucial for understanding the optical properties of MgO:LiTaO<sub>3</sub> and optimizing quasi-phase matching. This result is important for determining the optimal domain period  $\Lambda$  for quasi-phase matching, ensuring efficient energy transfer.

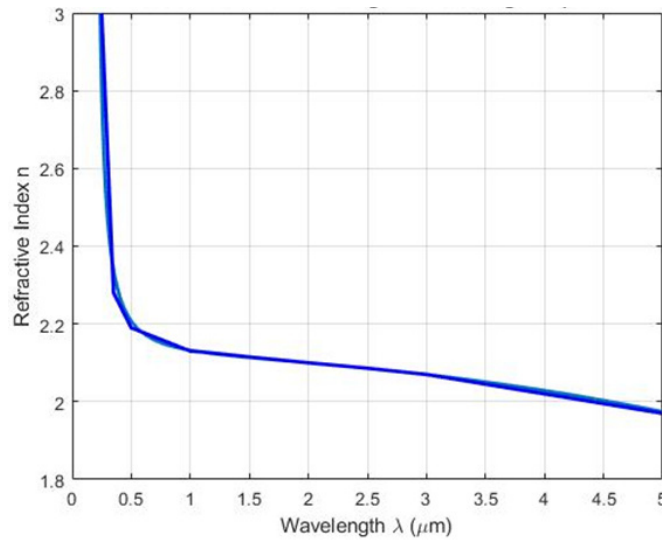


FIG. 1. Dependence of refractive index on wavelength

Figure 2 presents results obtained from the system of equations (4)–(6) with boundary conditions, accounting for all effects, including absorption. Here, the curves show the change in signal wave efficiency depending on the nonlinear photonic crystal length. The number of domains is about 1000. The solid line represents the case without absorption, while the dashed line shows the case with absorption ( $\alpha = 0.1 \text{ cm}^{-1}$ ). It is evident that energy exchange efficiency drops from 6 to 4.7 % due to linear absorption. This reduction is attributed to the exponential decay of the pump wave intensity, modeled as  $I(z) = I_0 \exp(-\alpha z)$ , which limits the energy available for transfer to the signal wave.

To address the role of the domain length, we analyzed its impact relative to the coherence length ( $L_c = 16.2594 \mu\text{m}$ ). Deviations of  $\pm 10 \%$  from the optimal domain length ( $d_0 = L_c$ ) were modeled to assess phase-matching sensitivity.

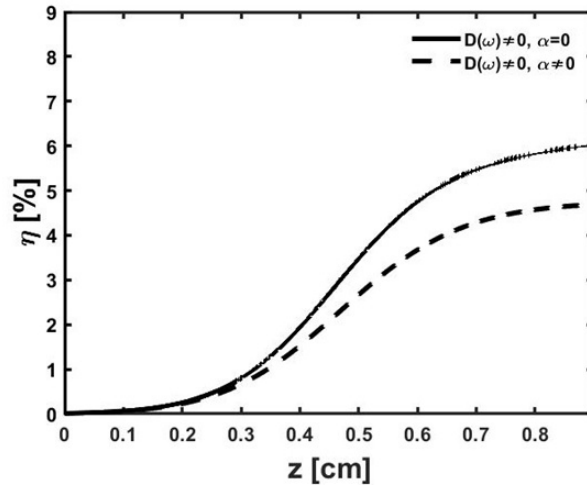


FIG. 2. Dependence of signal wave efficiency on the length of the nonlinear photonic crystal based on periodically poled MgO:LiTaO<sub>3</sub> ( $\tau = 10$  fs)

Calculations show that using femtosecond pulses can significantly increase efficiency if we reduce the domain length of the nonlinear photonic crystal. This is well illustrated in Fig. 3. The domain length is critical because it controls how well the waves stay in phase as they interact. Precise tuning of the domain lengths is essential for maintaining phase matching, as deviations from the coherence length degrade efficiency, as quantified below. Femtosecond pulses enhance nonlinear interactions due to high peak intensity, provided domain lengths are optimized, as discussed below. This makes the process more efficient, especially in a crystal with periodic structure like in our case.

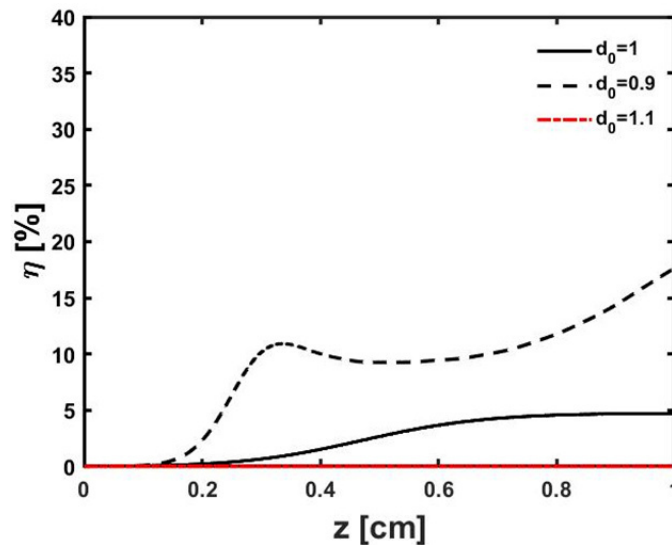


FIG. 3. Signal wave efficiency ( $\tau = 10$  fs) versus nonlinear photonic crystal length for different domain thicknesses

Figure 3 illustrates the dependence of signal wave formation efficiency on domain thickness in a periodic crystal structure, with fixed main and signal pulse durations of 10 fs. The domain length was varied by  $\pm 10\%$ . Reducing the domain length by 10% ( $d = 0.9L_c$ ) increases the efficiency to 15%, highlighting the process's sensitivity to changes in domain geometry. The solid line, representing the baseline case where the domain length remains unchanged ( $d_0 = L_c$ ), shows an efficiency of 10%. Increasing the domain length by 10% ( $d = 1.1L_c$ ), results in a sharp decrease in signal wave efficiency to 0.12% (this dependence is practically invisible), supporting the hypothesis that precise domain structure tuning is critical for enhancing efficiency. These results underscore the importance of accurate domain length optimization in achieving effective quasi-phase matching.

Next, we studied the role of pulse duration in signal wave efficiency formation. We examined this at different input pulse durations (100, 50, and 10 fs). The results are shown in Fig. 4. Pulse duration influences the interaction time and peak intensity of the waves, with shorter pulses (e.g., 10 fs) enhancing nonlinear effects due to higher intensity ( $I \propto E^2/\tau$ ), but requiring careful domain tuning to mitigate dispersion, as quantified below.

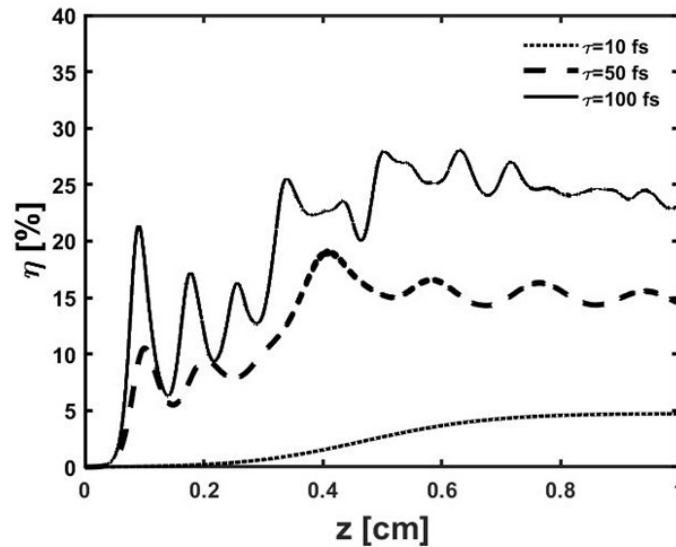


FIG. 4. Numerical calculation results of signal wave generation efficiency, considering all limiting factors, at pulse durations of 100, 50, and 10 fs

Figure 4 quantifies the combined effects of absorption and dispersion on signal wave formation. Here, the dependence of signal wave efficiency on crystal length with a regular domain structure is presented for different input pulse durations, denoted as  $\tau$ . The results indicate that the dispersion limits signal wave efficiency only when the main pulse duration is less than 10 fs. Thus, achieving maximum efficiency requires considering dispersion effects and selecting an appropriate pulse duration. For this range, an optimal domain length should be used, as shorter pulses (10 fs) achieve peak efficiency of 15 % with  $d = 0.9L_c$ , while longer pulses (100, 50 fs) stabilize at 8 – 10 % due to reduced dispersion but lower peak intensities.

Further, the study examined the role of domain thickness changes, calculated based on coherence length at a fixed crystal length, in forming the signal pulse. It was found that phase changes caused by dispersion effects can be partially compensated by adjusting the nonlinear lattice wave number. Fig. 5 shows the dependence of signal wave generation efficiency on the domain thickness at a fixed periodic crystal length (0.1 cm). Adjusting domain thickness optimizes quasi-phase matching, aligning wave interactions to mitigate dispersion effects, as quantified below.

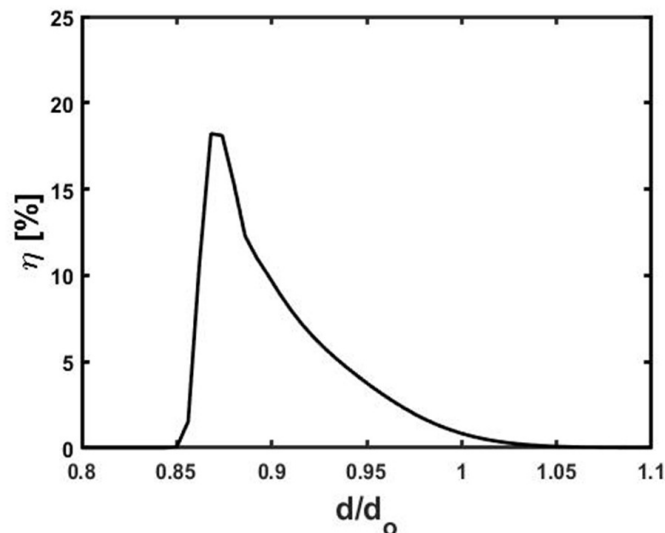


FIG. 5. Dependence of signal wave efficiency on domain thickness at a fixed crystal length (0.1 cm)

During the numerical experiment, it was observed that reducing domain thickness increases signal wave generation efficiency. The results showed that efficiency reaches 18 % when the value decreases to  $d = 0.9L_c$ , corresponding to an efficiency increase of about 13.2 % compared to  $d = L_c$  (4.8 %). This enhancement is due to improved quasi-phase

matching, modeled by the phase mismatch term  $\Delta k(z) = \Delta k_0 + \left(\frac{\partial k}{\partial \omega}\right) \Delta \omega$ , which allows partial compensation of dispersion-induced phase shifts.

Finally, Figure 6 shows the dependence of signal wave amplification efficiency on the length of the periodic crystal for different domain thicknesses. Calculations were performed for two cases: in the first, domain thickness equals the coherence length (solid curve,  $d = L_c$ ), and in the second, domain thickness differs from the coherence length (dashed curve,  $d/d_0 \approx 0.868$ ). As in the previous graph, a significant efficiency increase is clearly seen when domain thickness deviates from the coherence length. This confirms that precise tuning of domain geometry enhances energy transfer by maintaining phase coherence over longer crystal lengths, consistent with theoretical models of quasi-phase matching.

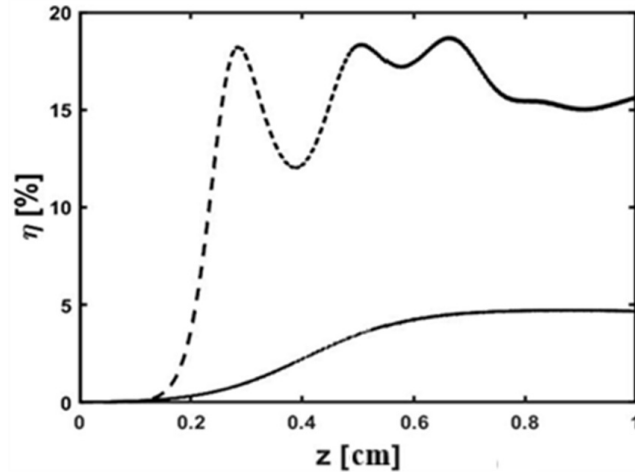


FIG. 6. Dependence of signal wave efficiency on periodic crystal length (dashed curve at  $d/d_0 \approx 0.868$ , solid curve at  $d/d_0 = 1$ ),  $d_0 = 16.25 \mu\text{m}$ ,  $\tau = 10 \text{ fs}$

#### 4. Conclusion

Thus, this work studied the parametric amplification process of femtosecond pulses in  $\text{MgO}:\text{LiTaO}_3$  crystals with periodic modulation of quadratic nonlinear susceptibility. By optimizing domain length to  $0.9d_0$ , we achieved a signal wave efficiency of 18 %, a significant improvement over the baseline 4.8 %, demonstrating the potential of precise domain tuning to mitigate dispersion and absorption effects. The calculation results showed that there is an optimal domain length at which a significant increase in frequency conversion efficiency is achieved in the nonstationary regime. Additionally, it was found that even a small deviation of domain size from the coherence length can lead to quasi-phase matching and partial compensation of phase shifts caused by medium dispersion effects. The influence of linear absorption was also studied; as calculations showed, it significantly affects the parametric light amplification process in this crystal. These results advance the understanding of femtosecond parametric amplification in the infrared range and provide a foundation for designing efficient optical devices, such as tunable IR lasers and amplifiers.

#### References

- [1] Kroll H. Parametric amplification in spatially extended media and application to the design of tunable oscillation at optical frequencies. *Physical Review*, 1962, **127**, 1207.
- [2] Yakovlev I.A., Akhmanov S.A., Khokhlov R.V. Problems of nonlinear optics. *Advances in Physical Sciences*, 1965, **85** (3), P. 579–581.
- [3] Kingston R.H. Parametric amplification and oscillation at optical frequencies. *Proceedings of the Institute of Radio Engineers*, 1962, **50** (4), 472.
- [4] Wang C.C., Racette G.W. Measurement of parametric gain accompanying optical difference frequency generation. *Applied Physics Letters*, 1965, **6** (8), P. 169–171.
- [5] Akhmanov S.A., Khokhlov R.V. Parametric amplifiers and light generators. *Advances in Physical Sciences*, 1966, **88** (3), P. 439–460.
- [6] Sabirov O.I., Assanto G., Sapaev U.K. Efficient third-harmonic generation by inhomogeneous quasi-phase-matching in quadratic crystals. *Photonics*, 2023, **10** (1).
- [7] Sabirov O.I., Akbarova N., Atadjanova N., Sapaev U. Efficient realization of infrared coherent radiation by the method of parametric light amplification in nonlinear photonic crystals. *J. of Physics: Conference Series*, 2021, **2131** (5).
- [8] Stensson K., Björk G., Gallo K. Green-pumped parametric downconversion in hexagonally poled  $\text{MgO}:\text{LiTaO}_3$ . *Proceedings of the Conference "Advanced Solid-State Lasers"*, 2014, Atu3A-5, P. 47–49.
- [9] Liu Y.H., Xie Z.D., Ling W., Yuan Y., Lv X.J., Lu J., Hu X.P., Zhao G., Zhu S.N. Efficiency-enhanced optical parametric down conversion for mid-infrared generation on a tandem periodically poled  $\text{MgO}$ -doped stoichiometric lithium tantalate chip. *Opt. Express*, 2011, **19**, P. 17500–17505.
- [10] Satoshi E., Ashihara S. Comparative study on light-induced absorption between  $\text{MgO}:\text{LiNbO}_3$  and  $\text{MgO}:\text{LiTaO}_3$ . *J. of Applied Physics*, 2011, **110** (6).
- [11] Sabirov O.I., et al. High efficient optical parametric amplification of femtosecond pulses in  $\text{MgO}$  doped PPLN crystals at  $3.4 \mu\text{m}$ . *Optical and Quantum Electronics*, 2023, **55** (8).

- [12] Dolev I., et al. Linear and nonlinear optical properties of MgO:LiTaO<sub>3</sub>. *Applied Physics B*, 2009, **96**, P. 423–432.
- [13] Alexandrovski A.L., et al. UV and visible absorption in LiTaO<sub>3</sub>. *Laser Material Crystal Growth and Nonlinear Materials and Devices*, 1999, **3610**, P. 44–51.
- [14] Sapaev U.K., Kutzner J., Finsterbusch K. Optimization of type-II frequency doubling of spatial and temporal limited laser light in nonlinear crystals. *Optical and Quantum Electronics*, 2005, **37**, P. 515–527.
- [15] Sabirov O.I., et al. On the theoretical analysis of parametric amplification of femtosecond laser pulses in crystals with a regular domain structure. *Physics of Wave Phenomena*, 2022, **30** (4), P. 277–282.

---

Submitted 28 March 2025; revised 21 May 2025; accepted 26 May 2025

*Information about the authors:*

*Obid I. Sabirov* – Urgench State University, Kh. Alimjan Str. 14, Urgench, 220100, Khorezm Region, Uzbekistan; ORCID 0009-0002-8210-2387; obid7432505@gmail.com

*Alisher E. Rajabov* – Urgench State University, Kh. Alimjan Str. 14, Urgench, 220100, Khorezm Region, Uzbekistan

*Anvar R. Matnazarov* – Urgench Innovative University, Gurlan-2 Str., Urgench, 220100, Khorezm Region, Uzbekistan

*Bakhodir Kh. Eshchanov* – Chirchik State Pedagogical University, Amir Temur Str. 104, Chirchik, Tashkent Region, Uzbekistan; ORCID 0000-0003-1168-2572; bakhodir.eshchanov@gmail.com

*Shavkat Otajanov* – National University of Uzbekistan named after Mirzo Ulugbek, University Str. 4, Tashkent, 100174, Uzbekistan

*Usman K. Sapaev* – Tashkent Branch of the Russian Gubkin University, Durmon Yuli Street 34, Tashkent, 100125, Uzbekistan; ORCID 0000-0001-8040-4395; usapaev@gmail.com

*Conflict of interest:* the authors declare no conflict of interest.

## Fast forward of adiabatic quantum dynamics: an application to planar Dirac systems

Iwan Setiawan<sup>1</sup>, Riska Ekawita<sup>2</sup>, Ryan Sugihakim<sup>3</sup>, Bobby Eka Gunara<sup>3</sup>

<sup>1</sup>Physics Education Department, University of Bengkulu, Kandang Limun, Bengkulu 38371, Indonesia

<sup>2</sup>Physics Department, University of Bengkulu, Kandang Limun, Bengkulu 38371, Indonesia

<sup>3</sup>Institut Teknologi Bandung, Jalan Ganesha 10, Bandung 40132, Indonesia

<sup>a</sup>[iwansetiawan@unib.ac.id](mailto:iwansetiawan@unib.ac.id), <sup>b</sup>[rekawita@unib.ac.id](mailto:rekawita@unib.ac.id), <sup>c</sup>[ryan.s.hakim@gmail.com](mailto:ryan.s.hakim@gmail.com), <sup>d</sup>[bobby@itb.ac.id](mailto:bobby@itb.ac.id)

Corresponding author: I. Setiawan, [iwansetiawan@unib.ac.id](mailto:iwansetiawan@unib.ac.id)

**ABSTRACT** We study a scheme of fast-forward adiabatic quantum dynamics of a  $(2 + 1)$  Dirac particle. This scheme was originally proposed by Masuda and Nakamura. In this scheme, we include the adiabatic parameter that maintains the adiabatic motion of the particle and fast forward its motion by introducing a time scaling parameter. The fast forward adiabatic state is obtained by determining the regularization term and driving potential. We introduce the proposed method to the system with the Dirac particle using a  $(2 + 1)$  dimension-time-dependent Dirac equation and obtain the regularization term, the driving scalar potential  $V_{FF}$  and the driving vector potential  $A_{FF}$ . By tuning the driving electric field, this method can accelerate the adiabatic dynamics of an electron as a Dirac particle trapped in the ground state in the plane  $xy$  and an electric field in the  $x$  direction and a constant magnetic field in the  $y$  direction. This acceleration will preserve the ground state of the wave function from the initial time to the final time.

**KEYWORDS** fast forward, adiabatic, planar Dirac

**ACKNOWLEDGEMENTS** I.S. thanks Prof. Katsuhiko Nakamura for a valuable discussion. I.S. thanks Hibah Kolaborasi Internasional Universitas Bengkulu 2024 and Hibah Fundamental DRTPM Kemdikbudristek 2024. I.S. and B.E.G. acknowledge the World Class Professor Program (WCP) from Kemdikbudristek 2023 for financial support.

**FOR CITATION** Setiawan I., Ekawita R., Sugihakim R., Gunara B.E. Fast forward of adiabatic quantum dynamics: an application to planar Dirac systems. *Nanosystems: Phys. Chem. Math.*, 2025, **16** (3), 298–305.

### 1. Introduction

Attempting to control the dynamics of quantum systems is one of humanity's biggest dreams in this millennium. To achieve this, some theoretical frameworks have been developed. The theory currently being developed and widely used is an adiabatic quantum theorem [1–6], which allows us to maintain the quantum state during the evolution of the system. Adiabatic quantum dynamics is crucial in understanding how quantum systems evolve, especially in quantum computing and quantum annealing [7]. However, challenges such as small energy gaps and slow evolution times are significant hurdles that must be overcome for practical implementation. It takes a very long time to obtain the desired target state, which is less beneficial when manufacturing a massive product or designing large macroscopic systems. Some methods have been developed to solve this problem. The fast-forward method is one of the promising methods developed in many aspects of quantum systems [8–10]. Another method called a shortcut to adiabaticity (STA) has also attracted much attention [11–14]. A wide variety of techniques have been developed in terms of STA. Transitionless quantum driving [15, 16], and the STA method from the classical point of view [17–19]. The STA method has also been considered in terms of open quantum systems [20]. The fast-forward scheme is developed to accelerate the adiabatic quantum dynamics by modifying the original Hamiltonian by introducing the adiabatic time parameter that goes very slow and tends to zero. Then, by obtaining the additional Hamiltonian to satisfy the Schrodinger equation, the adiabatic time parameter is replaced by the time scaling magnification factor that goes to infinity. Fast forward methods recently have been developed to accelerate adiabatic quantum dynamics of quantum spin systems [21–24], quantum tunneling [25, 26], stochastic heat engine [27] and also on how to accelerate the dynamics of particle which include non-equilibrium steady states of charged particle [28]. The fast-forward technique and STA method has a strong correlation and it has been also reported [29]. Some methods are considering the relativistic quantum dynamics that governed by the Dirac equation [30–32]. The technique of STA on a relativistic quantum system has been found by using time-rescaling methods [33]. Key features of Dirac dynamics include its relativistic nature, prediction of antiparticles, spin-1/2 particle behavior, and Lorentz invariance, making it essential for understanding the quantum dynamics of relativistic systems [34, 35]. In this study, we design a method to accelerate relativistic quantum dynamics using a fast-forward scheme on  $(2 + 1)$  dimensional using the Dirac equation. By applying the fast forward method to the  $(2 + 1)$  Dirac particle, we can derive the expression of driving energy in terms of driving scalar potential, driving vector potential, and driving electric field. These driving

energy can accelerate the adiabatic dynamics of an electron as a Dirac particle trapped in the ground state of the  $xy$  plane. The adiabatic acceleration that preserve the ground state of the wave function from the initial time to the final time, is essential to improve the unique properties of such two dimensional material like graphene. These techniques aim to tailor graphene's unique characteristics to specific applications, such as improving electrical conductivity, and electron mobility. Recently, this study has developed and attracted a lot of attention due to the ability to describe quasi-particles in graphene, a revolutionary material with a host of exceptional and remarkable properties [36, 37]. Graphene, a single layer of carbon atoms arranged in a two-dimensional honeycomb lattice. One of its most intriguing features is its ability to host massless Dirac fermions. This connection between graphene and Dirac particles arises due to the special nature of its electronic band structure [38]. Application of fast-forward approach gives one useful protocol to understand and control this two-dimensional honeycomb lattice which is important for their applications in nanoscale electronic sensors, heat conductive material, and energy harvesting devices [39]. In Section 2, we shall introduce a time-dependent  $(2 + 1)$  Dirac equation. Section 3 considers about adiabatic dynamics of the Dirac equation. Sections 4 and 5 consider the fast forward of adiabatic dynamics of the Dirac particle and the example respectively. Section 6 is devoted to the conclusion.

## 2. Dirac equation

In this section, we briefly introduce and review the literature on the time-dependent Dirac equation. The  $(2+1)$  dimension Dirac equation is written as [40]

$$i\hbar \frac{\partial \Psi(x, y, t)}{\partial t} = H_D \Psi(x, y, t), \quad (1)$$

with Hamiltonian is defined as

$$H_D = (p_x + A_x)\sigma_x + (p_y + A_y)\sigma_y + mc^2\sigma_z + V_0\mathbb{I}, \quad (2)$$

where  $\sigma_{x,y,z}$ ,  $p_{x(y)}$ ,  $A_{x(y)}$ ,  $V_0$  are the Pauli matrices, momenta, vector potentials and scalar potentials, respectively. By substituting the above Hamiltonian, the time dependent Dirac equation can be rewritten as

$$i\hbar \frac{\partial \Psi(x, y, t)}{\partial t} = [(-i\hbar\partial_x + A_x)\sigma_x + (-i\hbar\partial_y + A_y)\sigma_y + mc^2\sigma_z + V_0\mathbb{I}] \Psi(x, y, t). \quad (3)$$

For convenience in notation, we denote prior wave functions  $(\Psi_1, \Psi_2)$ . The matrix form of the Dirac equation is written as

$$i\hbar \begin{pmatrix} \frac{\partial \Psi_1}{\partial t} \\ \frac{\partial \Psi_2}{\partial t} \end{pmatrix} = \begin{pmatrix} mc^2 + V_0 & \pi_- \\ \pi_+ & -mc^2 + V_0 \end{pmatrix} \begin{pmatrix} \Psi_1 \\ \Psi_2 \end{pmatrix}, \quad (4)$$

where  $\pi_{\pm} = \pi_x \pm i\pi_y$ , and

$$\pi_{x(y)} = -i\hbar \frac{\partial}{\partial x(y)} + A_{x(y)}. \quad (5)$$

## 3. Regularization scheme

We begin by considering a Hamiltonian  $H_0$  for the massless Dirac system in  $(2 + 1)$  dimensions. The Hamiltonian of this system is written as

$$H_0 = v_F (p_x + A_x) \sigma_x + v_F (p_y + A_y) \sigma_y - V_0\mathbb{I}, \quad (6)$$

with the effective Fermi velocity  $v_F = c/300$ , and  $p_x$ ,  $p_y$  are the components of momentum,  $A_x$ ,  $A_y$  are the components of the vector potential, and  $V_0$  is the scalar potential. Meanwhile, there is the corresponding spinor  $\Psi_0$  for the system that satisfies the adiabatic dynamics where there is a time-dependent parameter  $R(t)$  that is slowly changing over time such that

$$R(t) = R_0 + \epsilon t. \quad (7)$$

Here  $\epsilon \ll 1$ . Such a spinor can be written as

$$\Psi_0 = e^{i\delta_n(t)} \begin{pmatrix} \phi_{1,n}(x, y, R(t)) \\ \phi_{2,n}(x, y, R(t)) \end{pmatrix}, \quad (8)$$

where  $\delta_n$  is the dynamical phase.

To accelerate the adiabatic evolution with a slowly changing time-dependent parameter  $R(t, \epsilon)$ , a huge time scaling factor, denoted by  $\alpha$  is necessary. Thus, we must create a scheme to regularize the system so that  $\alpha\epsilon$  is finite. This procedure is used by modifying the wave function into an adiabatic wave function  $\Psi^{reg}$  as written in Eq. (8), and modifying

the potentials as

$$v_F A_x(x, y, R(t))\sigma_x \rightarrow v_F A_x(x, y, R(t))\sigma_x + \epsilon v_F W, \quad (9)$$

$$v_F A_y(x, y, R(t))\sigma_y \rightarrow v_F A_y(x, y, R(t))\sigma_y + \epsilon v_F W, \quad (10)$$

$$-V_0(x, y, R(t))\mathbb{I} \rightarrow -V_0(x, y, R(t))\mathbb{I} - \epsilon W, \quad (11)$$

where  $W$  is a  $2 \times 2$  matrix, and its components  $W_{ij} = W_{ij}(x, y, R(t))$ .

Then, after modifying the potentials of system, we have a regularized Hamiltonian  $H^{reg}$  written as

$$H^{reg} = H_0(R(t)) + \epsilon \mathcal{H}, \quad (12)$$

where

$$\mathcal{H} = (2v_F - 1)W. \quad (13)$$

The governing dynamical equation for regularized system is

$$i\partial_t \Psi^{reg} = H^{reg} \Psi^{reg}. \quad (14)$$

By using Eq. (14) and collecting the  $O(1)$ , we have

$$H_0 \Psi^{reg} = -\partial_t \delta_n \Psi^{reg}, \quad (15)$$

and  $O(\epsilon)$  terms

$$i\partial_R \Psi^{reg} = (2v_F - 1)W \Psi^{reg}. \quad (16)$$

Here in the limit  $\epsilon \rightarrow 0$ ,  $\alpha \rightarrow \infty$ , and  $\epsilon\alpha \sim 1$ , we can suppress the terms of  $O(\epsilon^2)$ . Eq. (15) results in the eigenvalue equation for the Hamiltonian  $H_0$ . This implies  $E_n = -\partial_t \delta_n$ . Meanwhile, we solve Eq. (16) to obtain the matrix  $W$ .

The components of the regularized spinor  $\Psi^{reg}$  and the matrix  $W$  are complex numbers. Expanding them into real and imaginary parts, we have

$$au_{11} + cu_{12} - bv_{11} - dv_{12} = -(2v_F - 1)^{-1} \partial_R b, \quad (17)$$

$$au_{21} + cu_{22} - bv_{21} - dv_{22} = -(2v_F - 1)^{-1} \partial_R d, \quad (18)$$

$$bu_{11} + du_{22} + av_{11} + cv_{12} = (2v_F - 1)^{-1} \partial_R a, \quad (19)$$

$$bu_{21} + du_{22} + av_{21} + cv_{22} = (2v_F - 1)^{-1} \partial_R c, \quad (20)$$

where

$$W = \begin{pmatrix} u_{11} & u_{12} \\ u_{21} & u_{22} \end{pmatrix} + i \begin{pmatrix} v_{11} & v_{12} \\ v_{21} & v_{22} \end{pmatrix}, \quad (21)$$

$$\Psi^{reg} = \begin{pmatrix} a \\ c \end{pmatrix} + i \begin{pmatrix} b \\ d \end{pmatrix}. \quad (22)$$

Eq. (21) is the main equation for the present work. Here,  $W$  has a role as a regularization term to fulfill the Dirac equation. By obtaining  $W$ , we can preserve the spinor state of the systems during the evolution of time. However, this will result in four freedoms of choice of solutions for  $W$ .

### 3.1. The solution of regularization matrix

The system of equations of our regularization matrix is given by

$$\begin{pmatrix} a & c & 0 & 0 & -b & -d & 0 & 0 \\ 0 & 0 & a & c & 0 & 0 & -b & -d \\ b & d & 0 & 0 & a & c & 0 & 0 \\ 0 & 0 & b & d & 0 & 0 & a & c \end{pmatrix} \begin{pmatrix} u_{11} \\ u_{12} \\ u_{21} \\ u_{22} \\ v_{11} \\ v_{12} \\ v_{21} \\ v_{22} \end{pmatrix} = \frac{1}{2v_F - 1} \begin{pmatrix} -\partial_R b \\ -\partial_R d \\ \partial_R a \\ \partial_R c \end{pmatrix}. \quad (23)$$

We find the row echelon form of the equation is

$$\begin{pmatrix} 1 & \frac{c}{a} & 0 & 0 & -\frac{b}{a} & -\frac{d}{a} & 0 & 0 \\ 0 & 1 & 0 & 0 & \frac{a^2 + b^2}{ad - bc} & \frac{ac + bd}{ad - bc} & 0 & 0 \\ 0 & 0 & 1 & \frac{c}{a} & 0 & 0 & -\frac{b}{a} & -\frac{d}{a} \\ 0 & 0 & 0 & 1 & 0 & 0 & \frac{a^2 + b^2}{ad - bc} & \frac{ac + bd}{ad - bc} \end{pmatrix} \begin{pmatrix} u_{11} \\ u_{12} \\ u_{21} \\ u_{22} \\ v_{11} \\ v_{12} \\ v_{21} \\ v_{22} \end{pmatrix} = \frac{1}{2v_F - 1} \begin{pmatrix} -\frac{\partial_R b}{a} \\ \frac{a\partial_R a + b\partial_R b}{ad - bc} \\ -\frac{\partial_R d}{a} \\ \frac{a\partial_R c + b\partial_R d}{ad - bc} \end{pmatrix}. \quad (24)$$

From the above equation, we see that there are four free variables, which are  $\{v_{11}, v_{12}, v_{21}, v_{22}\}$ .

To solve the algebraic equation in Eq. (24), we should pick up only four unknown variables so that the number of equations and the number of variables are matched. Here we assume that all imaginary parts of  $W$  are zero, that is,  $v_{ij} = 0$ . So,

$$u_{11} = \frac{1}{2v_F - 1} \left( -\frac{a\partial_R a + b\partial_R b}{ad - bc} \frac{c}{a} - \frac{\partial_R b}{a} \right), \quad (25)$$

$$u_{12} = \frac{1}{2v_F - 1} \frac{a\partial_R a + b\partial_R b}{ad - bc}, \quad (26)$$

$$u_{21} = \frac{1}{2v_F - 1} \left( -\frac{a\partial_R c + b\partial_R d}{ad - bc} \frac{c}{a} - \frac{\partial_R d}{a} \right), \quad (27)$$

$$u_{22} = \frac{1}{2v_F - 1} \frac{a\partial_R c + b\partial_R d}{ad - bc}. \quad (28)$$

#### 4. Fast-forward of adiabatic Dirac dynamics

We define the fast-forwarded spinor as

$$\Psi_{FF}(x, y, t) = \Psi^{reg}(x, y, R(\Lambda(t))) = \begin{pmatrix} \phi_1^{reg}(x, y, R(\Lambda(t))) \\ \phi_2^{reg}(x, y, R(\Lambda(t))) \end{pmatrix} e^{i\delta_n(\Lambda(t))} \quad (29)$$

while in this time  $\delta_n(\Lambda(t)) = -\int_0^t ds E_n(R(\Lambda(s)))$  in natural units. Here  $\Lambda(t)$  is defined by

$$\Lambda(t) = \int_0^t \alpha(t') dt', \quad (30)$$

with the standard time  $t$ .  $\alpha(t)$  is an arbitrary magnification time scale factor that satisfies  $\alpha(0) = 1$ ,  $\alpha(t) > 1$  ( $0 < t < T_{FF}$ ) and  $\alpha(t) = 1$  ( $t \geq T_{FF}$ ). For a long final time  $T$  in the original adiabatic dynamics, we can consider the fast forward dynamics with a new time variable which reproduces the target state  $\Psi_0^{(n)}(R(T))$  in a shorter final time  $T_{FF}$  defined by

$$T = \int_0^{T_{FF}} \alpha(t) dt. \quad (31)$$

The simplest expression for  $\alpha(t)$  in the fast-forward range ( $0 \leq t \leq T_{FF}$ ) is given by [9] as :

$$\alpha(t) = \bar{\alpha} - (\bar{\alpha} - 1) \cos\left(\frac{2\pi}{T_{FF}} t\right), \quad (32)$$

where  $\bar{\alpha}$  is the mean value of  $\alpha(t)$  given by  $\bar{\alpha} = T/T_{FF}$ , while the limit  $\bar{\alpha} \rightarrow \infty$  and  $\epsilon \rightarrow 0$  under the constraint of  $\bar{\alpha}\epsilon \equiv \bar{v}$ . Here  $R(\Lambda(t))$  is given by [9]

$$R(\Lambda(t)) = R_0 + 2\bar{v} \left( \frac{t}{2} - \frac{T_{FF} \sin\left(\frac{2\pi t}{T_{FF}}\right)}{4\pi} \right). \quad (33)$$

We postulate that the fast-forwarded spinor satisfies the Dirac equation as follows

$$i\frac{\partial\Psi_{FF}}{\partial t} = \begin{pmatrix} m + V_{FF} + V_0^{reg} & \pi_-^{FF} \\ \pi_+^{FF} & -m + V_{FF} + V_0^{reg} \end{pmatrix} \Psi_{FF}, \quad (34)$$

where

$$V_0^{reg} = V_0 + \epsilon\tilde{W}, \quad (35)$$

$$\pi_+^{FF} = -i\frac{\partial}{\partial x} + \frac{\partial}{\partial y} + A_x^0 + iA_y^0 + A_x^{FF} + iA_y^{FF}, \quad (36)$$

$$\pi_-^{FF} = -i\frac{\partial}{\partial x} - \frac{\partial}{\partial y} + A_x^0 - iA_y^0 + A_x^{FF} - iA_y^{FF}. \quad (37)$$

By substituting  $\Psi_{FF}$  in Eq. (29) to Eq. (34), we see

$$i\frac{\partial\Psi_{reg}}{\partial t} = \begin{pmatrix} m + V_{FF} + V_0^{reg} & \pi_-^{FF} \\ \pi_+^{FF} & -m + V_{FF} + V_0^{reg} \end{pmatrix} \begin{pmatrix} \phi_1^{reg} \\ \phi_2^{reg} \end{pmatrix} \quad (38)$$

We apply the time rescaled  $t \rightarrow \Lambda(t)$  as

$$i\frac{\partial\Psi_{reg}}{\partial\Lambda(t)} = \begin{pmatrix} m + V_0^{reg} & \pi_-^0 \\ \pi_+^0 & -m + V_0^{reg} \end{pmatrix} \Psi_{reg}, \quad (39)$$

where

$$\pi_{\pm}^0 = -i\frac{\partial}{\partial x} \pm \frac{\partial}{\partial y} + A_x^0 \pm iA_y^0 \quad (40)$$

By taking the time derivation of Eq. (39) and noting  $d\Lambda(t) = \alpha(t)dt$ , with the limit  $\epsilon \rightarrow 0$  and  $\alpha \rightarrow \infty$ ,  $\alpha\epsilon \rightarrow v(t)$ , we see (the detailed derivation given at Appendix)

$$\begin{pmatrix} V_{FF} & A_x^{FF} - iA_y^{FF} \\ A_x^{FF} + iA_y^{FF} & V_{FF} \end{pmatrix} \begin{pmatrix} \bar{\phi}_1 \\ \bar{\phi}_2 \end{pmatrix} = v(t) \begin{pmatrix} W & W - iW \\ W + iW & W \end{pmatrix} \begin{pmatrix} \bar{\phi}_1 \\ \bar{\phi}_2 \end{pmatrix} \quad (41)$$

The electric and magnetic fields are related to the driving vector potential  $V_{FF}$  and the driving vector potential  $A_{FF}$  as  $E_{FF} = -\frac{dA_{FF}}{dt} - \nabla V_{FF}$  and  $B_{FF} = \nabla \times A_{FF}$ , respectively.

## 5. Examples

We apply our calculation to a system that has a constant magnetic field perpendicular to the graphene plane in the positive direction of the  $z$  axis. This is the very well-known case of Landau levels [41]. We use their solution, for  $n > 0$ , written as:

$$\begin{pmatrix} \phi_1^n \\ \phi_2^n \end{pmatrix} = e^{iky} \begin{pmatrix} \varphi_{n-1}(x) \\ i\varphi_n(x) \end{pmatrix}, \quad (42)$$

where the eigenfunctions are given in terms of the Hermite polynomials, which correspond to harmonic oscillator potential:

$$\varphi_n(x) = c_n e^{-z^2/2} H_n(z(x)), \quad z(x) = \sqrt{\frac{\omega}{2}} \left( x - \frac{2k}{\omega} \right). \quad (43)$$

We define the adiabatic parameter as transforming the spatial variable of  $x$  as

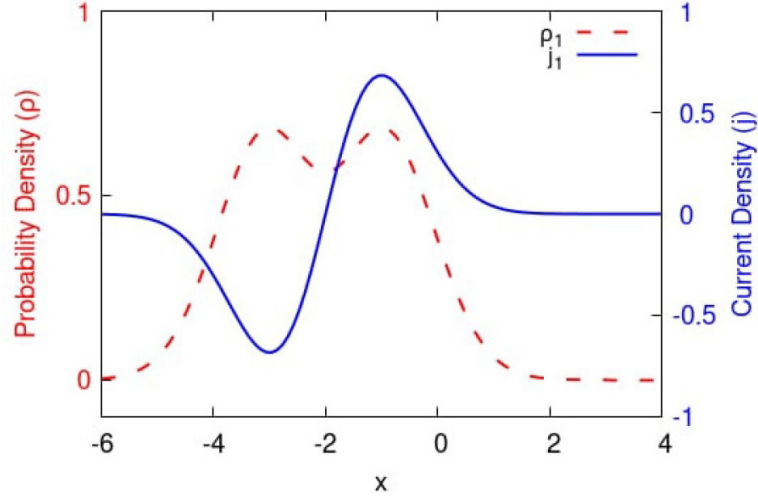
$$x \rightarrow x - R(t). \quad (44)$$

After calculation from Eqs. 25-28, we found the solution for  $W$ ,

$$W = \sqrt{\frac{\omega}{2}} \frac{1}{2v_F - 1} \begin{pmatrix} 0 & z\frac{\varphi_{n-1}}{\varphi_n} - 2(n-1)\frac{c_{n-1}}{c_{n-2}}\frac{\varphi_{n-2}}{\varphi_n} \\ z\frac{\varphi_n}{\varphi_{n-1}} - 2n\frac{c_n}{c_{n-1}} & 0 \end{pmatrix}. \quad (45)$$

For a constant magnetic field  $B(x) = 1/2$  and  $\omega = k = 1$ , the density of the wave function  $\rho$  (solid line) and the current density  $j$  (dotted line) with  $n = 1$  are depicted in Fig. 1. Using the regularization term  $W$ , we obtained the same wave function from the initial to the final time of evolution, and the time to obtain the target state is shorter. The regularization term preserves the wave function, and the final state is obtained in a shorter time.

The regularization term for  $(2+1)$  Dirac systems appears only in terms of the real part. There are four freedoms of choice to solve the regularization term. Here, we suppress the imaginary part of  $W$  in order to become more practical in realization. We see that the regularization term  $W$  fulfills the Dirac equation and guarantees the adiabatic wave function.


 FIG. 1. Probability and current density of wave function with constant magnetic field and  $n = 1$ 

Once the driving scalar and vector potential have been obtained, the targeted wave function will be obtained in a shorter time.

## 6. Conclusion

We have presented the fast-forward method of adiabatic quantum dynamics for a Dirac particle. This scheme is proposed to accelerate the spinor component of the wave function without disturbing the eigenstate of the system. During the evolution, we will obtain exactly the same eigenstate from the initial time to the final time. Using this scheme, we can reach the target state at any desired time. The strategy used in this scheme is the combination of two opposite ideas: infinitely large time-magnification factor ( $\bar{\alpha}$ ) and infinitely small growth rate ( $\epsilon$ ) of the adiabatic parameter. To accelerate the adiabatic wave function we have to obtain the regularization term of Hamiltonian to guarantee the adiabatic motion. Then, by calculating the driving scalar potential and the driving vector potential, the time to obtain the target state will be shorter. As a typical example, we considered the adiabatic dynamics of the Dirac particle. We obtain the driving scalar potential  $V_{FF}$  and the driving vector potential  $A_{FF}$ . By tuning the electric field, we can accelerate the adiabatic electron dynamics in the ground state trapped in the plane  $xy$ , an electric field in the  $x$  direction, and a constant magnetic field in the  $z$  direction. This acceleration will preserve the ground state of the wave function from the initial time to the final time. The fast-forward method gives one a useful protocol for understanding and controlling graphene as a two-dimensional honeycomb lattice, which is important for their applications in nanoscale electronic devices and superconductor.

## Appendix : Derivation for the driving potential in (2 + 1) Dirac equation

We see on the left hand side of Eq. (39)

$$i\hbar \frac{\partial \Psi_{reg}}{\alpha(t) \partial t} = i\hbar \left[ -\frac{i}{\hbar} \alpha E \Psi_{reg} + \frac{\partial \Psi_{reg}}{\partial t} \right] e^{i\delta_n(\Lambda(t))}, \quad (\text{A.46})$$

and on the right hand side

$$\alpha \begin{pmatrix} m + V_0^{reg} & \pi_-^0 \\ \pi_+^0 & -m + V_0^{reg} \end{pmatrix} \Psi_{reg}, \quad (\text{A.47})$$

then we have

$$\alpha E \begin{pmatrix} \phi_1^{reg} \\ \phi_2^{reg} \end{pmatrix} + i\hbar \frac{\partial}{\partial t} \Psi_{reg} = \alpha \begin{pmatrix} m + V_0^{reg} & \pi_-^0 \\ \pi_+^0 & -m + V_0^{reg} \end{pmatrix} \Psi_{reg}. \quad (\text{A.48})$$

By deleting  $\frac{\partial \Psi_{reg}}{\partial t}$ , and from Eq. (38) and Eq. (A.48), we see

$$\begin{pmatrix} m + V_{FF} + V_0^{reg} & \pi_-^{FF} \\ \pi_+^{FF} & -m + V_{FF} + V_0^{reg} \end{pmatrix} \begin{pmatrix} \phi_1^{reg} \\ \phi_2^{reg} \end{pmatrix} = \alpha \begin{pmatrix} m + V_0^{reg} & \pi_-^0 \\ \pi_+^0 & -m + V_0^{reg} \end{pmatrix} \Psi_{reg} - (\alpha - 1) E \begin{pmatrix} \phi_1^{reg} \\ \phi_2^{reg} \end{pmatrix} \quad (\text{A.49})$$

Now we apply

$$\Psi_{reg}(x, y, R(t)) = \Psi^{reg}(x, y, R(t)) = \begin{pmatrix} \bar{\phi}_1(x, y, R(\Lambda(t))) \\ \bar{\phi}_2(x, y, R(\Lambda(t))) \end{pmatrix} \quad (\text{A.50})$$

Substituting above spinor state to Eq. (A.49), we see

$$\begin{pmatrix} m + V_{FF} + V_0^{reg} & \pi_-^{FF} \\ \pi_+^{FF} & -m + V_{FF} + V_0^{reg} \end{pmatrix} \begin{pmatrix} \bar{\phi}_1 \\ \bar{\phi}_2 \end{pmatrix} = \alpha \begin{pmatrix} m + V_0^{reg} & \pi_-^0 \\ \pi_+^0 & -m + V_0^{reg} \end{pmatrix} \begin{pmatrix} \bar{\phi}_1 \\ \bar{\phi}_2 \end{pmatrix} - (\alpha - 1)E \begin{pmatrix} \bar{\phi}_1 \\ \bar{\phi}_2 \end{pmatrix} \quad (\text{A.51})$$

From Eq. (A.51), we see the eigen value problem as

$$-(\alpha - 1) \begin{pmatrix} m + V_0 & \pi_-^0 \\ \pi_+^0 & -m + V_0 \end{pmatrix} \begin{pmatrix} \bar{\phi}_1 \\ \bar{\phi}_2 \end{pmatrix} = -(\alpha - 1)E \begin{pmatrix} \bar{\phi}_1 \\ \bar{\phi}_2 \end{pmatrix} \quad (\text{A.52})$$

Eq. (A.51) can be rewritten as

$$\begin{pmatrix} V_{FF} & A_x^{FF} - iA_y^{FF} \\ A_x^{FF} + iA_y^{FF} & V_{FF} \end{pmatrix} \begin{pmatrix} \bar{\phi}_1 \\ \bar{\phi}_2 \end{pmatrix} = \epsilon(\alpha - 1) \begin{pmatrix} W & W - iW \\ W + iW & W \end{pmatrix} \begin{pmatrix} \bar{\phi}_1 \\ \bar{\phi}_2 \end{pmatrix} \quad (\text{A.53})$$

Noting  $d\Lambda(t) = \alpha(t)dt$  and taking the limit  $\epsilon \rightarrow 0$  and  $\alpha \rightarrow \infty$ ,  $\alpha\epsilon \rightarrow v(t)$ , we will obtain Eq. (41)

## References

- [1] Demirplak M., Rice S.A. Adiabatic population transfer with control fields. *J. Phys. Chem. A*, 2003, **89**, P. 9937.
- [2] Demirplak M., Rice S.A. Assisted adiabatic passage revisited. *J. Phys. Chem. B*, 2005, **109**, P. 6838.
- [3] Berry M.V. Transitionless quantum driving. *J. Phys A : Math. Theor.*, 2009, **42**, P. 365303.
- [4] Kato T. On the Adiabatic Theorem of Quantum Mechanics. *J. Phys. Soc. Jpn.*, 1950, **5**, P. 435.
- [5] Berry M.V. Geometric Amplitude Factors in Adiabatic Quantum Transitions. *Proc. R. Soc. London Ser. A*, 1990, **430**, P. 405.
- [6] N.V. Vitanov et al. Laser-induced population transfer by adiabatic passage techniques. *Annu. Rev. Phys. Chem.*, 2001, **52**, P. 763.
- [7] Albash T., Lidar D.A. Adiabatic quantum computation. *Rev. Mod. Phys.*, 2018, **90**, P. 015002.
- [8] Masuda S., Nakamura K. Fast-forward problem in quantum mechanics. *Phys. Rev. A*, 2008, **78**, P. 062108.
- [9] Masuda S., Nakamura K. Fast-forward of adiabatic dynamics in quantum mechanics. *Proc. R. Soc. A*, 2010, **466**, P. 1135–1154.
- [10] Masuda S., Nakamura K. Acceleration of adiabatic quantum dynamics in electromagnetic fields. *Phys. Rev. A*, 2011, **84**(4), P. 043434.
- [11] Lewis H.R., Riesenfeld W.B. An exact quantum theory of the time-dependent harmonic oscillator and of a charged particle in a time-dependent electromagnetic field. *J. Math. Phys A*, 1969, **10**, P. 1458.
- [12] Chen X., Ruschhaupt A., del Campo A., GuLery-Odelin D., Muga J.G. Fast optimal frictionless atom cooling a harmonic traps: Shortcut to adiabaticity. *Phys. Rev. Lett.*, 2010, **104**, P. 063002.
- [13] Odelin D.G., Ruschhaupt A., Kiely A., Torriontegui E., Garaot S.M., and Muga J.G. Shortcuts to adiabaticity: Concepts, methods, and applications, *Rev. Mod. Phys.*, 2019, **91**, P. 045001.
- [14] Torriontegui E., Ibanez M., Martinez-Garaot M., Modugno M., del Campo A., Guery-Odelin D., Ruschhaupt A., Chen X., Muga J.G. Shortcut to adiabaticity *Adv.At. Mol. Opt. Phys.*, 2013, **62**, P. 117.
- [15] Chen X., Torriontegui E., and Muga J.G. Lewis-Riesenfeld invariants and transitionless quantum driving. *Phys. Rev. A*, 2011, **83**, P. 062116.
- [16] Takahashi K. Transitionless quantum driving for spin systems, *Phys. Rev. E*, 2013, **87**, P. 062117.
- [17] Deffner S., Jarzynski C., and Campo D. Classical and Quantum Shortcuts to Adiabaticity for Scale-Invariant Driving. *Phys. Rev. X*, 2014, **4**, P. 021013.
- [18] Jarzynski C. Generating shortcuts to adiabaticity in quantum and classical dynamics. *Phys. Rev. A*, 2013, **88**, P. 040101(R).
- [19] Jarzynski C., Deffner S., Patra A., and Subaşı Y. Fast forward to the classical adiabatic invariant. *Phys. Rev. E*, 2017, **95**, P. 032122.
- [20] Dann R., Tobalina A., and Kosloff R. Shortcut to Equilibration of an Open Quantum System. *Phys. Rev. Lett.*, 2019, **122**, P. 250402.
- [21] Setiawan I., Gunara B.E., Masuda S., Nakamura K. Fast forward of entangled spin dynamics. *Phys. Rev. A*, 2017, **96**, P. 052106.
- [22] Setiawan I., Gunara B.E., Avazbaev S., Nakamura K. Fast forward of adiabatic spin cluster: Geometry dependent of driving interaction. *Phys. Rev. A*, 2019, **99**, P. 062116.
- [23] Takahashi K. Fast-forward scaling in a finite-dimensional Hilbert space *Phys. Rev. A*, 2014, **89**, P. 042113.
- [24] Setiawan I., Ekawita R., Sugihakim R., Gunara B.E. Fast-forward adiabatic quantum dynamics of XY spin model on three spin system. *Phys. Scr.*, 2023, **98**, P. 025405.
- [25] Khujakulov A., Nakamura K. Scheme for accelerating quantum tunneling dynamics. *Phys. Rev. A*, 2016, **93**, P. 022101.
- [26] Nakamura K., Khujakulov A., Masuda S. Fast forward of adiabatic control of tunneling states. *Phys. Rev. A*, 2017, **95**, P. 062108.
- [27] Nakamura K., Matrasulov J., Izumida Y. Fast-forward approach to stochastic heat engine. *Phys. Rev. E*, 2020, **102**, P. 012129.
- [28] Setiawan I., Sugihakim R., Gunara B.E., Masuda S., Nakamura K. Fast-forward generation of non-equilibrium steady states of a charged particle under the magnetic field. *Progress of Theoretical and Experimental Physics*, 2023, P. 063A04.
- [29] Torriontegui E., Martinez-Garaot M., Ruschhaupt A., Muga J.G. Shortcut to adiabaticity: fast-forward approach. *Phys. Rev. A*, 2012, **86**, P. 013601.
- [30] Deffner S. Shortcuts to adiabaticity: suppression of pair production in driven Dirac dynamics. *New J. Phys.*, 2016, **18**, P. 012001.
- [31] Xue-Ke Song, Fu-Guo Deng, Lamata L., and Muga J.G. Robust state preparation in quantum simulations of Dirac dynamics. *Phys. Rev. A*, 2017, **95**, P. 022332.
- [32] Roychowdhury A., Deffner A. Time-rescaling of Dirac dynamics: Shortcuts to adiabaticity in ion traps and Weyl semimetals. *Entropy*, 2021, **23**(1), P. 81.
- [33] Bernardo B.d.L. Time-rescaled quantum dynamics as a shortcut to adiabaticity. *Phys. Rev. Res.*, 2020, **2**, P. 013133.
- [34] Thaller B. *The Dirac Equation*. Springer, Berlin, Germany, 1956.
- [35] Peskin M.E., Schroeder D.V. *An Introduction to Quantum Field Theory (Frontiers in Physics)*. Westview Press, Boulder, CO, USA, 1995.

- [36] Wehling T.O., Black-Schaffer A.M., and Balatsky A.V. Dirac materials. *Adv. Phys.*, 2014, **63**, P. 1.
- [37] Zhang X.W., Ren Y., Wang C., Cao T., Xiao D. Gate-Tunable Phonon Magnetic Moment in Bilayer Graphene. *Phys. Rev. Lett.*, 2023, **130**, P. 226302.
- [38] Valderrama J.F.M., Mao D., and Chowdhury D. Low-Energy Optical Sum Rule in Moire Graphene. *Phys. Rev. Lett.*, 2024, **133**, P. 196501.
- [39] Ribetto F.D., Elaskar S.A., Calvo H.L., Bustos-Marun R.A. Fluctuation-induced currents in suspended graphene nanoribbons: Adiabatic quantum pumping approach. *Phys. Rev. B.*, 2023, **108**, P. 245408.
- [40] Setiawan I., Sugihakim R., Gunara B.E. Fast forward Adiabatic Quantum Dynamics On Two Dimensional Dirac Equation. *J. Phys.Conf. Ser.*, 2021, **1842**, P. 012057.
- [41] Kuru S., Negro J. and Nieto L.M. Exact analytic solutions for a Dirac electron moving in graphene under magnetic fields. *J. Phys.: Condens. Matter.*, 2009, **21**, P. 455305.

---

*Submitted 25 April 2025; revised 20 May 2025; accepted 21 May 2025*

*Information about the authors:*

*Iwan Setiawan* – Physics Education Department, University of Bengkulu, Kandang Limun, Bengkulu 38371, Indonesia; ORCID 0000-0001-5962-4844; iwansetiawan@unib.ac.id

*Riska Ekawita* – Physics Department, University of Bengkulu, Kandang Limun, Bengkulu 38371, Indonesia; ORCID 0000-0001-5634-4695; rekawita@unib.ac.id

*Ryan Sugihakim* – Theoretical High Energy Physics, Institut Teknologi Bandung, Jalan Ganesha 10, Bandung 40132, Indonesia; ORCID 0000-0002-2219-1405; ryan.s.hakim@gmail.com

*Bobby Eka Gunara* – Theoretical High Energy Physics, Institut Teknologi Bandung, Jalan Ganesha 10, Bandung 40132, Indonesia; ORCID 0000-0002-6529-7664; bobby@itb.ac.id

*Conflict of interest:* the authors declare no conflict of interest.

## Effect of electron-phonon interaction on the first excited energy level of a Gaussian GaAs quantum dot

Soma Mukhopadhyay<sup>1,a</sup>, Ch. Vidyullatha<sup>2,b</sup>, Pooja Saini<sup>3,c</sup>, Zahid Malik<sup>4,d</sup>

<sup>1</sup>CVR college of Engineering, Mangalpalli, Ibrahimpatnam, Hyderabad 501510, Telangana, India

<sup>2</sup>CMR College of Engineering and Technology, Medchal, Hyderabad 50140, Telangana, India

<sup>3</sup>Institute of Physics, Bhubaneswar, 751005, Odisha, India

<sup>4</sup>North Carolina State University, Raleigh, 27606, USA

<sup>a</sup>soma9r9@gmail.com, <sup>b</sup>vidyullathakodur@gmail.com, <sup>c</sup>pooja.saini@iopb.res.in, <sup>d</sup>mzmalik@ncsu.edu

Corresponding author: Soma Mukhopadhyay, soma9r9@gmail.com

PACS 71.38.-k, 73.21.La

**ABSTRACT** The effect of electron-phonon interaction on the first excited state of a three-dimensional polar semiconductor quantum dot with Gaussian confinement is studied using the second-order Rayleigh-Schrödinger perturbation theory. An analytical expression for the first excited state polaronic correction is obtained under a plausible approximation. It is shown that this energy depends both on the strength and range of the Gaussian potential. Finally our theory is applied to a GaAs quantum dot and it is shown that the polaronic effect to the first excited level can be significantly large if the size of the dot is small. Since the information of the excited states is important for the study of decoherence phenomena, our results could be useful for quantum information processing.

**KEYWORDS** electron-phonon interaction; first excited state; GaAs quantum dot

**ACKNOWLEDGEMENTS** One of the authors (C.V.) gratefully acknowledges the financial support from DST (SR/WOS-A/PM-92/2017).

**FOR CITATION** Soma Mukhopadhyay, Ch. Vidyullatha, Pooja Saini, Zahid Malik Effect of electron-phonon interaction on the first excited energy level of a Gaussian GaAs quantum dot. *Nanosystems: Phys. Chem. Math.*, 2025, **16** (3), 306–310.

### 1. Introduction

The subject of quantum dot (QD) has been extensively studied both theoretically [1–3] and experimentally [4,5] over the last four decades and a wealth of data on the electronic, thermodynamics optical and magnetic properties of QDs have piled up in the literature. One of the essential information that is required to carry out a theoretical investigation for the electronic and several other properties of a QD is the nature of the potential that is responsible for the confinement of the electrons in the QD. Several initial investigations have considered the confinement potential as a square well. According to this potential, the force experienced by the particles inside a QD is zero which is of course not true. Thus, the square-well potential is an over-simplified approximation of a realistic QD. Later, it has been shown based on the generalized Kohn theorem and the magneto-optical experiments that the confinement potential in a QD is essentially harmonic in character [6, 7]. This triggered a large number of theoretical studies in this area [8–10] as the parabolic potential can be handled much more easily. Some relatively recent experimental observations have advocated that the QD confinement potential does not truly conform to the parabolic form but in reality has an anharmonic character. Motivated by these new observations, Adamowsky and collaborators [11] have considered an attractive Gaussian potential as a model for the QD confinement potential to investigate certain properties of a QD. It turns out that a Gaussian potential is a much better model for quantum confinement in a QD than the parabolic potential or the square-well potential. The Gaussian potential mimics the behaviour of a harmonic potential near the minimum and therefore it does satisfy the generalized Kohn's theorem for low-lying states [6]. Because of its finite depth, the Gaussian potential can take care of realistic phenomena like ionization and tunneling processes which are not possible with a parabolic potential. Also, since this potential is smooth at the dot boundary, it is mathematically more convenient to handle [12, 13]. Another advantage of the Gaussian potential over the power law anharmonic potentials is that the latter can lead to divergences at larger distances.

Since in polar semiconductor QDs, the scale of the electron-longitudinal-optical (LO)-phonon interaction energy is of the same order as that of the confinement energy and the repulsive Coulomb energy, the electron-LO-phonon interaction is expected to influence the electronic properties equally as the other potentials do [1–3, 8–10, 13]. Indeed, the electron-phonon interaction has been shown to produce pronounced effects on the various properties of a polar Semiconductor QD. Most studies in this context have been essentially confined to the ground state (GS) [12, 13] and the investigations on the

excited states [14] have been only few and far between. Also the research studies have been mostly limited to square well and parabolic confining potentials [7–9, 15].

Chatterjee and collaborators [13] have carried out extensive studies on the GS polaronic properties of a Gaussian QD (GQD) using several approximate methods. The purpose of the present paper is to explore the nature of the polaronic correction to the first excited state (ES) of a one-electron QD. Since the contribution of the electron-phonon interaction to the polaronic correction according to the first-order Rayleigh-Schrodinger perturbation theory (RSPT) vanishes, we will use the second-order RSPT in this work to obtain the lowest-order polaronic effect [14–18]. The knowledge of the excited states would be important for the study of optical properties of a QD system. We will formulate our theory for a general  $N$ -dimensional (ND) QD and finally get results for a 3D QD.

## 2. Main results

Let us consider a system of an electron that moves in an ND GQD and interacts with its LO phonons of dispersionless frequency  $\omega_0$ . The system under consideration can be modeled by the modified Frohlich Hamiltonian in the Feynman dimensionless units as [8, 19]

$$H = \frac{\mathbf{p}^2}{2} - V_o e^{-\frac{r^2}{2R^2}} + \sum_{\mathbf{q}} b_{\mathbf{q}}^\dagger b_{\mathbf{q}} + \sum_{\mathbf{q}} (\xi_{\mathbf{q}} e^{-i\mathbf{q}\cdot\mathbf{r}} b_{\mathbf{q}}^\dagger + h.c.), \quad (1)$$

where all the vectors are  $N$  dimensional,  $\mathbf{r}$  ( $\mathbf{p}$ ) is the electron position (momentum) operator,  $V_o$  ( $R$ ) is the depth (range) of the Gaussian confinement potential,  $b_{\mathbf{q}}^\dagger$  ( $b_{\mathbf{q}}$ ) is the creation (annihilation) operator the LO phonons of wave vector  $\mathbf{q}$  and energy  $\hbar\omega_0$  and  $\xi_{\mathbf{q}}$  is the electron-phonon interaction coefficient which is given by [1, 5, 8]

$$|\xi_{\vec{q}}|^2 = \left[ \frac{\Gamma\left(\frac{(N-1)}{2}\right) 2^{(N-\frac{3}{2})} \pi^{\frac{(N-1)}{2}}}{v_N q^{N-1}} \right] \alpha, \quad (2)$$

where  $\alpha$  is the dimensionless electron-phonon coupling constant which depends on the material parameters and  $v_N$  is the dimensionless volume of the  $N$ -dimensional QD. In 3D,  $|\xi_{\vec{q}}|^2$  is given by the usual expression:

$$|\xi_{\vec{q}}|^2 = \left( \frac{2\sqrt{2}\pi}{v_N q^2} \right) \alpha \quad (3)$$

We assume that at least for low-lying states, it is possible to write the Gaussian potential as a sum of a harmonic potential and a small perturbative potential [20, 22]. So we rewrite Eq. (1) as

$$H = \frac{\mathbf{p}^2}{2} + \frac{1}{2}\tilde{\omega}_h^2 r^2 - V_o + \sum_{\mathbf{q}} b_{\mathbf{q}}^\dagger b_{\mathbf{q}} + \lambda \left[ -V_o \left( e^{-\frac{r^2}{2R^2}} - 1 \right) - \frac{1}{2}\tilde{\omega}_h^2 r^2 \right] + \sum_{\vec{q}} \left( \xi_{\vec{q}} e^{-i\vec{q}\cdot\vec{r}} b_{\vec{q}}^\dagger + h.c. \right), \quad (4)$$

where we have added and subtracted a parabolic potential and introduced a parameter  $\lambda$ . For  $\lambda = 0$ , the confinement potential becomes parabolic while for  $\lambda = 1$ , Eq. (4) describes a Gaussian confinement potential. We choose:  $\tilde{\omega}_h = \sqrt{V_o}/R$  so that the lowest-order perturbative term for the confinement potential becomes quartic in  $(r/R)$ . Let us now write the Hamiltonian (4) as

$$H = H_0 + H_1 + H_2, \quad (5)$$

where

$$H_0 = \frac{\mathbf{p}^2}{2} + \frac{1}{2}\tilde{\omega}_h^2 r^2 - V_o + \sum_{\mathbf{q}} b_{\mathbf{q}}^\dagger b_{\mathbf{q}}, \quad (6)$$

$$H_1 = \lambda \left[ -V_o \left( e^{-\frac{r^2}{2R^2}} - 1 \right) - \frac{1}{2}\tilde{\omega}_h^2 r^2 \right], \quad (7)$$

$$H_2 = \sum_{\vec{q}} \left( \xi_{\vec{q}} e^{-i\vec{q}\cdot\vec{r}} b_{\vec{q}}^\dagger + h.c. \right), \quad (8)$$

where  $H_0$  is exactly soluble, the harmonic oscillator part having the GS wave function  $\phi_0^{ND}(\mathbf{r})$  and  $H_1$  and  $H_2$  can be treated as perturbations. We approximate the  $\lambda$ -term by its average w.r.t.  $\phi_0^{ND}(\mathbf{r})$ . Thus, we write:

$$\begin{aligned} \lambda \left[ -\frac{V_o}{r^2} \left( e^{-\frac{r^2}{2R^2}} - 1 \right) - \frac{1}{2}\tilde{\omega}_h^2 \right] r^2 &\approx -\lambda \left\langle \phi_0^{ND}(\mathbf{r}) \left| \left[ \frac{1}{2}\tilde{\omega}_h^2 + \frac{V_o}{r^2} \left( e^{-\frac{r^2}{2R^2}} - 1 \right) \right] \right| \phi_0^{ND}(\mathbf{r}) \right\rangle r^2 = \\ &= \lambda V_o \left[ \frac{2\tilde{\omega}_h}{N-2} - \frac{1}{R^2} - \frac{4R^2\tilde{\omega}_h^{N/2}}{(N-2)(2R^2\tilde{\omega}_h+1)^{(N-2)/2}} \right] r^2. \end{aligned} \quad (9)$$

Substituting Eq. (9) in (5), we have an effective parabolic QD problem given by the effective Hamiltonian:

$$H_{eff} = \frac{\mathbf{p}^2}{2} + \frac{1}{2}\tilde{\omega}_h^2 r^2 - V_o + \sum_{\mathbf{q}} b_{\mathbf{q}}^\dagger b_{\mathbf{q}} + H_2 = H_{har} - V_o + \sum_{\mathbf{q}} b_{\mathbf{q}}^\dagger b_{\mathbf{q}} + H_2 = H_o^{eff} + H_2, \quad (10)$$

where

$$H_o^{eff} = H_{har} - V_o + \sum_{\mathbf{q}} b_{\mathbf{q}}^{\dagger} b_{\mathbf{q}}, \quad (11)$$

$$H_{har} = \frac{\mathbf{p}^2}{2} + \frac{1}{2}\omega_h^2 r^2, \quad \omega_h = \left[ (1-\lambda)\tilde{\omega}_h^2 + \frac{4\lambda V_o \tilde{\omega}_h}{(N-2)} \left( 1 - \left\{ \left( 1 + \frac{\tilde{\omega}_h}{2V_o} \right) \frac{N}{2} - 1 \right\}^{-1} \right) \right]^{1/2}. \quad (12)$$

We shall consider  $H_o^{eff}$  as an unperturbed Hamiltonian and  $H_2$  as the perturbation. The eigenstate of  $H_o^{eff}$  can be written as  $|\phi_j^{ND}\rangle \otimes |n\rangle$ , where  $|\phi_j^{ND}\rangle$  satisfies the Schrödinger equation

$$H_{har}\phi_j^{ND}(r) = E_j^{ND}\phi_j^{ND}(r), \quad (13)$$

with

$$\phi_j^{ND}(r) = \left( \frac{\omega_h^{N/2}}{\pi^{N/2} 2^{j_1+j_2+\dots+j_N} (j_1! j_2! \dots j_N!)} \right)^{1/2} \times H_{j_1}(\sqrt{\omega_h}x_1) H_{j_2}(\sqrt{\omega_h}x_2) \dots H_{j_N}(\sqrt{\omega_h}x_N) e^{-\frac{1}{2}\omega_h r^2}, \quad (14)$$

$H_{j_i}(\sqrt{\omega_h}x_i)$  being the Hermite polynomial and

$$E_j^{ND} = \left( j_1 + j_2 + \dots + j_N + \frac{1}{2}N \right) \omega_h, \quad (15)$$

and  $|n\rangle = \prod_{\mathbf{q}} |n_{\mathbf{q}}\rangle$ , where  $n_{\mathbf{q}} = 0, 1, 2, 3 \dots$  etc., is the eigen state of  $H_{ph} = \sum_{\mathbf{q}} b_{\mathbf{q}}^{\dagger} b_{\mathbf{q}}$  belonging to the eigen value  $n$  i.e.,

$$H_{ph}|n\rangle = \sum_{\mathbf{q}} b_{\mathbf{q}}^{\dagger} b_{\mathbf{q}} |n\rangle = \sum_{\mathbf{q}} n_{\mathbf{q}} |n\rangle = n |n\rangle,$$

where  $|0\rangle = \prod_{\mathbf{q}} |0_{\mathbf{q}}\rangle$ ,  $b_{\mathbf{q}}|0_{\mathbf{q}}\rangle = 0$  for all  $\mathbf{q}$  and  $\sum_{\mathbf{q}} n_{\mathbf{q}} = n$ . As we have already mentioned, the lowest-order perturbative contribution from the electron-phonon interaction  $H_2$  comes from the second-order RSPT. We are here interested in calculating the polaronic correction to the first ES energy of  $H_o^{eff}$  due to  $H_2$  [3, 13].

The second-order RSPT correction of the electron-phonon interaction  $H_2$  to the first ES energy of  $H_o^{eff}$  is given by the expression [14, 15]:

$$\Delta E_1^{ND} = - \sum_{j_n} \frac{|\langle \phi_j^{ND} | \langle n | H_2 | 0 \rangle | \phi_1^{ND} \rangle|^2}{E_j^{ND} - E_1^{ND} + n}, \quad (16)$$

which can be easily simplified to

$$\Delta E_1^{ND} = \sum_j \sum_{\mathbf{q}} \frac{|\langle \phi_j^{ND} | \xi_{\mathbf{q}} e^{-i\mathbf{q}\cdot\mathbf{r}} | \phi_1^{ND} \rangle|^2}{E_j^{ND} - E_1^{ND} + 1} \quad (17)$$

Applying the transformation

$$\frac{1}{E_j^{ND} - E_1^{ND} + 1} = \int_0^{\infty} e^{-(E_j^{ND} - E_1^{ND} + 1)t} dt \quad (18)$$

and the sum rule for the Hermite Polynomials

$$\begin{aligned} & \sum_n \frac{1}{2^n n!} H_n(\lambda x) H_n(\lambda x') \times \exp \left[ -\frac{\lambda^2}{2} (x^2 + x'^2) - 2np \right] = \\ & = \frac{e^p}{\sqrt{2\sinh(2p)}} \exp \left\{ -\frac{1}{4}\lambda^2 \left[ (x+x')^2 \tanh(p) \right] + (x-x')^2 \coth(p) \right\}, \end{aligned} \quad (19)$$

we obtain

$$\Delta E_1^{ND} = -\frac{\alpha}{8\sqrt{\omega_h}} \frac{\Gamma((N-1)/2)}{\Gamma(N/2+1)} \times \left[ (2N-1) B\left(\frac{1}{\omega_h}, \frac{1}{2}\right) + B\left(\frac{1}{\omega_h}-1, \frac{1}{2}\right) \right], \quad (20)$$

$B(x, y)$  being the beta function. Finally, in terms of simpler functions, the first ES polaron energy is given in second-order RSPT as

$$E_{1,per}^{ND} = \frac{N+2}{2}\omega_h - \frac{\alpha\sqrt{\pi}}{2l} \frac{\Gamma(\frac{N-1}{2})}{\Gamma(\frac{N}{2})} \frac{\Gamma(\frac{1}{\omega_h}+1)}{\Gamma(\frac{1}{\omega_h}+\frac{1}{2})} \times \left( 1 + \frac{\omega_h}{4N(1-\omega_h)} \right). \quad (21)$$

which can be calculated numerically to give the first ES energy of a GQD with polaronic interaction. One may note that the present approximation leads to a divergent result in 2D and therefore it cannot be applied to a 2D QD. This however is not a matter of concern here since we are interested in a 3D QD in this work, as mentioned earlier. For the sake of

completeness, we would like to mention that a slightly different approximation can be made to obtain results for a 2D GQD. For example, Eq. (9) can alternatively be approximated as

$$\lambda \left[ -\frac{V_0}{r^2} \left( e^{-\frac{r^2}{2R^2}} - 1 \right) - \frac{1}{2} \tilde{\omega}_h^2 \right] r^2 \approx -\lambda \left\langle \phi_0^{ND}(\mathbf{r}) \left| \left[ \frac{1}{2} \tilde{\omega}_h^2 + \frac{V_0}{r^2} \left( e^{-\frac{r^2}{2R^2}} - 1 \right) \right] \right| \phi_0^{ND}(\mathbf{r}) \right\rangle r^2 \approx$$

$$\approx -\lambda \left[ \frac{1}{2} \tilde{\omega}_h^2 + \frac{V_0}{\langle \phi_0^{ND}(\mathbf{r}) | r^2 | \phi_0^{ND}(\mathbf{r}) \rangle} \left( \langle \phi_0^{ND}(\mathbf{r}) | e^{-\frac{r^2}{2R^2}} | \phi_0^{ND}(\mathbf{r}) \rangle - 1 \right) \right] r^2, \quad (22)$$

which gives

$$\omega_h = \left[ (1 - \lambda) \tilde{\omega}_h^2 + 2\lambda V_0 \tilde{\omega}_h \left\{ 1 - 2\tilde{\omega}_h R^2 (1 + 2\tilde{\omega}_h R^2)^{-1} \right\} \right]^{1/2}. \quad (23)$$

One can easily see that the approximation made in Eq. (9) is supposed to give better results in all dimensions except in 2D. Therefore, we use Eq. (21) in this work, as we are interested here in a 3D GQD.

We are interested in applying our theory to a realistic material. Since GaAs QD is a useful QD for technological applications, we apply in this work our theory to a GaAs QD with Gaussian confinement. For GaAs, we have considered  $m = 0.066 m_0$ ,  $\alpha = 0.068$  and  $\hbar\omega_0 = 36.7$  meV [3,21]. Fig. 1. shows the behaviour of the ES polaronic correction  $-\Delta E$  (in meV) with respect to the effective QD size  $R$  (in nm) for GQD of GaAs for different strengths of the confinement potential ( $V_0$ ) [22]. One may note that in the effective parabolic problem, the energy of the first excited state electron plus the zero phonon energy is degenerate with the electron GS energy plus the one LO-phonon energy. Because of this degeneracy, an electron in the first ES of the effective QD problem is unstable to the emission of an LO phonon. This instability is expected to show up in the first ES polaronic correction in the form of a singularity. Indeed, the singularity structure is clearly visible in Fig. 1. For different potential strengths  $V_0$ , the singularity in the ES polaronic correction occurs at different values of the range  $R$ . As  $V_0$  increases, the value of  $R$  at which the singularity appears also increases. Thus, the singularity point can be tuned by tuning the potential. In general (except around the singularity), the polaronic correction increases as the QD size decreases. The figure also shows that, as the confinement length is sufficiently reduced, the polaronic correction may become substantially large. For large values of  $R$ , the electron-phonon interaction corrections appear to be independent of  $R$ , as one would naturally expect in the case of bulk material. Therefore, we may conclude that the effect of electron-phonon interaction on the first ES of a GQD is really important when the size of the size of the GQD is small.

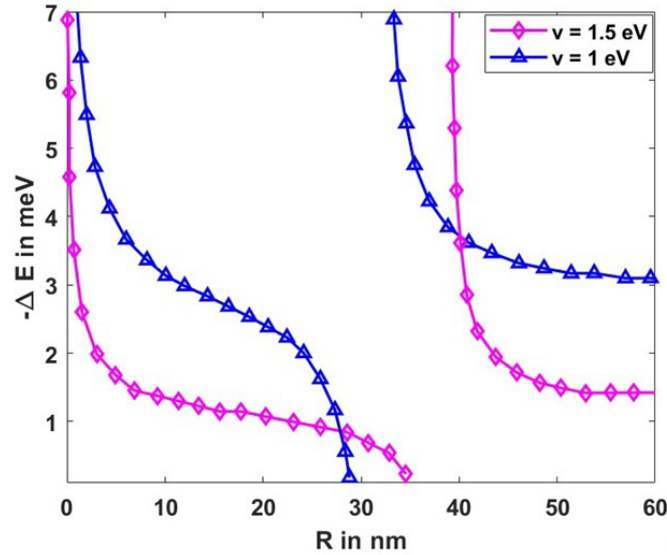


FIG. 1. Polaronic correction  $\Delta E$  (in meV) to the first ES energy of an electron in GQD of GaAs with respect to  $R$  (in nm)

### 3. Conclusion

In conclusion, we have studied the effect of electron-LO-phonon interaction on the first ES energy level of an electron in a 3D GQD using second order RSPT. We have obtained an analytical expression for the first ES polaronic energy under a plausible approximation. Since we are interested in a realistic material, we have applied our results to a GaAs polar semiconductor QD. We have shown how the polaronic correction to the first ES energy of an electron in a GQD of GaAs behaves as a function of the effective confinement length for two values of the potential strengths. The energy curves show the singularity behaviour that corresponds to the instability of the first ES electron to the emission of an LO phonon.

Our results show that the polaronic effect to the electron in the ES of a GaAs QD can be significantly large if the size of the QD is small. Since the information of the energies and wave functions of the excited state is important for the study of decoherence phenomena particularly the decoherence time, our results could be useful for quantum information processing.

## References

- [1] Ren Z., Shi Z., Feng H., Xu Z., Hao W. Recent Progresses of Polarons: Fundamentals and Roles in Photocatalysis and Photoelectrocatalysis. *Adv. Sci.*, 2024, **11**, P. 2305139.
- [2] Vasilchenko V. and Gonze X. Polarons in the cubic generalized Frohlich model: Spontaneous symmetry breaking. *Phys. Rev. B*, 2024, **109**, P. 184301.
- [3] Chatterjee A., Mukhopadhyay S., Book: Polarons and Bipolarons – An Introduction. Taylor and Francis, 2018 and Ref. there in.
- [4] Demel T., Heitmann D., Grambow P., Ploog K. Nonlocaldynamic response and level crossings in quantum-dot structures. *Phys. Rev. Lett.*, 1990, **64**, P. 788.
- [5] Lorke A., Kotthaus J.P., Ploog K. Coupling of quantum dots on GaAs. *Phys. Rev. Lett.*, 1990, **64**, P. 2559.
- [6] Kohn W. Cyclotron Resonance and de Haas-van Alphen Oscillations of an Interacting Electron Gas. *Phys. Rev.*, 1961, **123**, P. 1242.
- [7] Boda A., Boyacioglu B., Chatterjee A. Ground state properties of a two-electron system in a three-dimensional GaAs quantum dot with Gaussian confinement in a magnetic field. *J. Appl. Phys.*, 2013, **114**, P. 044311.
- [8] Mukhopadhyay S., Chatterjee A. Polaronic correction to the first excited electronic energy level in semiconductor quantum dots with parabolic confinement. *Phys. Lett. A*, 1998, **240**, P. 100.
- [9] Mukhopadhyay S., Chatterjee A. Relaxed and effective mass excited states of a quantum dot polaron. *Phys. Rev. B*, 1998, **58**, P. 2088.
- [10] Mukhopadhyay S., Chatterjee A. Suppression of Zeeman splitting in a GaAs quantum dot. *Phys. Rev. B*, 1999, **59**, P. R7833.
- [11] Adamowski J., Sobkowicz M., Szafran B., Bednarek S. Electron pair in a Gaussian confining potential. *Phys. Rev. B*, 2000, **62**, P. 4234.
- [12] Germain M., Kartheuser E., Gurskil A. L., Lutsenko E.V., Marko I.P., Pavlovskii V.N., Yablonskii G.P., Heime K., Heuken M., Schineller B. Effects of electron-phonon interaction and chemical shift on near-band-edge recombination in GaN. *J. Appl. Phys.*, 2002, **91**, P. 9827.
- [13] Yanar S., Sevim A., Boyacioglu B., Saglam M., Mukhopadhyay S., Chatterjee A. Polaronic effects in a Gaussian quantum dot. *Superlattices & Microstructures*, 2008, **43**, P. 208.
- [14] Mukhopadhyay S., Chatterjee A. The ground and the first excited states of an electron in a multidimensional polar semiconductor quantum dot: an all-coupling variational approach. *J. Phys. Cond. Matter*, 1999, **11**, P. 2071.
- [15] Szafran B., Adamowski J., Bednarek S. Ground and excited states of few-electron systems in spherical quantum dots. *Physica E*, 1999, **4**, P. 1.
- [16] Cohen M. On the Schrodinger equation with a Gaussian potential. *J. Phys. A*, 1984, **17**, P. L101.
- [17] Chatterjee A. 1/N expansion for the Gaussian potential. *J. Phys. A*, 1985, **18**, P. 2403.
- [18] Feng D.H., Xu Z.Z., Jia T.Q., Li X.X., Li C.B., Sun H.Y., Xu S.Z. Polaronic correction to the first excited electronic energy level in an anisotropic semiconductor quantum dot. *Euro Phys. J. B*, 2005, **44**, P. 15.
- [19] Luhlul Jahan K., Chatterjee A. Effect of Temperature on the Single-Particle Ground-State and Self Energy of a Polar Quantum Dot with Gaussian Confinement. *Physica B*, 2020, **579**, P. 411892.
- [20] Mukhopadhyay S., Boyacioglu B., Saglam M., Chatterjee A. Quantum size effect on the phonon-induced Zeeman splitting in a GaAs quantum dot with Gaussian and parabolic confining potentials. *Physica E*, 2008, **40**, P. 2779.
- [21] Saini P., Boda A., Chatterjee A. Effect of Rashba and Dresselhaus spin-orbit interactions on a D0 impurity in a two-dimensional Gaussian GaAs quantum dot in the presence of an external magnetic field. *J. Mag. Mag. Mat.*, 2019, **485**, P. 407.
- [22] Monisha P.J., Mukhopadhyay S. The pinning effect in a polar semiconductor quantum dot with Gaussian confinement: A study using the improved Wigner-Brillouin perturbation theory. *Physica B*, 2015, **464**, P. 38.

---

*Submitted 28 April 2025; revised 20 May 2025; accepted 21 May 2025*

### *Information about the authors:*

*Soma Mukhopadhyay* – Department of Physics, CVR college of Engineering, Mangalpalli, Ibrahimpatnam, Hyderabad 501510, Telangana, India; ORCID 0000-0002-8198-2872; soma9r9@gmail.com

*Ch. Vidyullatha* – Department of Humanities and Sciences, CMR College of Engineering and Technology, Medchal, Hyderabad 50140, Telangana, India; ORCID 0009-0003-5041-0833; vidyullathakodur@gmail.com

*Pooja Saini* – Institute of Physics, Bhubaneswar, 751005, Odisha, India; ORCID 0000-0002-1949-2012; pooja.saini@iopb.res.in

*Conflict of interest:* the authors declare no conflict of interest.

## Properties of multi-moded phase-randomized coherent states

Mikhail S. Guselnikov<sup>1,a</sup>, Andrei A. Gaidash<sup>1,2,b</sup>, George P. Miroshnichenko<sup>1,c</sup>, Anton V. Kozubov<sup>1,2,d</sup>

<sup>1</sup>ITMO University, Saint Petersburg, Russia

<sup>2</sup>Steklov Mathematical Institute of Russian Academy of Sciences, Moscow, Russia

<sup>a</sup>[msguselnikov@itmo.ru](mailto:msguselnikov@itmo.ru), <sup>b</sup>[andrewdggk@gmail.com](mailto:andrewdggk@gmail.com), <sup>c</sup>[gpmirosh@gmail.com](mailto:gpmirosh@gmail.com), <sup>d</sup>[avkozubov@itmo.ru](mailto:avkozubov@itmo.ru)

Corresponding author: Gaidash A.A., [andrewdggk@gmail.com](mailto:andrewdggk@gmail.com)

**ABSTRACT** Phase-randomized coherent states are widely used in various applications of quantum optics. They are best known to be the core part of decoy-state quantum key distribution protocols with phase-coding. From the perspective of future development of quantum protocol architecture, it is important to determine whether phase randomization can be applied at an arbitrary stage of an optical scheme without affecting the informational properties of the quantum system. In this paper, using the superoperator formalism, we have shown that phase randomization of a two-mode coherent state commutes with linear optical transformations. This implies that phase randomization can be applied virtually at any point within the optical setup. We further demonstrate that the Holevo bound for such a state coincides with that of regular coherent states, bearing in mind that the Holevo bound quantifies only the maximum amount of information accessible to an eavesdropper. Advantages of phase-randomized coherent states compare to regular ones in particular cases of eavesdropper's strategies should be considered separately. Also, these findings indicate that phase randomization can be directly applied to a subcarrier wave quantum key distribution type of systems, opening prospects for its future development.

**KEYWORDS** coherent states, phase randomization, phase-averaged coherent states, quantum key distribution, Holevo bound, subcarrier wave quantum key distribution.

**ACKNOWLEDGEMENTS** Contribution to the work of A. A. Gaidash and A. V. Kozubov was financially supported by Russian Science Foundation (project 20-71-10072) and performed at Steklov Mathematical Institute of Russian Academy of Sciences.

**FOR CITATION** Guselnikov M.S., Gaidash A.A., Miroshnichenko G.P., Kozubov A.V. Properties of multi-moded phase-randomized coherent states. *Nanosystems: Phys. Chem. Math.*, 2025, **16** (3), 311–316.

### 1. Introduction

Phase-randomized or phase-averaged coherent states (PHAVs) are peculiar quantum optical states: a mixture of Fock states with Poissonian distribution. In particular, they are known to be utilized in the study of generalized Hong-Ou-Mandel effect [1]. However, they are best known in the context of quantum key distribution (QKD) protocols based on weak coherent states. Especially, two-moded ones are widely used in protocols with phase-coding, implying utilization of Mach-Zehnder interferometer [2, 3], or other interferometric schemes [4–8]. Compare to single photons, attenuated laser radiation - treated as weak coherent states - can contain more than one photon, which may compromise the security of such protocols for quantum communication, and PHAVs have proven to be an effective tool for enhancing the security of weak coherent state QKD protocols [9], leading to the development of decoy-state QKD protocols [10]. Since then, PHAVs have become critically important in quantum communication. Their properties have been extensively studied, revealing the non-Gaussian nature of their Wigner functions, simple methods of generation, and a growing range of applications [11–17].

Practical decoy-state QKD protocols with phase-coding utilize multi-mode (precisely, two-mode) PHAVs. The main difference compare to single-mode PHAVs is that multi-mode ones may contain relative phase. And, unlike single-mode PHAVs, the informational properties of multimode PHAVs remain incompletely characterized. In this paper, we focus on exploration in regards to the order of optical transformations including phase-randomization taken place in QKD optical schemes, and how this order might affect the informational aspects. In other words, our goal is to elaborate on whether phase randomization in two-mode systems commutes with linear optical transformations and what consequences of the ordering choice are.

## 2. Commutation of phase-randomization with transformations of linear optics

First, consider a density matrix  $\rho$  of a two-mode phase-randomized state constructed from coherent states  $|\alpha\rangle$  and  $|\beta\rangle$ , where  $\alpha = |\alpha|e^{i\theta}$  and  $\beta = |\beta|e^{i(\theta+\phi)}$  are complex amplitudes of coherent states, respectively,

$$\rho(\phi) = \int |\alpha\rangle\langle\alpha| \otimes |\beta\rangle\langle\beta| \frac{d\theta}{2\pi}. \quad (1)$$

Density matrix above can be expressed in terms of superoperator notation:

$$\begin{aligned} \rho(\phi) &= N \int e^{\overleftarrow{(\alpha a_1^\dagger + \beta a_2^\dagger)} + \overrightarrow{(\alpha^* a_1 + \beta^* a_2)}} |0\rangle\langle 0| \frac{d\theta}{2\pi} = \\ &= N \sum_{n=0}^{\infty} \sum_{k=0}^n \frac{\overleftarrow{(|\alpha| a_1^\dagger + |\beta| e^{i\phi} a_2^\dagger)^{n-k}} \overrightarrow{(|\alpha| a_1 + |\beta| e^{-i\phi} a_2)^k} \delta_{n-2k,0}}{(n-k)!k!} |0\rangle\langle 0| = \\ &= N \sum_{n=0}^{\infty} \frac{\overleftarrow{(|\alpha| a_1^\dagger + |\beta| e^{i\phi} a_2^\dagger)} \overrightarrow{(|\alpha| a_1 + |\beta| e^{-i\phi} a_2)}}{n!n!} |0\rangle\langle 0| = \\ &= N \sum_n \frac{(\mathcal{K}_{R(\phi)}^{(+)})^n}{n!n!} |0\rangle\langle 0|, \quad R(\phi) = \begin{pmatrix} |\alpha|^2 & |\alpha\beta|e^{-i\phi} \\ |\alpha\beta|e^{i\phi} & |\beta|^2 \end{pmatrix}, \end{aligned} \quad (2)$$

where we have integrated over the common phase  $\theta$  of the two coherent states;  $a_i^\dagger (a_i)$  is the creation (annihilation) operator of the  $i^{\text{th}}$  mode,  $N = e^{-|\alpha|^2 - |\beta|^2}$  is normalization constant, also  $\mathcal{K}_{R(\phi)}^{(+)} = \sum_{ij} R(\phi)_{ij} \overleftarrow{a_i^\dagger} \overrightarrow{a_j}$  introduced in [18],

$\overleftarrow{AB} = AB$  and  $\overrightarrow{AB} = BA$  is left- and right-action notation for superoperators,  $(\cdot)^*$  denotes complex conjugation and  $(\cdot)^\dagger$  denotes the Hermitian conjugation,  $\delta_{ij}$  is the Kronecker delta-symbol. Obtained superoperator form provides some explicit insights on the properties of the state, that will be discussed further.

We discuss additional transformations applied to the state, that may take place before or after the phase randomization. Expression of the state in the superoperator notation (2) explicitly shows that any transformation that maps a set of creation (annihilation) operators to a different set of creation (annihilation) operators, in particular, of the form  $a_i^\dagger \rightarrow \sum_j M_{ij} a_j^\dagger$

for a given matrix  $M_{ij}$ , preserves the state to be phase-randomized. Basically, these are transformations that describe actions of linear optics devices. Note, it may even change the number of considered modes. The same holds true for the coherent state before the phase randomization, i.e. the same transformation preserves the state to be coherent. We may conclude, then, that this type of transformations should be commutative with phase-randomization. Consider sequential actions of the transformation (M) and phase-randomization (PR) and vice versa to show that they are indeed commutative:

$$\begin{aligned} \otimes_j |\alpha_j\rangle &= N_0 e^{\sum_j \overleftarrow{\alpha_j a_j^\dagger}} |0\rangle \xrightarrow{PR} N_0^2 \sum_{n=0}^{\infty} \frac{((\sum_j \overleftarrow{\alpha_j a_j^\dagger})(\sum_j \overrightarrow{\alpha_j^* a_j}))^n}{n!n!} |0\rangle\langle 0| \\ &\quad \downarrow M \\ N_0^2 \sum_{n=0}^{\infty} &\frac{((\sum_{jk} \overleftarrow{|\alpha_j| e^{i\phi_j} M_{jk} a_k^\dagger})(\sum_{jk} \overrightarrow{|\alpha_j| e^{-i\phi_j} M_{jk}^* a_k}))^n}{n!n!} |0\rangle\langle 0| \\ &\quad \uparrow PR \\ \otimes_j |\alpha_j\rangle &= N_0 e^{\sum_j \overleftarrow{\alpha_j a_j^\dagger}} |0\rangle \xrightarrow{M} N_0 e^{\sum_{jk} \overleftarrow{\alpha_j M_{jk} a_k^\dagger}} |0\rangle \end{aligned} \quad (3)$$

where  $N_0$  is normalization constant. Thus, phase randomization and transformation provided by elements of linear optics are commutative operations.

## 3. Consequences of the ordering choice for a QKD

As mentioned in the introduction, phase-randomized states are employed in QKD, especially in decoy-states schemes. The essential parts of such QKD schemes are beamsplitters as well as phase modulators (as a part of Mach-Zehnder interferometer scheme), where the latter can be described by the following transformation:  $e^{i\phi a^\dagger} a^\dagger e^{-i\phi a^\dagger} a = a^\dagger e^{i\phi}$ , that also agrees with the provided point above in regard to commutativity. The main idea of phase randomization in the decoy state method is to separate the single-photon fraction of the received mixture of Fock states. Thus, practically, the phase randomization process, according to the conclusions made above, can be applied to the state at any point of the optical scheme, even at the receiver's side, and, at the first glance, that may lead to a new design of protocols. Indeed, from the

point of view of legitimate user only, it does not affect the performance of QKD setup. However, and we shall emphasize that, position of phase-randomization obviously may impact the information accessible to an eavesdropper.

In order to elaborate on the latter issue, we shall estimate the difference of regular coherent states and phase-randomized coherent states in regard to provided to eavesdropper information. Thus, we propose to compare the Holevo bound for these two types of states as rather simple example without necessity of considering special cases, that is given by

$$\chi = S(\rho) - \sum_i p_i S(\rho(\phi_i)), \quad (4)$$

where  $\rho = \sum_i p_i \rho(\phi_i)$  is the density matrix of an ensemble,  $S(\rho) = -\text{Tr}(\rho \log_2 \rho)$  is von Neumann entropy. Further two phases  $\phi_0 = 0$  and  $\phi_1 = \pi$  within one informational basis will be considered. Also, their probabilities of choosing are equal, i.e.  $p_0 = p_1 = \frac{1}{2}$ . For coherent states, Holevo bound is well known and is given by

$$\chi_{CS} = h\left(\frac{1 - e^{-2|\beta|^2}}{2}\right), \quad (5)$$

$$h(x) = -x \log_2(x) - (1-x) \log_2(1-x), \quad (6)$$

where the latter is the binary entropy function. As for the phase-randomized states, von Neumann entropy can be estimated by eigenvalues  $\lambda_i$  of the density matrix:  $S(\rho) = -\sum_i \lambda_i \log_2 \lambda_i$ . Eigenvalues of  $\rho(\phi)$  can be easily calculated by introduced in [18] superoperator algebra: adjoint action of  $\mathcal{N}_{iV}^{(-)} = i \sum_{nm} V_{nm} (\overleftarrow{\hat{a}_n^\dagger \hat{a}_m} - \overrightarrow{\hat{a}_n^\dagger \hat{a}_m})$  provides unitary rotation of the matrix  $R(\phi)$  in  $\mathcal{K}_{R(\phi)}^{(+)}$  and thus can be diagonalized, i.e.

$$e^{\mathcal{N}_{iV}^{(-)}} \mathcal{K}_{R(\phi)}^{(+)} e^{-\mathcal{N}_{iV}^{(-)}} = \mathcal{K}_{e^{iV} R(\phi) e^{-iV}}^{(+)} = \mathcal{K}_{UR(\phi)U^\dagger}^{(+)}, \quad (7)$$

where  $U$  is given by

$$U = \frac{1}{\sqrt{|\alpha|^2 + |\beta|^2}} \begin{pmatrix} -|\beta|e^{i\phi} & |\alpha| \\ |\alpha|e^{i\phi} & |\beta| \end{pmatrix}. \quad (8)$$

According to (7),  $R$  has two eigenvalues: 0 and  $|\alpha|^2 + |\beta|^2$ , so  $\rho(\phi)$  can be expressed in its diagonalized form as follows:

$$\rho_{\text{diag}}(\phi) = N \sum_{n=0}^{\infty} \frac{(|\alpha|^2 + |\beta|^2)^n}{n!} |n\rangle \langle n| \otimes |n\rangle \langle n|. \quad (9)$$

Since

$$[g(n)|n\rangle \langle n| \otimes |n\rangle \langle n|, g(k)|k\rangle \langle k| \otimes |k\rangle \langle k|] = 0, \quad (10)$$

$$g(n) = \frac{(|\alpha|^2 + |\beta|^2)^n}{n!}, \quad (11)$$

where  $[\cdot, \cdot]$  stands for commutator, operators under the sum can be diagonalized by the same eigenoperators, and non-zero eigenvalue of  $\rho(\phi)$  can be determined as

$$\lambda = N \sum_n \frac{(|\alpha|^2 + |\beta|^2)^n}{n!} = 1. \quad (12)$$

Both  $\rho(0)$  and  $\rho(\pi)$  have the same non-zero eigenvalue:  $\lambda = 1$ . Thus, they do not contribute to the Holevo bound quantity. However, for the ensemble density matrix  $\rho = \frac{1}{2}(\rho(0) + \rho(\pi))$  introduced superoperator algebra cannot be directly applied, since superoperators of  $(\mathcal{K}_{R(0)}^{(+)})^n + (\mathcal{K}_{R(\pi)}^{(+)})^n$  cannot be simultaneously diagonalized. So, firstly, we express the density matrix in the Fock basis in its general form as follows:

$$\rho = N \sum_{n=0}^{\infty} \sum_{k,p=0}^n \frac{|\alpha|^{2n-(k+p)} |\beta|^{k+p} (1 + (-1)^{k-p})}{2\sqrt{(n-k)!(n-p)!k!p!}} |n-k\rangle \langle n-p| \otimes |k\rangle \langle p|. \quad (13)$$

Note, that

$$\left[ A(n, k, p), A(m, k', p') \right] = 0, \quad (14)$$

$$A(n, k, p) = \sum_{k,p=0}^n f(n, k, p) |n-k\rangle \langle n-p| \otimes |k\rangle \langle p|, \quad (15)$$

$$f(n, k, p) = \frac{|\alpha|^{2n-(k+p)} |\beta|^{k+p} (1 + (-1)^{k-p})}{2\sqrt{(n-k)!(n-p)!k!p!}}, \quad (16)$$

as well, so operators  $A(n, k, p)$  under the sum for different values of  $n$  in  $\rho$  share the same eigenoperators, and thus they can be diagonalized simultaneously. Therefore eigenvalues of  $\rho$  are determined by the sum of eigenvalues of  $A(n, k, p)$  for all values of  $n$ . Characteristic equation for each  $A(n, k, p)$  is given by

$$\lambda^{n-1} \left( (-1)^{n+1} \lambda^2 + \left( \frac{(-|\alpha|^2 - |\beta|^2)^n}{n!} \right) \lambda + \frac{(-1)^{n+1} |\alpha\beta|^2}{n!n!} \sum_{m=0}^{n-1} \left( \binom{2n}{2m+1} \frac{|\alpha|^{4(n-m-1)} |\beta|^{4m}}{2} \right) \right) = 0, \quad (17)$$

and there are only two non-zero eigenvalues, thus

$$\lambda_{\pm} = N \sum_{n=0}^{\infty} \lambda_{n,\pm} = N \sum_{n=0}^{\infty} \frac{(|\alpha|^2 + |\beta|^2)^n \pm (|\alpha|^2 - |\beta|^2)^n}{2(n!)} = \frac{1 \pm e^{-2|\beta|^2}}{2}, \quad (18)$$

and, respectively, the Holevo bound for two-mode phase-randomized coherent state  $\chi_{PR}$  is equal to the Holevo bound for regular coherent states  $\chi_{CS}$ . Dependence of the Holevo bound on  $|\beta|$  is shown in Fig. 1.

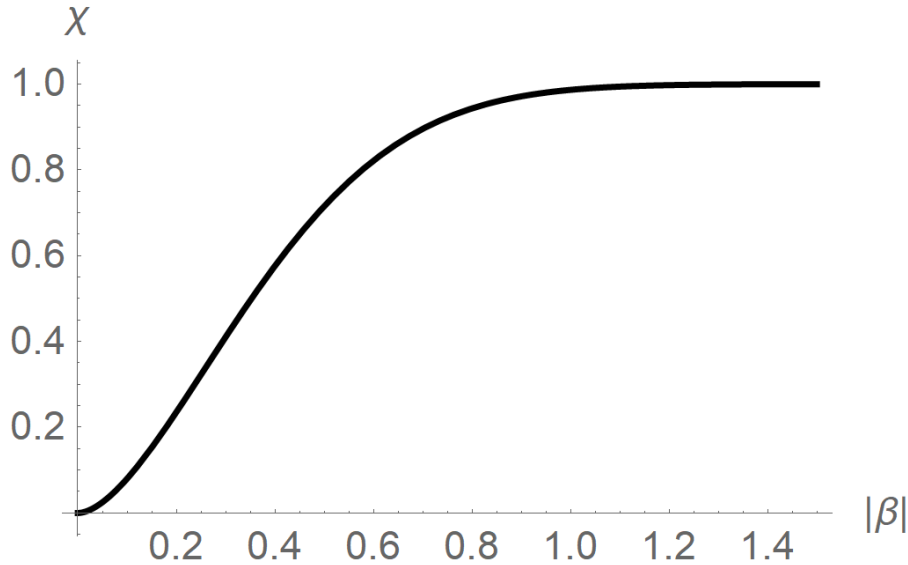


FIG. 1. Dependence of the Holevo bound  $\chi$  for PHAV ensemble state  $\rho = \frac{1}{2}(\rho(0) + \rho(\pi))$ , where  $\rho(\phi)$  is defined in Eq. (2), on the absolute value of the amplitude of the coherent state  $|\beta|$  as it shown in Eq. (6)

At this point, we have shown that the phase randomization of two-mode coherent state do not influence the maximum of accessible for an eavesdropper information. Unfortunately, consideration of special cases of eavesdropper's interactions with the states, whether they are regular coherent or PHAV ones, is obligatory for a security analysis. For instance, in case of unambiguous state discrimination (USD) [19–23], an eavesdropper can easily construct positive operator-valued measure (POVM) for a set of linearly independent pure states, such as a set of coherent states. However, mixed states may introduce linear dependency, and in this case USD POVM cannot be constructed.

#### 4. Implementation to subcarrier wave quantum key distribution

Another thing to note is that, from the observations, it immediately follows that multi-moded phase-randomized coherent state can be created by applying multi-mode (generalized) beamsplitter to a single-mode phase-randomized coherent state. Therefore, phase modulation with harmonic signal, as it is employed in subcarrier wave (SCW) QKD

[23–27], also produce multi-moded phase-randomized coherent state, since the provided transformation of annihilation (creation) operator is given by

$$a_i = \sum_{j=-S}^S D_{ij}^S(\mu, \nu, \eta) a_j, \quad (19)$$

where  $D_{ij}^S(\mu, \nu, \eta)$  is the Wigner D-function with  $S$  being a number of interaction modes,  $\mu, \nu$ , and  $\eta$  are some angles that define axes of rotation [28]. Considering the stated above, it appears that the decoy-state method may be directly applied to an SCW QKD protocol as well, providing a new variation of the protocol. However, in order to make a final decision on that and elaborate full decoy-state protocol for an SCW setup, a few points should be addressed prior in regards. The first one is accurate selection of single-photon fraction of the signal, that may be non-trivial problem for a multi-mode states with high (approaching to infinity) amount of modes, and parameter estimation, such as quantum bit error of detection events that have originated from single-photon signals. The second is required analysis of discrete phase-randomization, as it was provided recently for the original decoy-state protocol. Estimation of closeness between full phase-randomized states and the discrete phase-randomized [29–31] ones and conclusion regarding the necessary amount of discrete phases for them to be close enough in case of SCW setup are essential for practical implementations.

## 5. Conclusion

In this paper, we have investigated two-mode PHAVs from the point of view of the superoperator formalism, that provide useful insights on its properties. In particular, observations demonstrate preservation of state's type (phase-randomized) under a linear optical transformation. Therefore, this approach clearly shows that the phase randomization transformation commutes with one provided by linear optics. In context of QKD applications, phase randomization can be applied at any point within the optical scheme, at least, from the point of view of legitimate users.

At the same time, utilization of phase-randomization may significantly influence accessible to an eavesdropper information. Hence, we have estimated the Holevo bound for ensemble of two-mode phase-randomized coherent states ( $\rho = \frac{1}{2}(\rho(0) + \rho(\pi))$ ) and found it matches with the Holevo bound for regular coherent states with the same phase difference within the ensemble. However, the Holevo bound quantifies the maximum of accessible to an eavesdropper information and consideration of particular attacks may vary the outcome. For instance, USD probabilities are heavily affected by the type of considered states to be measured, especially for pure and mixed states. Therefore, additional estimations for particular cases may be considered for a full informational characterization of PHAVs.

Also, if phase-randomization commutes with transformation provided by linear optics, it appears, that phase-randomization may be directly applied to SCW QKD type of systems. It may open prospects to a new kind of SCW QKD protocol with PHAVs.

## References

- [1] Zhang Y., Wei K., Xu F. Generalized Hong-Ou-Mandel quantum interference with phase-randomized weak coherent states. *Physical Review A*, 2020, **101**(3), P. 033823.
- [2] Bennett C., Bessette F., Brassard G., Salvail L., and Smolin J. Experimental quantum cryptography. *Journal of cryptology*, 1992, **5**(3).
- [3] Gobby C., Yuan Z., and Shields A. Quantum key distribution over 122 km of standard telecom fiber. *Applied Physics Letters*, 2004, **84**, P. 3762.
- [4] Bogdanski J., Ahrens J., Bourennane M. Sagnac quantum key distribution and secret sharing. In *Quantum Communications Realized II, SPIE*, 2009, **7236**, P. 120–127.
- [5] Mo X., Zhu B., Han Z., Gui Y., Guo G. Faraday-Michelson system for quantum cryptography. *Optics Letters*, 2005, **30**(19), P. 2632–2634.
- [6] Brougham T., Barnett S., McCusker K., Kwiat P., Gauthier D. Security of high-dimensional quantum key distribution protocols using Franson interferometers. *Journal of Physics B: Atomic, Molecular and Optical Physics*, 2013, **46**(10), P. 104010.
- [7] Vorontsova I., Goncharov R., Kynev S., Kiselev F., Egorov V. Measurement-device-independent continuous variable quantum key distribution protocol operation in optical transport networks. *Nanosystems: Physics, Chemistry, Mathematics*, 2023, **14**(3), P. 342–348.
- [8] Latypov I.Z., Chistiakov V.V., Fadeev M.A., Sulimov D.V., Khalturinsky A.K., Kynev S.M., Egorov V.I. Hybrid quantum communication protocol for fiber and atmosphere channel. *Nanosystems: Physics, Chemistry, Mathematics*, 2024, **15**(5), P. 654–657.
- [9] Lo H.-K., Preskill J. Phase randomization improves the security of quantum key distribution. *arXiv preprint quant-ph/0504209*, 2005.
- [10] Lo H.K., Ma X., and Chen K. Decoy state quantum key distribution. *Physical review letters*, 2005, **94**(23), P. 230504.
- [11] Allevi A., Bondani M., Marian P., Marian T., and Olivares S. Characterization of phase-averaged coherent states. *Journal of the Optical Society of America B*, 2013, **30**(10), P. 2621–2627.
- [12] Allevi A., Olivares S., Bondani M. Manipulating the non-Gaussianity of phase-randomized coherent state. *Optics Express*, 2012, **20**(22), P. 24850–24855.
- [13] Wang Q., Wang X.B. Simulating of the measurement-device independent quantum key distribution with phase randomized general sources. *Scientific reports*, 2014, **4**(1), P. 4612.
- [14] Valente P., Lezama A. Probing single-photon state tomography using phase-randomized coherent states. *Journal of the Optical Society of America B*, 2017, **34**(5), P. 924–929.
- [15] Moschandreou E., Garcia J.I., Rollick B.J., Qi B., Pooser R., and Siopsis G. Experimental study of Hong-Ou-Mandel interference using independent phase randomized weak coherent states. *Journal of Lightwave Technology*, 2018, **36**(17), P. 3752–3759.
- [16] Glerean F., Rigoni E.M., Jarc G., Mathengattil S.Y., Montanaro A., Giusti F., et al. Ultrafast pump-probe phase-randomized tomography. *Light: Science and Applications*, 2018, **14**(1), P. 115.

- [17] Zhao Y., Qi B., and Lo H.K. Experimental quantum key distribution with active phase randomization. *Applied physics letters*, 2007, **90**(4), P. 044106.
- [18] Gaidash A., Kozubov A., Kiselev A., and Miroshnichenko G. Algebraic approach for investigation of a multi-mode quantum system dynamics. *arXiv preprint arXiv:2207.01383*, 2022.
- [19] Ivanovic A.D. How to differentiate between non-orthogonal states. *Physics Letters A*, 1987, **123**(6), P. 257–259.
- [20] Peres A., Terno D.R. Optimal distinction between non-orthogonal quantum states. *Journal of Physics A: Mathematical and General*, 1998, **31**(34), P. 7105.
- [21] Chefles A. Unambiguous discrimination between linearly independent quantum states. *Physics Letters A*, 1998, **239**(6), P. 339–347.
- [22] Kozubov A., Gaidash A., and Miroshnichenko G. Quantum control attack: Towards joint estimation of protocol and hardware loopholes. *Physical Review A*, 2021, **104**(2), P. 022603.
- [23] Gaidash A., Miroshnichenko G., and Kozubov A. Sub-carrier wave quantum key distribution with leaky and flawed devices. *Journal of the Optical Society of America B*, 2022, **39**(2), P. 577–585.
- [24] Miroshnichenko G., Kozubov A., Gaidash A., Gleim A.V., and Horoshko D.V. Security of subcarrier wave quantum key distribution against the collective beam-splitting attack. *Optics express*, 2018, **26**(9), P. 11292–11308.
- [25] Sajeed Sh., Chaiwongkhot P., Huang A., Qin H., Egorov V., Kozubov A., Gaidash A., Chistiakov V., Vasiliev V., Gleim A., et al. An approach for security evaluation and certification of a complete quantum communication system. *Scientific Reports*, 2021, **11**(1), P. 1–16.
- [26] Chistiakov V., Kozubov A., Gaidash A., Gleim A., and Miroshnichenko G. Feasibility of twin-field quantum key distribution based on multi-mode coherent phase-coded states. *Optics express*, 2019, **27**(25), P. 36551–36561.
- [27] Samsonov E., Goncharov R., Gaidash A., Kozubov A., Egorov V., and Gleim A. Subcarrier wave continuous variable quantum key distribution with discrete modulation: mathematical model and finite-key analysis. *Scientific Reports*, 2020, **10**(1), P. 1–9.
- [28] Miroshnichenko G., Kiselev A., Trifanov A., Gleim A. Algebraic approach to electro-optic modulation of light: exactly solvable multimode quantum model. *Journal of the optical society of America B*, (2017), **34**(6), P. 1177–1190.
- [29] Cao Zh., Zhang Zh., Lo H.-K., and Ma X. Discrete-phase-randomized coherent state source and its application in quantum key distribution. *New Journal of Physics*, 2015, **17**(5), P. 053014.
- [30] Wang R.-Q., Yin Zh.-Q., Jin X.-H., Wang R., Wang Sh., Chen W., Guo G.-C., and Han Zh.-Fu. Finite-key analysis for quantum key distribution with discrete-phase randomization. *Entropy*, 2023, **25**(2), P. 258.
- [31] Nahar Sh., Upadhyaya T., and Lütkenhaus N. Imperfect phase randomization and generalized decoy-state quantum key distribution. *Physical Review Applied*, 2023, **20**(6), P. 064031.

---

Submitted 21 April 2025; revised 11 May 2025; accepted 12 May 2025

*Information about the authors:*

*Mikhail S. Guselnikov* – ITMO University, 3b Kadetskaya Line, 199034 Saint Petersburg, Russia; ORCID 0000-0002-0809-8431; msguselnikov@itmo.ru

*Andrei A. Gaidash* – ITMO University, 3b Kadetskaya Line, 199034 Saint Petersburg, Russia; Steklov Mathematical Institute of Russian Academy of Sciences, 8 Gubkina Street, 119991 Moscow, Russia; ORCID 0000-0001-9870-9285; andrewdgk@gmail.com

*George P. Miroshnichenko* – ITMO University, 3b Kadetskaya Line, 199034 Saint Petersburg, Russia; ORCID 0000-0002-4265-8818; gpmirosh@gmail.com

*Anton V. Kozubov* – ITMO University, 3b Kadetskaya Line, 199034 Saint Petersburg, Russia; Steklov Mathematical Institute of Russian Academy of Sciences, 8 Gubkina Street, 119991 Moscow, Russia; ORCID 0000-0002-4468-5406; avkozubov@itmo.ru

*Conflict of interest:* the authors declare no conflict of interests.

## Optimality of linear vacancy defect for skyrmion nucleation

Maria N. Potkina<sup>1,a</sup>, Igor S. Lobanov<sup>1,b</sup><sup>1</sup>ITMO University, 197101 St. Petersburg, Russia<sup>a</sup>potkina.maria@yandex.ru, <sup>b</sup>lobanov.igor@gmail.com

Corresponding author: M. N. Potkina, potkina.maria@yandex.ru

PACS 82.20.Pm, 34.10.+x, 75.40.Mg

**ABSTRACT** Magnetic skyrmions offer a pathway to ultra-dense, low-power memory, but writing them efficiently remains a challenge. Using atomistic spin simulations and minimum energy path calculations in a PdFe/Ir(111) film, we show that deliberately placing linear chains of four atomic vacancies cuts the skyrmion nucleation barrier nearly in half-down to 44.7 meV at 3.75 T-compared to 85 meV in a pristine track. Linear defects excel because they remove high-energy core regions during skyrmion creation while minimally disturbing its outer negative energy halo during depinning. This geometry-driven effect relies only on generic energy density profiles, making it broadly applicable to all skyrmion-hosting materials.

**KEYWORDS** transition state theory, topological magnetic solitons, nucleation, racetrack memory.

**ACKNOWLEDGEMENTS** The study was supported by the Russian Science Foundation grant No. 24-72-00089, <https://rscf.ru/en/project/24-72-00089/>.

**FOR CITATION** Potkina M.N., Lobanov I.S. Optimality of linear vacancy defect for skyrmion nucleation. *Nanosystems: Phys. Chem. Math.*, 2025, **16** (3), 317–324.

### 1. Introduction

Magnetic skyrmions (Sks) are topological spin structures that arise in chiral magnetic materials [1,2]. Their nanometer-scale size, high mobility, and the low current densities required for their manipulation make them promising candidates for information carriers in future storage devices [3]. The intentional creation, destruction, and control of Sk are essential challenges that must be addressed to facilitate their application in future spintronic technologies.

One of the factors that influences the control of Sks is their interaction with impurities that are inevitably present in the sample. Impurity-induced pinning has been shown to affect Sk mobility [4], potentially leading to slower operation of spintronic devices. Furthermore, pinned Sks exhibit lower stability compared to free Sks [5–8], which may lead to a shorter information storage lifespan.

Impurities can also serve a beneficial role in skyrmionic applications. For instance, impurities can be utilized to create repelling and attracting rails for Sks guides [8–10]. Boundary notches can be employed to position Sks by creating potential wells [11–13]. Experimental evidence shows that Sks nucleate more readily on impurities [14], suggesting that artificially created impurities can act as effective nucleation centers for Sks. Additionally, the destructive effects of defects on Sks have been proposed for use in the development of Sk deletion devices [15].

Effective use of Sks requires a thorough understanding of their interactions with defects of various types, sizes, and geometries. Numerous studies have focused on the theoretical studies using various approaches, including atomistic models [7–9, 16–18], micromagnetic models through the solution of the Landau-Lifshitz-Gilbert equation [19–26], rigid models described by the Thiele equation [25–27], as well as analytical approaches [28–30].

However, Sk nucleation on impurities remains insufficiently explored. This paper will focus on investigating the influence of the geometry and size of atomic-scale non-magnetic defects on the processes of Sk creation and depinning. By calculating the activation barriers for Sk creation and depinning, we aim to determine the optimal defect type for efficient Sk nucleation in future memory and computing devices.

### 2. Method and simulated system

A thin magnetic film is modelled within the generalized Heisenberg model, which is a standard tool for Sk simulation with atomistic resolution. Symmetric (Heisenberg) exchange, Dzyaloshinskii-Moriya interaction (DMI), anisotropy, and the Zeeman energy of interaction with an external field  $\mathbf{B}$  contribute to the total energy  $E$ :

$$E = -J \sum_{\langle i,j \rangle} \mathbf{S}_i \cdot \mathbf{S}_j - \sum_{\langle i,j \rangle} \mathbf{D}_{ij} \cdot (\mathbf{S}_i \times \mathbf{S}_j) - \mu \sum_i \mathbf{B} \cdot \mathbf{S}_i - K \sum_i S_{i,z}^2. \quad (1)$$

The summation is taken over all pairs  $\langle i, j \rangle$  of nearest neighbours atoms, and over all atoms  $i$  of the crystal lattice, except for non-magnetic impurities (vacancies). Here  $J$  is the symmetric exchange parameter;  $\mathbf{D}_{ij}$  is the DMI vector, which

lies in the film plane and is perpendicular to the vector connecting atomic sites  $i$  and  $j$ , thus stabilizes Néel-type Sk.  $K > 0$  is the anisotropy constant corresponding to an easy axis along the coordinate axis  $z$  perpendicular to the film;  $\mathbf{B}$  is the external magnetic field, applied parallel to  $z$ -axis; and  $\mathbf{S}_i$  is a three-dimensional unit vector in the direction of the magnetic moment at the site  $i$ . The magnitude of the magnetic moment,  $\mu$ , is assumed to be the same at all sites. Impurities are treated as vacancies without magnetic moments in the lattice. The system parameters correspond to experimentally observed Sk in a Pd/Fe bilayer on an Ir(111) substrate: a triangular crystal lattice,  $\mu B = 0.093J$ ,  $K = 0.07J$ ,  $D = |\mathbf{D}_{ij}| = 0.32J$ , and  $J = 7$  meV [31]. The parameters correspond to an isolated free Sk with a radius of approximate  $4a = 1.08$  nm, where  $a = 0.27$  nm is the lattice constant. We apply periodic boundary conditions along the  $x$ -axis and assume free boundaries along the  $y$ -axis, thereby simulating a track of finite width. Track length  $l_x = 60a$  and width  $l_y = 60a \sin \frac{\pi}{3}$  are the same for all simulations and are large enough to prevent Sk self interaction and interaction with the track boundaries. Nonmagnetic impurity cluster (IC) is simulated by removing a cluster of the spins and excluding corresponding terms from energy (1).

(Meta)stable states correspond to local minima on the multidimensional energy surface defined by equation (1) for  $E$ , as a function of the directions of all magnetic moments  $\mathbf{S}$ . For the given set of parameters, the ground state corresponds to the ferromagnetic (FM) state, with a perturbation near the IC and rotating moments at the free boundary. A Sk pinned (attached) to the IC and a free Sk form two distinct metastable states. Metastable states were computed using a constrained nonlinear conjugate gradient method adapted for magnetic systems [32]. Activation barriers for the transition between pinned, depinned Sk and FM phase were computed using minimum energy path (MEP), which provides the most probable transition scenario [33]. The energy maximum along the MEP determines the first-order saddle point on the energy surface (transition state). Activation barrier is computed as difference between energies of the transition state and the initial one. MEP is approximated by its discretization defined by several states of magnetization vectors (called images) computed numerically. In our computations we used 15 to 50 images along each path and employed the string method for the numerical optimization of the MEP [34, 35]. For all paths, the initial state was FM and final state corresponds to the relaxed isolated Sk, completely separated from the IC.

### 3. Results

We investigated the processes of Sk nucleation on multiatomic nonmagnetic impurities, taking into account their geometry and size. To this end, we calculated MEP between two states: the initial state represented a FM configuration with the IC, while the final state corresponded to a Sk that was separated from the IC. We considered three types of IC shapes: compact, angular, and linear. A compact IC is defined as a cluster of atoms arranged in such a way that it has the smallest boundary for a given number of atoms. Examples of compact ICs are shown in the upper row of the right panel in Fig. 1. A linear IC refers to a cluster of atoms aligned along a lattice vector, thus maximizing the boundary; examples are shown in the lower row of Fig. 1. An angular IC consists of two linear ICs oriented along different lattice vectors that originate from a single lattice site. We denote the number of atoms forming the IC as  $N$ . The resulting nucleation barriers for the three types of ICs as a function of  $N$  are presented in the left panel of Fig. 1.

For  $N = 1$  and 2, the ICs of different types are identical; however, starting from  $N \geq 3$ , the ICs differ in geometry, which, as shown in the plot, leads to variations in the corresponding nucleation barriers. For all values of  $N$ , linear ICs yield the lowest barrier for Sk nucleation. It is also evident that, for all types of ICs, there exists an optimal impurity size at which the barrier is minimized. The reasons for these two observations are discussed below.

**Effect of Linear IC Size on the Nucleation Barrier.** The mechanism of Sk nucleation on a linear IC is illustrated in the lower panel of Fig. 2. As the domain wall winds around the IC, it begins to expand until a Sk core is formed. The Sk then shifts toward one end of the IC and subsequently detaches from it. It is worth noting that for long ICs, Sk creation occurs on one side of the impurity, while the magnetization texture on the other side remains unaffected, until very late stages of the creation process.

The upper panel of Fig. 2 presents the MEPs for several values of  $N$ . Each path exhibits an intermediate minimum corresponding to a Sk pinned to the IC. Thus, the nucleation process can be divided into two stages. The first stage involves the creation of a Sk on the IC, where the initial state is a homogeneous FM configuration with an IC, and the final state is a Sk localized at the IC (insets 1-2-3 in Fig. 2). The second stage is the depinning of the Sk from the IC, where the initial state is a Sk localized at the IC and the final state is a free Sk (insets 3-4-5 in Fig. 2). For clarity, we will refer to the first stage as *creation*, while encompassing both stages-including depinning from the IC-as *nucleation*.

The nucleation barrier is defined by the maximum energy along the MEP, with the energy of the FM state set to zero. As illustrated in Fig. 2, the energy of the transition state for creation rapidly decreases with increasing  $N$ , while the energy for depinning increases moderately. Energy of intermediate metastable state (the pinned Sk) also decreases with increase of  $N$ , but more slowly. For large  $N$ , the energy of the pinned Sk approaches the energy of the transition state for the creation process.

The obtained dependencies of the energy maxima for both stages, within the range of  $N$  up to 15, are presented in Fig. 3a. For small IC sizes up to  $N = 4$ , the barrier for creation dominates. However, as the size increases, depinning starts to take precedence. The maximum along the entire path determines the barrier for Sk nucleation at a specific  $N$

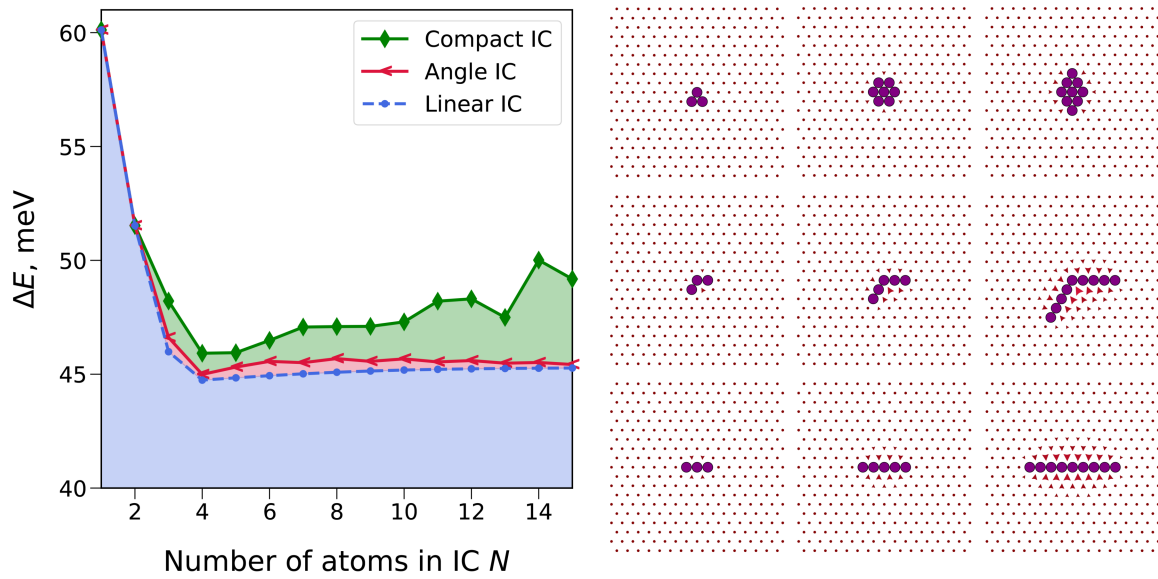


FIG. 1. (Left panel): Energy barrier for nucleation as a function of the number of atoms in the IC, shown for three types: compact, angled, and linear. (Right panel): Dark circles indicate IC atoms for compact (top row), angled (middle row), and linear (bottom row) configurations. Arrows represent the magnetization orientation in the ground state.

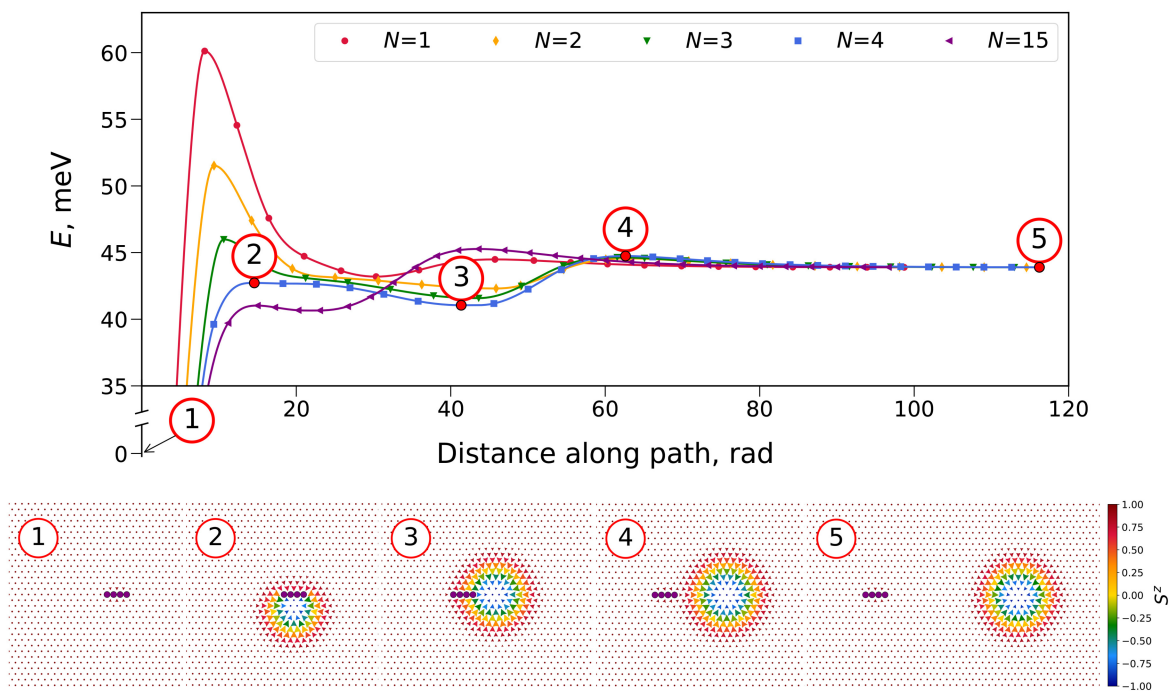


FIG. 2. MEPs for the nucleation of a Sk at linear IC of various sizes. The insets in the bottom show magnetic configurations along the MEP in case  $N = 4$ . States 1, 3 and 5 correspond to minima, state 2 corresponds to saddle point of creation and state 4 to saddle point of depinning from IC. The color in insets indicates the value of the out-of-plane component of the magnetic moments.

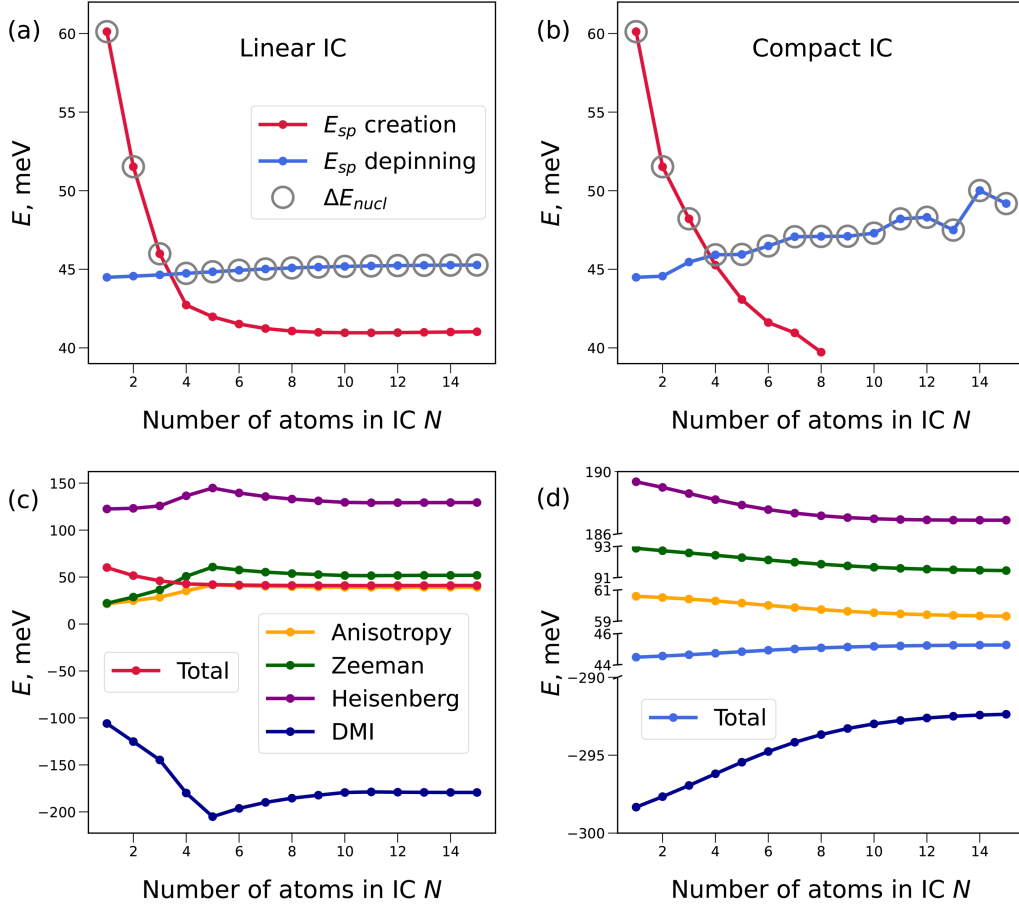


FIG. 3. Energy of saddle points for creation and depinning as a function of size of IC for line type (a) and for compact type (b). The dominant energy is indicated by empty circles. Energy contributions to saddle point for creation (c) and depinning (d) from linear IC as a function of  $N$ . Total energy in (c) corresponds to the energy of saddle point for creation, shown in red in (a). Total energy in (d) corresponds to the energy of saddle point for depinning, shown in blue in (a). Labels for Anisotropy, Zeeman, Heisenberg and DMI energy are the same for (c) and (d).

(indicated by empty circles in Fig. 3a). The maximum determines energy barrier in Fig. 1. We are interested in identifying the optimal value of  $N$  at which the nucleation barrier is minimized, thus Sk nucleation is fastest. Since both dependencies are monotonic, this minimum occurs at their intersection. In our case, with discrete values of  $N$ , the optimal size is the smallest  $N$  at which the barrier for depinning exceeds that for creation. Thus, in our analysis, we find that  $N_{\text{opt}} = 4$ .

To explain the contrasting behaviour of the barriers as  $N$  increases in Fig. 3a, we examine the spin configurations at the saddle points for both creation and depinning across three different sizes, along with the corresponding energy density distributions (see Figs. 4 and 5). During the creation process, we observe that the impurity is situated in a region of maximum positive energy (relatively the FM state). Introducing an IC – essentially removing atoms from this region – results in a decrease in energy. For small  $N$ , as illustrated in Figs. 4a and b, an increase in the size of the linear IC is accompanied by an increase in the radius of the saddle point. In this case, a larger radius of the Sk-like transition state configuration leads to a reduction in energy, since exchange energy in a micromagnetic framework behaves as  $R^{-1}$  for small  $R$  [36]. It is worth noting that the presence of the IC allows the Sk to bypass the small-radius phase during creation, since its minimum diameter is constrained by the size of the IC. Thus, two factors contribute to the sharp decrease in creation energy at small  $N$ : the increase in the subtracted positive energy as the IC size increases and the expansion of the saddle point radius.

At the saddle point, the energy densities associated with exchange, anisotropy, and Zeeman terms are positive, while the DMI energy density is negative. In the outer region of Sk, the DMI contribution dominates, resulting in a negative total energy density, whereas in the inner region, the other contributions prevail, leading to a positive total energy density. Introducing vacancies without changing the radius of the transition state would typically reduce the total energy, as the vacancies lie in the inner region of the Sk along the MEP. However, if the shape of the saddle point is assumed to remain fixed, the energy should decrease monotonically with the addition of impurities. This monotonic decrease is not observed

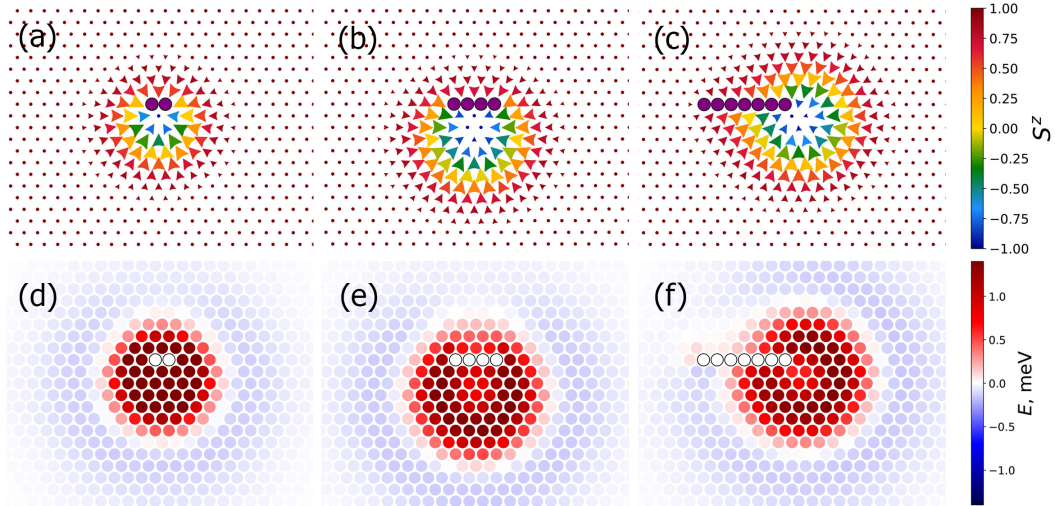


FIG. 4. Creation of Sk at linear IC: spin configurations of saddle point for  $N=2, 4$  and  $7$  (a, b, c) and corresponding distribution of energy per atom (d, e, f).

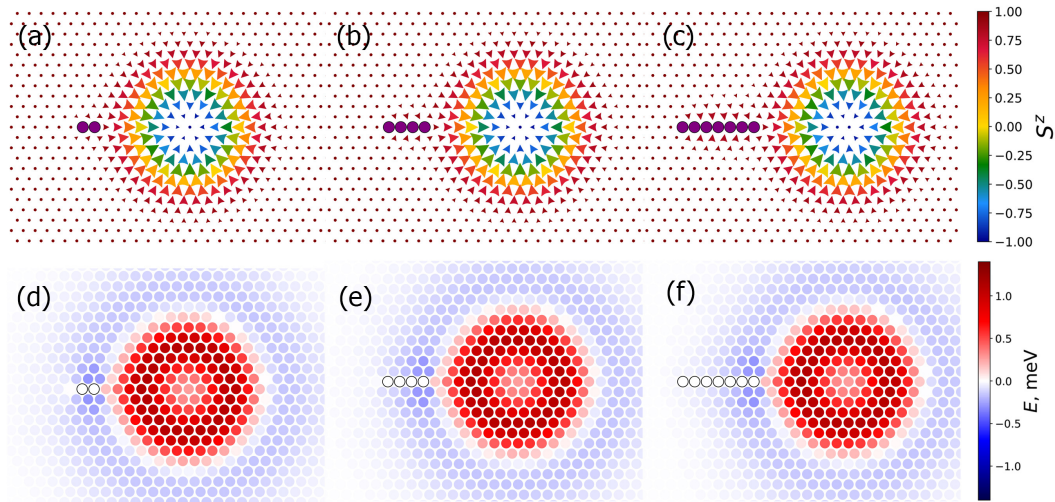


FIG. 5. Depinning of Sk from linear IC: spin configurations of saddle point for  $N=2, 4$  and  $7$  (a, b, c) and corresponding distribution of energy per atom (d, e, f).

in Fig. 3c, which shows that the contributions from anisotropy, Zeeman, and symmetric exchange interactions actually increase at small  $N$ . This indicates that the energy reduction due to an increasing Sk radius has a stronger effect than the energy reduction from IC removal alone.

Inside the Sk, the energy density is positive, so removing atoms from this region reduces the energy barrier. However, it is energetically unfavourable for the saddle-point configuration to exceed the typical size of the Sk. As a result, beyond a certain IC size (in our case,  $N = 5$ ), the IC can no longer be fully contained within the positive-energy region. At this point, some IC atoms extend into areas of zero or even negative energy density (see Fig. 4c), diminishing the effectiveness of energy reduction. This explains why the energy contributions in Fig. 3c exhibit a change of trend at point  $N=5$ . From the energy density distribution shown in Figs. 4d, e, and f, it is evident that in the negative energy regions, the energy density is relatively low and decreases gradually. This behaviour explains why the energy for creation begins to change only slightly for  $N > 5$  (as depicted in Fig. 3a).

The depinning process involves the transition from a Sk localized at an IC to a free Sk. The saddle-point configurations associated with this process (see Fig. 5, upper panel) can be qualitatively understood as follows. The energy density distribution (Fig. 5, lower panel), shows that the maximum of positive energy in the inner region of the Sk decreases with radial distance  $r$  from the center, becomes negative, and reaches a minimum at a finite distance  $R_1$ . Beyond  $r > R_1$ , the negative energy density decreases in magnitude with further increase in  $r$ . As the Sk detaches from the IC, it traverses this region of negative energy. Introducing an IC into this region effectively removes contributions with negative energy,

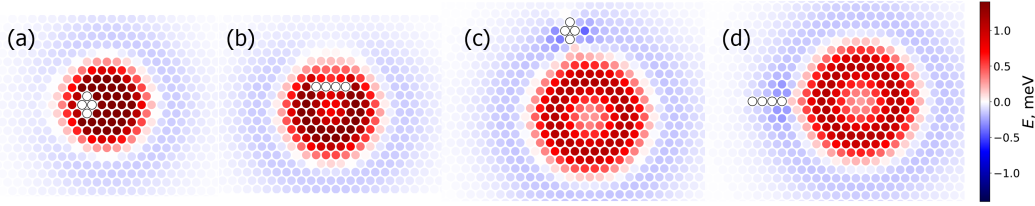


FIG. 6. Distribution of energy per atom in transition state for creation and depinning of Sk from compact IC (a) and (c) and linear IC (b) and (d).

thus increasing the total energy. Consequently, the maximum energy along the depinning path occurs when the IC coincides with the region of minimum energy density. Since we are interested in the minimum energy path, the path must be arranged to minimize this maximum energy. The total energy also depends on the orientation of the linear IC relative to the Sk's radial direction. Because the negative energy density diminishes for  $r > R_1$ , the lowest-energy configuration is achieved when the IC is aligned radially with respect to the Sk.

Adding atoms to the IC corresponds to removing additional atoms from the negative energy region, progressively further from the Sk center (see Fig. 5d, e, f). As shown, the energy density in the negative region is relatively low compared to that in the central part and also decreases with increasing distance from the center. This behavior accounts for the minimal change in the depinning barrier as  $N$  increases, as shown in Fig. 3a. It is worth noting that the variation in the depinning barrier with  $N$  is primarily driven by changes in the DMI energy contribution, as illustrated in Fig. 3d, which plots the energy components at the depinning saddle point as a function of  $N$ .

**Effect of IC Geometry on Nucleation Barrier.** In the previous section, we analyzed the influence of linear IC size on Sk nucleation. Another key factor is the geometry of the IC maximizing Sk nucleation rate. As mentioned earlier, for all values of  $N$ , linear ICs yield lower nucleation barriers compared to angular and compact ICs geometries. To understand the origin of this trend, we examine nucleation on compact IC more closely. During the Sk creation process, a compact IC – like a linear one – is located in a region of maximum energy. However, the radius of the saddle point associated with a compact IC is smaller (see Fig. 6a, b), leading to a higher creation barrier compared to that of a linear IC for  $N$  values up to 6 (as shown by the red curves in Fig. 3).

As previously noted, for  $N > 6$ , the linear IC no longer fits entirely within the Sk and begins to overlap with regions of negative energy, whereas the compact IC remains fully confined to the positive energy region. In this regime, the compact IC exhibits a lower creation barrier than the linear one (see  $N = 7$  and  $8$  in Fig. 3a and b).

Regarding the depinning process, a linear IC consistently yields a lower energy barrier than a compact IC for all values of  $N$  (see Fig. 3a and b). This can be attributed to the fact that a compact IC, situated in the region of minimum negative energy, will inevitably remove atoms with a higher magnitude of negative energy (Fig. 6c), whereas a linear IC extends along the gradient where the negative energy density gradually decreases (Fig. 6d).

The crossover point between the creation and depinning barriers for a compact IC occurs at  $N = 4$ . For smaller  $N$ , the creation barrier dominates and is higher for compact ICs than for linear ones. For  $N \geq 4$ , the depinning barrier becomes dominant and remains higher for compact ICs as well. As a result, the nucleation barrier for a compact IC exceeds that for a linear IC across all values of  $N$ , as shown in Fig. 1.

It is worth noting that the depinning energy varies non-monotonically with  $N$  for compact ICs (Fig. 3b). This nonmonotonic behavior arises because adding impurities can create sharp angles that contribute to a reduction in the depinning barrier.

It is also important to note that the creation process for compact ICs effectively “disappears” when the size reaches  $N = 9$  (see Fig. 3b). As demonstrated in the work by Potkina et al. [7], as the size of the compact IC increases, the barrier for the collapse of the Sk localized on it decreases, ultimately reaching zero at  $N = 9$ . Consequently, the metastable state associated with the Sk localized on the IC vanishes, leading to a transition from a two-stage nucleation process to a single process in which a Sk is created while simultaneously detaching from the IC.

In addition to the types of ICs discussed, intermediate variants are also possible, such as an angular IC. This type differs from a linear IC by having a break at one point, resulting in a more compact shape, which leads to intermediate values of nucleation energies, as shown in Fig. 1. As can be observed, the difference between the energies associated with an angular IC and those of a linear IC is not high. Therefore, minor imperfections in the fabrication of a linear IC do not significantly compromise the effect of reducing the nucleation energy.

#### 4. Discussion

Based on the calculated energies of the transition states, we have identified a trend indicating that elongated ICs are more favorable for Sk nucleation compared to compact ones. We have provided a qualitative explanation for this observed effect, independent of the specific parameters of Hamiltonian (1) and the type of lattice used. This supports the universality of our findings.

In addition to geometry, the size of the linear IC also influences the nucleation energy. An increase in the IC size reduces the barrier for creation, but simultaneously raises the barrier for depinning. Therefore, the optimal size is determined by balancing the energies of the transition states for creation and depinning. Since these energies generally depend on the parameters of the system, the optimal IC size will also vary accordingly. It is important to note that for certain system parameters, there may be no crossover between the energies of creation and depinning, or nucleation may occur in a single stage without an intermediate minimum corresponding to a Sk localized on the IC. These scenarios warrant further investigation.

The superiority of the linear defect geometry is further supported by our earlier findings on nucleation at boundary defects [37]. We discovered that among all possible notch geometries, the most favorable configuration for nucleation is a needle-shaped notch with sufficient depth. However, this option is still less effective than a linear IC. For instance, in the studied PdFe/Ir(111) system at a magnetic field of  $B = 3.75$  T, the nucleation barrier for a needle-shaped notch is 45.65 meV, whereas for a linear IC consisting of 4 atoms, it is 44.74 meV, resulting in an energy gain of approximately 2%. This difference arises from the additional exclusion of atoms from the region of negative energy density in the case of the notch, which adversely affects the energy required for depinning.

It is interesting to compare nucleation on ICs with other types of Sk nucleation on a track that we have previously investigated [6]. The barriers for Sk nucleation within the track and at its boundary were found to be 85.07 meV and 75.62 meV, respectively. In contrast, a linear IC of optimal size, as well as a needle-shaped notch, can reduce the nucleation barriers by nearly half in the PdFe/Ir(111) system under consideration at a magnetic field of  $B = 3.75$  T.

The energies of the saddle points for creation and depinning are measured from a homogeneous FM state with an IC that does not contain a Sk. To investigate the reverse process – the annihilation of a Sk on ICs – the obtained energies of the transition states should be referenced from the energy of a free Sk, which is independent of the shape and geometry of the IC. Consequently, the behavior of the transition state energies for pinning and collapse qualitatively aligns with those reported for creation and depinning. This indicates that, for erasing information, it is also most advantageous to utilize a linear IC of optimal size.

In experimental studies [38–41], notches at boundaries have been employed to create Sk. Our findings suggest that boundary notches of any geometry are less energy-efficient for Sk creation compared to a linear defect. It is also worth noting that the minimum possible nucleation barrier is determined by the difference in the energy of the final free Sk and the energy of the initial ferromagnetic state. A linear cluster of optimal size yields a barrier only slightly higher than this value (44.74 meV versus 43.9 meV). We hope that these results will encourage further experimental research into Sk nucleation at defects.

In summary, we have demonstrated that a linear defect of optimal size minimizes the energy required for Sk nucleation, which could be advantageous in the design of Sk-based magnetic memory and computing devices.

## References

- [1] Bogdanov A.N., Rössler U.K. Chiral Symmetry Breaking in Magnetic Thin Films and Multilayers. *Phys. Rev. Lett.*, 2001, **87**, P. 037203.
- [2] Romming N., Hanneken C., Menzel M., Bickel J.E., Wolter B., von Bergmann K., Kubetzka A., Wiesendanger R. Writing and Deleting Single Magnetic Skyrmions. *Science*, 2013, **341**(6146), P. 636–639.
- [3] Fert A., Cros V., Sampaio J. Skyrmions on the track. *Nat. Nanotechnol.*, 2013, **8**, P. 152–156.
- [4] Woo S., Litzius K., Krüger B., Im M.-Y., Caretta L., Richter K., Mann M., Krone A., Reeve R. M., Weigand M., Agrawal P., Lemesh I., Mawass M.-A., Fischer P., Kläui M., Beach G. S. D. Observation of room-temperature magnetic skyrmions and their current-driven dynamics in ultrathin metallic ferromagnets. *Nat. Mater.*, 2016, **15**, P. 501.
- [5] Uzdin V.M., Potkina M.N., Lobanov I.S., Bessarab P.F., Jónsson H. The effect of confinement and defects on the thermal stability of skyrmions. *Physica B: Condensed Matter*, 2018, **549**, P. 6–9.
- [6] Uzdin V.M., Potkina M.N., Lobanov I.S., Bessarab P.F., Jónsson H. Energy surface and lifetime of magnetic skyrmions. *J. Magn. Magn. Mater.*, 2018, **459**, P. 236–240.
- [7] Potkina M.N., Lobanov I.S., Uzdin V.M. Nonmagnetic impurities in skyrmion racetrack memory. *Nanosystems: Phys., Chem., Math.*, 2020, **11**(6), P. 628–635.
- [8] Stosic D., Ludermir B.T., Milošević V.M. Pinning of magnetic skyrmions in a monolayer Co film on Pt(111): Theoretical characterization and exemplified utilization. *Phys. Rev. B*, 2017, **96**(21), P. 214403.
- [9] Fernandes I.L., Bouaziz J., Blügel S., Lounis S. Universality of defect-skyrmion interaction profiles. *Nat. Commun.*, 2018, **9**(1), P. 4395.
- [10] Castell-Queralt J., González-Gómez L., Del-Valle N., Sanchez A., Navau C. Accelerating, guiding, and compressing skyrmions by defect rails. *Nanoscale*, 2019, **11**(26), P. 12589–12594.
- [11] Suess D., Vogler C., Bruckner F., Heistracher P., Slanovc F., Abert C. Spin torque efficiency and analytic error rate estimates of skyrmion. *Sci. Rep.*, 2019, **9**, P. 4827.
- [12] Morshed M.G., Vakili H., Ghosh A.W. Positional stability of skyrmions in a racetrack memory with notched geometry. *Phys. Rev. Applied*, 2022, **17**, P. 064019.
- [13] Belrhazi H., El Hafidi M. Nucleation and manipulation of single skyrmions using spin-polarized currents in antiferromagnetic skyrmion-based racetrack memories. *Sci. Rep.*, 2022, **12**, P. 15225.
- [14] Hanneken C., Kubetzka A., von Bergmann K., Wiesendanger R. Pinning and movement of individual nanoscale magnetic skyrmions via defects. *New J. Phys.*, 2016, **18**(5), P. 055009.
- [15] Li W., Wang X., Dai Y., Bian Y., Huang Q., Zhang X., Su L., Zhang B., Tang D., Yang Y. Voltage-controlled skyrmion deletion device based on magnetic defects. *J. Phys. D: Appl. Phys.*, 2021, **54**, P. 445001.
- [16] Potkina M.N., Lobanov I.S., Uzdin V.M. Fine energy structure of a magnetic skyrmion localized on a nonmagnetic impurity in an external magnetic field. *Physics of Complex Systems*, 2020, **1**(4), P. 165–168.

- [17] Choi H.C., Lin S.Z., Zhu J.X. Density functional theory study of skyrmion pinning by atomic defects in MnSi. *Phys. Rev. B*, 2016, **93**, P. 115112.
- [18] Arjana I.G., Fernandes I.L., Chico J., Lounis S. Sub-nanoscale atom-by-atom crafting of skyrmion-defect interaction profiles. *Sci. Rep.*, 2020, **10**, P. 14655.
- [19] Iwasaki J., Mochizuki M., Nagaosa N. Universal current-velocity relation of skyrmion motion in chiral magnets. *Nat. Commun.*, 2013, **4**(1), P. 1463.
- [20] Koshibae W., Nagaosa N. Theory of current-driven skyrmions in disordered magnets. *Sci. Rep.*, 2018, **8**(1), P. 6328.
- [21] Toscano D., Leonel S.A., Coura P.Z., Sato F. Building traps for skyrmions by the incorporation of magnetic defects into nanomagnets: Pinning and scattering traps by magnetic properties engineering. *J. Magn. Magn. Mater.*, 2019, **480**, P. 171.
- [22] Everschor-Sitte K., Sitte M., Valet T., Abanov A., Sinova J. Skyrmion production on demand by homogeneous DC currents. *New J. Phys.*, 2017, **19**, P. 092001.
- [23] Mulkers J., Waeyenberge B.V., Milošević M.V. Effects of spatially engineered Dzyaloshinskii-Moriya interaction in ferromagnetic films. *Phys. Rev. B*, 2017, **95**, P. 144401.
- [24] Derras-Chouk A., Chudnovsky E.M. Skyrmions near defects. *J. Phys.: Condens. Matter*, 2021, **33**, P. 195802.
- [25] Müller J., Rosch A. Capturing of a magnetic skyrmion with a hole. *Phys. Rev. B*, 2015, **91**(5), P. 054410.
- [26] Liu Y.H., Li Y.Q. A mechanism to pin skyrmions in chiral magnets. *J. Phys.: Condens. Matter*, 2013, **25**, P. 076005.
- [27] Martínez J.C., Jalil M.B.A. Topological dynamics and current-induced motion in a skyrmion lattice. *New J. Phys.*, 2016, **18**, P. 033008.
- [28] Navau C., Del-Valle N., Sanchez A. Interaction of isolated skyrmions with point and linear defects. *J. Magn. Magn. Mater.*, 2018, **465**, P. 709.
- [29] Lin S.Z., Reichhardt C., Batista C.D., Saxena A. Particle model for skyrmions in metallic chiral magnets: Dynamics, pinning, and creep. *Phys. Rev. B*, 2013, **87**, P. 214419.
- [30] González-Gómez L., Castell-Queralt J., Del-Valle N., Sanchez A., Navau C. Analytical modeling of the interaction between skyrmions and extended defects. *Phys. Rev. B*, 2019, **100**, P. 054440.
- [31] Hagemeister J., Romming N., von Bergmann K., Vedmedenko E.Y., Wiesendanger R. Stability of single skyrmionic bits. *Nat. Commun.*, 2015, **6**(1), P. 8455.
- [32] Lobanov I.S., Uzdin V.M. The lifetime of micron scale topological chiral magnetic states with atomic resolution. *Comp. Phys. Commun.*, 2021, **269**, P. 108136.
- [33] Bessarab P.F., Uzdin V.M., Jónsson H. Harmonic transition-state theory of thermal spin transitions. *Phys. Rev. B*, 2012, **85**(18), P. 184409.
- [34] Weinan E., Ren W., Vanden-Eijnden E. String method for the study of rare events. *Phys. Rev. B*, 2002, **66**, P. 052301.
- [35] Lobanov I.S., Potkina M.N., Jónsson H., Uzdin V.M. Truncated minimum energy path method for finding first order saddle points. *Nanosystems: Phys., Chem., Math.*, 2017, **8**(5), P. 586–595.
- [36] Wang X.S., Yuan H.Y., Wang X.R. A theory on skyrmion size. *Commun. Phys.*, 2018, **1**, P. 31.
- [37] Potkina M.N., Lobanov I.S. Nucleation of magnetic skyrmions at a notch. *Nanosystems: Phys., Chem., Math.*, 2024, **15**(2), P. 192–200.
- [38] Wang W., Song D., Wei W., Nan P., Zhang S., Ge B., Tian M., Zang J., Du H. Electrical manipulation of skyrmions in a chiral magnet. *Nat. Commun.*, 2022, **13**, P. 1593.
- [39] Yu X. Z., Morikawa D., Nakajima K., Shibata K., Kanazawa N., Arima T., Nagaosa N., Tokura Y. Motion tracking of 80-nm-size skyrmions upon directional current injections. *Sci. Adv.*, 2020, **6**, P. eaaz9744.
- [40] Twitchett-Harrison A.C., Loudon J.C., Pepper R.A., Birch M.T., Fangohr H., Midgley P.A., Balakrishnan G., Hatton P.D. Confinement of skyrmions in nanoscale FeGe device-like structures. *ACS Appl. Electron. Mater.*, 2022, **4**(9), P. 4427–4437.
- [41] Büttner F., Lemesh I., Schneider M., Pfau B., Günther C.M., Hessaing P., Geilhufe J., Caretta L., Engel D., Krüger B., Viehhaus J., Eisebitt S., Beach G.S.D. Field-free deterministic ultrafast creation of magnetic skyrmions by spin-orbit torques. *Nat. Nanotech.*, 2017, **12**, P. 1040–1044.

---

Submitted 12 April 2025; revised 29 May 2025; accepted 30 May 2025

*Information about the authors:*

Maria N. Potkina – Infochemistry Scientific Center, ITMO University, 197101 St. Petersburg, Russia; ORCID 0000-0002-1380-2454; potkina.maria@yandex.ru

Igor S. Lobanov – Faculty of Physics, ITMO University, 197101 St. Petersburg, Russia; ORCID 0000-0001-8789-3267; lobanov.igor@gmail.com

*Conflict of interest:* the authors declare no conflict of interest.

## Magnetic structure of domain walls in stressed cylindrical wires

Ksenia A. Chichay, Igor S. Lobanov, Valery M. Uzdin

<sup>1</sup>Department of Physics, ITMO University, St. Petersburg, 197101, Russia

<sup>a</sup>ks.chichay@gmail.com, <sup>b</sup>lobanov.igor@gmail.com, <sup>c</sup>v.uzdin@mail.ru

Corresponding author: K. A. Chichay, ks.chichay@gmail.com

PACS 75.60.Ch, 75.30.Gw

**ABSTRACT** We investigate the internal structure and dynamics of transverse domain walls in amorphous, stressed ferromagnetic microwires by comparing two magnetoelastic anisotropy models. In the complete model, all three principal stress components (axial, radial, circumferential) extracted from a realistic stress profile are converted into spatially varying anisotropies; in the reduced model, only the dominant stress component in each radial region is retained. Micromagnetic simulations reveal that the reduced model produces exaggerated peripheral deviations—stronger radial magnetization projections and deeper penetration of the disturbed layer—compared to the complete model. Energy analysis shows that omitting non-dominant anisotropy leads to underestimation of domain wall-defect interactions and a sharp, shell-like radial ordering at higher values of surface anisotropy. Furthermore, dissipation calculations based on the Thiele approach indicate that the reduced model overestimates domain wall velocity by up to 50%. These results demonstrate that incorporating the full stress tensor is essential for accurate prediction of both static domain wall profiles and their dynamic response in stressed microwires.

**KEYWORDS** Domain wall, cylindrical wire, amorphous ferromagnetic microwires, micromagnetics, magnetoelastic anisotropy, internal mechanical stress.

**ACKNOWLEDGEMENTS** This work was funded by the Russian Science Foundation (project No. 23-72-10028, <https://rscf.ru/en/project/23-72-10028/>). K.A.Ch. acknowledges the support of ITMO Fellowship Program.

**FOR CITATION** Chichay K.A., Lobanov I.S., Uzdin V.M. Magnetic structure of domain walls in stressed cylindrical wires. *Nanosystems: Phys. Chem. Math.*, 2025, **16** (3), 325–332.

### 1. Introduction

The use of magnetoelastic interactions controlled by mechanical deformations in solids for the development of new information, sensor, and energy-saving technologies has led to the creation of a new direction in micro and nanoelectronics, called straintronics [1, 2]. Mechanical stresses can be associated with the magnetic or ferroelectric material, which manifests itself both in dynamic and static properties, and allows manipulation of the magnetic state and change in magnetic characteristics [3].

One such class of systems is the the amorphous ferromagnetic glass-coated microwires, which are a composite object with cylindrical symmetry consisting of a metallic nucleus and a glass shell [4, 5]. The peculiarity of such a microwire is the amorphous and stressed state of its metallic nucleus, due to its production using the Ulitovsky-Taylor method [6], which includes melt drawing and rapid quenching. Several types of stress coexist in an amorphous ferromagnetic microwire: i) stresses arising during rapid cooling, ii) stresses arising during the drawing process, and iii) stresses arising due to the difference in the thermal expansion coefficients of the metal and glass [7, 8].

Such coexistence of stresses leads to a certain, rather complex distribution of the three components of the mechanical stress tensor along the radius of the metal nucleus: axial ( $\sigma_{zz}$ ), radial ( $\sigma_{\rho\rho}$ ) and circumferential ( $\sigma_{\phi\phi}$ ). The magnitude of internal mechanical stresses ranges from fractions to several units of gigapascals. Currently, there are several theoretical works that predict this distribution. In particular, the distribution of all three components of the mechanical stress tensor along the radius of the microwire, taking into account the solidification process, was calculated in [9].

Mechanical stresses together with the magnetostriction [10] effect determine the magnitude of magnetoelastic energy and, due to the amorphous state of the metallic nucleus along with the cylindrical shape, play a major role in the formation of the magnetic state and magnetic characteristics of the wire [9, 11–14]. In works published in the early 2000s, the authors considered the formation of magnetic anisotropy, directly dependent on the distribution of internal mechanical stresses along the radius of the metallic nucleus of the microwire [13]. Calculations were carried out for a microwire of composition  $\text{Fe}_{77.5}\text{Si}_{7.5}\text{B}_{15}$  with a positive magnetostriction coefficient, a metallic nucleus diameter of 25  $\mu\text{m}$  and a glass thickness of 15  $\mu\text{m}$ . The authors determine the type and value of anisotropy in each part of the wire by taking into account the dominant component of mechanical stress.

In the distribution of stresses along the radius of the microwire, two regions can be distinguished: the region where the axial component has the largest value and is positive (tensile stress), and the region in which the circumferential and axial components of stress are negative (compressive stress) and have the greatest absolute value [9, 13]. We will call these two areas conditionally the center and the periphery. If we take into account only the dominant component of mechanical stresses, then the determination of the anisotropy type occurs in the following way. In the case of positive magnetostriction, axial tensile stresses in the center will then induce an easy-axis axial anisotropy, which will prevail in almost the entire volume of the metallic nucleus of the wire with the average value of  $K^{\text{rad}} = 3 \cdot 10^4 \text{ J/m}^3$ . At the peripheral layer, where negative circumferential stresses are dominant in magnitude, the resulting easy-axis anisotropy must be perpendicular to this direction, so it will be either axial or radial. But since in this region the axial compressive stresses are also large, the resulting direction of easy-axis anisotropy satisfying both types of stresses will be radial with the maximum value of  $K^{\text{rad}} = 5.6 \cdot 10^4 \text{ J/m}^3$  (the value corresponds to circumferential mechanical stresses at the periphery). It is this distribution of anisotropy that is usually taken into account when discussing the formation of the domain structure of microwires and domain wall configuration.

In this work, we consider how taking into account all three types of stress affects the structure of transverse domain wall. We refer to such consideration as the complete model and compare it with the results obtained for the reduced model (when only the dominant component is taken). We discuss the change in the domain wall internal structure with a change in the anisotropy value at the periphery and analyze the energy contributions for the both cases of complete and reduced models.

## 2. Model

We simulate magnetic domain walls (DWs) in a cylindrical wire using a custom-developed Magnes software. The system under study is a wire with fixed geometry: length  $L$  and radius  $R$ . Equilibrium DW configurations are obtained by minimizing the micromagnetic energy functional, containing contributions of symmetric exchange  $E^{\text{ex}}$  and three anisotropies: axial  $E^{\text{ax}}$ , radial  $E^{\text{rad}}$ , and circumferential  $E^{\text{circ}}$ :

$$E = E^{\text{ex}} + E^{\text{ax}} + E^{\text{rad}} + E^{\text{circ}}. \quad (1)$$

The first term in (1) corresponds to the exchange energy, with exchange stiffness  $A = 2 \cdot 10^{-11} \text{ J/m}$

$$E^{\text{ex}} = \frac{A}{2} \iiint \left[ \left( \frac{\partial \mathbf{S}}{\partial \rho} \right)^2 + \frac{1}{\rho^2} \left( \frac{\partial \mathbf{S}}{\partial \phi} \right)^2 + \left( \frac{\partial \mathbf{S}}{\partial z} \right)^2 \right] dV,$$

where  $\mathbf{S}(\rho, \phi, z)$  is the magnetization vector field. The z-axis is aligned with the wire axis, while  $\rho$  and  $\phi$  are polar coordinates in the cross-sectional plane. Three anisotropy contributions are defined by corresponding spatially varying parameters  $K^i(\rho)$  and axis  $\mathbf{e}^i$ , where  $\mathbf{e}^z$  is unit vector along z-axis,  $\mathbf{e}^{\text{rad}} = \mathbf{e}^\rho$  and  $\mathbf{e}^{\text{circ}} = \mathbf{e}^\phi$  are local orthonormal basis in polar coordinates in the wire cross section:

$$E^i = - \iiint K^i(\rho) (\mathbf{S} \cdot \mathbf{e}^i)^2 dV, \quad i = \text{ax, rad, circ}.$$

The energy density corresponding to energy contribution  $E^i$  is denoted  $w^i$ . In our simulations, we consider a wire of radius  $R = 10^{-7} \text{ m}$  and length  $L = 10^{-6} \text{ m}$ .

The micromagnetic problem was discretized on a cylindrical grid with the following resolution:  $N_\rho = 15$  points in the radial direction (from the wire center to the boundary),  $N_\phi = 40$  angular divisions, and  $N_z = 200$  points along the wire axis. The energy functional was approximated using central finite differences for spatial derivatives and the trapezoidal rule for numerical integration. This discretization scheme yields a second-order accuracy, with an error scaling as  $O(h^2)$  for the exchange energy, where  $h$  denotes the grid spacing [15].

The non-zero anisotropy contributions and the spatial distribution of the magnetoelastic anisotropy  $K_i(\rho)$  were defined differently in the two modeling approaches mentioned above. In both cases, the magnetoelastic anisotropy arises from internal mechanical stresses and is given by

$$K_{\text{me}}^i = \frac{3}{2} \lambda_S \sigma_{ii}, \quad i = \text{ax, rad, circ},$$

where  $\lambda_S$  is saturation magnetostriction coefficient and  $\sigma_{ii}$  is the diagonal stress component. In both models, we also account for the effective shape anisotropy of the cylinder, arising from the demagnetizing field. This contribution is included as an additional uniaxial anisotropy term with strength  $K_{\text{eff}}^{\text{ax}} = 1/4 \mu_0 M_s^2$  where  $M_s = 500 \text{ kA/m}$  is the saturation magnetization. Radial and circumferential anisotropy contain only the magnetoelastic anisotropy:

$$K^{\text{ax}} = K_{\text{me}}^{\text{ax}} + K_{\text{eff}}^{\text{ax}}, \quad K^{\text{circ}} = K_{\text{me}}^{\text{circ}}, \quad K^{\text{rad}} = K_{\text{me}}^{\text{rad}}.$$

In the first approach, referred to as the *reduced model*, only a single dominant magnetoelastic anisotropy component was assigned to each region of the wire, reflecting the prevailing stress orientation and magnitude. Specifically, in the wire core, an easy-axis axial anisotropy was imposed, with a average value of  $K_{\text{me}}^{\text{ax}} = 3 \cdot 10^4 \text{ J/m}^3$ . At the periphery, an

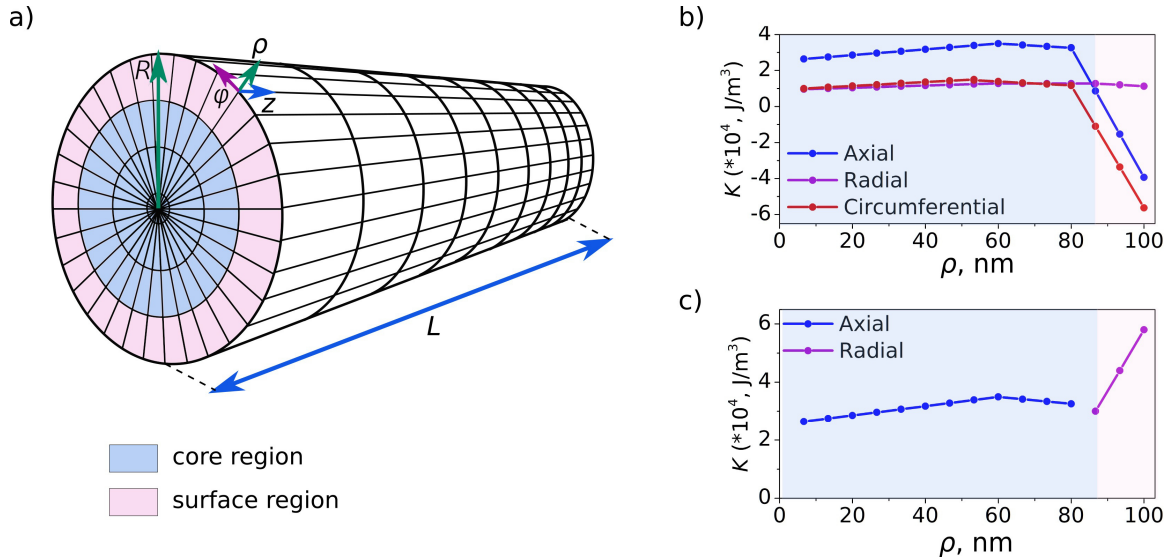


FIG. 1. a) Schematic representation of a wire in cylindrical coordinate system.  $R$  is the wire radius,  $L$  is the length of the wire. b) and c) Radial dependence of magnetoelastic anisotropy components in the complete and reduced models, respectively. Light blue and light pink areas correspond to the core and surface regions

easy-axis radial anisotropy was applied, reaching up to  $K_{\max}^{\text{rad}} = 5.6 \cdot 10^4 \text{ J/m}^3$  at the surface layer. Further details can be found in the previously cited work [13]. Radial profiles of magnetoelastic anisotropies are shown in Fig. 1c.

The second approach, referred to as the *complete model*, incorporates all three components of internal stress (axial, radial, and circumferential) each distributed along the wire radius (Fig. 1b). Following the methodology of [13], tensile stresses are translated into easy-axis anisotropy, while compressive stresses correspond to easy-plane anisotropy. As a result, all three types of anisotropy are present throughout the entire wire volume, with their radial distributions directly reflecting the magnitude and sign of the underlying stresses. The stress profile was adopted from [13], and the magnetostriction coefficient was set to  $\lambda_S = 25 \cdot 10^{-6}$ , a typical value for Fe-based microwires. The maximum anisotropy values at the wire surface were  $K_{\max}^{\text{circ}} = -5.6 \cdot 10^4 \text{ J/m}^3$  for the circumferential component and  $K_{\max}^{\text{ax}} = -3.9 \cdot 10^4 \text{ J/m}^3$  for the axial component. The radial profiles of the anisotropy components reveal two distinct regions: a *core region*  $\rho < 87 \text{ nm}$ , and a *surface region*  $\rho > 87 \text{ nm}$ , which are shown in Fig. 1a. In the core, all three anisotropies remain virtually constant, but the axial anisotropy dominates in magnitude. In contrast, in the surface layer both the axial and circumferential anisotropy components vary more strongly with  $\rho$ , and notably, change sign as one moves to the surface, while radial anisotropy maintains its value practically constant. This sign reversal reflects the shift from tensile to compressive stress regimes across the wire radius.

To investigate the influence of peripheral anisotropy  $K^i(R)$  we kept the anisotropy constants fixed in the inner region of the wire and modified them only within the surface region. To ensure smooth spatial variation, a linear interpolation was applied between the anisotropy values in the inner region and those at the surface. The maximum absolute anisotropy value was always attained at the surface. Surface anisotropy was controlled by a scaling factor  $k$  such that  $K^i(R) = kK_{\max}^i$ , where  $K_{\max}^i$  denotes the maximum anisotropy strength. The same scaling factor was applied to both the radial easy-axis magnetoelastic anisotropy component in reduced model and easy-plane axial and circumferential components of magnetoelastic anisotropy in the complete model.

### 3. Domain wall structure

We consider a metastable state of a cylindrical microwire, comprising two oppositely magnetized domains separated by a transverse head-to-head domain wall. As demonstrated in our previous work [16], radially inhomogeneous anisotropy can lead to deviations from the conventional internal structure of the domain wall. In the present case, these deviations emerge near the wire periphery, where the strong anisotropy favors directions other than the axial easy axis. In contrast, near the wire center (where the axial easy-axis anisotropy dominates) the magnetization remains predominantly transverse. Under these conditions, the transverse domain wall can be viewed as consisting of two sectors (typically symmetric), each characterized by a magnetization component with a radial projection. In one sector, the magnetization points inward toward the wire center; in the other, outward. Both sectors are aligned with the preferred transverse direction at the wire core. This configuration represents a compromise between a conventional transverse domain wall and one where the magnetization is entirely radial. A domain wall with such an internal structure is illustrated in Fig. 2.

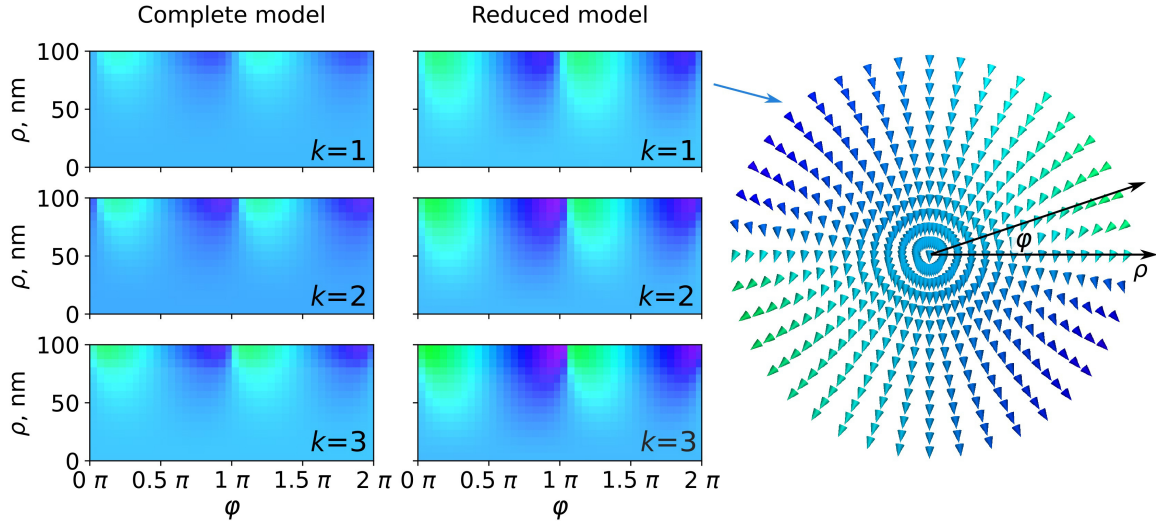


FIG. 2. Evolution of the magnetic configuration of the transverse DW with a change of the anisotropy value at the periphery for the cases of complete and reduced models. For each anisotropy value  $k$ , an unrolled view of the  $\rho - \phi$  DW cross section is given.

To provide a more intuitive visualization, we present domain wall structures using an unrolled  $\rho - \phi$  view instead of a circumferential cross-section. Fig. 2 illustrates domain wall configurations at the wire periphery for different values of the scaling factor  $k$ , comparing the complete and reduced anisotropy models. The top row in each column corresponds to  $k = 1$ , with parameters taken from [13]. In both models, the same general type of domain wall is stabilized; however, the extent of peripheral magnetization deviation differs significantly. In the reduced model, deviations from the ideal transverse wall are much more pronounced. Specifically, magnetic moments near the surface exhibit larger angular deviations from the transverse direction imposed by the wire center. Additionally, the perturbation penetrates deeper into the wire compared to the complete model. As the peripheral anisotropy strength increases (i.e., as  $k$  increases), the models exhibit more pronounced deviations, characterized by stronger radial projections of the magnetization and deeper penetration into the wire core. Nevertheless, even at  $k = 3$ , the complete model shows smaller deviations than the reduced model at  $k = 1$ . This highlights the stabilizing effect of including all three anisotropy components in the complete model, which helps preserve the transverse domain wall structure across a broad range of peripheral anisotropy values.

To gain deeper insight into the domain wall structure, we analyze the contributions of each anisotropy component separately. Fig. 3a presents the spatial distribution of the axial anisotropy energy density,  $w^{\text{ax}}$  across the domain wall cross-section for various values of the peripheral anisotropy scaling factor  $k$ . Each cross-section reveals two distinct regions: a central zone (in blue) and a peripheral zone (in green), separated by a narrow transition region characterized by a minimum in anisotropy energy density (dark blue). Importantly, the magnitude and spatial uniformity of  $w^{\text{ax}}$  in the wire center remain unchanged with increasing  $k$ , reflecting the fact that the axial anisotropy constant is held fixed in this region. In contrast, the peripheral value of  $w^{\text{ax}}$  increases proportionally with  $k$ . Notably, the thickness of the outer shell where  $w^{\text{ax}}$  approaches zero behaves differently in the two models: it remains constant in the complete model, whereas in the reduced model it increases with  $k$ . This indicates a more pronounced sensitivity of the reduced model to peripheral anisotropy modulation.

Figure 3b shows how the total axial anisotropy energy,  $E^{\text{ax}}$ , varies with the peripheral anisotropy scaling factor  $k$ . The energy is computed relative to that of a uniformly magnetized (homogeneous ferromagnetic) reference state. The plot reveals that  $E^{\text{ax}}$  at the wire center is identical for both the complete and reduced models only at  $k = 1$ . As  $k$  varies, the two models exhibit opposite trends: in the complete model,  $E^{\text{ax}}$  increases slightly, while in the reduced model it decreases. This energy dependence highlights a key feature of the micromagnetic structure obtained in the reduced model. Beyond a certain threshold value  $k > X$ , the domain wall at the wire surface becomes significantly wider. In this regime, the radial orientation of the magnetic moments at the periphery begins to spread symmetrically outward from the domain wall, forming a radially ordered “shell”. The sharp drop in  $E^{\text{ax}}$  observed for the reduced model starting at  $k = 2$  corresponds to the formation of this shell throughout the wire volume.

Figure 3c shows the spatial distribution of the radial anisotropy energy density,  $w^{\text{rad}}$ , across the domain wall cross-section. In the reduced model, radial anisotropy is applied only in the peripheral layer of the wire, resulting in  $w^{\text{rad}} = 0$  in the central region. In contrast, the complete model assigns radial anisotropy throughout the entire wire volume, though its magnitude remains constant with respect to  $k$ . Consequently, the spatial pattern of  $w^{\text{rad}}$  remains largely unchanged across different values of  $k$  in the complete model. The minima of  $w^{\text{rad}}$  (indicated by dark blue regions) correspond to areas where the magnetization aligns closely with the radial direction. As  $k$  increases, the radial projection of the magnetization

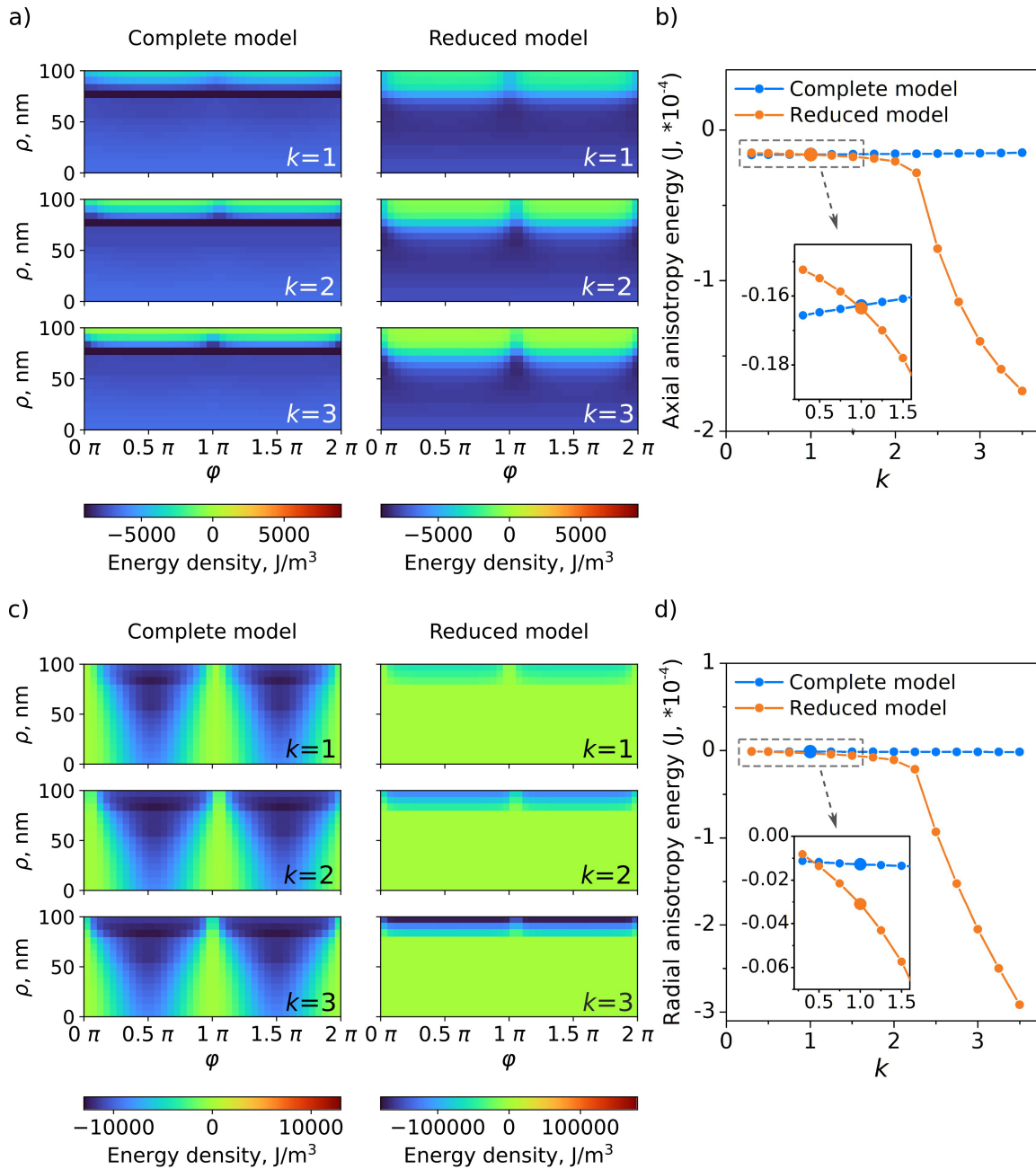


FIG. 3. (a) and (c) Distributions of axial and radial anisotropy energy density for an unrolled  $\rho - \phi$  DW cross section for different values of  $k$ . The color bar indicates the energy density value from the lowest negative (dark blue) to the highest positive (dark red) value. (b) and (d) Axial and radial anisotropy energy as a function of anisotropy value at the periphery  $k$  for the cases of complete and reduced models. The largest dots on the graph are related to the  $k = 1$ .

grows in both halves of the wall, causing the low-energy regions near the surface to expand slightly. The corresponding dependence of the total radial anisotropy energy,  $E^{\text{rad}}$  on the scaling factor  $k$  is presented in Fig. 3d. The two models agree only at small values of  $k$ . For the reduced model, a sharp drop in  $E^{\text{rad}}$  occurs as  $k$  increases, which reflects the emergence of a fully formed radially ordered layer that extends along the wire surface. This pronounced difference in  $w^{\text{rad}}$  between the complete and reduced models is expected to significantly influence both the structure and dynamic behavior of moving domain walls, including their shape and velocity.

Figure 4a presents the distribution of circumferential anisotropy energy density,  $w^{\text{circ}}$ , for the complete model only, as circumferential anisotropy is not included in the reduced model. In the domain wall cross-sections, nonzero values of  $w^{\text{circ}}$  are observed exclusively in “transitional” regions—specifically, at the boundary between two sectors where the magnetization points radially inward in one and outward in the other. Notably, circumferential anisotropy is the only anisotropy component for which the energy density assumes both positive and negative values. The extrema of  $w^{\text{circ}}$

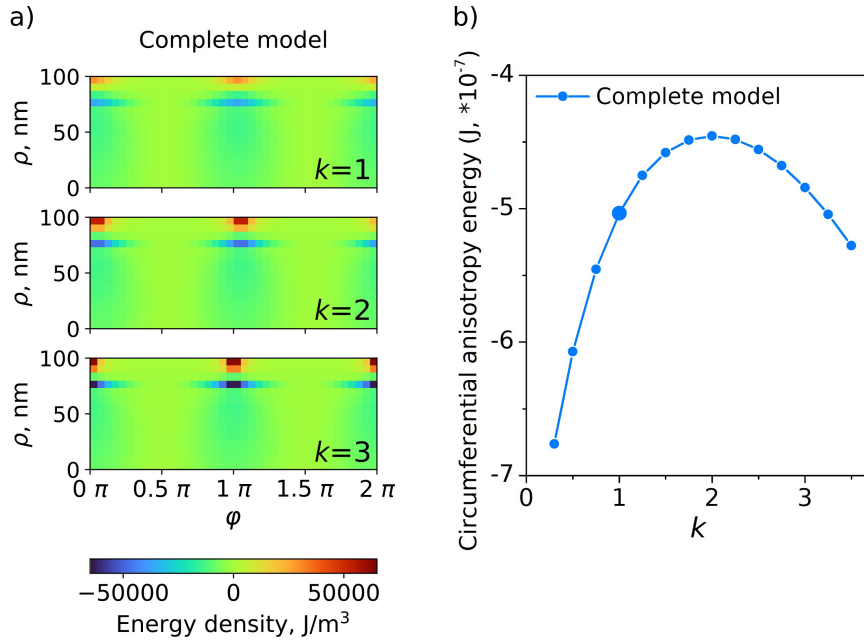


FIG. 4. Distribution of circumferential anisotropy energy density for an unrolled  $\rho$ – $\phi$  DW cross section for different values of  $k$ . (b) Circumferential anisotropy energy as a function of anisotropy value at the periphery  $k$  for the case of complete model. The largest dot on the graph is related to the  $k = 1$ .

are highly localized in both angular and radial coordinates. This spatial confinement may play an important role in domain wall interactions with defects and impurities. Such interactions can be considered from two perspectives. First, because the maxima and minima of  $w^{\text{circ}}$  are sharply localized and occur at specific depths, the nature of the domain wall's interaction with a given impurity—whether attractive or repulsive—depends critically on the impurity's radial position. Second, domain walls in cylindrical wires exhibit azimuthal rotation during motion due to the cylindrical symmetry (i.e., energetic equivalence of all transverse directions). As a result, interaction with an impurity also depends on whether the rotating anisotropy features (such as the localized maxima/minima of  $w^{\text{circ}}$ ) spatially overlap with the impurity, and on the impurity's size. This interplay can have a significant impact on domain wall dynamics, particularly affecting the domain wall velocity and the nucleation field (i.e., the critical magnetic field required to nucleate a domain wall inside the microwire). Since circumferential anisotropy is omitted in the reduced model, it may underestimate the strength and complexity of domain wall-defect interactions.

The behavior of the total circumferential anisotropy energy,  $E^{\text{circ}}$  shown in Fig. 4b, exhibits a non-monotonic trend: it increases with the scaling factor  $k$  up to  $k = 2$ , and then begins to decrease. This trend likely arises from the interplay between the localized minima and maxima of the energy density  $w^{\text{circ}}$ , which evolve with increasing  $k$ . As  $k$  increases, the radial extent of magnetization deviations at the wire periphery also increases. Consequently, the region at the boundary between the two radially magnetized sectors of the domain wall—where the magnetization momentarily aligns in the circumferential direction—expands. This expansion can lead to a faster growth in the magnitude of the negative (minimum) values of  $w^{\text{circ}}$ , which may dominate the total energy and result in the observed decrease in  $E^{\text{circ}}$  beyond a certain  $k$ .

Figure 5a shows the total energy of the wire as a function of the scaling factor  $k$ , revealing opposite trends for the complete and reduced models: the system energy slightly grows in the complete model and decreases in reduced model. Note, that the energy is computed relative to that of a uniformly magnetized (homogeneous ferromagnetic) reference state. For small  $k$  the energies of obtained magnetic states are almost coincides. As the anisotropy in the surface layer  $k$  increases, the differences in energies become noticeable. Hence, it can be assumed that for large anisotropies at the periphery the applicability of the reduced model is questionable.

#### 4. Domain wall movement

Domain walls (DWs) in magnetic wires are typically driven by external magnetic fields. In the simplest scenario, a uniform field  $H$  is applied along the axis of the wire. One domain, aligned with the field, is energetically favored, while the oppositely oriented domain becomes unfavorable. As the system relaxes, the domain aligned with the field expands, and the opposing domain shrinks.

The dynamics of such a system are governed by the Landau-Lifshitz-Gilbert (LLG) equation, which can lead to complex phenomena, including the formation, motion, and detachment of singularities in the magnetization texture. However, in this study, we provide a simplified estimate of the DW velocity by assuming the domain wall maintains a fixed shape during motion.

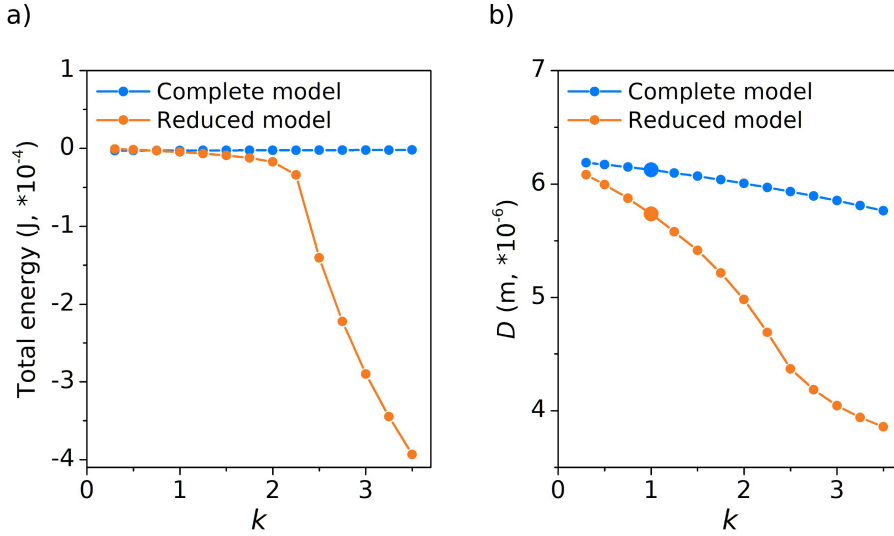


FIG. 5. (a) Total energy as a function of anisotropy value at the periphery  $k$  for the cases of complete and reduced models. (b) Value of the dissipation  $D$  as a function of anisotropy value at the periphery  $k$ .

Under the assumption that only the DW position changes while all internal degrees of freedom remain fixed, the LLG equation reduces to the Thiele equation [17]. Let the domain wall be described by a traveling ansatz of the form:

$$\mathbf{S}(\mathbf{r}, t) = \mathbf{S}_0(\mathbf{r} - R(t)\mathbf{e}^z),$$

where  $\mathbf{S}_0$  is the static DW profile,  $R$  is the DW position at time  $t$ . Substituting this ansatz into the LLG equation and projecting onto the subspace spanned by  $\partial\mathbf{S}/\partial R$ , we obtain the Thiele equation in the general form [18]:

$$\alpha DV - GV = F,$$

where  $V = \dot{R}$  is the DW velocity,  $\alpha$  is the Gilbert damping parameter,  $D$  is the dissipation matrix,  $G$  is the gyrotropic tensor, and  $F$  is the net force (or generalized torque) acting on the wall. In our case, the DW position is described by a single parameter  $R$ , and the gyrotropic term  $G$  vanishes due to the antisymmetry of the gyrotropic tensor and the absence of azimuthal precession in the ansatz. The dissipation reduces to a scalar quantity given by:

$$D = \int_{\Omega} \left( \frac{\partial \mathbf{S}}{\partial z} \right)^2 dV,$$

which corresponds to the portion of the exchange energy associated with deformations along the wire axis. The driving force  $F$  is given by derivative of total energy  $E$  with respect to the DW position:

$$F = -\frac{\partial E}{\partial R} = 2M_s H s,$$

where  $s$  is the cross-sectional area of the wire. This result follows from translational symmetry: shifting the DW by  $dR$  effectively reverses the magnetization in a volume  $s \cdot dR$ , yielding a change in Zeeman energy proportional to  $H$ . Assuming the DW shape remains unchanged during motion, the force  $F$  becomes independent of position, and the DW velocity simplifies to:

$$V = \frac{F}{\alpha D} \sim \frac{1}{D}.$$

We computed the dissipation coefficient  $D$  for both the reduced (1-axis) and complete (3-axis) anisotropy models across a range of surface anisotropy strengths. The results are presented in Fig. 5b. Under the considered parameters, the domain wall in the complete model moves approximately 1.5 times slower than in the reduced model, due to higher dissipation. This implies that simulations based on the simplified reduced model are likely to overestimate DW velocity. The discrepancy becomes even more pronounced at higher anisotropy strengths.

## 5. Conclusion

We studied the structure of transverse domain walls (DWs) in amorphous, stress-induced magnetic wires using two models of magnetoelastic anisotropy: the complete model, which accounts for all stress components throughout the wire volume, and the reduced model, which includes only the dominant stress component, converted into anisotropy. While both models yield domain walls of the same general type, their internal structures differ significantly.

In the reduced model, deviations of the magnetization near the wire surface are more pronounced, and these disturbances penetrate deeper into the wire compared to the complete model. An analysis of how the DW structure evolves with

increasing anisotropy at the periphery reveals that the complete model better preserves the transverse character of the DW over a wider range of anisotropy strengths.

Notably, the omission of circumferential anisotropy in the reduced model may lead to an underestimation of the domain wall's interaction with defects and impurities. At the same time, it tends to overestimate the DW velocity, due to lower calculated dissipation in the system.

## References

- [1] Bukharaev A.A., Zvezdin A.K., Pyatakov A.P., Fetisov Y.K. Straintronics: a new trend in micro- and nanoelectronics and materials science. *Physics-Uspeski*, 2018, **61**(12), P. 1175.
- [2] Bandyopadhyay S., Atulasimha J., and Barman A. Straintronics: Manipulating the Magnetization of Magnetostrictive Nanomagnets with Strain for Energy-Efficient Applications. *Applied Physics Reviews*, 2021, **8**, P. 041323.
- [3] Pyatakov A., Zvezdin A. Magnetolectric and multiferroic media. *Physics-Uspeski*, 2012, **55**(6), P. 557–581.
- [4] Alam J., et.al. Cylindrical micro and nanowires: Fabrication, properties and applications. *J. Magn. Magn. Mater.*, 2020, **513**, P. 167074.
- [5] Chiriac H., Corodeanu S., Lostun M., Stoian G., Ababei G., and Óvári T.A. Rapidly solidified amorphous nanowires. *J. Appl. Phys.*, 2011. **109**(6), P. 063902.
- [6] Baranov S.A., Larin V.S., Torcunov A.V., Technology, Preparation and Properties of the Cast Glass-Coated Magnetic Microwires. *Crystals*, 2017. **7**(136).
- [7] Chiriac H., Ovari T.A. and Pop Gh. Internal stress distribution in glass-covered amorphous magnetic wires. *Phys. Rev. B*, 1995, **42**, P. 10104.
- [8] Liu K., Lu Z., Liu T., Li D. Measurement of internal tensile stress in  $\text{Co}_{68.2}\text{Fe}_{4.3}\text{Cr}_{3.5}\text{Si}_{13}\text{B}_{11}$  glass-coated amorphous microwires using the stress sensitivity of saturation magnetostriction. *J. Magn. Magn. Mater.*, 2013. **339**, P. 124–126.
- [9] Chiriac H., Ovari T.-A., Switching field calculations in amorphous microwires with positive magnetostriction. *J. Magn. Magn. Mater.*, 2002, **249**, P. 141–145.
- [10] Churyukanova M., Semenkov V., Kaloshkin S., Shuvaeva E., Gudoshnikov S., Zhukova V., and Zhukov A., Magnetostriction investigation of soft magnetic microwires. *Phys. Stat. Sol. (a)*, 2016, **213**(2), P. 363–367.
- [11] Aksenova O.I., Orlova N., Churyukanova M.N., Aronin A.S. Stress state effect on the magnetic properties of amorphous microwires. *J. Magn. Magn. Mater.*, 2020, **495**, P. 165878.
- [12] Nematov M.G., Baraban I., Yudanov N.A., Rodionova V., Qin F.X., Peng H.-X., Panina L.V., Evolution of the magnetic anisotropy and magnetostriction in Cobased amorphous alloys microwires due to current annealing and stress-sensory applications. *J. Alloys. Compd.*, 2020, **837**, P. 155584.
- [13] Chiriac H., Ovari T.-A., Zhukov A. Magnetoelastic anisotropy of amorphous microwires. *J. Magn. Magn. Mater.*, 2003, **496**, P. 254–255.
- [14] Zhukova V., Blanco J.M., Ipatov M., Zhukov A. Magnetoelastic contribution in domain wall dynamics of amorphous microwires. *Physica B*, 2012, **407**, P. 1450–1454.
- [15] Chichay K.A., Lobanov I.S. Uzdin V.M. Stability and transformations of domain walls in cylindrical wires. *Nanosystems: Phys. Chem. Math.*, 2024, **15**(3), P. 332–339.
- [16] Chichay K.A., Lobanov I.S., Uzdin V.M. The structure of magnetic domain walls in cylindrical nano- and microwires with in- homogeneous anisotropy. *Nanosystems: Phys. Chem. Math.*, 2023, **15**(1), P. 55–59.
- [17] Thiele A.A. Steady-state motion of magnetic domains. *Phys. Rev. Lett.*, 1973, **30**, P. 230–233.
- [18] Lobanov I.S., Uzdin V.M. Dynamics of "Breathing" Skyrmions. *JETP Letters*, 2024, **119**(10), P. 768–774.

---

*Submitted 6 April 2025; revised 6 May 2025; accepted 7 May 2025*

### Information about the authors:

*Ksenia A. Chichay* – Department of Physics, ITMO University, St. Petersburg, 197101, Russia; ORCID 0000-0002-6921-6075; ks.chichay@gmail.com

*Igor S. Lobanov* – Department of Physics, ITMO University, St. Petersburg, 197101, Russia; ORCID 0000-0001-8789-3267; lobanov.igor@gmail.com

*Valery M. Uzdin* – Department of Physics, ITMO University, St. Petersburg, 197101, Russia; ORCID 0000-0002-9505-0996; v.uzdin@mail.ru

*Conflict of interest:* the authors declare no conflict of interest.

## Sub-Poissonian light in fluctuating thermal-loss bosonic channels

Iliia Stepanov<sup>1,a</sup>, Roman Goncharov<sup>1,2,3,b</sup>, Alexei D. Kiselev<sup>2,4,c</sup><sup>1</sup>Quantum Information Laboratory, ITMO University, Saint Petersburg, Russia<sup>2</sup>Laboratory for Quantum Communications, ITMO University, Saint Petersburg, Russia<sup>3</sup>SMARTS-Quanttelecom LLC, Saint Petersburg, Russia<sup>4</sup>Laboratory of Quantum Processes and Measurements, ITMO University, Saint Petersburg, Russia<sup>a</sup>[i.stepanov@itmo.ru](mailto:i.stepanov@itmo.ru), <sup>b</sup>[rkgoncharov@itmo.ru](mailto:rkgoncharov@itmo.ru), <sup>c</sup>[adkiselev@itmo.ru](mailto:adkiselev@itmo.ru)Corresponding author: I. Stepanov, [i.stepanov@itmo.ru](mailto:i.stepanov@itmo.ru)

**ABSTRACT** We study the photon statistics of a single-mode sub-Poissonian light propagating in the lossy thermal bosonic channel with fluctuating transmittance which can be regarded as a temperature-dependent model of the turbulent atmosphere. By assuming that the variance of the transmittance can be expressed in terms of the fluctuation strength parameter we show that the photon statistics of the light remains sub-Poissonian provided the averaged transmittance exceeds its critical value. The critical transmittance is analytically computed as a function of the input states' parameters, temperature, and the fluctuation strength. The results are applied to study special cases of the one-mode squeezed states and the odd optical Schrödinger cats.

**KEYWORDS** Sub-Poissonian light; fluctuations; bosonic channel

**ACKNOWLEDGEMENTS** This work was supported by the Russian Science Foundation (project No. 24–29–00786).

**FOR CITATION** Stepanov I., Goncharov R., Kiselev A.D. Sub-Poissonian light in fluctuating thermal-loss bosonic channels. *Nanosystems: Phys. Chem. Math.*, 2025, **16** (3), 333–342.

### 1. Introduction

The nonclassical properties of optical fields lie at the heart of quantum optics and, from its very beginning, they have been the subject of numerous intense studies. There are a number of indicators introduced to measure the quantumness (nonclassicality) of light such as negativity of the Wigner function [1], squeezing [2, 3] and sub-Poissonian statistics [4] (see also a recent review on quantumness quantifiers based on Husimi quasiprobability [5]).

Note that, for the squeezing and the sub-Poissonian statistics, the indicators are formulated in terms of second-order moments of fluctuations of the experimentally measured quantities. For nonclassical fields, these moments violate certain inequalities. For example, the sub-Poissonian light is indicated when the Fano factor, defined as the ratio of the photon number variance and the mean photon number, is less than unity.

Aside from its fundamental importance, light nonclassicality plays a vital role in quantum metrology [6]. For sub-Poissonian fields that will be our primary concern, there are various experimental techniques used to generate sub-Poissonian light [7–11] and their applications in quantum imaging are reviewed in [12] (higher-order sub-Poissonian statistics is discussed in [13, 14]). Security analysis of BB84 protocol with sub-Poissonian light sources was performed in [15]. Influence of temporal filtering of sub-Poissonian single-photon pulses on the expected secret key fraction, the quantum bit error ratio, and the tolerable channel losses is analyzed in [16].

It is well known that continuous variable quantum states of non-classical light used in quantum metrology and quantum communication protocols [17, 18] are subject to loss and added noise, leading to degradation of non-classicality and quantum correlations.

For free-space communication links [19–22], a widely used general theoretical approach to modeling environment-induced decoherence effects is based on Gaussian quantum channels with fluctuating parameters. Specifically, a pure-loss channel with fluctuating transmittance exemplifies a popular model that describes the propagation of quantum light in a turbulent atmosphere (see a review on propagation of classical electromagnetic waves through a turbulent atmosphere [23]).

This model has been extensively used to study nonclassical properties and quantum correlations of light propagating in turbulent atmospheres [24–27]. In Ref. [28], Bell inequalities in turbulent atmospheric channels are explored using the probability distribution of transmittance (PDT) in the elliptic-beam approximation with parameters suitable for the weak to moderate-turbulence channels [29]. Gaussian entanglement in turbulent atmosphere and a protocol that enables entanglement transfer over arbitrary distances [30, 31]. The evolution of higher-order non-classicality and entanglement criteria in atmospheric fluctuating-loss channels are investigated in [32]. Theory of the classical effects associated with

geometrical features of light propagation, such as beam wandering, widening, and deflection, is developed in [33, 34]. In Ref. [35], the PDT derived by numerical simulations is compared with the analytical results.

In this paper, we adapt a generalized model of the channel and use the thermal-loss channel with fluctuating transmittance to examine how the temperature effects combined with the fluctuating losses influence the sub-Poissonian light.

The paper is structured as follows. In Sec. 2 we describe a thermal-loss channel and the parameters expressed in terms of the first-order and second-order moments of the photon number used to identify sub-Poissonian light fields. In particular, we deduce the input-output relation for the  $q$ -parameter introduced as an unnormalized version of the Mandel  $Q$ -parameter. In Sec. 3 this relation is generalized to the case of the thermal-loss channel with fluctuating transmittance. After parameterization of the transmittance variance, it is shown that the output light will be sub-Poissonian only if the average transmittance exceeds its critical value. In Sec. 4 we apply the theoretical results to the special cases of squeezed states, odd optical cats and Fock states and study how the critical transmittance depends on the temperature and the strength of transmittance fluctuations. Finally, concluding remarks are given in Sec. 5.

## 2. Channel and moments

We consider a single-mode quantized light with the annihilation and creation operators,  $\hat{a}$  and  $\hat{a}^\dagger$ , propagating through a quantum Gaussian channel. The simplest and widely used method to describe the channel is to introduce an additional bosonic mode representing the degree of freedom of the environment and assume that the interaction between the light and noise modes is determined by the channel unitary  $\hat{U}_\tau$  giving the beam splitter transformation of the form:

$$\hat{U}_\tau^\dagger \hat{a} \hat{U}_\tau \equiv \hat{a}_\tau = \sqrt{\tau} \hat{a} + \sqrt{1-\tau} \hat{b}, \quad (1)$$

where  $\tau$  is the channel transmittance and  $\hat{b}$  is the annihilation operator of the noise mode.

For the temperature loss channel, the input state of the bipartite system is the product of the density matrices given by

$$\hat{\rho} = \hat{\rho}_{\text{in}} \otimes \hat{\rho}_{\text{th}}, \quad (2)$$

where  $\hat{\rho}_{\text{in}}$  is the density matrix of radiation

$$\hat{\rho}_{\text{in}} = |\psi_{\text{in}}\rangle\langle\psi_{\text{in}}| \quad (3)$$

prepared in the pure state  $|\psi_{\text{in}}\rangle$ , whereas the environment is in the thermal state

$$\rho_{\text{th}} = \frac{1}{n_{\text{th}} + 1} \sum_{n=0}^{\infty} e^{-n\beta\hbar\omega} |n\rangle\langle n|, \quad n_{\text{th}} = \text{Tr}\{\hat{b}^\dagger \hat{b} \rho_{\text{th}}\} = \frac{1}{e^{\beta\hbar\omega} - 1}. \quad (4)$$

where  $\beta = 1/(k_B T)$  is the inverse temperature parameter ( $k_B$  is the Boltzmann constant and  $T$  is the temperature),  $\hbar$  is the Planck constant,  $\omega$  is the photon frequency,  $n_{\text{th}}$  is the average number of thermal photons (the mean thermal photon number).

Temporal evolution of the density matrix (2) is governed by the channel unitary (1) as follows

$$\hat{\rho}(\tau) = \hat{U}_\tau \hat{\rho} \hat{U}_\tau^\dagger. \quad (5)$$

We can now use Eqs. (1) and (5) to obtain the normally ordered characteristic function of the light as a function of the channel transmittance

$$\chi(\alpha, \tau) = \text{Tr}\{\hat{D}(\alpha) : \hat{\rho}(\tau)\} = \chi_{\text{in}}(\sqrt{\tau}\alpha) \chi_{\text{th}}(\sqrt{1-\tau}\alpha), \quad (6)$$

where  $\hat{D}(\alpha) := \exp(\alpha \hat{a}^\dagger - \alpha^* \hat{a}) := \exp(\alpha \hat{a}^\dagger) \exp(-\alpha^* \hat{a})$  is the normally ordered displacement operator;  $\chi_{\text{in}}$  and  $\chi_{\text{th}}$  are the input and thermal characteristic functions given by

$$\chi_{\text{in}}(\alpha) = \text{Tr}\{\hat{D}(\alpha) : \hat{\rho}_{\text{in}}\}, \quad \chi_{\text{th}}(\alpha) = \text{Tr}\{\hat{D}(\alpha) : \hat{\rho}_{\text{th}}\} = \exp(-n_{\text{th}}|\alpha|^2). \quad (7)$$

Note that the form of this result reproduces the characteristic function derived by solving the thermal single-mode Lindblad equation (see, e.g., [36]) so that the beam splitter transformation representation (1) and the approach based on the Lindblad dynamics appear to be equivalent tools for modeling the temperature loss quantum channel.

Given the transmittance  $\tau$ , it is not difficult to find the average photon number of the output state  $n_\tau$ :

$$n_\tau = \text{Tr}\{\hat{n} \hat{\rho}(\tau)\} = \text{Tr}\{\hat{n}_\tau \hat{\rho}\} \equiv \langle \hat{n}_\tau \rangle = \tau n_{\text{in}} + (1-\tau) n_{\text{th}}, \quad (8)$$

$$n_{\text{in}} = \text{Tr}\{\hat{n} \hat{\rho}_{\text{in}}\} = \langle \psi_{\text{in}} | \hat{n} | \psi_{\text{in}} \rangle, \quad (9)$$

where  $\hat{n} = \hat{a}^\dagger \hat{a}$  and  $\hat{n}_\tau = \hat{a}_\tau^\dagger \hat{a}_\tau$ .

Since  $\hat{n}^2 - \hat{n} = \hat{a}^\dagger \hat{a}^\dagger \hat{a} \hat{a} \equiv \hat{n}^2$ , the difference between the variance and the mean photon number for the quantum state  $\hat{\rho}(\tau)$  can be computed as the  $q$ -parameter given by

$$q_\tau = \text{Tr}\{\hat{n}^2 : \hat{\rho}(\tau)\} - n_\tau^2. \quad (10)$$

Clearly, for  $\hat{\rho}(\tau)$ , the photon statistics is sub-Poissonian if and only if the parameter (10) is negative. Note that the ratio  $q_\tau/n_\tau$  gives the well-known Mandel  $Q$ -parameter [37],  $Q_\tau^{(M)}$ , introduced in Refs. [38, 39]. Note that the  $Q$ -parameter

is also related to the normalized second-order correlation function  $g_\tau^{(2)}(0) = Q_\tau^{(M)}/n_\tau + 1$  and the Fano factor  $F_\tau = Q_\tau^{(M)} + 1$ .

We can now use the relation

$$\langle : \hat{n}_\tau^2 : \rangle = \tau^2 \langle : \hat{n}^2 : \rangle + 2(1 - \tau)^2 n_{\text{th}}^2 + 4\tau(1 - \tau)n_{\text{in}}n_{\text{th}} \quad (11)$$

derived with the help of the identity  $\langle \hat{b}^\dagger \hat{b}^\dagger \hat{b} \hat{b} \rangle = 2n_{\text{th}}^2$  to deduce the explicit expression for the parameter (10)

$$q_\tau = \langle : \hat{n}_\tau^2 : \rangle - n_\tau^2 = \tau^2 q_{\text{in}} + (1 - \tau)^2 n_{\text{th}}^2 + 2\tau(1 - \tau)n_{\text{in}}n_{\text{th}}, \quad (12)$$

where

$$q_{\text{in}} = \text{Tr}\{ : \hat{n}^2 : \rho_{\text{in}} \} - n_{\text{in}}^2 = \langle : \hat{n}^2 : \rangle - n_{\text{in}}^2. \quad (13)$$

In the zero-temperature limit with  $n_{\text{th}} = 0$ , formula (12) shows that losses cannot destroy the sub-Poissonian statistics of input light. The latter is generally no longer the case at non-zero temperatures. In the subsequent section, we will discuss the conditions for negativity of the parameter  $q_\tau$ .

### 3. Fluctuating losses and critical transmittance

Now we extend the results of the preceding section to the case where the transmittance fluctuates and thus should be treated as a random variable. In this case, the output density matrix takes the generalized form:

$$\hat{\rho}_{\text{out}} = \int_0^1 P(\tau) \hat{\rho}(\tau) d\tau, \quad (14)$$

where  $P(\tau)$  is the probability density function (PDF) of the transmittance. We can use Eqs. (8) and (5) with  $\hat{\rho}(\tau)$  replaced by  $\hat{\rho}_{\text{out}}$  to introduce the output parameter  $q_{\text{out}}$  as follows

$$q_{\text{out}} = \text{Tr}\{ : \hat{n}^2 : \hat{\rho}_{\text{out}} \} - \text{Tr}\{ \hat{n} \hat{\rho}_{\text{out}} \}^2 = \langle \langle : \hat{n}_\tau^2 : \rangle \rangle_\tau - \langle n_\tau \rangle_\tau^2 = \langle q_\tau \rangle_\tau + [\langle n_\tau^2 \rangle_\tau - \langle n_\tau \rangle_\tau^2], \quad (15)$$

where  $\langle \dots \rangle_\tau = \int_0^1 \dots P(\tau) d\tau$ . After substituting formulas (8) and (10) into Eq. (15), we obtain the parameter  $q_{\text{out}}$  in the following explicit form:

$$q_{\text{out}} = \bar{\tau}^2 (q_{\text{in}} - n_{\text{in}}^2) + (\bar{\tau}n_{\text{in}} + (1 - \bar{\tau})n_{\text{th}})^2 + \text{Var}(\tau) \{ q_{\text{in}} - n_{\text{in}}^2 + 2(n_{\text{in}} - n_{\text{th}})^2 \}, \quad (16)$$

where  $\bar{\tau} = \langle \tau \rangle_\tau$  is the averaged transmittance and  $\text{Var}(\tau) = \langle \tau^2 \rangle_\tau - \bar{\tau}^2$  is the variance of the transmittance.

Since the transmittance varies from zero to unity,  $0 \leq \tau \leq 1$ , and the variance  $\text{Var}(\tau)$  cannot be negative,  $\text{Var}(\tau) \geq 0$ , the mean of the squared transmittance cannot exceed the average transmittance and must satisfy the condition:  $\bar{\tau}^2 \leq \langle \tau^2 \rangle_\tau \leq \bar{\tau}$ . As a result, the variance is bounded from above by the product  $(1 - \bar{\tau})\bar{\tau}$ :  $0 \leq \text{Var}(\tau) \leq (1 - \bar{\tau})\bar{\tau}$ . In our model, we assume that  $\langle \tau^2 \rangle_\tau = F\bar{\tau} + (1 - F)\bar{\tau}^2$ , so that the variance takes the following form

$$\text{Var}(\tau) = \langle \tau^2 \rangle_\tau - \bar{\tau}^2 = F(1 - \bar{\tau})\bar{\tau} \quad (17)$$

where  $0 \leq F \leq 1$  is the parameter characterizing the strength of fluctuations.

In what follows, we shall treat the fluctuation strength  $F$  as a phenomenological parameter which is independent of  $\bar{\tau}$ . The variance representation (17) can now be used to express the  $q$ -parameter (16) in terms of  $\bar{\tau}$  as follows

$$q_{\text{out}}(\bar{\tau}) = \bar{\tau}^2 (q_{\text{in}} - a) + \bar{\tau}(a - n_{\text{th}}^2) + n_{\text{th}}^2, \quad (18)$$

where

$$a = 2n_{\text{in}}n_{\text{th}} - n_{\text{th}}^2 + gF, \quad g = q_{\text{in}} - n_{\text{in}}^2 + 2(n_{\text{in}} - n_{\text{th}})^2. \quad (19)$$

In the limiting case of transparent medium described by the identity channel with  $\bar{\tau} = 1$ , the  $q$ -parameter is equal to its initial value  $q_{\text{in}}$  given by Eq. (13). For sub-Poissonian light, the parameter  $q_{\text{in}}$  is negative, so that  $q_{\text{out}}(1) = q_{\text{in}} < 0$ . In the opposite case with vanishing transmittance,  $\bar{\tau} = 0$ , from Eq. (18), the  $q$ -parameter is positive,  $q_{\text{out}}(0) = n_{\text{th}}^2 > 0$ . Clearly, this implies that the transmitted light will remain sub-Poissonian provided the average transmittance exceeds its critical value:  $\bar{\tau} > \tau_c$ .

From Eq. (18), it is not difficult to find the analytical expression for the critical transmittance (the transmittance threshold). So, we deduce the inequality

$$\bar{\tau} > \tau_c = - \frac{(a - n_{\text{th}}^2) + \sqrt{(a - n_{\text{th}}^2)^2 - 4n_{\text{th}}^2 q_{\text{in}}}}{2(q_{\text{in}} - a)} \quad (20)$$

giving the condition that effects of transmittance fluctuations and temperature fail to destroy the sub-Poissonian statistics of light and the  $q$ -parameter of the transmitted (output) light is negative,  $q_{\text{out}} < 0$ .

We conclude this section with the remark on two important special cases with  $T = 0$  and  $F = 0$ , respectively. In the zero-temperature limit, the expression of the transmittance threshold is simplified as follows

$$\tau_c|_{T=0} = \frac{F(q_{in} + n_{in}^2)}{F(q_{in} + n_{in}^2) - q_{in}}, \tag{21}$$

whereas the critical transmittance for the case, where fluctuations of the transmittance are negligible, is given by

$$\tau_c|_{F=0} = \frac{n_{th}}{n_{th} + \sqrt{n_{in}^2 - q_{in} - n_{in}}}. \tag{22}$$

Clearly, when  $F$  and  $T$  are both vanishing, the critical transmittance is zero. This is the well-known case of non-fluctuating pure-loss bosonic channel where  $q_{out} = \tau^2 q_{in}$  (see Eq. (12) with  $n_{th} = 0$ ).

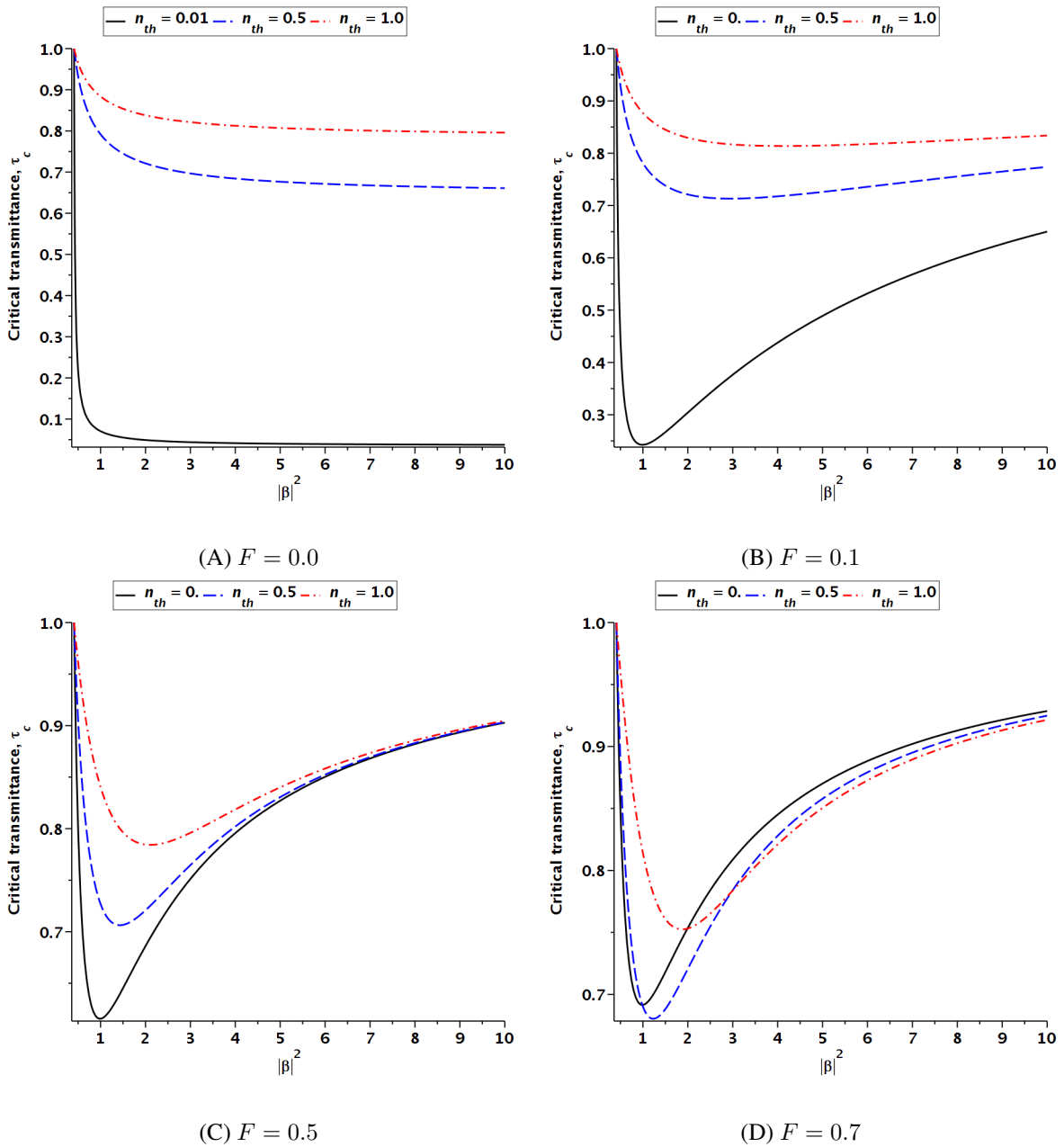


FIG. 1. Dependence of the critical transmittance  $\tau_c$  on the square of the displacement amplitude,  $|\beta|^2$ , for the squeezed state (23) computed at different values of the fluctuation strength parameter  $F$  for  $r = 0.4$  and  $\phi = \pi/2$

#### 4. Effects of fluctuations and temperature

In this section, we apply our analytical results to the two special cases of input states: the displaced squeezed states and the odd Schrödinger cat states. More specifically, we shall study how the temperature and transmittance fluctuations influence the transmittance threshold for these states.

##### 4.1. Squeezed light

The density matrix

$$\hat{\rho}_{\text{in}} = |\psi_{\text{sq}}\rangle\langle\psi_{\text{sq}}|, \quad |\psi_{\text{sq}}\rangle = \hat{D}(\beta)\hat{S}(\xi)|0\rangle \quad (23)$$

describes the case of displaced squeezed vacuum states expressed using the squeezing operator,  $\hat{S}(\xi)$ , and the displacement operator,  $\hat{D}(\beta)$ , given by

$$\hat{S}(\xi) = e^{(\xi(\hat{a}^\dagger)^2 - \xi^* \hat{a}^2)/2}, \quad \hat{D}(\beta) = e^{\beta \hat{a}^\dagger - \beta^* \hat{a}}, \quad (24)$$

$\xi = r e^{i\psi}$  is the squeezing parameter and  $\beta = |\beta| e^{i\theta}$  is the displacement. For the squeezed state (23), it is rather straightforward to derive the expressions for the parameters  $n_{\text{in}} = n_{\text{sq}}$  and  $q_{\text{in}} = q_{\text{sq}}$  that enter the expression for the critical transmittance (20):

$$n_{\text{sq}} = |\beta|^2 + \sinh^2 r, \quad q_{\text{sq}} = q_2 |\beta|^2 + \sinh^2 r \cosh 2r, \quad (25)$$

where  $q_2 = 2 \sinh^2 r + \sinh 2r \cos(2\phi)$  and  $\phi = \theta - \psi/2$ .

From formula (25), the case where the photon statistics of the squeezed light is sub-Poissonian with negative parameter  $q_{\text{sq}}$  may occur only when the coefficient  $q_2$  is negative. The latter requires the angle  $\phi$  and the squeezing parameter  $r$  to meet the inequality

$$|\tan \phi| > e^r, \quad (26)$$

so that the squeezed light will be sub-Poissonian only when the squared displacement amplitude is above its critical value:

$$|\beta|^2 > \frac{e^r \sinh r \cosh 2r}{2(\sin^2 \phi - e^{2r} \cos^2 \phi)} \equiv \beta_c^2. \quad (27)$$

Clearly, when  $\cos \phi = 0$ , the condition (26) is always fulfilled and  $\beta_c$  takes the minimal value that grows with  $r$ .

In Figs. 1 and 2, the threshold transmittance is plotted against the squared displacement amplitude,  $|\beta|^2$ , at  $\phi = \pi/2$ . The numerical results for  $\tau_c$  are evaluated using Eq. (20) with formula (25) giving the mean photon number  $n_{\text{in}}$  and the  $q$ -parameter  $q_{\text{in}}$ .

At  $|\beta| = \beta_c$ , the  $q$ -parameter vanishes, and thus the threshold transmittance equals unity. So, in the close vicinity of  $\beta_c$ , the transmittance  $\tau_c$  drops as  $|\beta|^2$  increases.

From Eq. (22), it is not difficult to show that, when fluctuations are negligible,  $\tau_c$  monotonically decreases with  $|\beta|^2$  approaching the value  $n_{\text{th}}/(n_{\text{th}} - q_2/2)$  (see Fig. 1a). By contrast, from the relation (21) describing the zero-temperature case, in the large displacement limit, the critical transmittance approaches unity. As a result, the  $|\beta|^2$ -dependence of  $\tau_c$  reveals nonmonotonic behaviour illustrated in Fig. 2a. It can also be seen that such behaviour where the critical transmittance exhibits a local minimum occurs at non-vanishing temperatures provided  $F \neq 0$ .

Normally, it is expected that the threshold will get higher at elevated temperatures. This is the case for the curves shown in Figs. 1a–1c.

Interestingly, in the case of intense fluctuations with sufficiently high values of fluctuation strength, the latter is no longer the case. From Figure 1 which shows the  $\tau_c$ -vs- $|\beta|^2$  curves computed at  $F = 0.7$ , it is seen that the long displacement part of the zero-temperature curve appears to be above the curves with non-zero  $n_{\text{th}}$ .

Similarly, the threshold is expected to increase with the fluctuation strength  $F$ . It is not difficult to show that the threshold  $\tau_c$  grows with  $F$  only if the coefficient  $g$  given by Eq. (19) is positive. According to formula (19), this coefficient quadratically depends on  $n_{\text{th}}$  and it takes negative values within the interval:

$$n_- < n_{\text{th}} < n_+, \quad n_{\pm} = n_{\text{in}} \pm \sqrt{\frac{n_{\text{in}}^2 - q_{\text{in}}}{2}}. \quad (28)$$

So, in the low temperature region where  $n_{\text{th}} < n_-$  the critical transmittance is an increasing function of the fluctuation strength. The curves presented in Figs. 2a–2b provide support to this conclusion.

For the cases of elevated temperatures illustrated in Figs. 2c–2d, the short displacement part of the curves where  $n_{\text{th}}$  meets the condition (28) is arranged differently. In this part, the curve with negligibly small fluctuations determines the largest value of  $\tau_c$ . Note that all the curves shown in Figs. 2c–2d intersect at the point where the coefficient  $g$  vanishes with  $n_{\text{th}} = n_-$ .

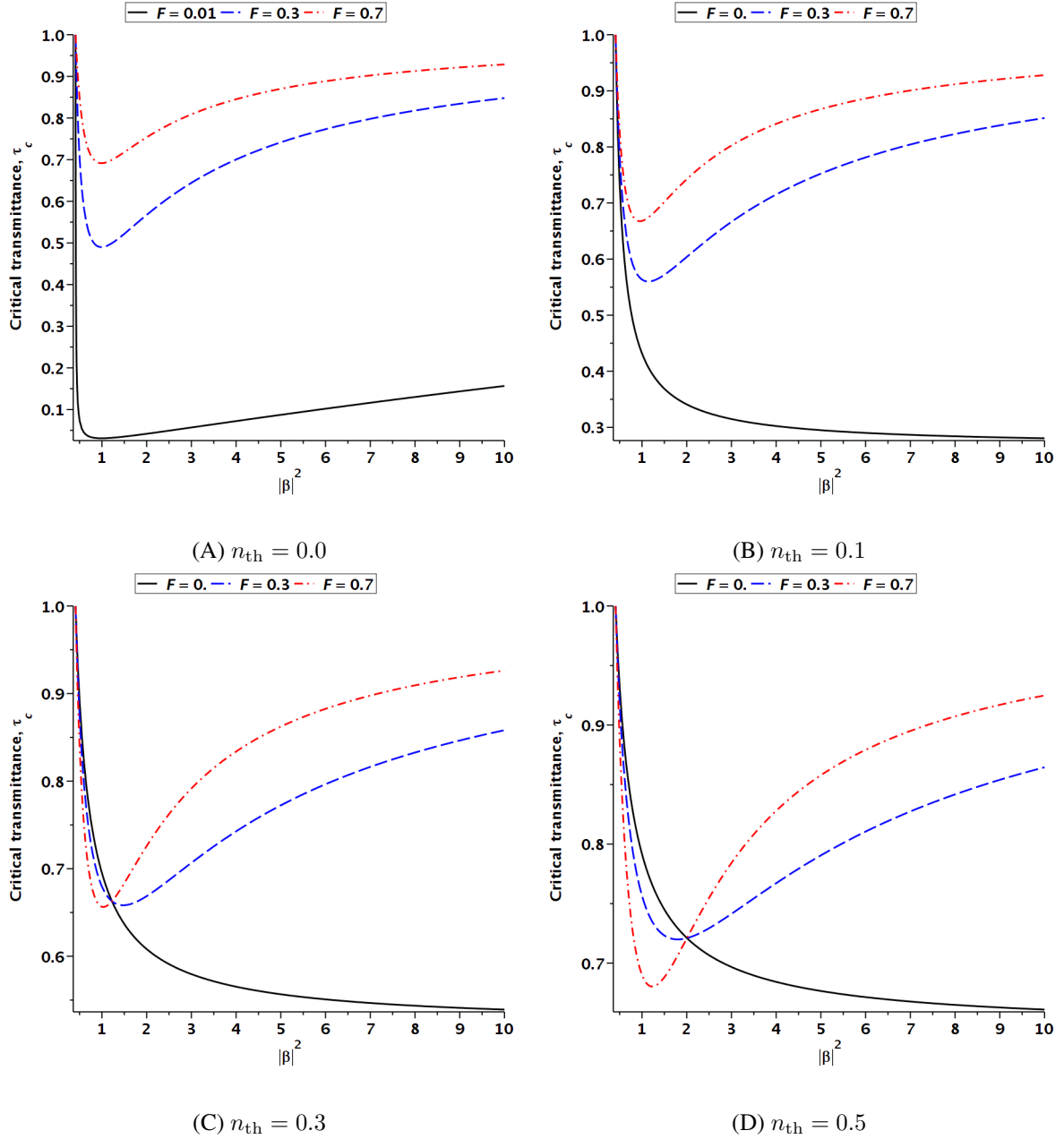


FIG. 2. Dependence of the critical transmittance  $\tau_c$  on the square of the displacement amplitude,  $|\beta|^2$ , for the squeezed state (23) with  $r = 0.4$  and  $\phi = \pi/2$  computed at different values of the mean thermal photon number  $n_{th}$

#### 4.2. Odd optical cats

Similar to the case of squeezed states, formulas

$$\hat{\rho}_{in} = |\psi_{cat}\rangle\langle\psi_{cat}|, \quad |\psi_{cat}\rangle = \frac{1}{\sqrt{2(1 - e^{-2|\beta|^2})}}(|\beta\rangle - |-\beta\rangle), \quad (29)$$

$$n_{cat} = |\tilde{\beta}|^2 \cosh |\beta|^2, \quad q_{cat} = -|\tilde{\beta}|^4, \quad (30)$$

where  $|\tilde{\beta}|^2 = \frac{|\beta|^2}{\sinh |\beta|^2}$ , present the analytical results needed to evaluate the critical transmittance for the odd (antisymmetric) cat states,  $|\psi_{cat}\rangle$ .

In Fig. 3 we show how the fluctuation strength affects the  $|\beta|^2$ -dependencies of the critical transmittance at different temperatures. From Eq. (22), in the weak fluctuation limit with  $F = 0$  (see Fig. 3a), the starting value of  $\tau_c$  is  $n_{th}/(n_{th} + \sqrt{2}-1)$  and it monotonically increases approaching unity. By contrast to the case of the squeezed states, for the odd optical cats, all the curves shown in Figs. 3 and 4 reveal similar behaviour. Similar to the squeezed states, it turned out that, at

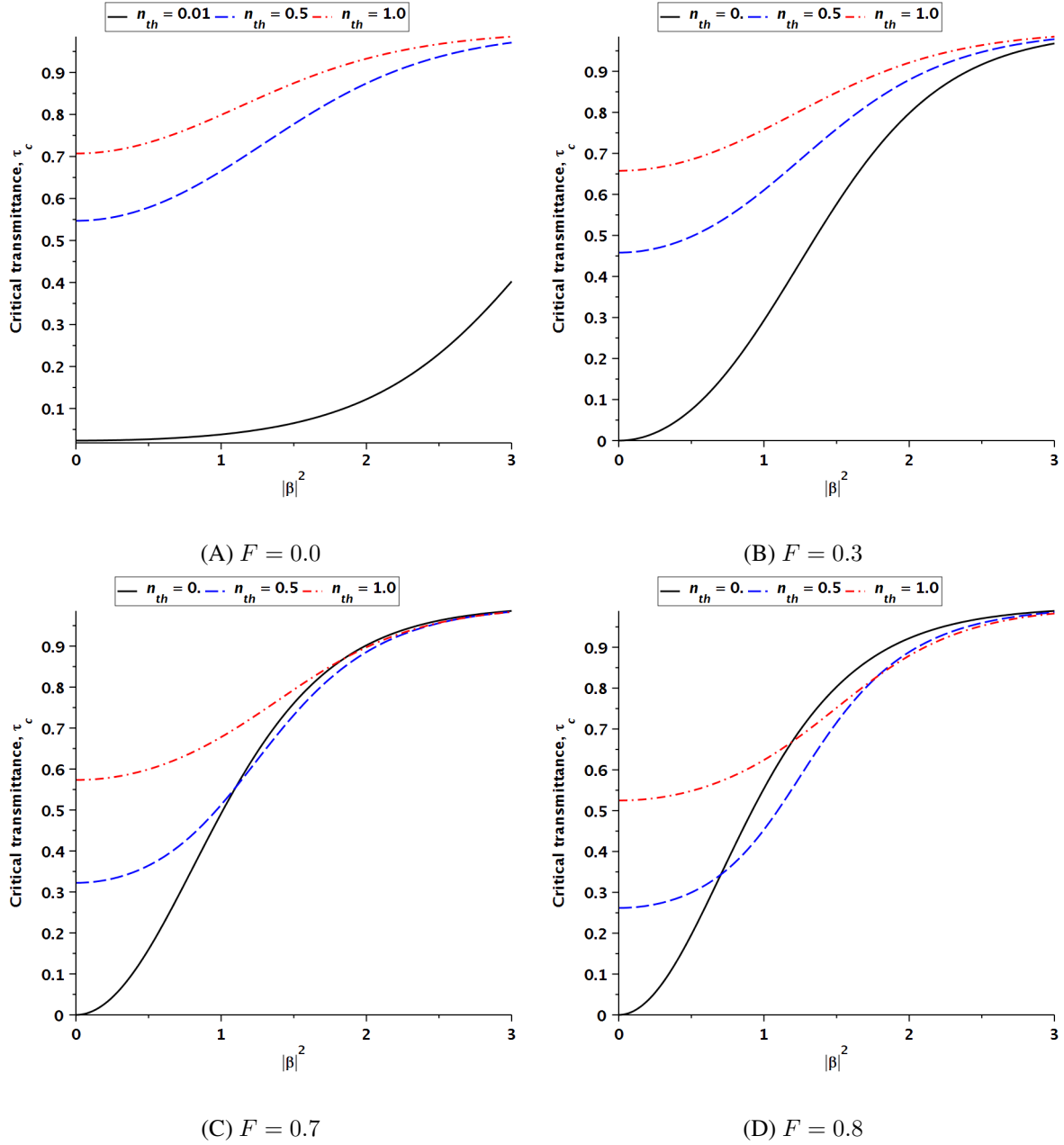


FIG. 3. Dependence of the critical transmittance  $\tau_c$  on the square of the displacement amplitude,  $|\beta|^2$ , for the odd cat state (29) computed at different values of the fluctuation strength parameter  $F$

sufficiently strong fluctuations (sufficiently large fluctuation strength  $F$ ) and sufficiently large  $|\beta|^2$ , the zero-temperature curve gives the largest value of  $\tau_c$ .

Figure 4 presents the graphs illustrating the temperature induced effects. Since, in the limiting case of a single photon state with  $\beta = 0$ , the mean photon number  $n_{cat}$  is unity and  $q_{cat} = -1$ , all the zero-temperature curves described by Eq. (21) start from zero (see Fig. 4a). As is depicted in Figs. 4b and 4c, at non-vanishing temperatures and sufficiently small  $|\beta|$ , the values of  $\tau_c$  are dominated by the zero-fluctuation curve with  $F = 0$  (for the single photon state, the zero-fluctuation value of  $\tau_c$  is  $n_{th}/(n_{th} + \sqrt{2} - 1)$ ). Referring to Fig. 4d, in the high temperature region with  $n_{th} \geq 0.9$ , the latter holds for all values of  $|\beta|$ .

Since in the zero amplitude limit with  $\beta = 0$ , the odd state (29) becomes the single-photon state  $|1\rangle$ , it is instructive to briefly discuss the case of the Fock states  $|n\rangle$ . For such states, we have  $m_{in} = -n$  and  $n_{in} = n$ . So, at low temperatures with  $n_{th} < n_- = n - \sqrt{n(n+1)}/2$ , an increase in  $F$  will enhance the threshold. Interestingly, in the special case with  $n = 1$ , we have  $n_- = 0$ . As a result, all the curves in Fig. 4a start from the zero and, in Figs. 4b–4d, the thresholds at  $\beta = 0$  are below the zero-fluctuation value of  $\tau_c$ :  $n_{th}/(n_{th} + \sqrt{2} - 1)$ .

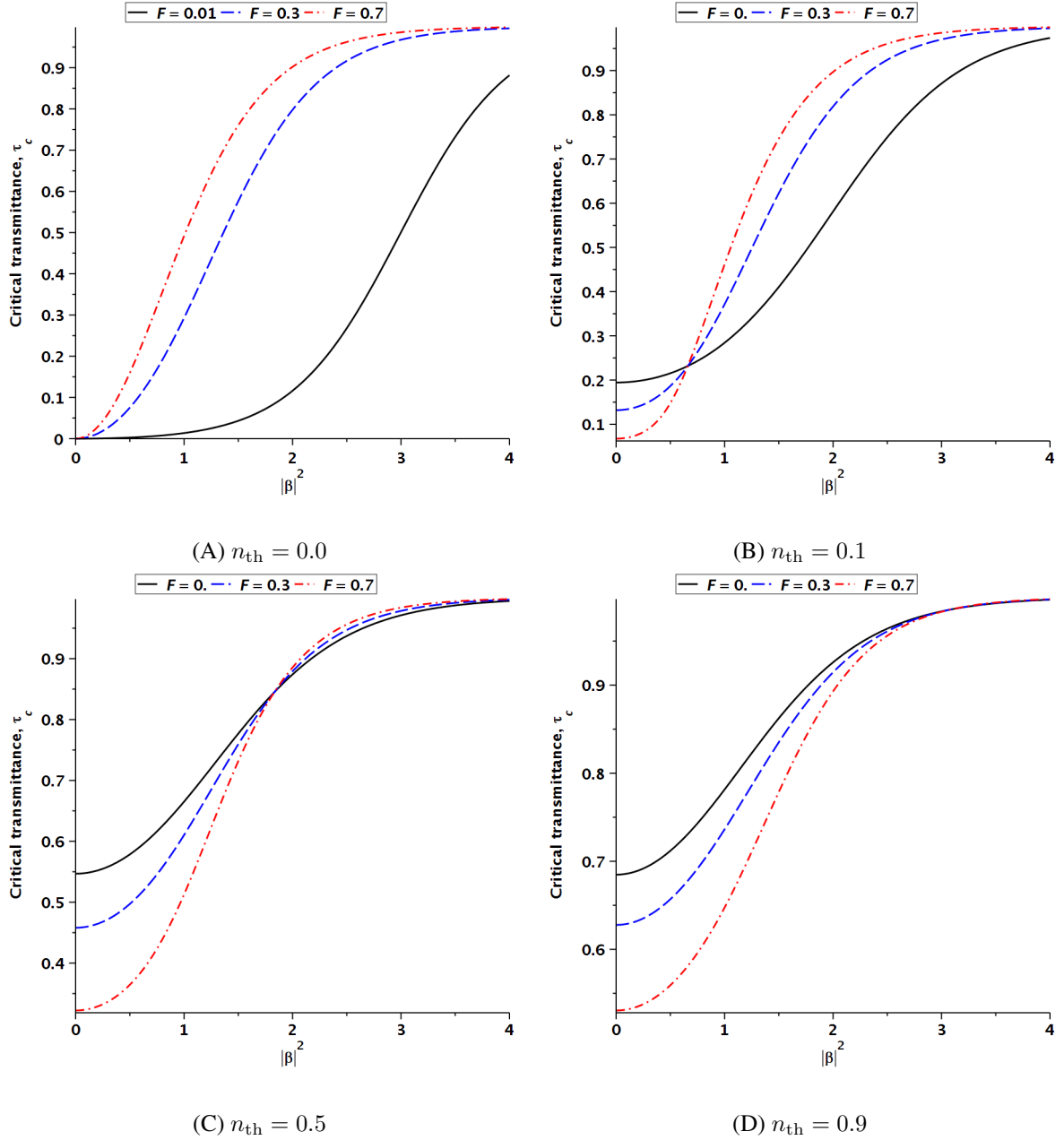


FIG. 4. Dependence of the critical transmittance  $\tau_c$  on the square of the displacement amplitude,  $|\beta|^2$ , for the odd cat state (see Eq. (29)) computed at different values of the mean thermal photon number  $n_{th}$

## 5. Conclusions

In this paper, we have studied effects of the thermal-loss channel with fluctuating transmittance on the sub-Poissonian light whose non-classicality is characterized by the  $q$ -parameter (see Eq. (10)). We have combined the input-output relation for the  $q$ -parameter (16) with the variance of the transmittance parameterized using the fluctuation strength parameter (17) to show that the condition for sub-Poissonian statistics of photon at the channel output is determined by the critical transmittance (20). For the cases of the displaced squeezed state (see Eq. (23)) and the odd optical cat state (see Eq. (29)), the critical transmittance is computed as a function of the squared displacement amplitude,  $|\beta|^2$ , at different values of temperature and the fluctuation parameter. In contrast to what is expected, under certain conditions, an increase in either the fluctuation strength or the temperature may result in a decrease in the critical transmittance.

Note that the key point greatly simplifying our analysis is the parameterization of the transmittance variance (17), where the fluctuation strength  $F$  is introduced as a phenomenological parameter which is independent of the mean transmittance  $\bar{\tau}$ . A more sophisticated treatment of the atmospheric channels [29, 33, 35] requires computing the first-order and second-order moments of the transmittance,  $\langle \tau \rangle = \bar{\tau}$  and  $\langle \tau^2 \rangle = \bar{\tau}^2$ , from the correlation functions derived using the phase approximation of the Huygens-Kirchhoff method [40, 41].

## References

- [1] Kenfack A. and Zyczkowski K. Negativity of the Wigner function as an indicator of non-classicality. *Journal of Optics B: Quantum and Semiclassical Optics*, 2004, **6**(10), P. 396.
- [2] Teich M.C. and Saleh B.E.A. Squeezed state of light. *Quantum Optics: Journal of the European Optical Society Part B*, 1989, **1**(2), P. 153–191.
- [3] Lvovsky A.I. *Squeezed Light*, ch. 5, P. 121–163. John Wiley & Sons, Ltd, 2015.
- [4] Davidovich L. Sub-Poissonian processes in quantum optics. *Rev. Mod. Phys.*, 1996, **68**, P. 127–173.
- [5] Goldberg A.Z., Klimov A.B., Grassl M., Leuchs G., and Sánchez-Soto L.L. Extremal quantum states. *AVS Quantum Science*, 2020, **2**(4), P. 044701.
- [6] Tan K.C. and Jeong H. Nonclassical light and metrological power: An introductory review. *AVS Quantum Science*, 2019, **1**(1) P. 014701.
- [7] Li R.-D., Choi S.-K., Kim C., and Kumar P. Generation of sub-Poissonian pulses of light. *Phys. Rev. A*, 1995, **51**, P. R3429–R3432.
- [8] Peřina J., Michálek V., Machulka R., and Haderka O. Two-beam light with simultaneous anticorrelations in photon-number fluctuations and sub-Poissonian statistics. *Phys. Rev. A*, 2021, **104**, P. 013712.
- [9] Iskhakov T.S., Usenko V.C., Andersen U.L., Filip R., Chekhova M.V., and Leuchs G. Heralded source of bright multi-mode mesoscopic sub-Poissonian light. *Opt. Lett.*, 2016, **41**, P. 2149–2152.
- [10] Lal N., Shajilal B., Anwar A., Perumangatt C., and Singh R.P., Observing sub-Poissonian statistics of twisted single photons using oscilloscope. *Review of Scientific Instruments*, 2019, **90**(11), P. 113104.
- [11] Samedov V.V. Discovery of sub-Poissonian statistics of light photons in scintillators that did not take place. *Physics of Atomic Nuclei*, 2019, **84**(11), P. 2048–2054.
- [12] Berchera I.R. and Degiovanni I.P. Quantum imaging with sub-Poissonian light: challenges and perspectives in optical metrology. *Metrologia*, 2019, **56**, P. 024001.
- [13] Erenso D., Vyas R., and Singh S. Higher-order sub-Poissonian photon statistics in terms of factorial moments. *J. Opt. Soc. Am. B*, 2002, **19**, P. 1471–1475.
- [14] Peřina J., Michálek V., and Haderka O. Higher-order sub-Poissonian-like nonclassical fields: Theoretical and experimental comparison. *Phys. Rev. A*, 2017, **96**, P. 033852.
- [15] Waks E., Santori C., and Yamamoto Y. Security aspects of quantum key distribution with sub-Poisson light. *Phys. Rev. A*, 2002, **66**, P. 042315.
- [16] Kupko T., M. von Helversen, Rickert L., Schulze J.-H., Strittmatter A., Gschrey M., Rodt S., Reitzenstein S., and Heindel T. Tools for the performance optimization of single-photon quantum key distribution. *npj Quantum Information*, 2020, **6**(1), P. 29.
- [17] Pirandola S., Andersen U.L., Banchi L., Berta M., Bunandar D., Colbeck R., Englund D., Gehring T., Lupo C., Ottaviani C., Pereira J.L., Razavi M., Shaari J.S., Tomamichel M., Usenko V.C., Vallone G., Villoresi P., and Wallden P., Advances in quantum cryptography. *Adv. Opt. Photon.*, 2020, **12**, P. 1012–1236.
- [18] Goncharov R.K., Kiselev A.D., Samsonov E.O., and Egorov V.I. Continuous-variable quantum key distribution: security analysis with trusted hard-ware noise against general attacks. *Nanosystems: Physics, Chemistry, Mathematics*, 2022, **13**, P. 372–391.
- [19] Peuntinger C., Heim B., Müller C.R., Gabriel C., Marquardt C., and Leuchs G. Distribution of squeezed states through an atmospheric channel. *Phys. Rev. Lett.*, 2014, **113**, P. 060502.
- [20] Heim B., Peuntinger C., Killoran N., Khan I., Wittmann C., Marquardt C., and Leuchs G. Atmospheric continuous-variable quantum communication. *New Journal of Physics*, 2014, **16**, P. 113018.
- [21] Derkach I., Usenko V.C., and Filip R. Squeezing-enhanced quantum key distribution over atmospheric channels. *New Journal of Physics*, 2020, **22**, P. 053006.
- [22] Pirandola S. Limits and security of free-space quantum communications. *Phys. Rev. Res.*, 2021, **3**, P. 013279.
- [23] Kravtsov Y.A. Propagation of electromagnetic waves through a turbulent atmosphere. *Reports on Progress in Physics*, 1992, **55**, P. 39–112.
- [24] Milonni P.W., Carter J.H., Peterson C.G., and Hughes R.J. Effects of propagation through atmospheric turbulence on photon statistics. *Journal of Optics B: Quantum and Semiclassical Optics*, 2004, **6**, P. S742.
- [25] Kiesel T., Vogel W., Parigi V., Zavatta A., and Bellini M. Experimental determination of a nonclassical Glauber-Sudarshan  $P$  function. *Phys. Rev. A*, 2008, **78**, P. 021804.
- [26] Semenov A.A. and Vogel W. Quantum light in the turbulent atmosphere. *Phys. Rev. A*, 2009, **80**, P. 021802.
- [27] Vasylyev D.Y., Semenov A.A., and Vogel W. Toward global quantum communication: Beam wandering preserves nonclassicality. *Phys. Rev. Lett.*, 2012, **108**, P. 220501.
- [28] Gumberidge M.O., Semenov A.A., Vasylyev D., and Vogel W., Bell nonlocality in the turbulent atmosphere. *Phys. Rev. A*, 2016, **94**, P. 053801.
- [29] Vasylyev D., Semenov A.A., and Vogel W. Atmospheric quantum channels with weak and strong turbulence. *Phys. Rev. Lett.*, 2016, **117**, P. 090501.
- [30] Bohmann M., Semenov A.A., Sperling J., and Vogel W. Gaussian entanglement in the turbulent atmosphere. *Phys. Rev. A*, 2016, **94**, P. 010302.
- [31] Avetisyan H. and Monken C.H. Higher order correlation beams in atmosphere under strong turbulence conditions. *Opt. Express*, 2016, **24**, P. 2318–2335.
- [32] Bohmann M., Sperling J., Semenov A.A., and Vogel W. Higher-order nonclassical effects in fluctuating-loss channels. *Phys. Rev. A*, 2017, **95**, P. 012324.
- [33] Vasylyev D., Vogel W., and Semenov A.A. Theory of atmospheric quantum channels based on the law of total probability. *Phys. Rev. A*, 2018, **97**, P. 063852.
- [34] Vasylyev D., Vogel W., and Moll F. Satellite-mediated quantum atmospheric links. *Phys. Rev. A*, 2019, **99**, P. 053830.
- [35] Klen M. and Semenov A.A. Numerical simulations of atmospheric quantum channels. *Phys. Rev. A*, 2023, **108**, P. 033718.
- [36] Kiselev A.D., Ali R., and Rybin A.V. Lindblad dynamics and disentanglement in multi-mode bosonic systems. *Entropy*, 2021, **23**(11), P. 1409.
- [37] Mandel L. and Wolf E. *Optical Coherence and Quantum Optics*. Cambridge, Cambridge University Press, 1995.
- [38] Mandel L. Sub-Poissonian photon statistics in resonance fluorescence. *Opt. Lett.*, 1979, **4**, P. 205–207.
- [39] Short R. and Mandel L. Observation of sub-Poissonian photon statistics. *Phys. Rev. Lett.*, 1983, **51**, P. 384–387.
- [40] Banakh V.A. and Mironov V.L. Phase approximation of the Huygens–Kirchhoff method in problems of laser-beam propagation in the turbulent atmosphere. *Opt. Lett.*, 1977, **1**(5), P. 172–174.
- [41] Banakh V.A. and Mironov V.L. Phase approximation of the Huygens–Kirchhoff method in problems of space-limited optical-beam propagation in turbulent atmosphere. *Opt. Lett.*, 1979, **4**(8), P. 259–261.

*Information about the authors:*

*Ilya Stepanov* – Quantum Information Laboratory, ITMO University, Kadetskaya Line, 3, St. Petersburg, 199034, Russia; i.stepanov@itmo.ru

*Roman Goncharov* – Quantum Information Laboratory, ITMO University, Kadetskaya Line, 3, St. Petersburg, 199034, Russia; Laboratory for Quantum Communications, ITMO University, Birzhevaya Line, 16, Saint Petersburg, 199034, Russia; SMARTS-Quanttelecom LLC, 6th Vasilyevskogo Ostrova Line, 59, Saint Petersburg, 199178, Russia; ORCID 0000-0002-9081-8900; rkgoncharov@itmo.ru

*Alexei D. Kiselev* – Laboratory for Quantum Communications, ITMO University, Birzhevaya Line, 16, Saint Petersburg, 199034, Russia; Laboratory of Quantum Processes and Measurements, ITMO University, Kadetskaya Line 3b, Saint Petersburg 199034, Russia; ORCID 0000-0002-1023-3284; adkiselev@itmo.ru

*Conflict of interest:* the authors declare no conflict of interest.

## Epoxide-mediated synthesis of germania aerogels in acetic acid

Olga M. Gajtko<sup>a</sup>, Svetlana V. Golodukhina<sup>b</sup>, Sergey Yu. Kottsov<sup>c</sup>, Alexandra G. Son<sup>d</sup>,  
Taisiya O. Kozlova<sup>e</sup>, Alexander E. Baranchikov<sup>f</sup>

Kurnakov Institute of General and Inorganic Chemistry of the Russian Academy of Sciences, Moscow, Russia

<sup>a</sup>olga.gajtko@igic.ras.ru, <sup>b</sup>golodukhina@igic.ras.ru, <sup>c</sup>skottsov@igic.ras.ru, <sup>d</sup>agson@igic.ras.ru,  
<sup>e</sup>taisiya@igic.ras.ru, <sup>f</sup>baranchikov@igic.ras.ru

Corresponding author: Olga M. Gajtko, olga.gajtko@igic.ras.ru

PACS 82.70.Gg, 61.46.-w, 81.20.-n

**ABSTRACT** A novel alkoxide-free method for the sol-gel synthesis of germania aerogels is proposed. The method is based on the hydrolysis of GeCl<sub>4</sub> by propylene oxide in concentrated acetic acid which is used as a solvent. The proposed protocol allows one to obtain monolithic amorphous germania aerogels constructed of a three-dimensional network of nanoscale (~ 20 nm) particles and possessing specific surface area of about 80 m<sup>2</sup>/g. The addition of hydrochloric acid to the reaction mixture results in the synthesis of nanocrystalline GeO<sub>2</sub> (hexagonal system) aerogels. The synthesized materials were characterized by X-ray diffraction, IR spectroscopy, scanning electron microscopy and low temperature nitrogen adsorption.

**KEYWORDS** sol-gel synthesis, germanium dioxide, propylene oxide, supercritical drying

**ACKNOWLEDGEMENTS** This study is performed within the ARIADNA Collaboration operating under the NICA facility as a part of State Assignment “Solving topical problems with NICA charged particle beams (Ref. # 124110600054-0)”. This research was performed using the equipment of the JRC PMR IGIC RAS.

**FOR CITATION** Gajtko O.M., Golodukhina S.V., Kottsov S.Yu., Son A.G., Kozlova T.O., Baranchikov A.E. Epoxide-mediated synthesis of germania aerogels in acetic acid. *Nanosystems: Phys. Chem. Math.*, 2025, **16** (3), 343–351.

### 1. Introduction

Nanodispersed germanium oxide is unique material possessing outstanding thermal, optical and electrical properties. Germanium dioxide is characterised by a large band gap energy (5 eV), high refractive index, intense blue photoluminescence, high reversible capacity and excellent thermal stability [1–3], giving this material a wide range of diverse applications [4–13]. In view of the considerable practical interest, a number of different approaches to synthesising nanostructured GeO<sub>2</sub> have been described in the literature, including gas transport reactions, chemical vapor deposition, electrospinning, sol-gel precipitation, and others [14–21]. The aforementioned methods result in germanium dioxide in the form of dispersed nanoparticles, 1D or 2D structures; however, the methods for the production of ultralight and highly porous GeO<sub>2</sub> aerogels are extremely limited [22–24]. At the same time, the conjunction of the physicochemical properties of GeO<sub>2</sub> with the unique structure of aerogels could result in new functional materials with unusual characteristics, e.g. electrochemical.

Currently, the common method to obtain metal oxide aerogels is the alkoxide-mediated synthesis, which includes the hydrolysis and polycondensation of an alkoxide of the corresponding metal with subsequent drying of a wet-gel. The most typical example of oxide aerogels is silica aerogels, and the wide variety of the methods for their synthesis is extensively presented in literature [25]. Surprisingly, despite the similar chemical properties of silicon and germanium, the synthetic approaches for GeO<sub>2</sub> aerogels are extremely scarce. Presumably, this is due to the markedly higher rate of germanium alkoxide hydrolysis relative to the hydrolysis of silicon alkoxides [26–29]. Thus, special approaches for the synthesis of GeO<sub>2</sub> lyogels should be used. In particular, Kucheyev *et al.* [30] carried out a controlled hydrolysis of germanium methoxide in acetonitrile, followed by a rapid supercritical drying. As a result, aerogel formed consisting of elongated nanoligaments of amorphous GeO<sub>2</sub> which possessed specific surface area of ~60 m<sup>2</sup>/g. Zhang *et al.* obtained GeO<sub>2</sub> lyogel using germanium ethoxide dissolved in absolute ethanol and dilute hydrochloric acid as a gelation catalyst [31,32]. GeO<sub>2</sub> aerogels were synthesized upon the supercritical drying of the lyogels, they possessed high degree of crystallinity, specific surface area up to 155 m<sup>2</sup>/g and strong blue luminescence.

Due to the high cost of metal alkoxides as well as their high hydrolysis rates, epoxide-mediated method has also been proposed as an alternative for the synthesis of metal oxide aerogels [33,34]. Nevertheless, to the best of our knowledge, the use of this versatile method for the synthesis of GeO<sub>2</sub> aerogels has been documented in only a single report. Briefly, this approach involves the synthesis of amorphous and crystalline germanium dioxide aerogels using a propylene oxide as a hydrolysing agent, aprotic solvents (butyl/ethyl acetate), and hydrochloric acid as a controlled source of protons [35,36].

In the present work, it was hypothesised that acetic acid being a common reagent for the synthesis of metal oxide sol-gel materials [37–42] can also be used for the synthesis of germania aerogels as a solvent and a source of protons.

## 2. Experimental section

The following materials were used as received: germanium chloride  $\text{GeCl}_4$  (Acros Organics, 99.99 %), acetic acid (Aldosa, pure grade), hydrochloric acid (Sigma Tec, extra-pure grade), propylene oxide (Thermo Scientific, 99.5 %).

The synthesis scheme is shown in Fig. 1. To obtain germanium oxide lyogels, 0.10 ml (0.87 mmol) of germanium chloride was dissolved in 1 – 4 ml (17.4 – 69.6 mmol) of glacial acetic acid (AcOH). Subsequently, 0.61 ml (8.7 mmol) of propylene oxide (PO) was added to the resulting solution, which was then cooled to  $\sim 18^\circ\text{C}$ . In some cases, up to 0.16 ml (8.7 mmol) of concentrated 36.5 wt. % hydrochloric acid was additionally added to the cooled solution under sonication. The final molar ratios of the components in the reaction mixtures as well as the visual observations are presented in Table 1.

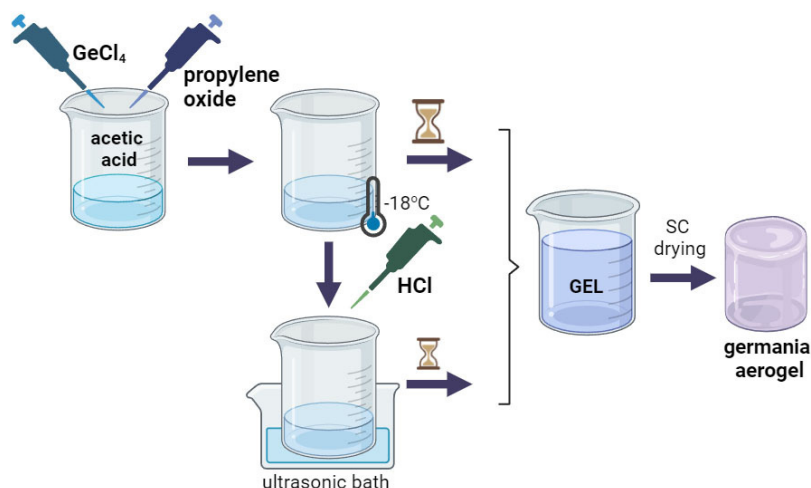


FIG. 1. The scheme of the synthesis of germania aerogels synthesised from the mixtures of  $\text{GeCl}_4$ , acetic acid and propylene oxide as starting reagents

TABLE 1. Designations and synthesis parameters of the germanium oxide aerogels

Sample	Molar ratio $\text{GeCl}_4:\text{AcOH}:\text{HCl}:\text{PO}$	Gelation time	Lyogels stability	Supercritical drying
Ac20	1:20:0:10	$\sim 20$ days	Monolithic gel $\geq 1$ week	+
Ac60	1:60:0:10	$\sim 9$ days	Monolithic gel $\geq 1$ week	+
Ac80	1:80:0:10	$\sim 9$ days	Monolithic gel $\geq 1$ week	+
Ac60_HCl2.5	1:60:2,5:10	$\sim 60$ min	Monolithic gel $\geq 1$ week	+
Ac60_HCl5	1:60:5:10	$\sim 15$ min	Monolithic gel $\geq 1$ week	+
Ac80_HCl5	1:80:5:10	$\sim 120$ min	Monolithic gel $\geq 1$ week	+

The monolithic lyogels which formed during the synthesis were subjected to supercritical drying, carbon dioxide was used as a solvent. Supercritical drying (SC) in  $\text{CO}_2$  was carried out in a setup consisting of a high-pressure pump Supercritical 24 (SSI, USA), a steel reactor with a capacity of 50 ml, and a backpressure regulator BPR (Goregulator, Waters, USA). Each sample was washed with liquid  $\text{CO}_2$  for 2 h at a temperature of  $20^\circ\text{C}$  and a pressure of 15 MPa, then the temperature in the reactor was increased to  $50^\circ\text{C}$  and the sample was washed with supercritical  $\text{CO}_2$  (15 MPa) for at least 5 h. Then, the pressure in the heated autoclave was gradually (over 30 – 40 min) reduced to atmospheric pressure, after which the autoclave was cooled and opened.

The Bruker D8 Advance X-ray diffractometer ( $\text{CuK}\alpha$  radiation, Ni filter and Lynxeye detector) was used to identify the phase composition of the products. Diffraction data were collected in the range of  $2\theta$  from  $7^\circ$  to  $65^\circ$  with a step of  $0.02^\circ$  and accumulation time of 0.3 s/step. The identification of the diffraction peaks was carried out using the ICDD database. The full-profile analysis of diffraction patterns with quantitative determination of the crystallite sizes was performed using the Rietveld method applied using the MAUD software (version 2.99).

The morphology of the samples was studied by scanning electron microscopy (SEM) at Amber GMH (Tescan, Brno, Czech Republic) or NVision 40 (Carl Zeiss, Oberkochen, Germany) microscope using a secondary electron detector. The SEM images were acquired at acceleration voltage of 1 kV. Energy-dispersive X-ray spectroscopy (EDX) data were obtained using an Ultim Max (Oxford Instruments, Abingdon, UK) detector at an accelerating voltage of 20 kV.

The textural characteristics of the materials were determined by ATX-06 analyzer (Katakona, Russia). The samples were degassed at 80 °C in nitrogen current (1 atm) during 2 hours. The specific surface area was defined with the use of The Brunauer–Emmett–Teller (BET) model, based on 7 points within the range of nitrogen partial pressures ( $P/P_0$ ) from 0.05 to 0.25.

Diffuse reflection IR spectra were recorded using a laboratory IR Fourier spectrometer FSM 2202 relative to KBr in the range of 400 – 4000  $\text{cm}^{-1}$  with a resolution of 2  $\text{cm}^{-1}$ , the averaging of 100 spectra was applied. To register the spectra, the samples were diluted in potassium bromide to a weight fraction of 3 %.

Raman spectra were collected using a Confotech NR-500 spectrometer (Sol Instruments), equipped with a 1,800  $\text{mm}^{-1}$  grating and a 785 nm laser with 25 mW output power at the sample surface. The  $\times 20$  objective lens ( $NA = 0.55$ ) was used.

Photoluminescence spectra were recorded at room temperature on a Perkin Elmer LS-55 single-beam luminescence spectrometer (resolution 0.5 nm) in the wavelength range from 300 to 800 nm at  $\lambda_{\text{em}} = 440$  and 530 nm and at  $\lambda_{\text{exc}} = 390$  and 240 nm, the optical slit sizes were 10 nm.

### 3. Results and discussion

As illustrated in Table 1, the gelation times for the solutions of  $\text{GeCl}_4$  in acetic acid depended strongly on the molar ratio of acetic acid-to-propylene oxide. Unexpectedly, the higher was the AcOH:PO ratio in the reaction mixture, the lower was the gelation time (see samples Ac20–Ac80 in Table 1). For the mixtures containing AcOH and PO at molar ratios of 2:1 and 8:1, the gelation times differed approximately twofold. Importantly, under the selected experimental conditions, for the reaction mixtures containing germanium chloride, acetic acid and propylene oxide, the gelation time exceeded one week. Addition of an aqueous solution of hydrochloric acid (36.5 wt. %) to the reaction media allowed to obtain lyogels in a several minutes or tens of minutes. Such a significant change in the gelation rate could be induced by free hydroxonium cations which appear upon the addition of strong hydrochloric acid and water and protonate the molecules of propylene oxide due to nucleophilic attack with subsequent triatomic ring opening [43]. Presumably, the rate of these processes in glacial acetic acid is very low due to the low value of the autoprotolysis constant of AcOH which is close to the autoprotolysis constant of water [44].

The appearance of the obtained lyogels is shown in Fig. 2a, all of them were transparent and retained their transparency after the supercritical drying (Fig. 2b), the aerogels possessed extreme fragility and can hardly be handled.

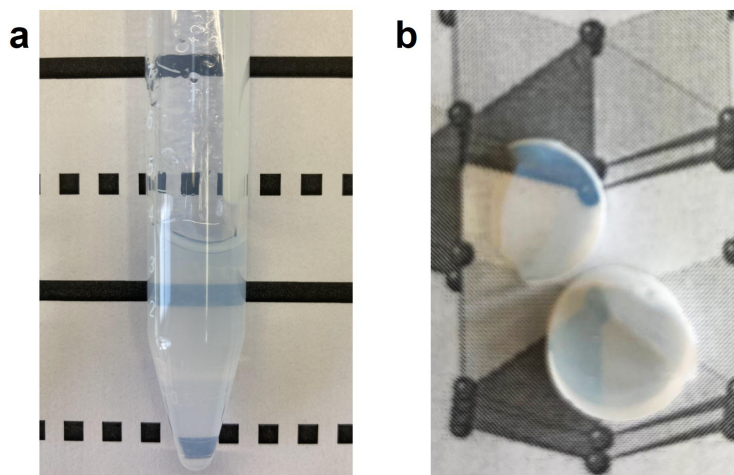


FIG. 2. The visual appearance of the a) germania lyogel formed from  $\text{GeCl}_4$ , acetic acid and propylene oxide as starting reagents (sample Ac60\_HCl2.5) and b) the corresponding germania aerogel

According to X-ray diffraction data, the aerogels obtained without the addition of hydrochloric acid in the reaction mixture regardless of the molar content of acetic acid, were amorphous. In contrast, aerogels synthesized in the presence of hydrochloric acid showed diffraction patterns characteristic of hexagonal  $\text{GeO}_2$  (Fig. 3). The estimations of crystallite size for the samples Ac60\_HCl2.5, Ac60\_HCl15, Ac80\_HCl15 amounted to  $24 \pm 2$ ,  $20 \pm 1$  and  $20 \pm 1$  nm, respectively.

Thus, very slow gelation of the solution containing acetic acid, germanium chloride and propylene oxide results in the formation of X-ray amorphous materials while fast gel formation which occurs upon the addition of aqueous HCl to the reaction mixture, results in the formation of nanocrystalline germanium oxide. The exact reasons for such a dramatic

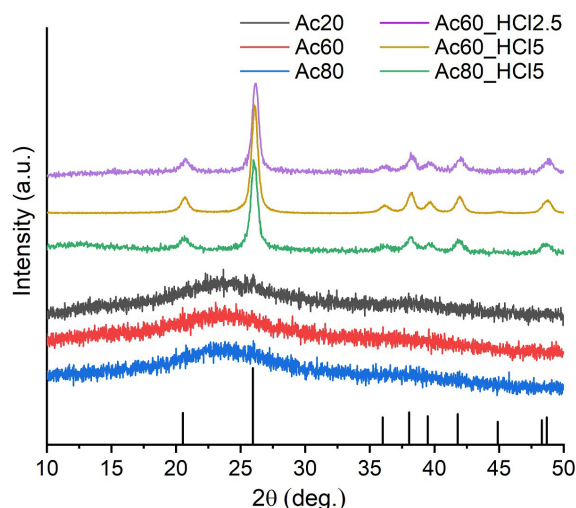


FIG. 3. X-ray diffraction patterns of germania aerogels synthesised from the mixtures of  $\text{GeCl}_4$ , acetic acid and propylene oxide as starting reagents. The Bragg peak positions of  $\text{GeO}_2$  (PDF No. 36-1463) are shown as a reference

difference in the structure of  $\text{GeO}_2$  aerogels is unclear, they can be related to the very different rates of gelation. One should also consider the chemistry of germanium complexes with acetic acid: their formation and hydrolysis mechanism. Despite the formation of such complexes is discussed in the literature [45] their composition and chemical behavior is underexplored.

IR spectroscopy data for the aerogels are presented in Fig. 4a. All the spectra show two main absorption bands in the region of  $1000 - 790$  and  $620 - 480 \text{ cm}^{-1}$ , related to antisymmetric stretching and deformation vibration of  $\text{Ge-O-Ge}$  in hexagonal  $\text{GeO}_2$ , correspondingly [46–50]. Absorption band at  $755 \text{ cm}^{-1}$  can be assigned to the  $\text{Ge-O}$  stretching vibration, or more probably, to the  $\text{Ge-OH}$  vibration [32, 51]. The coincidence of the positions and intensity ratios of all the main absorption bands in the IR spectra of amorphous and crystalline samples provides indirect evidence that, in terms of composition, the X-ray amorphous samples also represent germanium dioxide. In the IR spectrum of the Ac60\_HCl5 sample in the wavenumber range from  $1800$  to  $1000 \text{ cm}^{-1}$ , the most pronounced absorption bands are most likely related to the characteristic vibrations of the acetic acid and propylene oxide molecules [52–54], which remained in the aerogel after supercritical drying. The IR spectroscopy data matched well with the Raman ones (Fig. 4b). The band at  $262 \text{ cm}^{-1}$  corresponded to the  $\text{Ge-O}$  bending modes and three bands in range from  $440$  to  $590 \text{ cm}^{-1}$  are associated with  $\text{Ge-Ge}$  stretching motions [55]. Weak peaks in high-frequency region (up to  $970 \text{ cm}^{-1}$ ) are typically assigned to  $\text{Ge-O}$  stretching motions within tetrahedral  $\text{GeO}_4$  groups. Vibrations of the organic residues are manifested in the range above  $2800 \text{ cm}^{-1}$ . Similar to the IR spectra, the magnitude of these oscillations is most pronounced in the Ac60\_HCl5 sample.

From the chemical sense, the mechanism of the formation of germanium oxide through sol-gel route should include the interaction of germanium-containing species with water molecules or hydroxy groups followed by the condensation of germanoles. In the mixtures of  $\text{GeCl}_4$ , glacial acetic acid and propylene oxide one can hardly expect the presence of free water molecules. However, the formation of  $\text{GeO}_2$  as a result of interaction of  $\text{GeCl}_4$  with benzyl alcohols was recently reported [56]. In that case, the formation of water in the reaction mixture was either due to the  $\text{GeCl}_4$  catalysed interaction of alcohols and the formation of ethers, or due to the alkyl chloride elimination reaction. Thus, it can be expected that the mechanism of  $\text{GeO}_2$  formation in glacial acetic acid and propylene oxide can include either the formation of acetic anhydride or, more probably, acetyl chloride.

Note that, according to EDX data, for all the germania aerogels, the presence of chlorine did not exceed 0.1 atomic percent, which indicates that the hydrolysis of germanium tetrachloride occurred quantitatively, and supports the formation of  $\text{GeO}_2$ .

The microstructure of amorphous samples Ac20, Ac60, Ac80 can be described as a three-dimensional network consisting of nanosized ( $\sim 20 \text{ nm}$ ) particles. In turn, crystalline samples (Ac60\_HCl2.5, Ac60\_HCl5, Ac80\_HCl5) consist of micron sized ellipsoid-like aggregates of ultrasmall particles nearly  $20 \text{ nm}$  in size (Fig. 5). The latter observation is in a good agreement with the results of X-ray diffraction.

Table 2 presents the values of the specific surface area of the obtained aerogels. For the series of amorphous samples, the obtained values are very close to each other ( $\sim 80 \text{ m}^2/\text{g}$ ), which agrees with the SEM data. Conversely, the specific surface of the crystalline samples differs greatly from each other. The lowest specific surface ( $\sim 5 \text{ m}^2/\text{g}$ ) was registered for the Ac60\_HCl5 sample, which may be due to the presence of the reaction by-products (see the IR spectroscopy

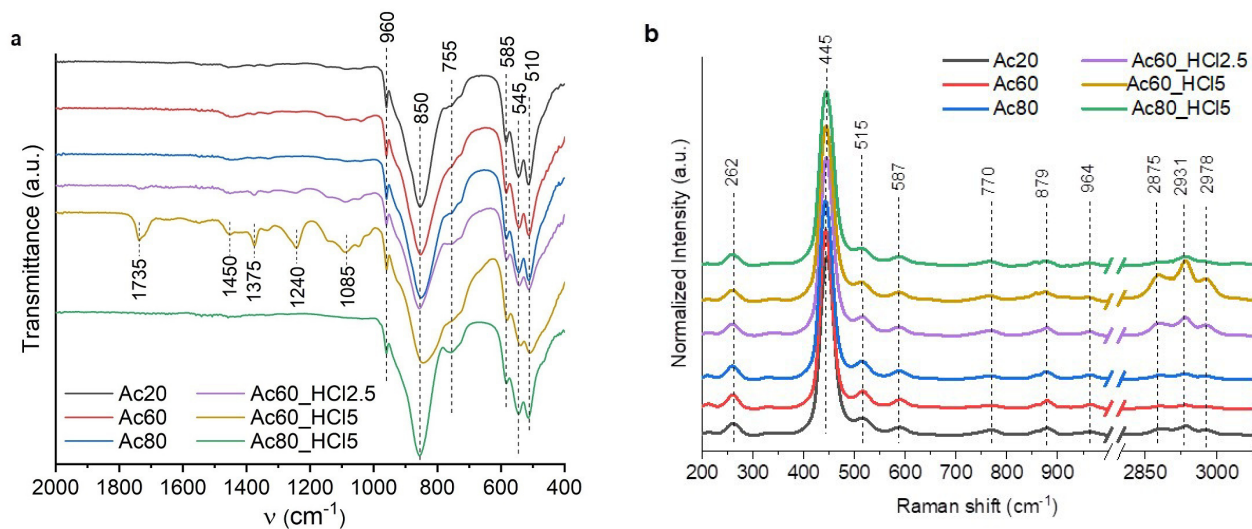


FIG. 4. (a) IR and (b) Raman spectra of germania aerogels synthesised from the mixtures of  $\text{GeCl}_4$ , acetic acid and propylene oxide as starting reagents

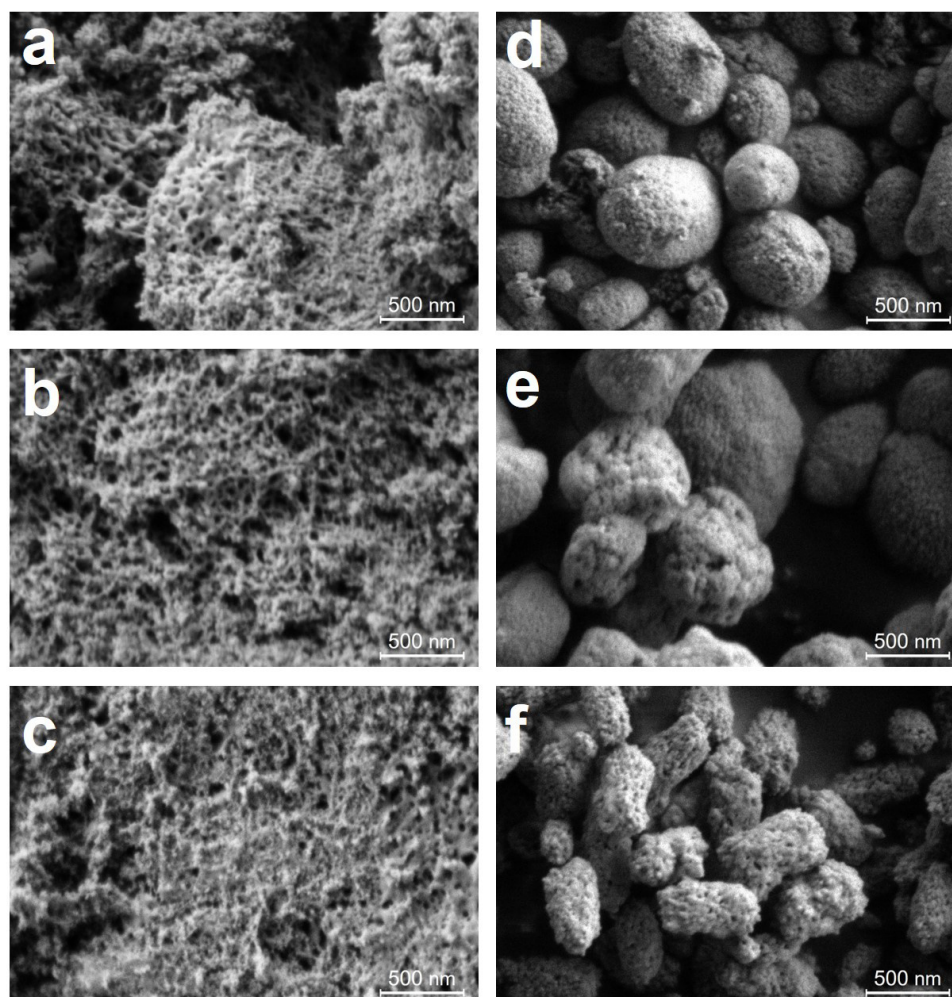


FIG. 5. SEM images of a) Ac20; b) Ac60; c) Ac80; d) Ac60\_HCl2.5; e) Ac60\_HCl5; f) Ac80\_HCl5 samples

data). Despite the fact that, according to SEM data, the Ac60\_HCl2.5 sample consists of agglomerates about 500 nm in size, it possessed the largest surface area ( $\sim 113 \text{ m}^2/\text{g}$ ) among all the samples. Probably, the chosen ratio of reagents makes it possible to achieve the most optimal gelation time. The gelation time was low enough to prevent the strong coalescence (ageing) of individual particles, yet high enough for the formation of the 3D aerogel network with reasonable mechanical strength.

Analysis of the luminescent properties has shown that the shape and position of the main bands in the excitation and emission spectra of the obtained aerogels coincide with those for aerogels obtained by both the decomposition of ammonium germanate [50] and the epoxide-induced sol-gel synthesis in an aprotic solvent [36]. The most pronounced bands in the excitation spectra (Fig. 6) recorded at 440 and 530 nm are localized in the region of 238 and 390 nm.

TABLE 2. Specific surface area of germanium dioxide aerogels

Sample	Molar ratio GeCl <sub>4</sub> :Ac:HCl:Prop	Gel formation duration	$S_{\text{BET}}, \text{m}^2/\text{g}$
Ac20	1:20:0:10	$\sim 20$ days	79
Ac60	1:60:0:10	$\sim 9$ days	74
Ac80	1:80:0:10	$\sim 9$ days	83
Ac60_HCl2.5	1:60:2,5:10	$\sim 60$ min	113
Ac60_HCl5	1:60:5:10	$\sim 15$ min	5
Ac80_HCl5	1:80:5:10	$\sim 120$ min	44

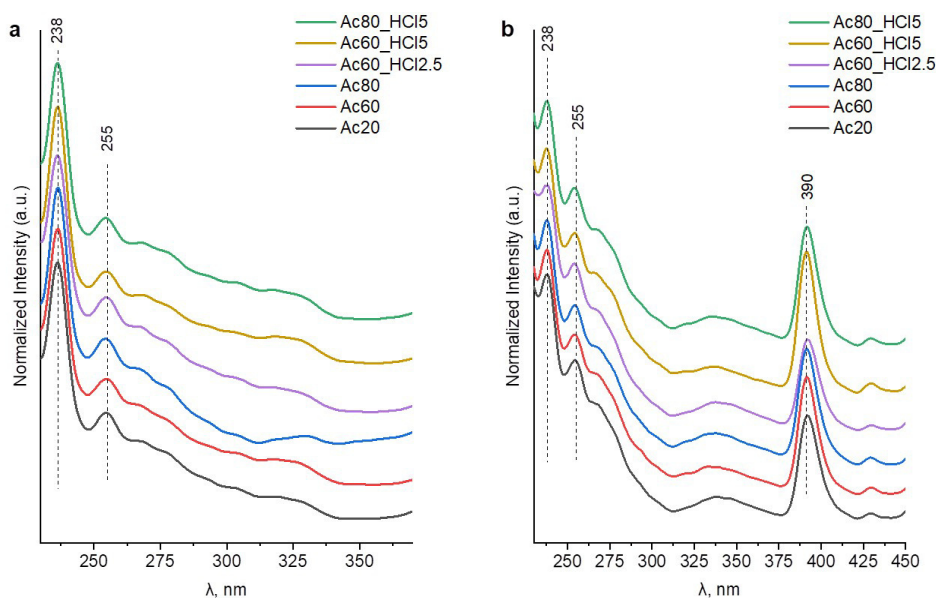


FIG. 6. Excitation spectra recorded at 440 nm (a) and 530 nm (b) of germania aerogels synthesised from the mixtures of GeCl<sub>4</sub>, acetic acid and propylene oxide as starting reagents

The luminescence spectrum obtained under excitation at 390 nm reveals three well-defined bands in the blue-green spectral range at 447, 487, and 530 nm (Fig. 7a). It is a common point, that the blue and green photoluminescence of GeO<sub>2</sub> powder is associated to radiative recombination processes involving different defects, first of all oxygen and oxygen-germanium vacancies centers [19, 57]. The ratio of the blue and green bands varies for different samples. One plausible explanation for this phenomenon could be attributed to the variation in the number of oxygen vacancies present on the surface of the aerogel materials. When excited by radiation with a higher energy (at 240 nm), the emission spectrum becomes more complex (Fig. 7b). Additional bands appear in the violet region of the spectrum around 370 – 430 nm. The origin of violet photoluminescence is typically ascribed to the presence of neutral oxygen vacancies in germanium oxide [7].

Thus, it has been shown that the use of acetic acid as a solvent for GeCl<sub>4</sub> and propylene oxide as a gelation agent leads to the successful formation of monolithic lyogels, in contrast to the previously proposed synthesis with butyl/ethyl acetate,

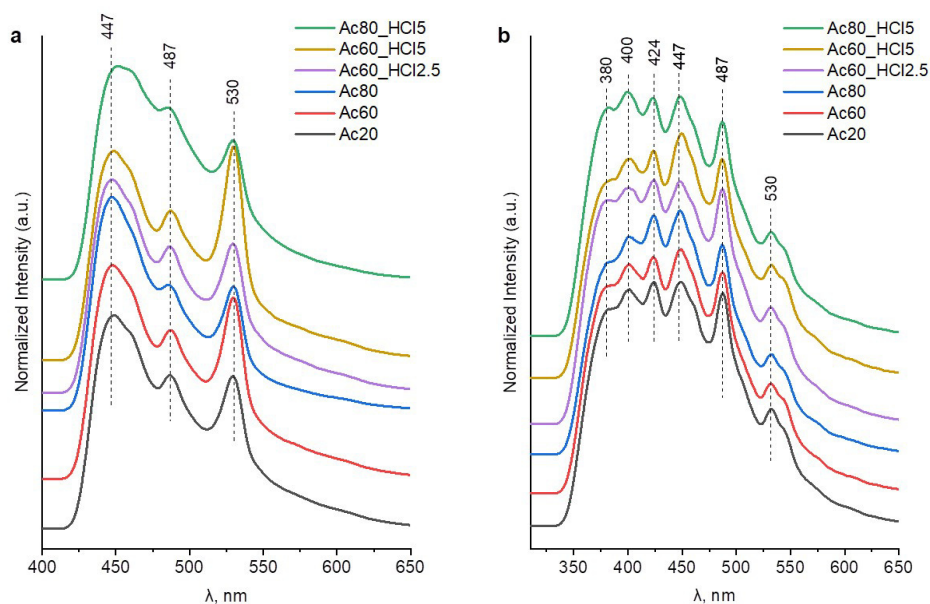


FIG. 7. Emission spectra excited at 390 nm (a) and 240 nm (b) of germania aerogels synthesised from the mixtures of  $\text{GeCl}_4$ , acetic acid and propylene oxide as starting reagents

which also required the use of hydrochloric acid [35, 36]. Although it is evident that the formation of germanium oxide occurs through the non-hydrolytic sol-gel process, further research is needed for establishing the reaction mechanism. Employing supplementary methods, particularly NMR spectroscopic studies of the reaction mixtures at different stages of the gelation process can contribute to understanding of the mechanism. Most importantly, the role of the hydrochloric acid should be elucidated, whether it alters the reaction mechanism or merely accelerates the rate of the reaction. It should be noted that the sol-gel synthesis of crystalline aerogels presents a challenging task for modern materials science [58]. The discovery of the potential to synthesize germanium dioxide aerogels with desired and high textural characteristics through minor alterations of the synthesis route can be a significant advance from a fundamental standpoint. This approach offers the flexibility to tailor the functional properties of the resulting materials, a capability that holds immense promise for diverse applications [59, 60].

#### 4. Conclusions

For the first time, a method for producing germanium dioxide aerogels by the epoxide-induced sol-gel method using acetic acid as a solvent has been proposed. It was found that the molar content of acetic acid used (20–80-fold molar excess relative to  $\text{GeCl}_4$ ) has virtually no effect on the composition and microstructure of the products – the resulting aerogels are X-ray amorphous with a particle size of about 20 nm and a specific surface area of about  $80 \text{ m}^2/\text{g}$ . Moreover, the addition of hydrochloric acid to the reaction medium leads to a significantly higher rate of gelation of the initial lyogels and the production of aerogels of crystalline germanium dioxide (hexagonal syngony) with a crystallite size of about 20 nm. The morphology and degree of crystallinity of aerogels did not have a direct impact on their luminescent properties. The general appearance of the excitation and emission spectra was similar for all samples. However, when excited at 390 nm, the ratio of the intensities of the green and blue bands differed between samples.

#### References

- [1] Bioud Y.A., Paradis E., Boucherif A., Drouin D., Arès R. Shape Control of Cathodized Germanium Oxide Nanoparticles. *Electrochem. Commun.*, 2021, **122**, 106906.
- [2] Almuslem A.S., Hanna A.N., Yapici T., Wehbe N., Diallo E.M., Kutbee A.T., Bahabry R.R., Hussain M.M. Water Soluble Nano-Scale Transient Material Germanium Oxide for Zero Toxic Waste Based Environmentally Benign Nano-Manufacturing. *Appl. Phys. Lett.*, 2017, **110** (7), 074103.
- [3] Simanzhenkov V., Ifeacho P., Wiggers H., Knipping J., Roth P. Synthesis of Germanium Oxide Nanoparticles in Low-Pressure Premixed Flames. *J. Nanosci. Nanotechnol.*, 2004, **4** (1), P. 157–161.
- [4] Zhao Q., Lorenz H., Turner S., Lebedev O.I., Van Tendeloo G., Rameshan C., Klötzer B., Konzett J., Penner S. Catalytic Characterization of Pure  $\text{SnO}_2$  and  $\text{GeO}_2$  in Methanol Steam Reforming. *Appl. Catal. A Gen.*, 2010, **375** (2), P. 188–195.
- [5] Kim W.J., Soshnikova V., Markus J., Oh K.H., Anandapadmanaban G., Mathiyalagan R., Perez Z.E.J., Kim Y.J., Yang D.C. Room Temperature Synthesis of Germanium Dioxide Nanorods and Their in Vitro Photocatalytic Application. *Optik (Stuttg.)*, 2019, **178**, P. 664–668.
- [6] Trukhin A.N. Luminescence of Polymorph Crystalline and Glassy  $\text{SiO}_2$ ,  $\text{GeO}_2$ : A Short Review. *J. Non. Cryst. Solids*, 2009, **355** (18–21), P. 1013–1019.
- [7] Shi R., Zhang R., Chen X., Yang F., Zhao Q., Yu J., Zhao H., Wang L., Liu B., Bao L., Chen Y., Yang H. Controllable Growth of  $\text{GeO}_2$  Nanowires with the Cubic and Hexagonal Phases and Their Photoluminescence. *J. Cryst. Growth*, 2011, **336** (1), P. 6–13.

- [8] Bose N., Basu M., Mukherjee S. Study of Optical Properties of GeO<sub>2</sub> Nanocrystals as Synthesized by Hydrothermal Technique. *Mater. Res. Bull.*, 2012, **47** (6), P. 1368–1373.
- [9] Walker B., Dharmawardhana C.C., Dari N., Rulis P., Ching W.Y. Electronic Structure and Optical Properties of Amorphous GeO<sub>2</sub> in Comparison to Amorphous SiO<sub>2</sub>. *J. Non. Cryst. Solids*, 2015, **428**, P. 176–183.
- [10] Zhang J., Yu T., Chen J., Liu H., Su D., Tang Z., Xie J., Chen L., Yuan A., Kong Q. Germanium-Based Complex Derived Porous GeO<sub>2</sub> Nanoparticles for Building High Performance Li-Ion Batteries. *Ceram. Int.*, 2018, **44** (1), P. 1127–1133.
- [11] Arro C.R., Mohamed A.T.I., Bensalah N. Impact of Ge Content on the Electrochemical Performance of Germanium Oxide/Germanium/ Reduced Graphene (GeO<sub>2</sub>/Ge/r-GO) Hybrid Composite Anodes for Lithium-Ion Batteries. *Mater. Today Commun.*, 2022, **30** (January), 103151.
- [12] Han L., Wei Q., Chen H., Tang J., Wei M. Open-Framework Germanates Derived GeO<sub>2</sub>/C Nanocomposite as a Long-Life and High-Capacity Anode for Lithium-Ion Batteries. *J. Alloys Compd.*, 2021, **881**, 160533.
- [13] Mo R., Rooney D., Sun K. Hierarchical Graphene-Scaffolded Mesoporous Germanium Dioxide Nanostructure for High-Performance Flexible Lithium-Ion Batteries. *Energy Storage Mater.*, 2020, **29**, P. 198–206.
- [14] Wu Y., Yang P. Germanium Nanowire Growth via Simple Vapor Transport. *Chem. Mater.*, 2000, **12** (3), P. 605–607.
- [15] Jiang Z., Xie T., Wang G.Z., Yuan X.Y., Ye C.H., Cai W.P., Meng G.W., Li G.H., Zhang L.D. GeO<sub>2</sub> Nanotubes and Nanorods Synthesized by Vapor Phase Reactions. *Mater. Lett.*, 2005, **59** (4), P. 416–419.
- [16] Mathur S., Shen H., Sivakov V., Werner U. Germanium Nanowires and Core-Shell Nanostructures by Chemical Vapor Deposition of [Ge(C<sub>5</sub>H<sub>5</sub>)<sub>2</sub>]. *Chem. Mater.*, 2004, **16** (12), P. 2449–2456.
- [17] Zhang X., Que W., Chen J., Zhang X., Hu J., Liu W. Concave Micro-Lens Arrays Fabricated from the Photo-Patternable GeO<sub>2</sub>/Ormosils Hybrid Sol-Gel Films. *Opt. Mater.*, 2013, **35** (12), P. 2556–2560.
- [18] Hsu C.H., Lin J. Sen, He Y. Da, Yang S.F., Yang P.C., Chen W.S. Optical, Electrical Properties and Reproducible Resistance Switching of GeO<sub>2</sub> Thin Films by Sol-Gel Process. *Thin Solid Films*, 2011, **519** (15), P. 5033–5037.
- [19] Wu X.C., Song W.H., Zhao B., Sun Y.P., Du J.J. Preparation and Photoluminescence Properties of Crystalline GeO<sub>2</sub> Nanowires. *Chem. Phys. Lett.*, 2001, **349**, P. 210–214.
- [20] Zhang Y., Zhu J., Zhang Q., Yan Y., Wang N., Zhang X. Synthesis of GeO<sub>2</sub> Nanorods by Carbon Nanotubes Template. *Chem. Phys. Lett.*, 2000, **317**, P. 504–509.
- [21] Krupanidhi S.B., Sayer M., Mansingh A. Electrical Characterization of Amorphous Germanium Dioxide Films. *Thin Solid Films*, 1984, **113** (3), P. 173–184.
- [22] Pierre A.C., Pajonk G.M. Chemistry of Aerogels and Their Applications. *Chem. Rev.*, 2002, **102** (11), P. 4243–4266.
- [23] Ziegler C., Wolf A., Liu W., Herrmann A., Gaponik N., Eychmüller A. Modern Inorganic Aerogels. *Angew. Chemie Int. Ed.*, 2017, **56** (43), P. 13200–13221.
- [24] Feng J., Su B.-L., Xia H., Zhao S., Gao C., Wang L., Ogbeide O., Feng J., Hasan T. Printed Aerogels: Chemistry, Processing, and Applications. *Chem. Soc. Rev.*, 2021, **50** (6), P. 3842–3888.
- [25] Gurav J.L., Jung I.K., Park H.H., Kang E.S., Nadargi D.Y. Silica Aerogel: Synthesis and Applications. *J. Nanomater.*, 2010, 2010.
- [26] Krishnan V., Gross S., Müller S., Armelao L., Tondello E., Bertagnolli H. Structural Investigations on the Hydrolysis and Condensation Behavior of Pure and Chemically Modified Alkoxides. 2. Germanium Alkoxides. *J. Phys. Chem. B*, 2007, **111** (26), P. 7519–7528.
- [27] Livage J., Sanchez C. Sol-Gel Chemistry. *J. Non. Cryst. Solids*, 1992, **145**, P. 11–19.
- [28] Shen J., Li Q., Zhou B., Wang J., Chen L. SiO<sub>2</sub>-GeO<sub>2</sub> Binary Aerogels with Ultralow Density. *J. Non. Cryst. Solids*, 1997, **220** (1), P. 102–106.
- [29] Grandi S., Mustarelli P., Magistris A., Gallorini M., Rizzio E. Synthesis of GeO<sub>2</sub>-Doped SiO<sub>2</sub> Aerogels and Xerogels. *J. Non. Cryst. Solids*, 2002, **303** (2), P. 208–217.
- [30] Kucheyev S.O., Baumann T.F., Wang Y.M., van Buuren T., Poco J.F., Satcher J.H., Hamza A.V. Monolithic, High Surface Area, Three-Dimensional GeO<sub>2</sub> Nanostructures. *Appl. Phys. Lett.*, 2006, **88** (10), 103117.
- [31] Zhang L., Chen G., Chen B., Liu T., Mei Y., Luo X. Monolithic Germanium Oxide Aerogel with the Building Block of Nano-Crystals. *Mater. Lett.*, 2013, **104**, P. 41–43.
- [32] Chen G., Chen B., Liu T., Mei Y., Ren H., Bi Y., Luo X., Zhang L. The Synthesis and Characterization of Germanium Oxide Aerogel. *J. Non. Cryst. Solids*, 2012, **358** (23), P. 3322–3326.
- [33] Gash A.E., Tillotson T.M., Satcher J.H., Hrubesh L.W., Simpson R.L. New Sol-Gel Synthetic Route to Transition and Main-Group Metal Oxide Aerogels Using Inorganic Salt Precursors. *J. Non. Cryst. Solids*, 2001, **285** (1–3), P. 22–28.
- [34] Du A., Zhou B., Zhang Z., Shen J. A Special Material or a New State of Matter: A Review and Reconsideration of the Aerogel. *Materials (Basel)*, 2013, **6** (3), P. 941–968.
- [35] Veselova V.O., Kottsov S.Y., Golodukhina S. V., Khvoshchevskaya D.A., Gajtko O.M. Hydrophilic and Hydrophobic: Modified GeO<sub>2</sub> Aerogels by Ambient Pressure Drying. *Nanomaterials*, 2024, **14** (18), 1511.
- [36] Gajtko O.M., Golodukhina S. V., Kottsov S.Y., Subcheva E.N., Volkov V.V., Kopitsa G.P., Son A.G., Veselova V.O. Hydrophobic GeO<sub>2</sub> Aerogels by an Epoxide-Induced Process. *Gels*, 2025, **11** (4), 225.
- [37] Stöcker C., Baiker A. Zirconia Aerogels: Effect of Acid-to-Alkoxide Ratio, Alcoholic Solvent and Supercritical Drying Method on Structural Properties. *J. Non. Cryst. Solids*, 1998, **223** (3), P. 165–178.
- [38] Aguado-Serrano J., Rojas-Cervantes M.L. Titania Aerogels. *Microporous Mesoporous Mater.*, 2006, **88** (1–3), P. 205–213.
- [39] Dong W., Yen S., Paik J., Sakamoto J. The Role of Acetic Acid and Glycerol in the Synthesis of Amorphous MgO Aerogels. *J. Am. Ceram. Soc.*, 2009, **92** (5), P. 1011–1016.
- [40] Poco J., Satcher J., Hrubesh L. Synthesis of High Porosity, Monolithic Alumina Aerogels. *J. Non. Cryst. Solids*, 2001, **285** (1–3), P. 57–63.
- [41] Shimoyama Y., Ogata Y., Ishibashi R., Iwai Y. Drying Processes for Preparation of Titania Aerogel Using Supercritical Carbon Dioxide. *Chem. Eng. Res. Des.*, 2010, **88** (10), P. 1427–1431.
- [42] Sui R., Rizkalla A.S., Charpentier P.A. Synthesis and Formation of Silica Aerogel Particles By a Novel Sol-Gel Route in Supercritical Carbon Dioxide. *J. Phys. Chem. B*, 2004, **108** (32), P. 11886–11892.
- [43] Baumann T.F., Gash A.E., Satcher J.H. A Robust Approach to Inorganic Aerogels: The Use of Epoxides in Sol-Gel Synthesis. *Aerogels Handb.*, 2011, P. 155–170.
- [44] Rondinini S., Longhi P., Mussini P.R., Mussini T. Autoprotolysis Constants in Nonaqueous Solvents and Aqueous Organic Solvent Mixtures. *Pure Appl. Chem.*, 1987, **59** (12), P. 1693–1702.
- [45] Pokrovski G.S., Schott J. Experimental Study of the Complexation of Silicon and Germanium with Aqueous Organic Species: Implications for Germanium and Silicon Transport and Ge/Si Ratio in Natural Waters. *Geochim. Cosmochim. Acta*, 1998, **62** (21–22), P. 3413–3428.
- [46] Lobaz V., Rabyk M., Pánek J., Doris E., Nallet F., Štěpánek P., Hrubý M. Photoluminescent Polysaccharide-Coated Germanium(IV) Oxide Nanoparticles. *Colloid Polym. Sci.*, 2016, **294** (7), P. 1225–1235.

- [47] Javadi M., Yang Z., Veinot J.G.C. Surfactant-Free Synthesis of GeO<sub>2</sub> Nanocrystals with Controlled Morphologies. *Chemical Communications*, 2014, **50** (46), P. 6101–6104.
- [48] Micoulaut M., Cormier L., Henderson G.S. The Structure of Amorphous, Crystalline and Liquid GeO<sub>2</sub>. *J. Phys. Condens. Matter*, 2006, **18** (45), R753–R784.
- [49] Błaszczak K., Adamczyk A., Wędzikowska M., Rokita M. Infrared Studies of Devitrification Li<sub>2</sub>O–B<sub>2</sub>O<sub>3</sub>–2GeO<sub>2</sub> Glass. *J. Mol. Struct.*, 2004, **704** (1–3), P. 275–279.
- [50] Veselova V.O., Khvoshchevskaya D.A., Golodukhina S. V., Kottsov S.Y., Gajtko O.M. One Simple Approach to Novel Germania and Germanate Aerogels. *Microporous Mesoporous Mater.*, 2024, **379**, 113282.
- [51] Kawai T., Usui Y., Kon-No K. Synthesis and Growth Mechanism of GeO<sub>2</sub> Particles in AOT Reversed Micelles. *Colloids Surfaces A Physicochem. Eng. Asp.*, 1999, **149** (1–3), P. 39–47.
- [52] Gofurov S., Makhmanov U., Kokhkharov A., Ismailova O.B. Structural and Optical Characteristics of Aqueous Solutions of Acetic Acid. *Appl. Spectrosc.*, 2019, **73** (5), P. 503–510.
- [53] Hasan M.A., Zaki M.I., Pasupulety L. Oxide-Catalyzed Conversion of Acetic Acid into Acetone: An FTIR Spectroscopic Investigation. *Appl. Catal. A Gen.*, 2003, **243** (1), P. 81–92.
- [54] Hudson R.L., Loeffler M.J., Yocum K.M. Laboratory Investigations into the Spectra and Origin of Propylene Oxide: A Chiral Interstellar Molecule. *Astrophys. J.*, 2017, **835** (2), 225.
- [55] Madon M., Gillet P., Julien C., Price G.D. A Vibrational Study of Phase Transitions among the GeO<sub>2</sub> Polymorphs. *Phys. Chem. Miner.*, 1991, **18** (1), P. 7–18.
- [56] Kitschke P., Schulze S., Hietschold M., Mehring M. Synthesis of Germanium Dioxide Nanoparticles in Benzyl Alcohols – a Comparison. *Main Gr. Met. Chem.*, 2013, **36** (5–6).
- [57] Bose N., Basu M., Mukherjee S. Study of Optical Properties of GeO<sub>2</sub> Nanocrystals as Synthesized by Hydrothermal Technique. *Mater. Res. Bull.*, 2012, **47** (6), P. 1368–1373.
- [58] Takemoto M., Tokudome Y., Noguchi D., Ueoka R., Kanamori K., Okada K., Murata H., Nakahira A., Takahashi M. Synthesis of a Crystalline and Transparent Aerogel Composed of Ni–Al Layered Double Hydroxide Nanoparticles through Crystallization from Amorphous Hydrogel. *Langmuir*, 2020, **36** (32), P. 9436–9442.
- [59] Khan I., Saeed K., Khan I. Nanoparticles: Properties, Applications and Toxicities. *Arab. J. Chem.*, 2019, **12** (7), P. 908–931.
- [60] Tretyakov Y.D., Goodilin E.A. Key Trends in Basic and Application-Oriented Research on Nanomaterials. *Russ. Chem. Rev.*, 2009, **78** (9), P. 801–820.

---

Submitted 24 January 2025; revised 28 March 2025; accepted 5 May 2025

#### Information about the authors:

*Olga M. Gajtko* – Kurnakov Institute of General and Inorganic Chemistry of the Russian Academy of Sciences, Moscow, Russia; ORCID 0000-0001-6424-1282; olga.gajtko@igic.ras.ru

*Svetlana V. Golodukhina* – Kurnakov Institute of General and Inorganic Chemistry of the Russian Academy of Sciences, Moscow, Russia; ORCID 0000-0001-9317-1340; golodukhina@igic.ras.ru

*Sergey Yu. Kottsov* – Kurnakov Institute of General and Inorganic Chemistry of the Russian Academy of Sciences, Moscow, Russia; ORCID 0000-0001-8263-889X; skottsov@igic.ras.ru

*Alexandra G. Son* – Kurnakov Institute of General and Inorganic Chemistry of the Russian Academy of Sciences, Moscow, Russia; ORCID 0009-0006-7107-5714; agson@igic.ras.ru

*Taisiya O. Kozlova* – Kurnakov Institute of General and Inorganic Chemistry of the Russian Academy of Sciences, Moscow, Russia; ORCID 0000-0002-9757-9148; taisiya@igic.ras.ru

*Alexander E. Baranchikov* – Kurnakov Institute of General and Inorganic Chemistry of the Russian Academy of Sciences, Moscow, Russia; ORCID 0000-0002-2378-7446; baranchikov@igic.ras.ru

*Conflict of interest:* the authors declare no conflict of interest.

## TiO<sub>2</sub> nanotubes modified with cadmium oxide for photoelectrocatalytic oxidation of alcohols

Vitali A. Grinberg<sup>a</sup>, Victor V. Emets<sup>b</sup>, Aleksey V. Shapagin<sup>c</sup>, Aleksey A. Averin<sup>d</sup>, Andrei A. Shiryaev<sup>e</sup>

Frumkin Institute of Physical Chemistry and Electrochemistry, Russian Academy of Sciences, Moscow, Russia

<sup>a</sup>vitgreen@mail.ru, <sup>b</sup>Victoremets@mail.ru, <sup>c</sup>shapagin@mail.ru, <sup>d</sup>alx.av@yandex.ru, <sup>e</sup>a\_shiryaev@mail.ru

Corresponding author: Victor V. Emets, Victoremets@mail.ru

PACS 82.47.Jk

**ABSTRACT** TiO<sub>2</sub> nanotube (TNT) electrodes were fabricated by electrochemical anodization of titanium in ethylene glycol electrolyte with added NH<sub>4</sub>F (0.5 wt.%) and water (2 % w/w). The (TNT)-cadmium oxide (CdO) composite was fabricated using potentiostatic cathodic deposition. Structural properties of the obtained coatings have been investigated by scanning electron microscopy and X-Ray photoelectron spectroscopy, Raman spectroscopy, X-Ray diffraction and transmission electron microscopy. The TNT-CdO electrode demonstrates high efficiency in photoelectrochemical degradation of methanol, ethylene glycol, glycerol and sorbitol in aqueous solutions of 0.1 M Na<sub>2</sub>SO<sub>4</sub> upon irradiation by a simulated sunlight. The highest photooxidation currents were obtained for sorbitol. Intensity-modulated photocurrent spectroscopy shows that the photoelectrocatalysis efficiency is due to suppression of the electron-hole pairs' recombination and to increase in the rate of photo-induced charge transfer. Thus, the TNT-CdO composite is an effective photoanode for developing the technology of photoelectrochemical degradation of sorbitol and other alcohols by-products of biofuel production.

**KEYWORDS** Nanotubes, TiO<sub>2</sub>-CdO composite, photoelectrocatalytic oxidation, methanol, ethylene glycol, glycerol, sorbitol

**ACKNOWLEDGEMENTS** This research was financially supported by the Ministry of Science and Higher Education of the Russian Federation and performed using the equipment of the Center for Collective Use of Physical Investigation Methods of the IPCE RAS.

**FOR CITATION** Grinberg V.A., Emets V.V., Shapagin A.V., Averin A.A., Shiryaev A.A. TiO<sub>2</sub> nanotubes modified with cadmium oxide for photoelectrocatalytic oxidation of alcohols. *Nanosystems: Phys. Chem. Math.*, 2025, **16** (3), 352–363.

### 1. Introduction

Titania – TiO<sub>2</sub> – is widely used in very diverse fields due to its high photosensitivity, non-toxicity, simplicity of preparation and stability in a wide pH range [1,2]. Rich variety of nanostructured titania morphologies may be fabricated, such as nanoparticles, nanotubes and nanofibers. Harvesting solar energy by titania nanotubes (TNT) prepared by titanium anodization [3, 4] attracts considerable attention due to higher rate of photogenerated charge transfer in comparison with films made of titania nanoparticles [5,6]. Large band gap of TiO<sub>2</sub> limits light absorption to photons with energies close to UV-range. Absorption in the visible spectral range is made possible by introducing dopants narrowing the band gap; for example, CdS [7, 8], CdSe [9, 10], TiSi<sub>2</sub> [11], Fe<sub>2</sub>O<sub>3</sub> [12] and NiO [13]. In particular, admixture of CdO, a n-type semiconductor characterized by a 2.32 eV direct and 1.36 eV indirect band gaps [14], is promising for several applications. Nanostructured TNT-CdO materials could be obtained using different approaches including electrodeposition of CdO on TNT substrate [15] or soaking of TNT with cadmium salts with subsequent annealing in air [16]. These composites demonstrate noticeable enhancement of water photoelectrochemical oxidation relative to pure TNT.

Common approaches to decompose the alcohols into carbonyl compounds are characterized by harsh reaction conditions, formation of abundant harmful waste and low selectivity. Novel methods based on photo-, electro- and photoelectrocatalytic alcohols' oxidation to precursors and intermediates for production of pharmaceuticals and other substances [17] combined with simultaneous production of pure hydrogen are of considerable theoretical and applied interest. Among alcohols produced from renewable biomass sorbitol plays an important role due to possibility of its conversion into alkanes, methanol and hydrogen by reforming in aqueous medium [18–21]. Sorbitol also serves as a precursor for medications (e.g., isosorbide – a popular diuretic), polymers, solvents, fuel additives etc [22].

In this work we report influence of CdO promotion on photoelectrocatalytic activity of nanostructured titania photoanodes in reaction of selective photoelectrochemical sorbitol degradation under simulated Solar light. The photoanodes

were made by two-step anodisation of VT1-0 titanium alloy followed by cathodic deposition of CdO. Note that the current study does not address the composition of the products of photoelectrooxidation of the mentioned alcohols.

## 2. Experimental

### 2.1. Materials

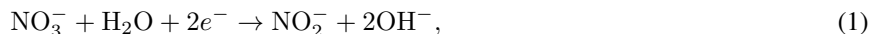
Chemically pure (>99 %) ammonium fluoride NH<sub>4</sub>F and ethylene glycol (99.9 %), methanol, ethylene glycol, glycerol, sorbitol, Cd(NO<sub>3</sub>)<sub>2</sub> · 4H<sub>2</sub>O, sodium bicarbonate (NaHCO<sub>3</sub>), sodium sulfate (Na<sub>2</sub>SO<sub>4</sub>) were purchased from (Aldrich, St. Louis, MO, USA) and used in the coating fabrication without further purification.

### 2.2. Preparation of TNT/Ti photoanodes

The electrodes were prepared by anodic oxidation of titanium foil (VT1-0 alloy, 99.5 % of Ti, 1.0 × 1.0 × 0.3 cm) at 20 °C in electrochemical cell, containing solution of ethylene glycol 0.5 % (w/w) NH<sub>4</sub>F and 2 % (w/w) H<sub>2</sub>O as supporting electrolyte, and a Pt–Ir plate (8 cm<sup>2</sup>) used as cathode. Two-step anodization procedure was employed to obtain stable and uniform structure [23–26]. The first step was performed at a constant voltage of 60 volts for 1 hour, followed by the coating removal in an ultrasonic bath in a 0.1 M HCl solution for 180 s. Next, the electrode was rinses with distilled water, air-dried at 50 °C and subjected to a second anodization step in the same solution at a constant voltage of 60 V for 1 hour. Subsequently, the TNT/Ti electrode was washed with deionized water, dried in air and annealed at 450 °C (heating rate 7 °C/min) for 1 h. After cooling in the oven for 12 h, the obtained samples coated with the uniform TNTs film were used for further investigations. The titania nanotubes grow due to two competitive reactions anodic oxidation and chemical dissolution of TiO<sub>2</sub> [27].

### 2.3. Preparation of TNT–CdO Photoanode

Cadmium oxide was deposited on the preformed TNT at a constant potential  $E = -0.75$  V (vs. Ag/AgCl) from a 5 mM Cd(NO<sub>3</sub>)<sub>2</sub> · 4H<sub>2</sub>O + 0.1 M KCl solution while stirring the electrolyte according to the procedure described in [28]. Depending on the deposition time, the electric charge that passed varied between 50 and 800 mC. CdO formation via generation of intermediate Cd(OH)<sub>2</sub> was proposed in [29].



Cd(OH)<sub>2</sub> is converted to CdO at temperatures above 280 °C by the following reaction [30]:



### 2.4. Characterization of the TNT–CdO photoanodes

**2.4.1. Study of the structure and phase composition of the TNT–CdO photoanodes.** Morphology of the deposited TNT and TNT–CdO, the phase composition and Raman spectra were recorded as in [31–33].

Morphology of the deposited TNT and TNT–CdO was assessed by Scanning Electron Microscopy (SEM) with a JEOL JSM-6060 SEM and JED-2300 Analysis Station (JEOL).

The phase composition of the deposited film coatings was studied by X-ray diffraction (XRD) analysis on an Empyrean X-ray diffractometer (Panalytical BV). Ni-filtered Cu-K $\alpha$  radiation was used; the samples were studied in the Bragg–Brentano geometry. The phase composition was identified using the ICDD PDF-2 diffraction database.

Raman spectra were recorded using an inVia “Reflex” Raman spectrometer (Renishaw) with a 50× objective. The 405-nm line of a diode laser was used for excitation, and laser power on the sample was less than 0.2 mW.

XPS spectra were obtained on an OMICRON ESCA+ spectrometer (Germany) with an aluminum anode, equipped with a monochromatic X-ray source XM1000 (AlK $\alpha$  1486.6 eV and a power of 252 W).

**2.4.2. Photoelectrooxidation.** Photoelectrochemical measurements were performed using a setup comprising photoelectrochemical three-electrode cell PECC-2 (Zahner Elektrik, Germany), a 150 W Solar spectrum simulator 96000 (Newport) with an AM1.5G filter, and an IPC-Pro MF potentiostat (IPChE RAS, Russia). The working electrode in the cell was a 1 cm<sup>2</sup> TNT and TNT–CdO photoanodes. A Pt wire with a surface area of approximately 3 cm<sup>2</sup> was used as an auxiliary electrode. All potentials are measured with a silver chloride electrode as a reference. Potentials relative to a reversible hydrogen electrode can be determined from the equation:  $E_{\text{RHE}} = E_{\text{Ag/AgCl}} + 0.059 \times \text{pH} + E_{\text{Ag/AgCl}}$ , where  $E_{\text{Ag/AgCl}} = 0.197$ .

Photoelectrochemical oxidation of alcohols (methanol, ethylene glycol, glycerol and sorbitol) and Intensity modulated photocurrent spectroscopy (IMPS) were carried out as described earlier in [31–33].

### 3. Results and discussion

Several photoanode samples were fabricated for research. The samples with pure titania nanotube coatings are designated as TNT. The photoanodes with modified TNT films are denoted as TNT-(0.05)CdO, TNT-(0.2)CdO, TNT-(0.8)CdO, where the number in parentheses denotes the electric charge spent on the electrodeposition of CdO in Coulombs per  $\text{cm}^2$  of the geometric surface of the photoanode. The technique for manufacturing photoanode samples is described in detail in the Experimental details section.

Nanotubular structure of the TNT and TNT-CdO samples annealed at  $450\text{ }^\circ\text{C}$  is clearly visible in scanning electron microscopy (SEM) images, see Fig. 1. The nanotubes are  $20 - 22\ \mu\text{m}$  long, average wall thickness is  $\sim 20\ \text{nm}$  and average diameter of nanotubes is  $\sim 100\ \text{nm}$ . Results of chemical analyses are shown in Fig. A1 and Tables A1–A4 (Appendix).

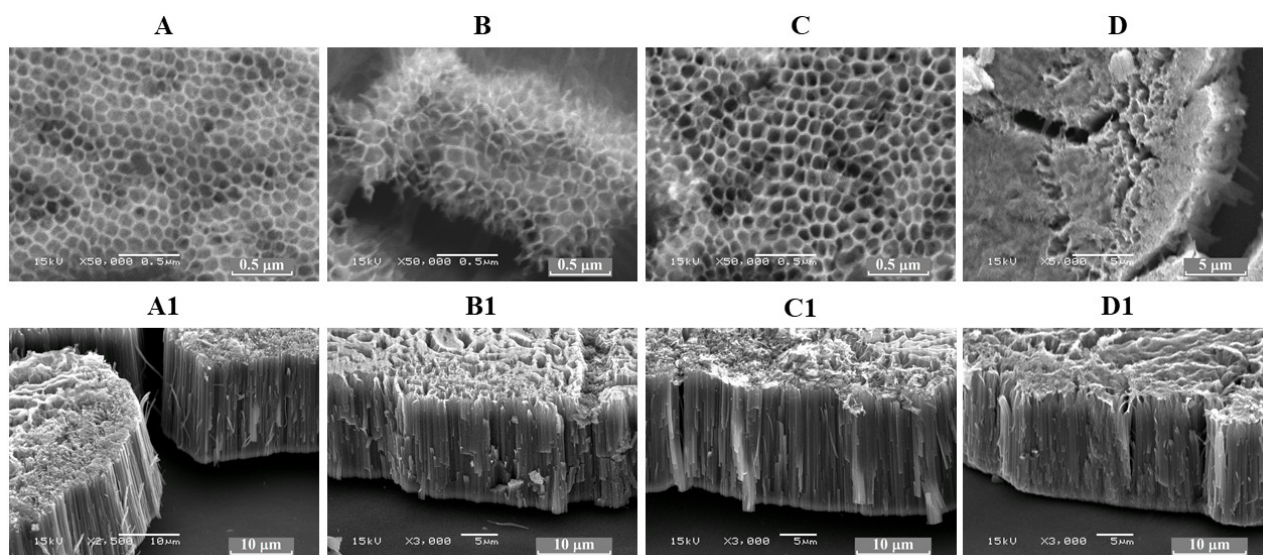


FIG. 1. SEM images (SE mode) of the TNT photoanodes obtained by two-stage titanium anodization (see text for detail). A – pure TNT film; B, C, D – CdO cathodically deposited with 50, 200 and 800 mC, respectively. Images A1, B1, C1, D1 were acquired at sample inclination of  $45^\circ$  relative to the incident electron beam

X-ray diffraction patterns and Raman spectra of the TNT-(0.05)CdO, TNT-(0.2)CdO, TNT-(0.8)CdO (Fig. 2) samples show absence of peaks due to CdO or  $\text{CdTiO}_3$ . The patterns/spectra are virtually identical and correspond to the anatase polymorph of  $\text{TiO}_2$ . The relative intensity of the 004 and 105 anatase reflections varies slightly between the samples, reflecting minor differences in texture of the deposited films. The 004 texture of the deposited TNT films is much less pronounced than in our previous study of the TNT-based photoanodes [33]. The only minor change in the Raman spectra is a slight decrease in intensity of the  $A_{1g}$  and of the  $B_{1g}$  peaks ( $517$  and  $395\ \text{cm}^{-1}$ , respectively) relative to the  $E_g$  mode observable for the two samples with the highest amount of the deposited CdO. These variations are difficult to discuss quantitatively, but may also correspond to texture. Fig. 1(D and D1) demonstrate that at the highest electric charge (0.8 C) during the CdO electrodeposition the surface of the TNT becomes “smeared”, presumably, due to large amount of defects. Nevertheless, even in this sample separate Cd-rich phase are not formed. This implies formation of cadmium solid solution in titania.

Positions of Ti 2p transitions in X-ray photoelectron spectra correspond to anatase. Positions of the Cd  $3d_{5/2}$  and  $3d_{3/2}$  peaks ( $405.6$  and  $412.5\ \text{eV}$ , respectively) are slightly higher than reported for CdO (e.g., compilation at <https://xpsdatabase.net/>, accessed on 13.11.2024), which implies lowering of the electron density on Cd ions, presumably, due to distortions of the  $\text{TiO}_2$ -CdO solid solution lattice and/or presence of vacancies (Fig. A2, Appendix). The shift may be also related to electron transfer from Cd to Ti as suggested in [15].

Figure A3 (Appendix) shows TEM image of a carbon replica from the TNT-(0.2)CdO sample. The TNT array is covered by micron-size spherulites. Most likely, the formation of the spherulites results from incorporation of large amount of Cd impurity into anatase lattice. Note that texture, pronounced in spherulites, is also manifested in Raman spectra.

#### 3.1. Photoelectrocatalytic degradation of methanol, ethylene glycol, glycerol and sorbitol aqueous solutions in $0.1\ \text{M}\ \text{Na}_2\text{SO}_4$

Figure 3A shows voltammograms of photoelectrochemical oxidation of water and of several alcohols on the prepared TNT photoanode. Addition of the alcohols into the aqueous solution shifts the photoanode potential towards the cathode

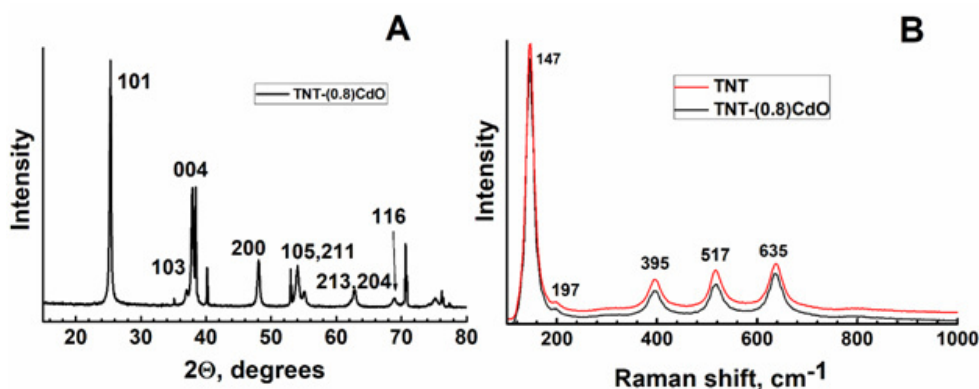


FIG. 2. Phase composition of the TNT-CdO samples after cathodic deposition of CdO. A – X-ray diffraction pattern, reflections of anatase are noted. Sharp peaks correspond to titanium substrate. B – the Raman spectrum of the initial TNT and of the TNT-(0.8)CdO sample, positions of the main anatase peaks are indicated. The curves are displaced vertically for clarity

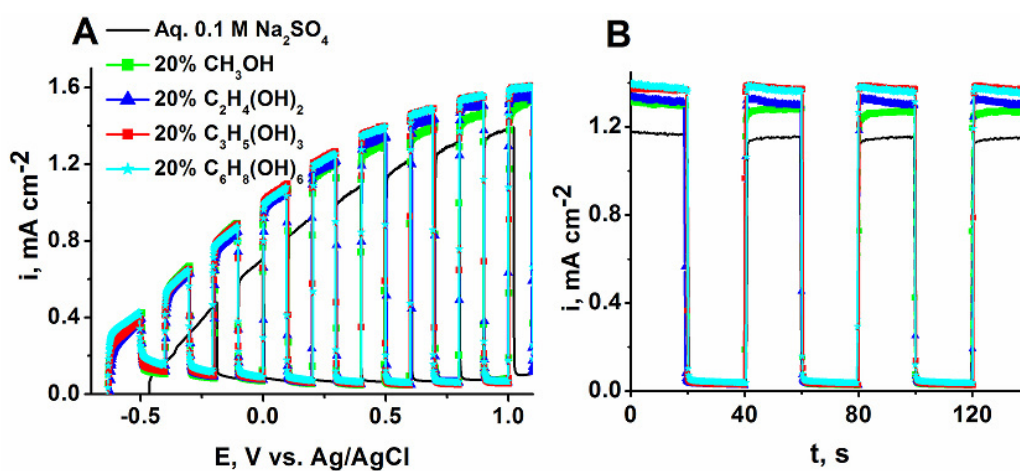


FIG. 3. Voltammetry of the TNT photoanode under the “light–dark” conditions. A – Voltammograms of the TNT photoanode; B – Photocurrent transients measured at  $E = 0.5$  V (vs. Ag/AgCl). The background solution (black curve) corresponds to aqueous 0.1 M Na<sub>2</sub>SO<sub>4</sub> solution. Other curves correspond to the background solution with 20 % addition of CH<sub>3</sub>OH, C<sub>2</sub>H<sub>4</sub>(OH)<sub>2</sub>, C<sub>3</sub>H<sub>5</sub>(OH)<sub>3</sub>, C<sub>6</sub>H<sub>8</sub>(OH)<sub>6</sub>, respectively. Illumination is performed by a sunlight simulator with a power density of 100 mW·cm<sup>-2</sup>. Potential scan rate is 10 mV·s<sup>-1</sup>

one; the oxidation photocurrents increase with the alcohol atomicity. Time-dependent transients of the oxidation photocurrents of water and of the alcohols on the TNT photoanode at a potential 0.5 V rel. Ag/AgCl (Fig. 3B) confirm the voltammetry results. The oxidation photocurrents of glycerin and sorbitol are virtually equal and are the highest (0.2 – 0.3 mA) among the studied compounds. This indicated that concentration of photogenerated holes reaches plateau and does not depend on number of hydroxyls (from 3 to 6) in the alcohol molecule.

Water photooxidation currents decrease in line with the increase of the CdO admixture to the TNT photoanode (Fig. 4A). This also follows from behavior of photocurrent transients (Fig. 4B), measured at a potential of 0.5 V relative to Ag/AgCl, as a function of the current spent for the Cd electrodeposition. Presumably, CdO admixture in TNT decreases the photoelectrocatalytic activity of the photoanode in oxidation of water molecules due to changes in rates of the relevant processes (recombination rate and rate of the charge transfer to a depolarizer molecule).

Earlier [31] we have shown that alcohol photoelectrooxidation current on an illuminated photoanode may correlate with number of alcohol structural groups. The highest photoelectrocatalytic currents were obtained for the sorbitol, the influence of the CdO modification of the TNT photoanodes is discussed on an example of this six-atomic alcohol. Fig. 5 shows that addition of 20 % (5.4 mM) of sorbitol into 0.1 M Na<sub>2</sub>SO<sub>4</sub> solution leads to considerable increase of integral photoelectrocatalytic process on all CdO-promoted TNT photoanodes in comparison with water oxidation. The largest effect is observed for the TNT-(0.8)CdO photoanode. Fig. 6 reveals that the photoelectrooxidation currents for the six-atomic sorbitol and for one-atomic methanol are virtually equal, but the molar sorbitol concentration is approximately six times lower.

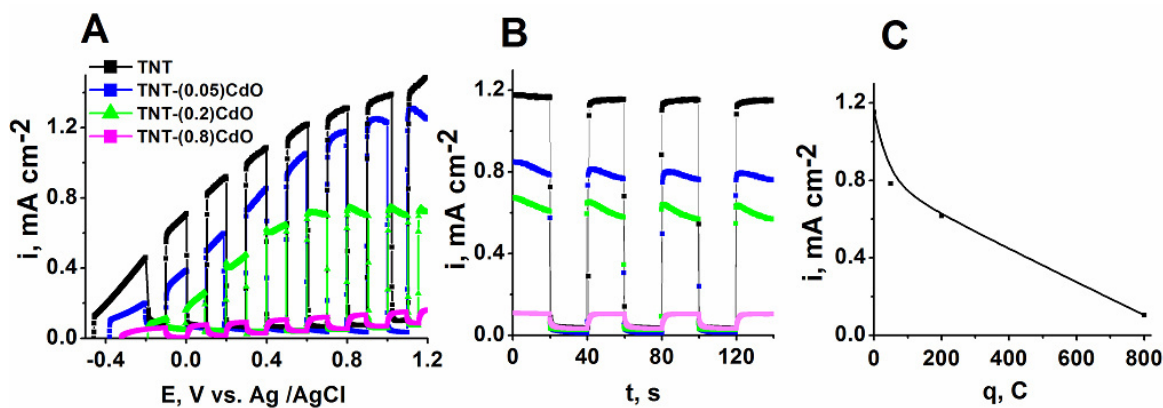


FIG. 4. Electrochemical measurements for the TNT-( $x$ )CdO photoanodes under “light–dark” conditions in 0.1 M  $\text{Na}_2\text{SO}_4$  aqueous solution. A – voltammograms curves; B – Photocurrent transients measured in 0.1 M  $\text{Na}_2\text{SO}_4$  aqueous solution at  $E = 0.5$  V (vs. Ag/AgCl); C – Dependence of the water photoelectrooxidation current at  $E = 0.5$  V (vs. Ag/AgCl) as a function of the amount of deposited CdO

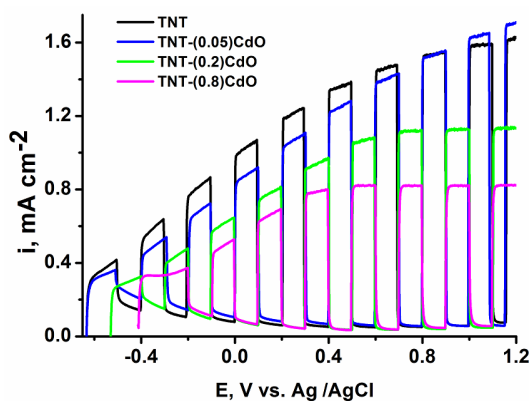


FIG. 5. Voltammograms under “light–dark” conditions in aqueous solution of 0.1 M  $\text{Na}_2\text{SO}_4$  + 20 %  $\text{C}_6\text{H}_8(\text{OH})_6$  for the photoanodes: TNT, TNT-(0.05)CdO, TNT-(0.2)CdO, TNT-(0.8)CdO

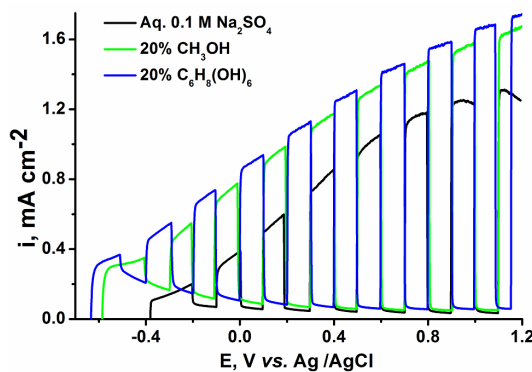


FIG. 6. Voltammograms of the TNT-(0.05)CdO photoanode under conditions “light–dark”. The background solution (black curve) is for the aqueous 0.1 M  $\text{Na}_2\text{SO}_4$  solution. Other curves correspond to the background solution with 20 % addition of  $\text{CH}_3\text{OH}$ ,  $\text{C}_6\text{H}_8(\text{OH})_6$ , respectively. Illumination is performed by a sunlight simulator with a power density of  $100 \text{ mW}\cdot\text{m}^{-2}$ . Potential scan rate is  $10 \text{ mV}\cdot\text{s}^{-1}$

Even minimal admixture of CdO in TNT increases partial currents of sorbitol photoelectrooxidation at least two times in comparison with pure TNT photoanode. Transients of the photoelectrooxidation currents are shown in Fig. 7. The dependence of the sorbitol photoelectrocatalysis on amount of deposited Cd is shown in Fig. 8.

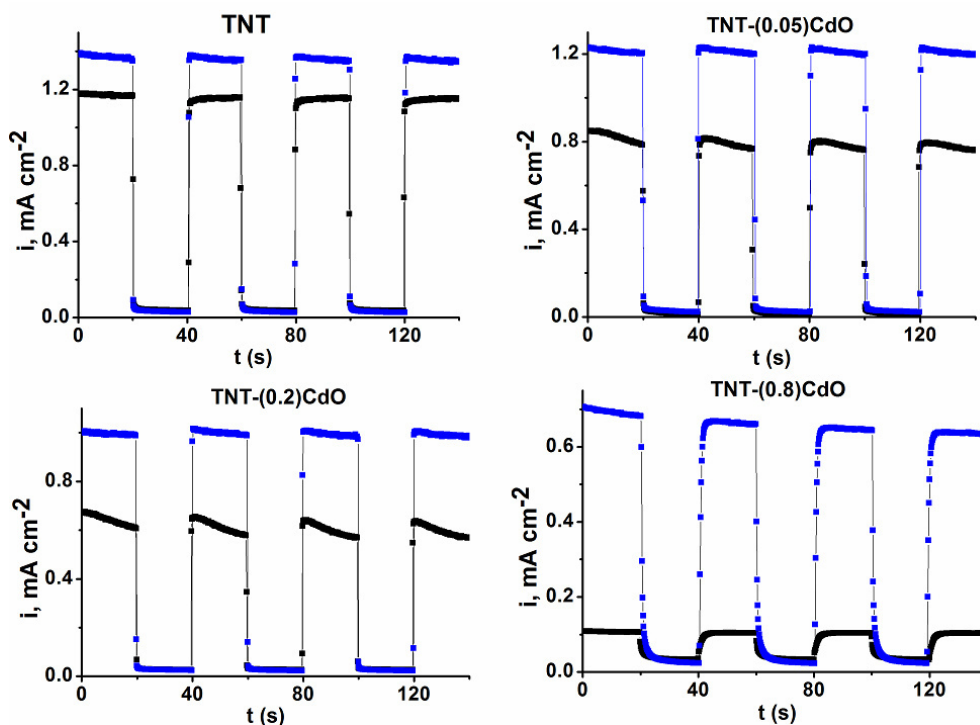


FIG. 7. Photocurrent transients measured in 0.1 M Na<sub>2</sub>SO<sub>4</sub> aqueous solution with addition of 20 % of C<sub>6</sub>H<sub>8</sub>(OH)<sub>6</sub> at  $E = 0.5$  V (vs. Ag/AgCl) for the TNT  $-(x)$ CdO photoanodes. For all panels, the blue curve corresponds to the solution with added C<sub>6</sub>H<sub>8</sub>(OH)<sub>6</sub>; the black curve – to the pure 0.1 M Na<sub>2</sub>SO<sub>4</sub> solution

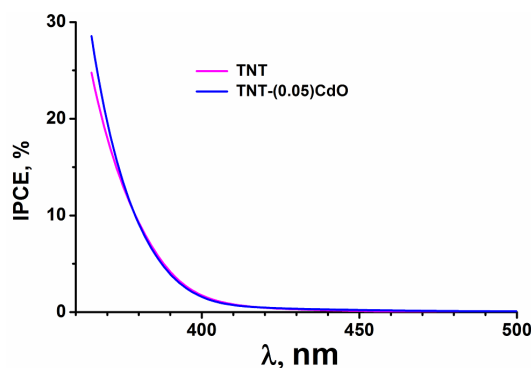


FIG. 8. Dependence of the partial current of photoelectrooxidation of 5.4 mM C<sub>6</sub>H<sub>8</sub>(OH)<sub>6</sub> at  $E = 0.5$  V (vs. Ag/AgCl) on the amount of deposited CdO

### 3.2. Estimation of recombination losses in the photoelectrooxidation of sorbitol

Figure A4 (Appendix) shows wavelength dependence of incident photon to current efficiency (IPCE %) for the TNT and TNT-(0.05)CdO photoanodes in 0.1 M Na<sub>2</sub>SO<sub>4</sub> aqueous solution. The sharp rise of the photocurrent is observed below  $\sim 400$  nm, which is consistent with crystalline anatase. Formation of the solid solution upon Cd addition does not shift neither the IPCE, nor the optical absorption spectra (relative to pure anatase in the latter case).

Recombination losses of photogenerated holes in the TNT photoanode in course of water and sorbitol photooxidation were studied using Intensity-modulated photocurrent spectroscopy (IMPS) [34–36]. Monochromatic light with wavelength of 385 nm ( $8 \text{ mW} \cdot \text{cm}^{-2}$  power density) was selected since it corresponds to IPCE % values (Fig. 9), providing sufficient precision of the IMPS measurements. The IMPS spectra were obtained in 0.1 M Na<sub>2</sub>SO<sub>4</sub> and in 0.1 M Na<sub>2</sub>SO<sub>4</sub> + 5.4 mM sorbitol solutions at 0.2 V potential. The high frequency intercept of the IMPS curve with the abscissa gives total

amount of photogenerated current  $I_2$ . The low-frequency part gives  $I_1$ , corresponding to oxidation of compounds present in the electrolyte. For the 0.1 M  $\text{Na}_2\text{SO}_4$  solution, high curvature of the IMPS trace in the first quadrant at low modulation frequency (Fig. 9A) points to recombination losses at the TNT photoanode in course of water oxidation. Subsequently,  $I_1 < I_2$ . Sorbitol addition markedly increases  $I_2$  value (the radius of the IMPS semi-circle increases). Larger  $I_2$  values reflect higher oxidation rate of sorbitol in comparison with water; weak bending of the IMPS curve in the first quadrant suggests lower recombination losses.

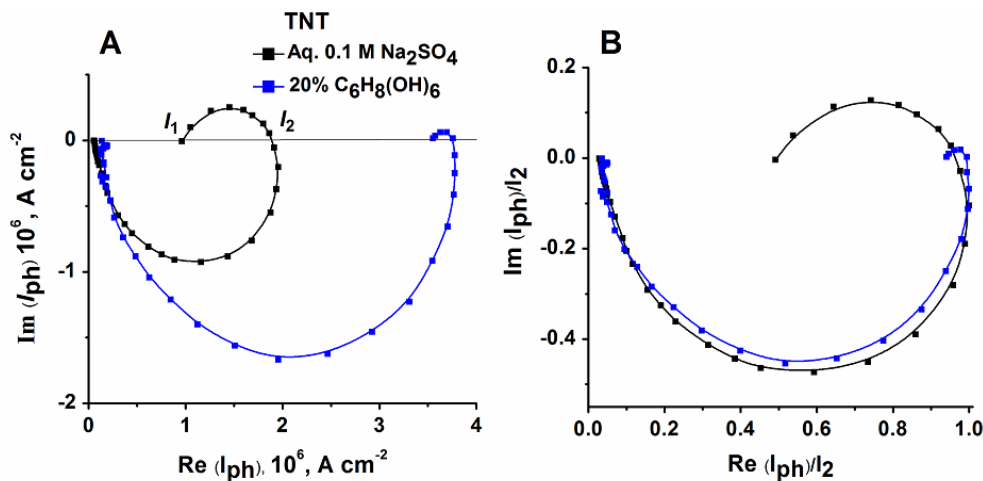


FIG. 9. IMPS (A) and normalized IMPS (B) dependences measured at  $E = 0.2$  V (vs. Ag/AgCl) on the TNT photoanode. Illumination is performed by monochromatic 385 nm light,  $8 \text{ mW}\cdot\text{cm}^{-2}$  power density

For quantitative analysis, the IMPS curves were normalized to  $I_2$  (Fig. 9). In 0.1 M  $\text{Na}_2\text{SO}_4$  at  $E = 0.2$  V, the water oxidation photocurrent reaches 50 % of the total photogenerated current,  $I_1/I_2 = 0.5$  (Fig. 9B, black curve); the recombination losses are also  $\sim 50$  %,  $(I_2 - I_1)/I_2 = 0.5$ . Addition of 5.4 mM of sorbitol reduces the losses to  $\sim 7$  % (Fig. 9B, blue curve), since higher photooxidation rate of sorbitol consume the holes from surface states of the TNT photoanode.

The IMPS measurements allow estimation of the recombination rate constant  $K_{\text{rec}}$  and charge transfer constant  $K_{\text{ct}}$ . The  $I_1/I_2$  ratio of the low frequency part of the IMPS spectrum is related to these constants as  $I_1/I_2 = K_{\text{ct}}/(K_{\text{rec}} + K_{\text{ct}})$ . The frequency of the light intensity in the semi-circle maximum in the first quadrant ( $f_{\text{max}}$ ) is related to  $K_{\text{rec}}$  and  $K_{\text{ct}}$  by the equation  $2\pi f_{\text{max}} = (K_{\text{rec}} + K_{\text{ct}})$ . In case of water photoelectrooxidation on the TNT photoanode at  $E = 0.2$  V the calculated values of  $K_{\text{ct}}$  and  $K_{\text{rec}}$  are  $0.247$  and  $0.247 \text{ s}^{-1}$ , respectively. For the sorbitol photoelectrooxidation  $K_{\text{ct}} = 0.46 \text{ s}^{-1}$  and  $K_{\text{ct}} \gg K_{\text{rec}} = 0.034 \text{ s}^{-1}$ ; thus, sorbitol is more efficient acceptor of the photogenerated holes than water molecules.

Figure 10 shows that even minute admixture of Cd in the titania nanotubes leads to marked decrease of the recombination losses (there is no bend in the IMPS in the first quadrant at low modulation frequency). This observation is in line with increase of partial photocurrents of sorbitol oxidation on the Cd-promoted anode in comparison with the pure TNT photoanode (Fig. 7). Consequently, a photoanode based on Cd-promoted titania nanotubes is an efficient photoelectrocatalyser of sorbitol degradation. Presumably, the enhancement of this photoanode properties is due to small recombination losses of the photogenerated charges ( $K_{\text{rec}} \ll 0.034 \text{ s}^{-1}$ ) and higher charge transfer rate ( $K_{\text{ct}} > 0.46 \text{ s}^{-1}$ ) to a stronger acceptor.

Modification of TNT with CdO markedly increases sorbitol photoelectrooxidation rate both because of the smaller recombination constant and due to larger constant of the charge transfer to more efficient holes acceptor. Therefore, CdO-modified photoanodes from titania nanotubes may be employed for photoelectrochemical degradation of sorbitol and of other alcohols, by-products of biofuel manufacturing.

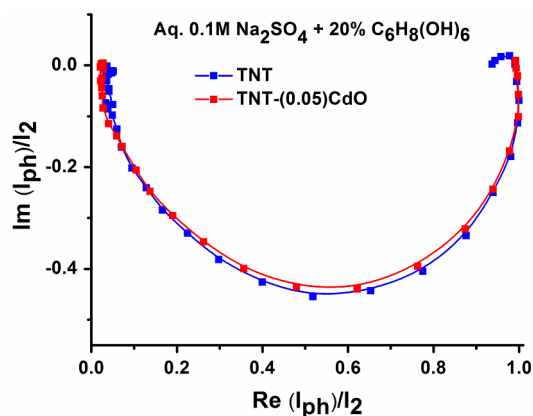


FIG. 10. IMPS dependences measured at  $E = 0.2$  V (vs. Ag/AgCl) on the TNT and TNT-(0.05)CdO photoanodes in aqueous 0.1 M Na<sub>2</sub>SO<sub>4</sub> with 20 % addition of C<sub>6</sub>H<sub>8</sub>(OH)<sub>6</sub>. Illumination is performed by monochromatic 385 nm light, 8 mW·cm<sup>-2</sup> power density

#### 4. Conclusions

Nanostructured photoanodes consisting of titania (anatase) nanotubes on a titanium substrate were fabricated by electrochemical anodization of Ti metal foil in ethylene glycol with addition of 0.5 wt.% NH<sub>4</sub>F and 2 wt.% of water. Subsequently, various amounts of CdO were electrochemically deposited. At the employed conditions solid solutions CdO-TiO<sub>2</sub> were formed. Under illumination with solar light simulator, obtained photoanodes demonstrate high activity in photoelectrochemical degradation of alcohols, and, in particular, of sorbitol (C<sub>6</sub>H<sub>8</sub>(OH)<sub>6</sub>) in aqueous 0.1 M Na<sub>2</sub>SO<sub>4</sub> solution. The photoactivity increases with amount of CdO in the photoanode. Results of intensity-modulated photocurrent spectroscopy show that despite significant reduction in recombination losses due to formation of the CdO-TiO<sub>2</sub> solid solution, rate of water oxidation drops, presumably due to decrease of the charge transfer constant to H<sub>2</sub>O molecules.

#### Appendix

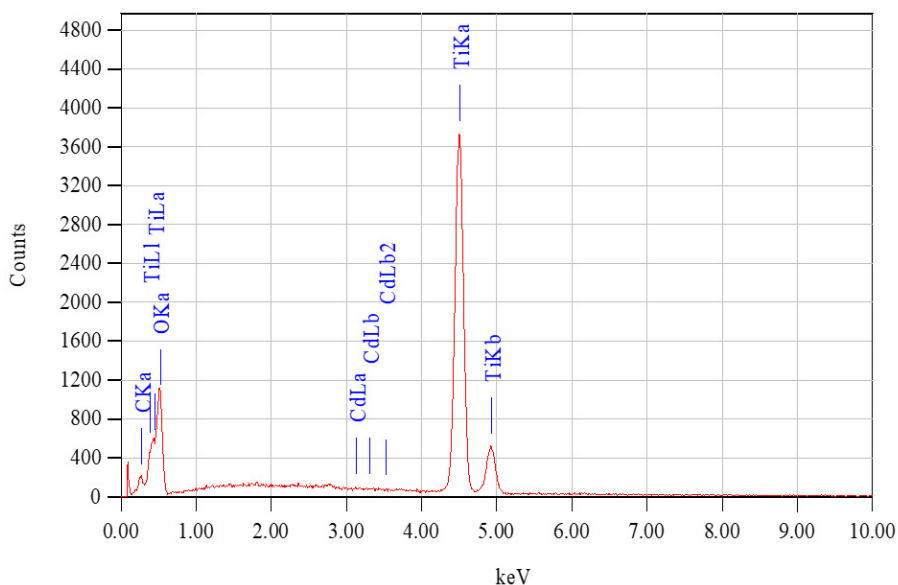


FIG. A1. Typical EDX spectrum of the samples TiO<sub>2</sub>-NTbs promoted by CdO and Standardless Quantitative Analysis of samples with different cadmium oxide content presented in the Tables A1-A3

TABLE A1. ZAF Method Standardless Quantitative Analysis (0.05 C). Fitting Coefficient: 0.2626

Element	(keV)	Mass %	Error %	At % Compound	Mass % Cation K
C K	0.277	1.97	0.05	4.73	1.2149
O K	0.525	30.27	0.47	54.57	12.6515
Ti K	4.508	67.46	0.34	40.63	85.7918
Cd L*	3.132	0.30	0.47	0.08	0.3418
Total		100.00		100.00	

TABLE A2. ZAF Method Standardless Quantitative Analysis (0.2 C). Fitting Coefficient: 0.2679

Element	(keV)	Mass %	Error %	At % Compound	Mass % Cation K
C K	0.277	2.17	0.05	5.02	1.3691
O K	0.525	33.10	0.43	57.51	14.6929
Ti K	4.508	64.45	0.33	37.40	83.6111
Cd L*	3.132	0.28	0.46	0.07	0.3269
Total		100.00		100.00	

TABLE A3. ZAF Method Standardless Quantitative Analysis (0.8 C). Fitting Coefficient: 0.2617

Element	(keV)	Mass %	Error %	At % Compound	Mass % Cation K
C K	0.277	1.62	0.05	3.91	1.0134
O K	0.525	30.89	0.45	55.88	13.1659
Ti K	4.508	65.86	0.33	39.79	83.9665
Cd L*	3.132	1.62	0.46	0.42	1.8542
Total		100.00		100.00	

TABLE A4. Binding energy and the composition of the sample TiO<sub>2</sub>-NTbs promoted by cadmium oxide (0.2 C/cm<sup>2</sup>)

Peak name		Eb, eV	Quant., at. %	
Ti2p	TiO <sub>2</sub>	459	25.95	25.95
Cd3d	Cd	405.6	0.12	0.12
	H <sub>2</sub> O	533	3.36	
O1s	C-O	531.8	10.81	73.93
	C=O	531	7.9	
	TiO <sub>2</sub>	530.2	51.86	

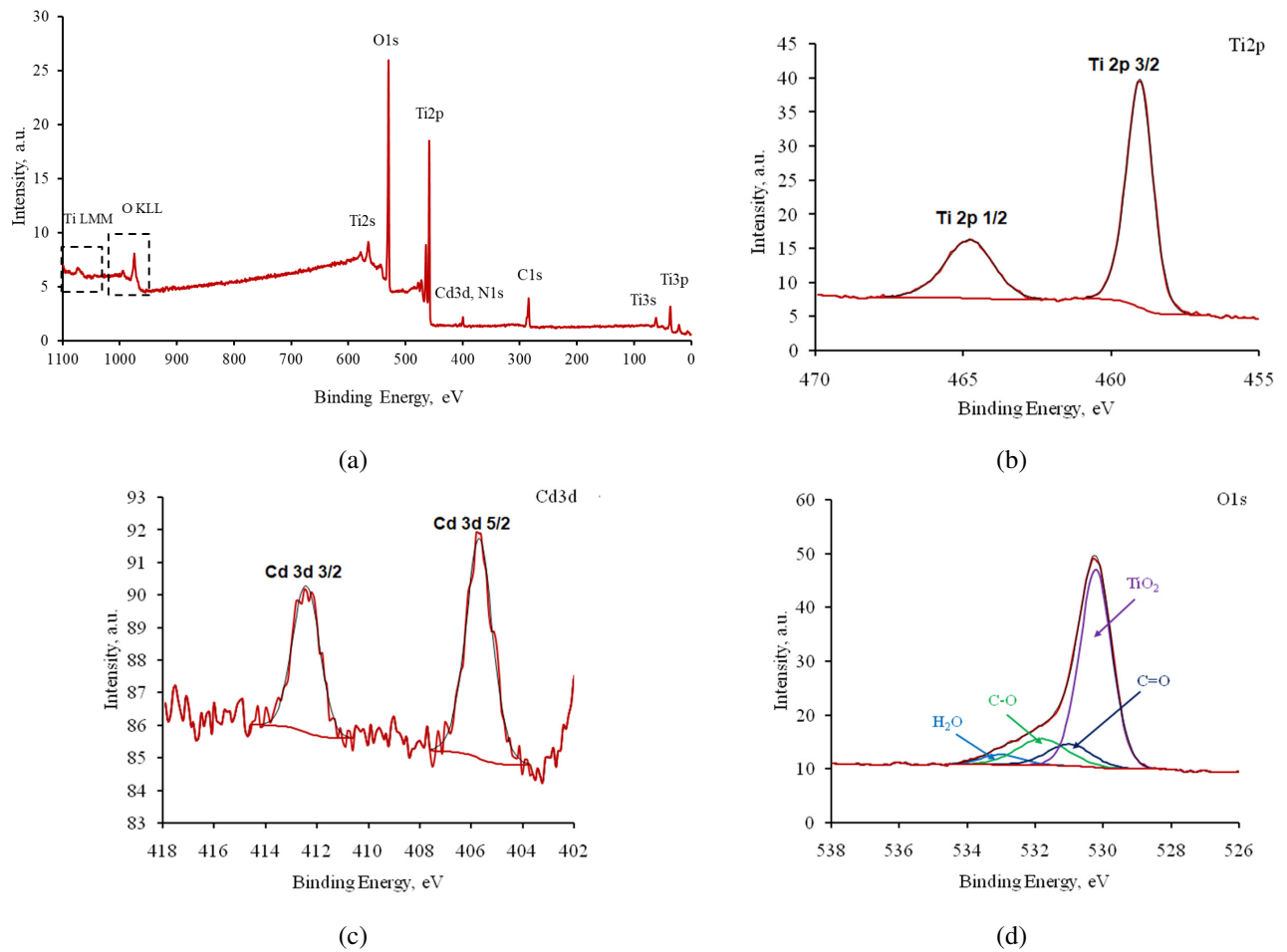


FIG. A2. XPS spectra of cadmium-modified TiO<sub>2</sub>-NTBs prepared by cathodic deposition of CdO (0.2 C/cm<sup>2</sup>) (a); High-resolution XPS spectra of Ti 2p, Cd 3d and O 1s (b–d). The sample was calcined at 450 °C in air for 1 h

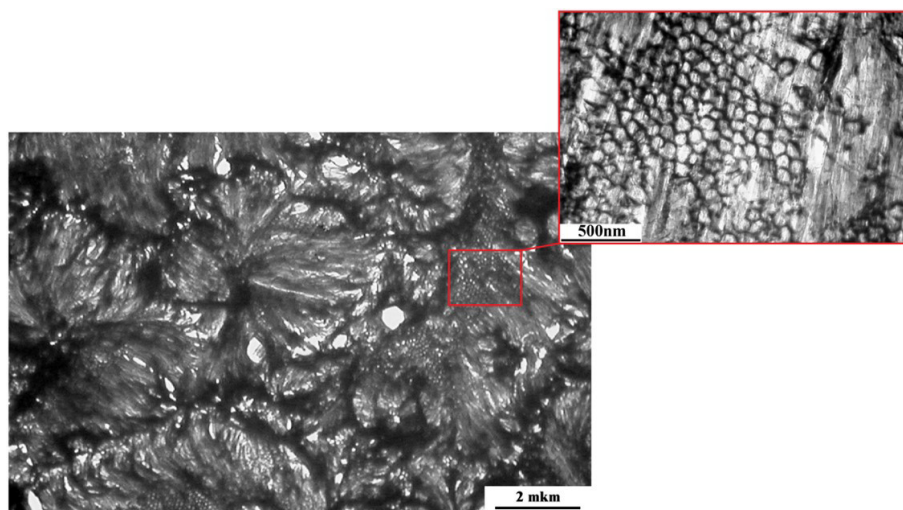


FIG. A3. TEM image of the supermolecular surface structure of TNT-(0.2)CdO

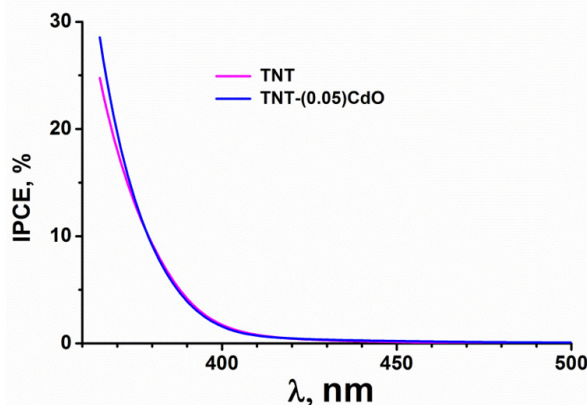


FIG. A4. Wavelength dependence of IPCE% for the TNT and TNT-(0.05)CdO photoanodes in 0.1 M  $\text{Na}_2\text{SO}_4$  aqueous solution

## References

- [1] Xia Y., Yang P., Sun Y., Wu Y., Mayers B., Gates B., et al. One-dimensional nanostructures: synthesis, characterization, and applications. *Adv. Mater.*, 2003, **15**, P. 353–389.
- [2] Banerjee S., Mohapatra S.K., Das P.P., Misra M. Synthesis of coupled semiconductor by filling 1D  $\text{TiO}_2$  nanotubes with CdS. *Chem Mater.*, 2008, **20**, P. 6784–6791.
- [3] Zwilling V., Darque-Ceretti E., Boutry-Forveille A., David D., Perrin M.Y., Aucouturier M. Structure and physicochemistry of anodic oxide films on titanium and TA6V alloy. *Surf. Interface Anal.*, 1999, **27**, P. 629–637.
- [4] Gong D., Grimes C.A., Varghese O.K., Hu W., Singh R.S., Chen Z., et al. Titanium oxide nanotube arrays prepared by anodic oxidation. *J. Mater. Res.*, 2001, **16** (12), P. 3331–3334.
- [5] Mohapatra S.K., Misra M., Mahajan V.K., Raja K.S. Design of a highly efficient photoelectrolytic cell for hydrogen generation by water splitting: Application of  $\text{TiO}_{2-x}\text{C}_x$  nanotubes as a photoanode and Pt/ $\text{TiO}_2$  nanotubes as a Cathode. *The J. of Physical Chemistry C*, 2007, **111** (24), P. 8677–8685.
- [6] Roy P., Berger S., Schmuki P.  $\text{TiO}_2$  Nanotubes: Synthesis and Applications. *Angew. Chem. Int. Ed.*, 2011, **50**, P. 2904–2939.
- [7] Smith Y.R., Subramanain V. Heterostructural Composites of  $\text{TiO}_2$  Mesh– $\text{TiO}_2$  Nanoparticles Photosensitized with CdS: A New Flexible Photoanode for Solar Cells. *J. Phys. Chem. C*, 2011, **115**, P. 8376–8385.
- [8] Liu Y., Zhou H., Zhou B., Li J., Chen H., Wang J., et al. Highly stable CdS-modified short  $\text{TiO}_2$  nanotube array electrode for efficient visible-light hydrogen generation. *Int. J. Hydrogen Energy*, 2011, **36**, P. 167–174.
- [9] Kongkanand A., Tvrdy K., Takechi K., Kuno M., Kamat P.V. Quantum Dot Solar Cells. Tuning Photoresponse through Size and Shape Control of CdSe– $\text{TiO}_2$  Architecture. *J. Am. Chem. Soc.*, 2008, **130**, P. 4007–4015.
- [10] Hossain M.F., Biswas S., Zhang Z.H., Takahashi T. Bubble-like CdSe nanoclusters sensitized  $\text{TiO}_2$  nanotube arrays for improvement in solar cell. *J. Photochem. Photobiol. A: Chem.*, 2011, **217**, P. 68–75.
- [11] Banerjee S., Mohapatra S.K., Misra M. Water Photooxidation by  $\text{TiSi}_2$ – $\text{TiO}_2$  Nanotubes. *J. Phys. Chem. C*, 2011, **115** (25), P. 12643–12649.
- [12] Mohapatra S.K., Banerjee S., Misra M. Synthesis of  $\text{Fe}_2\text{O}_3/\text{TiO}_2$  nanorod–nanotube arrays by filling  $\text{TiO}_2$  nanotubes with Fe. *Nanotechnology*, 2008, **19**, 315601.
- [13] Shrestha N.K., Yang M., Nah Y.-C., Paramasivam I., Schmuki P. Self-organized  $\text{TiO}_2$  nanotubes: Visible light activation by Ni oxide nanoparticle decoration. *Electrochem. Commun.*, 2010, **12**, P. 254–257.
- [14] Dong W., Zhu C. Optical properties of surface-modified CdO nanoparticles. *Opt. Mater.*, 2003, **22**, P. 227–233.
- [15] Sarma B., Smith Y., Mohanty S.K., Misra M. Electrochemical deposition of CdO on anodized  $\text{TiO}_2$  nanotube arrays for enhanced photoelectrochemical properties. *Materials Letters*, 2012, **85**, P. 33–36.
- [16] Wang X., Cheng K., Dou S., Chen Q., Wang J., Song Z., Zhang J., Song H. Enhanced photoelectrochemical performance of CdO– $\text{TiO}_2$  nanotubes prepared by direct impregnation. *Applied Surface Science*, 2019, **476**, P. 136–143.
- [17] Tang D., Lu G., Shen Z., Hu Y., Yao L., Li B., Zhao G., Peng B., Huang X. A review on photo-, electro- and photoelectro- catalytic strategies for selective oxidation of alcohols. *J. of Energy Chemistry*, 2023, **77**, P. 80–118.
- [18] Ruppert A.M., Weinberg K., Palkovits R. Hydrogenolyse goes Bio: Von Kohlenhydraten und Zuckerkohlen zu Plattformchemikalien. *Angew. Chem.*, 2012, **124**, P. 2614–2654.
- [19] Cortright R.D., Davda R.R., Dumesic J.A. Hydrogen from catalytic reforming of biomass-derived hydrocarbons in liquid water. *Nature*, 2002, **418**, P. 964–967.
- [20] Metzger J.O. Production of Liquid Hydrocarbons from Biomass. *Angew. Chem. Int. Ed.*, 2006, **45**, P. 696–698.
- [21] Huber G.W., Shabaker J.W., Dumesic J.A. Raney Ni–Sn Catalyst for  $\text{H}_2$  Production from Biomass-Derived Hydrocarbons. *Science*, 2003, **300**, P. 2075–2077.
- [22] de Almeida R.M., Li J., Nederlof C., O'Connor P., Makkee M., Moulijn J.A. Cellulose Conversion to Isosorbide in Molten Salt hydrate Media. *ChemSusChem*, 2010, **3**, P. 325–328.
- [23] Zhang Z., Wang P. Optimization of photoelectrochemical water splitting performance on hierarchical  $\text{TiO}_2$  nanotube arrays. *Energy Environ Sci.*, 2012, **5**, P. 6506–6512.
- [24] Kim H.I., Monllor-Satoca D., Kim W., Choi W. N-doped  $\text{TiO}_2$  nanotubes coated with a thin  $\text{TaO}_x\text{N}_y$  layer for photoelectrochemical water splitting: dual bulk and surface modification of photoanodes. *Energy Environ Sci.*, 2015, **8**, P. 247–257.
- [25] Denisenko A.V., Morozov A.N., Michailichenko A.I. Obtaining coating consisting of nanotubes  $\text{TiO}_2$  by anodizing the titanium in the electrolyte with an ethylene glycol with addition various amounts of water. *Adv. Chem & Chem. Techn.*, 2015, **29** (3), P. 71–73.

- [26] Ghicov A., Schmuki P. Self-Ordering Electrochemistry: A Review on Growth and Functionality of TiO<sub>2</sub> Nanotubes and Other Self-Aligned MO<sub>x</sub> Structures. *Chemical Communications*, 2009, **45**, P. 2791–2808.
- [27] Robin A., de Almeida Ribeiro M.B., Rosa J.L., Nakazato R.Z., Silva M.B. Formation of TiO<sub>2</sub> nanotube layer by anodization titanium in ethylene glycol-H<sub>2</sub>O electrolyte. *J. Surf. Eng. Mater. & Adv. Techn.*, 2014, **41**, P. 23–130.
- [28] Grinberg V.A., Emets V.V., Modestov A.D., Averin A.A., Shiryaev A.A. Thin-Film Nanocrystalline Zinc Oxide Photoanode Modified with CdO in Photoelectrocatalytic Degradation of Alcohols. *Coatings*, 2023, **13**, 1080.
- [29] Santamaria M., Bocchetta P., Quarto F.D. Room temperature electrodeposition of photoactive Cd(OH)<sub>2</sub> nanowires. *Electrochem. Commun.*, 2009, **11**, P. 580–584.
- [30] Gujar T.P., Shinde V.R., Kim W.Y., Jung K.D., Lokhande C.D., Joo O.S. Formation of CdO films from chemically deposited Cd(OH)<sub>2</sub> films as a precursor. *Appl. Surf. Sci.*, 2008, **254**, P. 3813–3818.
- [31] Grinberg V.A., Emets V.V., Mayorova N.A., Averin A. A., Shiryaev A.A. Photoelectrocatalytic Activity of ZnO-Modified Hematite Films in the Reaction of Alcohol Degradation. *Int. J. Mol. Sci.*, 2023, **24** (18), 14046.
- [32] Grinberg V.A., Emets V.V., Mayorova N.A., Averin A.A., Shiryaev A.A. Sn-Doped Hematite Films as Photoanodes for Photoelectrochemical Alcohol Oxidation. *Catalysts*, 2023, **13** (11), 1397.
- [33] Grinberg V.A., Emets V.V., Shapagin A.V., Averin A.A., Shiryaev A.A. Effect of the length of TiO<sub>2</sub> nanotubes on the photoelectrochemical oxidation of phenylacetic acid anions. *J. of Solid State Electrochemistry*, 2024, **29** (2), P. 629–638.
- [34] Peter L.M., Ponomarev E.A., Fermin D.J. Intensity-modulated photocurrent spectroscopy: Reconciliation of phenomenological analysis with multistep electron transfer mechanisms. *J. Electroanal. Chem.*, 1997, **427**, P. 79–96.
- [35] Peter L.M., Wijayantha K.G.U., Tahir A.A. Kinetics of light-driven oxygen evolution at a-Fe<sub>2</sub>O<sub>3</sub> electrodes. *J. Faraday Discuss.*, 2012, **155**, P. 309–322.
- [36] Klotz D., Ellis D.S., Dotana H., Rothschild A. Empirical in operando Analysis of the Charge Carrier Dynamics in Hematite Photoanodes by PEIS, IMPS and IMVS. *J. Phys. Chem. Chem. Phys.*, 2016, **18**, P. 23438–23457.

---

*Submitted 21 January 2025; revised 6 March 2025; accepted 5 May 2025*

#### *Information about the authors:*

**Vitali A. Grinberg** – Frumkin Institute of Physical Chemistry and Electrochemistry, Russian Academy of Sciences, Laboratory of processes in chemical current sources, Leninsky Prospekt 31, Building 4, 119071 Moscow, Russia; ORCID 0000-0003-3223-3194; vitgreen@mail.ru

**Victor V. Emets** – Frumkin Institute of Physical Chemistry and Electrochemistry, Russian Academy of Sciences, Electro-catalysis laboratory, Leninsky Prospekt 31, Building 4, 119071 Moscow, Russia; ORCID 0000-0003-2746-449X; Victoremets@mail.ru

**Aleksey V. Shapagin** – Frumkin Institute of Physical Chemistry and Electrochemistry, Russian Academy of Sciences, Laboratory of structural and morphological research, Leninsky Prospekt 31, Building 4, 119071 Moscow, Russia; ORCID 0000-0002-8866-0710; shapagin@mail.ru

**Aleksey A. Averin** – Frumkin Institute of Physical Chemistry and Electrochemistry, Russian Academy of Sciences, Laboratory of new physical and chemical problems, Leninsky Prospekt 31, Building 4, 119071 Moscow, Russia; ORCID 0000-0003-2895-8539; alx.av@yandex.ru

**Andrei A. Shiryaev** – Frumkin Institute of Physical Chemistry and Electrochemistry, Russian Academy of Sciences, Laboratory of new physical and chemical problems, Leninsky Prospekt 31, Building 4, 119071 Moscow, Russia; ORCID 0000-0002-2467-825X; a\_shiryaev@mail.ru

*Conflict of interest:* the authors declare no conflict of interest.

## Investigation of morphological features and thermal stability of regenerated wood cellulose from solutions in [BMIm]Cl

Mariya G. Mikhaleva<sup>1,a</sup>, Sergey V. Usachev<sup>1,b</sup>, Alexander S. Vedenkin<sup>1,2,c</sup>, Mariya I. Ikim<sup>1,d</sup>, Galina G. Politenkova<sup>1,e</sup>, Sergey M. Lomakin<sup>2,f</sup>

<sup>1</sup>N.N. Semenov Federal Research Center for Chemical Physics, Russian Academy of Sciences, Moscow, Russia

<sup>2</sup>Emanuel Institute of Biochemical Physics, Russian Academy of Sciences, Moscow, Russia

<sup>a</sup>maria.mikhaleva@chph.ras.ru, <sup>b</sup>usachevsv@inbox.ru, <sup>c</sup>alexander.vedenkin@chph.ras.ru,

<sup>d</sup>maria.ikim@chph.ras.ru, <sup>e</sup>galina.politenkova@chph.ras.ru, <sup>f</sup>lomakin@sky.chph.ras.ru

Corresponding author: Mariya G. Mikhaleva, maria.mikhaleva@chph.ras.ru

PACS 61.25.Hq

**ABSTRACT** A study of the morphological features of regenerated wood pulp LS-0 obtained from its solutions in [BMIm]Cl at concentrations ranging from 2 to 26 % has been performed. It was demonstrated that at concentrations of LS-0 up to 8 % in [BMIm]Cl, thermograms exhibited a reduction in thermal stability concomitant with an increase in coke residue. In samples of regenerated cellulose obtained from solutions with an LS-0 content of 14 % or more, two maxima are observed on the differential thermogravimetric curves (DTG). This phenomenon was explained by the presence of two phases formed during the dissolution-regeneration process. The impact of [BMIm]Cl on the structural characteristics of regenerated cellulose was investigated through IR spectroscopy and X-ray diffraction analysis.

**KEYWORDS** cellulose, ionic liquids, thermogravimetry, infrared spectroscopy, X-ray structural analysis

**ACKNOWLEDGEMENTS** The study was conducted under the state assignment of the Federal Research Center for Chemical Physics of the Russian Academy of Sciences.

**FOR CITATION** Mikhaleva M.G., Usachev S.V., Vedenkin A.S., Ikim M.I.M., Politenkova G.G., Lomakin S.M. Investigation of morphological features and thermal stability of regenerated wood cellulose from solutions in [BMIm]Cl. *Nanosystems: Phys. Chem. Math.*, 2025, **16** (3), 364–373.

### 1. Introduction

Cellulose, a renewable natural polymer, has long been the subject of considerable interest, both in terms of its potential applications in various spheres of human life and the study of its physicochemical properties [1–3]. The unique structure of cellulose is a combination of amorphous and crystalline particles that together determine its properties [4]. The fundamental monomeric unit is typically regarded as a cellobiose, which unites two glucose residues through a  $\beta$ -glycosidic bond [5]. In contrast to the typical  $\alpha$ -glycosidic linkages of starch, these linkages are more resistant to acid hydrolysis. The strength of the cellulose polymer chain is due to hydrogen bonds between hydroxyl groups included in cellobiose [6,7]. Interactions between adjacent chains lead to the formation of structural fragments – fibrils, which have an ordered structure and form microcrystalline regions [4]. This structure of cellulose determines its properties on the macro level. Depending on their origin, cellulose fibers have different degrees of polymerization (DP), which determine their field of application. Flax fibers have the greatest length [8], which allows them to be used in the production of ropes and in the textile industry. Cotton fibers have a lower DP and are primarily used in the textile industry. Wood cellulose, which is the most common, has a DP of 103 – 104 and is mainly used in paper production. Since cellulose does not allow direct processing, the chemical modification of its glycosidic units by the formation of ether groups has been used to expand the range of its applications [8]. This modification affects the hydroxyl groups of both amorphous and crystalline regions of cellulose. Based on this process, nitrocellulose [10], cellulose sulfite and acetate [11] were obtained. When cellulose is dissolved in Schweitzer's reagent (copper ammine) [12], spinning solutions are formed. When they are extruded into acidified water, free hydrated cellulose is formed. The dissolution of cellulose without its chemical modification has been demonstrated using dimethylacetamide with lithium chloride [13, 14], in aqueous solutions of transition metal complexes with amines, molten hydrates of inorganic salts [15], and various quaternary ammonium salts in DMSO [16, 17]. Other studies have used ionic liquids in DMSO [18] or N-methylimidazole [19], as well as a combination of the ionic liquid [BMIm]OAc with LiCl [14]. The use of mono-solvents allows them to be used in recycling. An illustrative example is N-methylmorpholin oxide (NMO), which was proposed in 1939 [20]. This compound was subsequently employed in the production of Liocell fibers. In this process, NMO is reused following its extraction from the wash water. Another group

of monosolvents are ionic liquids (ILs), formed by a cation-anion pair and having a melting point below 100 °C [21]. In 2002, a series of compounds based on an imidazolium cation with different anions were employed for the dissolution of cellulose [22]. In subsequent works, the range of IL employed for this process has been considerably expanded [23–25].

The interaction of ionic liquids with the polymer chains of cellulose results in the rupture of the hydrogen and intermolecular bonds that are present in its macro molecules. The dissolution of cellulose in IL involves a number of stages: infiltration, limited swelling, partial dissolution, dissociation, and complete dissolution [26]. Based on nuclear magnetic resonance (NMR) data, it has been revealed that the solvation of cellulose in the IL [BMIm]Cl occurs through the formation of hydrogen bonds between hydroxyl protons of the cellulose and the chloride ions that make up the IL [27]. Structural changes of microcrystalline cellulose (MCC) during its dissolution in [EMIm][OAc] over a wide concentration range (0 – 100 %) were investigated using small-angle X-ray scattering (SAXS) [28]. It was shown that at a cellulose content of about 35 % (mol) in solution, a cellulose/IL complex with high structural periodicity is formed, and a crystalline structure is observed at a concentration exceeding 40 % (mol). In addition to the study of solubility, an equally important issue is the study of the morphology of regenerated cellulose after its isolation from IL solutions [25, 29]. Previously, we published the results of studies of the structure of cellulose fibers obtained by extrusion of its solutions in [BMIm]Cl into water [30]. It was found that the fibers consist of a core consisting of pseudofibrils about 30 nm thick, and a shell. At the same time, the tensile strength averaged 250 MPa.

The aim of this work was to study the morphological features and thermal stability of wood cellulose LS-0, depending on its concentration in solutions based on the ionic liquid [BMIm]Cl.

## 2. Materials and methods

The ionic liquid 1-Butyl-3-methylimidazolium chloride [BMIm]Cl was prepared according to the procedure given previously [30].

FT-IR spectrum was recorded on a Bruker Tensor 27 spectrometer equipped with an ATR attachment (Pike MIRacle) with a germanium (Ge) crystal in the frequency range 800 – 4000 cm<sup>-1</sup> with 32 rescans and 4 cm<sup>-1</sup> resolution.

Thermogravimetric analysis (TGA) of cellulose samples was conducted on thermoanalytical scales TG 209 F1, manufactured by the Netzsch company, in an inert argon environment at a heating rate of 20 °C/min. The samples were suspended at a weight of 3 – 6 mg. The data were analyzed using the NETZSCH Proteus program (version 4.8.4).

X-ray radiographs (XRD) of cellulose samples were obtained at room temperature on a Rigaku Smartlab SE automated diffractometer using Cu K $\alpha$  radiation with a wavelength of 1.5406 Å (Bragg reflection geometry, 40 kV, 50 mA). The  $2\theta$  angle range was set to 10 – 50°, with a scanning step of 0.02° and a scanning speed of 5 °/min.

The electron microscopy analysis was made using a JSM 7500F scanning electron microscope (JEOL, Japan). The spatial resolution varied between 1.0 nm (15 kV of accelerating voltage) and 1.4 nm (1 kV).

Bleached wood sulfate pulp from a mixture of hardwoods (LS-0 grade, GOST 28172-89, manufacturer – JSC “Arkhangelsk PPM”, DP 900) was washed with water, filtered and dried at 55 °C to constant weight. 1-Methylimidazole (99 %, Acros Organics), 1-chlorobutane (99 %, Acros Organics). Methylene chloride and acetonitrile were purified by distillation and stored over 3 Å molecular sieves.

The preparation of samples of regenerated cellulose was conducted in accordance with the methodology outlined in reference [32]. A fixed quantity of wood cellulose (LS-0) was introduced into [BMIm]Cl solutions of varying concentrations (98, 92, 86, 80, and 74 %). Subsequently, the samples were heated at 65 – 70 °C to remove the acetonitrile. Once the solvent had been completely removed, the impregnated [BMIm]Cl was heated to 110 °C for a period of two hours. Solutions with LS-0 concentrations of 2, 8, 14, 20, and 26 % were obtained. Following a period of cooling to room temperature, 20 mL of distilled water was added to the resulting samples. After four hours, the water was drained off the precipitated cellulose, and 20 mL of water was added to the precipitate. This washing process was repeated five more times in order to completely remove the [BMIm]Cl. The regenerated cellulose was then dried at 55 °C until it reached a constant weight.

## 3. Results and discussion

### 3.1. Effect of dissolution of wood cellulose in [BMIm]Cl on its structure

The use of ionic liquids as a solvent for cellulose, discovered by Swatoski et al. [22], has gained widespread acceptance. In subsequent studies, a wide range of such compounds was investigated, in which the key elements are quaternized ammonium or phosphonium cations, and organic and inorganic acids are used as anions [25]. However, not all of them demonstrated satisfactory cellulose dissolving capacity. In addition to the structure of the IL, the degree of polymerization of the cellulose itself also influences the production of a homogeneous solution. Dissolution of microcrystalline cellulose (MCC), which is characterized by low DP, is the most effective. In this case, it is possible to obtain solutions with a high concentration, up to 20 %, using IL [BMIm]Cl [31]. In the previous work [32], devoted to the study of the dissolution of wood cellulose LS-0 in IL based on [BMIm]<sup>+</sup> with various anions, it was established that homogeneous solutions of LS-0 with a concentration of up to 8 % (wt.) are formed when using the Cl<sup>-</sup> anion. When the anion is replaced by Br<sup>-</sup> or CH<sub>3</sub>C(O)O<sup>-</sup>, the dissolution of LS-0 is significantly reduced, and the maximum concentration is 2 and 4 % (wt.),

respectively. It was also found that the imidazolium cation in [BMIm]OAc reacts with the aldehyde group of the open end of the carbohydrate chain. Therefore, our further studies aimed at dissolving cellulose LS-0 in IL were carried out using [BMIm]Cl.

For our study, LS-0 solutions in [BMIm]Cl with concentrations of 2, 8, 14, 20, and 26 % were prepared. After precipitation of LS-0 in water and subsequent removal of [BMIm]Cl from the cellulose matrix, the hydrogen bonds that were disrupted during dissolution are formed (Fig. 1).

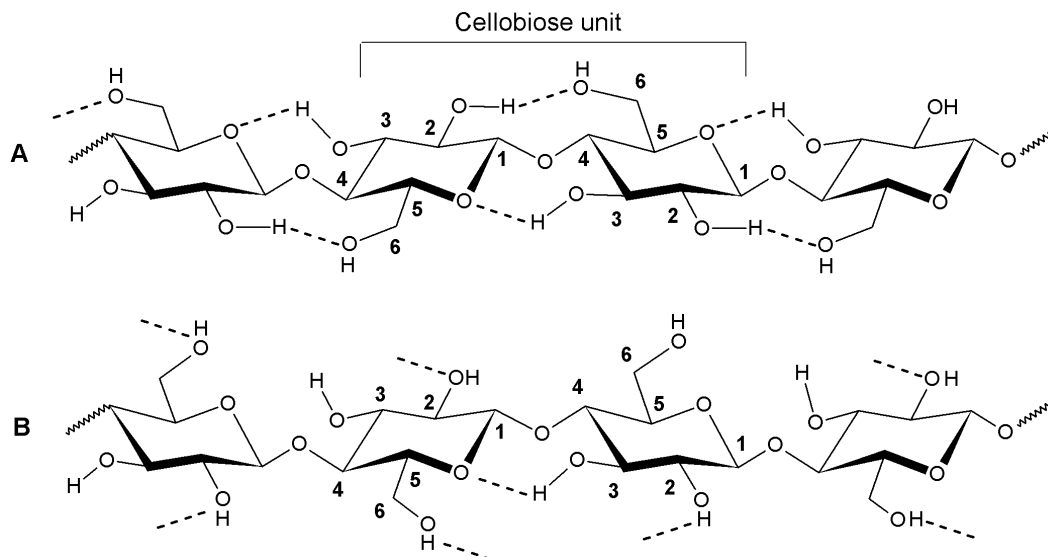


FIG. 1. Cellulose polymer chain and hydrogen bonds in the original cellulose (A) and in the regenerated cellulose (B) obtained by precipitation from its solutions in ionic liquid

Figure 1(A) illustrates that natural cellulose predominantly comprises intramolecular hydrogen bonds situated at the cellobiose unit [6, 7]. In the process of dissolution in IL, these bonds are disrupted as a result of the interaction between the hydroxyl groups and [BMIm]Cl. As the concentration of LS-0 in the IL increases, the efficiency of its dissolution is reduced. This is due to the insufficient quantity of IL capable to interact with hydroxyl groups. In this instance, a certain degree of initial ordering in the crystalline regions of the cellulose may be retained due to the retention of hydrogen bonds in the cellobiose unit. After treating the cellulose solution in IL with water, the solvent is removed, which leads to the formation of new intermolecular hydrogen bonds within the polymer (Fig. 1(B)). As a result, the cellulose molecules become more tightly packed and strongly bonded to each other. In some cases, such packaging reduces its reactivity, similar to what happens with cellulose II [6, 7]. This phenomenon was observed during the precipitation of LS-0 cellulose in water from its solutions in [BMIm]Cl with a concentration of up to 6 % [32].

Figure 2 illustrates the X-ray diffraction patterns of LS-0 cellulose solutions in [BMIm]Cl.

As evidenced by the provided diffractograms, the initial LS-0 sample exhibits the presence of crystalline formations [33]. The crystallinity is markedly diminished in [BMIm]Cl solutions. Nevertheless, the diffractograms do reveal

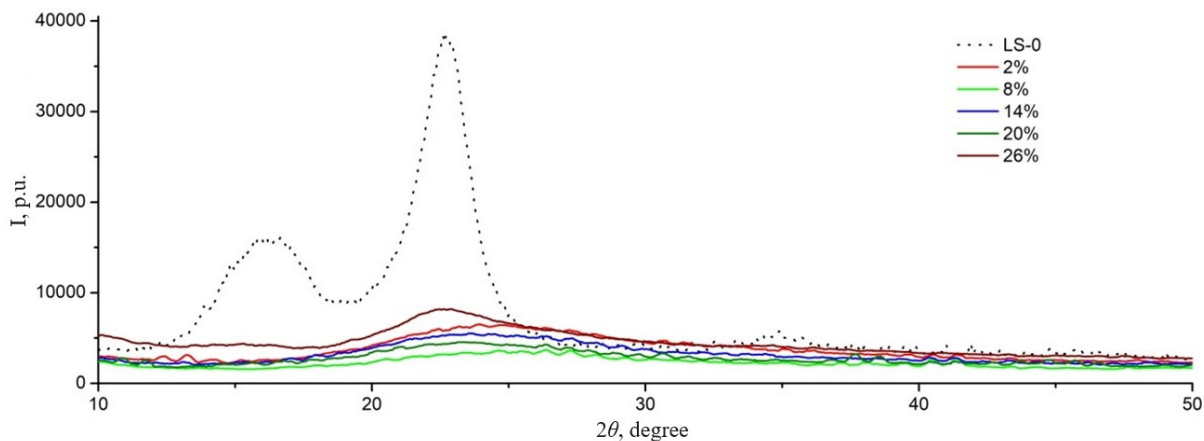


FIG. 2. Diffractograms of LS-0 cellulose solutions and its solutions in [BMIm]Cl. LS-0 content: 2, 8, 14, 20 and 26 %

the presence of weakly pronounced peaks, which can be taken to indicate the existence of a residual amount of ordered regions. This phenomenon is particularly evident at a concentration of 26 %. These ordered regions probably play a key role in the restoration of the structural features of cellulose during its precipitation in water upon removal of the IL. As a result of this process, structures are formed that resemble the original cellulose in their architecture. Fig. 3 shows scanning electron microscopy (SEM) images of recovered cellulose samples obtained from its solutions in [Bmim]Cl.

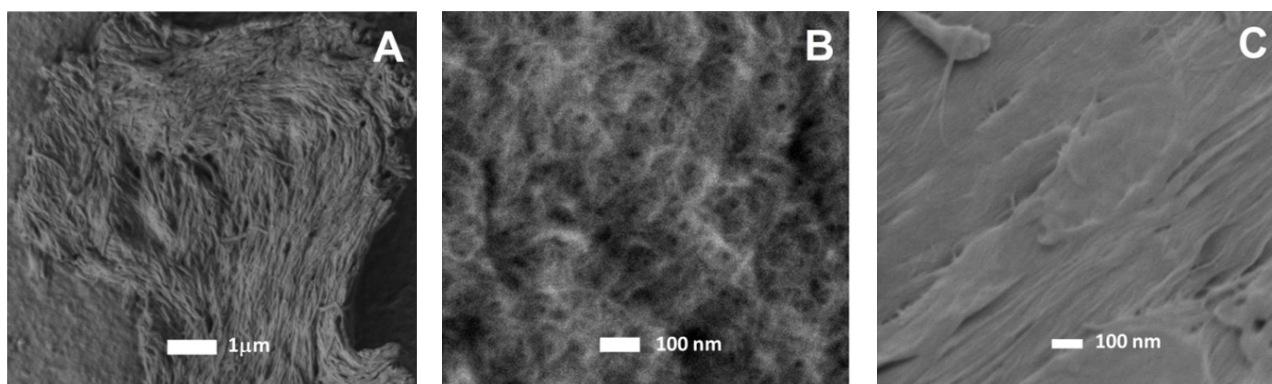


FIG. 3. SEM-image of precipitated (recovered) cellulose from its solutions in [Bmim]Cl: (1) fragment of precipitated cellulose 26 %, (2) film surface 2 %, (3) film surface 5 %

Scanning electron microscopy images (Fig. 3(A)) demonstrate that at high concentrations of LC-0 in [Bmim]Cl and its subsequent precipitation, the main structural fragments of cellulose are preserved. In this case, partial swelling of the fibrils occurs, while their morphological characteristics remain unchanged. This indicates that hydrogen bonds in the cellobiose units are practically unaffected. At a low concentration of cellulose, the dissolution process is particularly intense, which leads to the formation of transparent solutions. In this case, cellulose deposited on a glass substrate exhibits individual nanoscale fragments (Fig. 3(A,B)).

### 3.2. IR spectroscopy

Changes in the structural features of regenerated cellulose are clearly observed when analyzed using IR spectroscopy (Fig. 4).

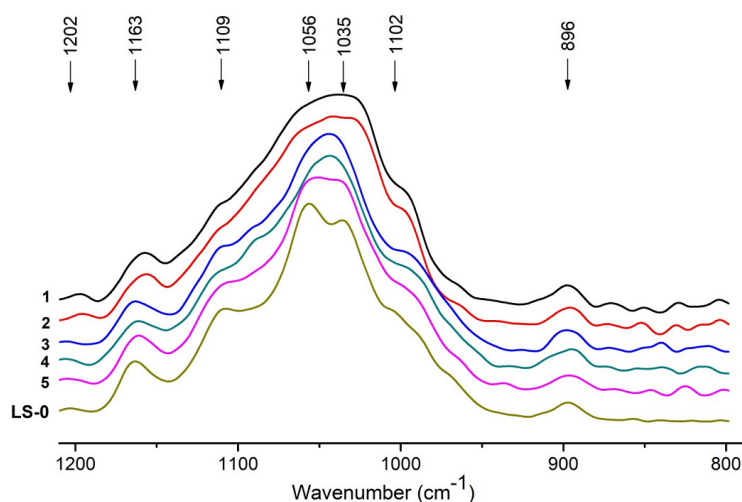


FIG. 4. IR spectra of precipitated wood cellulose LS-0 after dissolution in [BMIm]Cl. The percentages in IL: 1 – 2 %, 2 – 8 %, 3 – 14 %, 4 – 20 %, 5 – 26 %, and LS-0 is the original cellulose (wave numbers are given for the original cellulose LS-0)

Figure 3 illustrates the spectral characteristics of the initial LS-0 and those observed following a dissolution/precipitation cycle in water from its solutions in [BMIm]Cl with a concentration of 2 – 26 % (weight). The portion of the spectrum depicted in Fig. 3 pertains to the valence vibration region of the structural units constituting the cellobiose linkage. The band assignment of the IR spectrum of cellulose was conducted in accordance with the data presented in the sources cited in the references [34, 35]. It can be observed that in solutions with concentrations of 2 and 8 %, a notable amorphization of LS-0 occurs, as evidenced by the disappearance of the bands at 1056 and 1035  $\text{cm}^{-1}$ . These bands, which refer to

the valence vibrations of C–O (mainly C(3)–O(3)H) and deformation vibrations of C–O groups in the primary alcohol, respectively, are absent in the amorphous state. As the concentration of LS-0 in [BMIm]Cl increases, the bands in question become more pronounced. At a concentration of 26 %, two characteristic maxima are observed, which are typical of the original cellulose. A notable alteration in the regenerated LS-0's morphology is indicated by the broadening of the band at 1109  $\text{cm}^{-1}$ , which belongs to the asymmetric vibrations of the glucopyranose ring. Concurrently, the band at 1163  $\text{cm}^{-1}$  (asymmetric vibrations of the  $\beta$ -glycosidic C–O–C bond) undergoes a shift of 5  $\text{cm}^{-1}$ , which is particularly pronounced for low concentrations (Fig. 3). There is also an increase in the intensity of the weak band at 1202  $\text{cm}^{-1}$ , corresponding to in-plane deformation vibrations of OH groups. Although this band has insignificant intensity in the spectrum of LS-0 itself, the increase in its intensity indicates an increase in the content of alcohol groups that do not have hydrogen bonds with neighboring hydroxyls. On the other hand, the 896  $\text{cm}^{-1}$  band corresponding to the valence vibrations of the  $\beta$ -glycosidic C–O–C bond undergoes the least changes. Thus, the results of vibrational spectroscopy indicate significant changes occurring in the structure of LS-0 cellulose during dissolution in [BMIm]Cl and during its subsequent precipitation in water.

### 3.3. Thermal stability of regenerated cellulose

The thermal stability of cellulose is a characteristic that can be employed in the prediction of the stability of products subjected to temperature exposure. As demonstrated in reference [36], the thermochemical conversion of cellulose is contingent upon its associated components, namely hemicelluloses. Thermal stability of regenerated cellulose may also depend on the type of solvents used during its processing [37]. Regenerated celluloses obtained from their solutions in ionic liquids also show differences in TG analysis conditions. Using the example of microcrystalline celluloses dissolved in ionic liquids of different chemical compositions, it was found that the nature of the solvent affects both the crystallinity and the thermal stability of the recovered cellulose [38, 39].

In contrast to MCC, the wood cellulose LS-0 used in this work has a higher DP and contains both crystalline and amorphous regions in its composition. The thermal stability of the obtained regenerated cellulose samples was investigated using TGA. Fig. 5 shows the TG and DTG curves of wood pulp samples isolated from its solutions in [BMIm]Cl ionic liquid.

Figure 5 illustrates that all samples exhibit a slight mass loss in the low-temperature region (less than 100 °C) due to the evaporation of absorbed water. In the temperature range above 200 °C, there are notable differences in the behavior of TGA curves, as evidenced by the alteration in the maximum values of DTG curves and the values of the final residual mass (Fig. 5, Table 1).

TABLE 1. TGA/DTG results of cellulose samples before and after dissolution in [BMIm]Cl (LS-0 content in IL, 2 %; C – 8 %; D – 14 %; E – 20 %; F – 26 %)

Sample ( %, wt)	$T_{\text{mrd1}}$ (°C)	$T_{\text{mrd2}}$ (°C)	Coke residue ( %)
LS-0	290	348.3	9.5
2	— / —	318.7	20.7
8	— / —	333.4	18.3
14	291.9	358.7	15.7
20	284.8	352.5	14.0
26	297.0	364.2	12.6

$T_{\text{mrd1}}$  and  $T_{\text{mrd2}}$  – temperature of maximum decomposition rate at the first (1) and second (2) stages on the DTG curve

As evidenced by the data presented in Table 1, the temperature of maximum decomposition rate ( $T_{\text{mrd2}}$ ) of the original pulp is 348.3 °C, and the value of coke residue is 9.54 %. In the case of regenerated pulp samples, these parameters exhibit a markedly different profile. A decrease in the value of  $T_{\text{mrd2}}$  is observed in the case of LS-0 in [BMIm]Cl 2 and 8 % compared to the original cellulose. As the concentration increases, two well-defined temperature maxima are observed in the DTG curves. Concurrently, the  $T_{\text{mrd1}}$  value for LS-0 and all samples derived from ILs remains essentially unaltered, whereas  $T_{\text{mrd2}}$  shifts towards the high-temperature region. Additionally, a notable increase in coke residue is observed when the concentration of cellulose in [BMIm]Cl is reduced. This phenomenon can be attributed to alterations in the intermolecular interactions of cellulose chains. Apparently, the content of a large number of ordered structures (crystallites) in the original cellulose at the initial stage of thermal destruction can contribute to the acceleration of dehydration processes and the breakdown of glycosidic bonds (Fig. 1(A)). This leads to the formation of both volatile

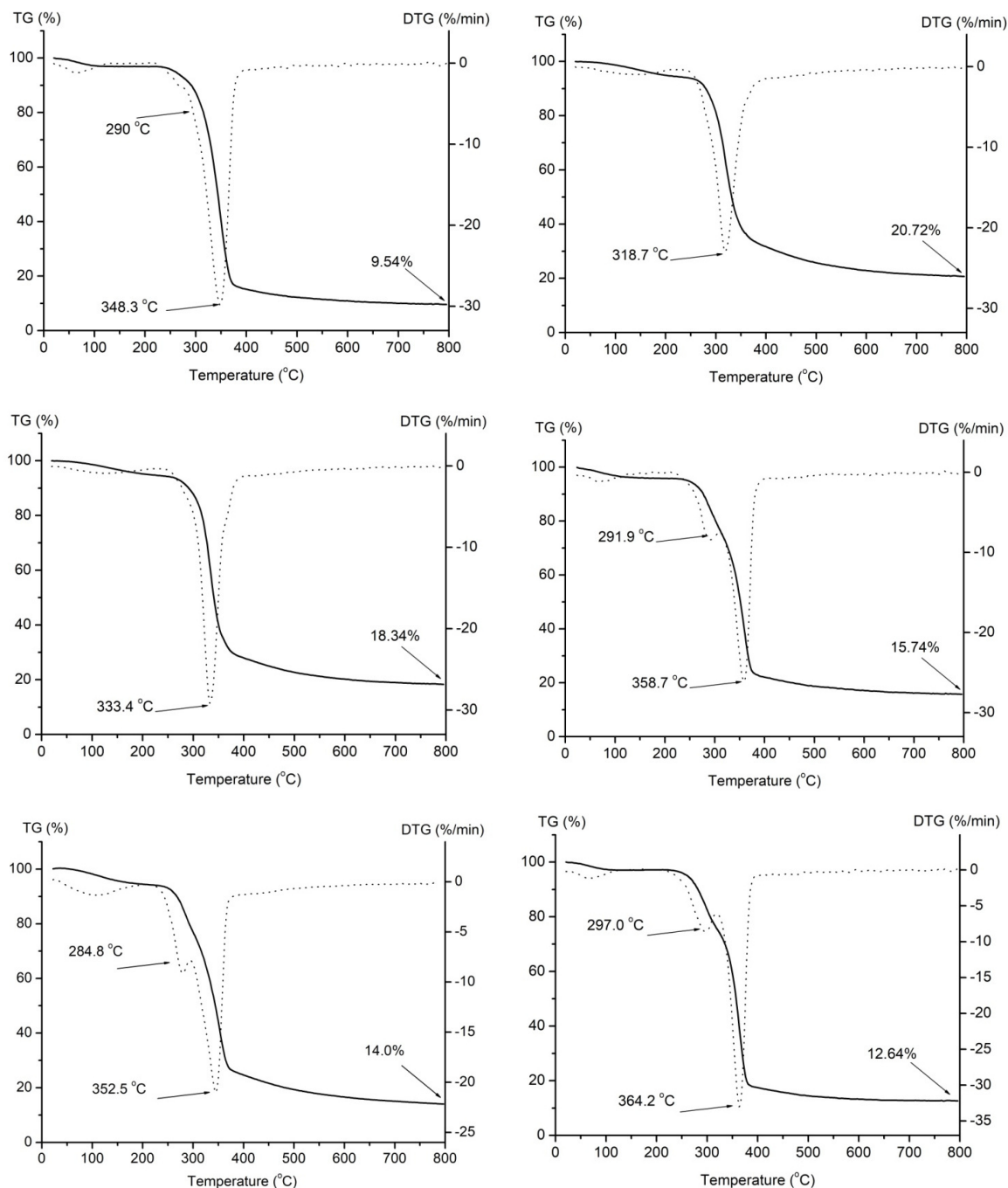


FIG. 5. TG/DTG analysis of LS-0 samples after dissolution in [BMIm]Cl: A – initial LS-0; B – 2 %; C – 8 %; D – 14 %; E – 20 %; F – 26 %

furan derivatives and levoglucosan [40], as well as solid products – unsaturated polyene structures capable of crosslinking and aromatization (coke formation) [41].

Similarly, coke residue is also formed in amorphous regions of cellulose with less ordered structures (Fig. 1(B)). Fig. 6 depicts a plot of the formal dependence of coke residue formation on the concentration of cellulose in [BMIm]Cl.

As illustrated in Fig. 6, an increase in LS-0 concentration within the ionic liquid is associated with a reduction in coke residue within the regenerated cellulose samples. At the same time, the rate of formation of volatile products is observed to increase, as evidenced by a decline in  $T_{\text{mrd}2}$  (Table 1). This phenomenon may be attributed to the complete destruction of the initial hydrogen-bonded structure at concentrations up to 8 %. After removal of the ionic liquid, cellulose undergoes chaotic restoration of hydrogen bonds, which leads to its amorphization. As the concentration of cellulose in [BMIm]Cl increases, the dissolution process becomes more difficult, which contributes to the partial preservation of crystalline regions. It can be assumed that after precipitation in water and removal of IL from cellulose, pseudofibrils are formed on the basis of partially ordered fragments [30]. The listed circumstances allow us to assume that the thermal destruction of

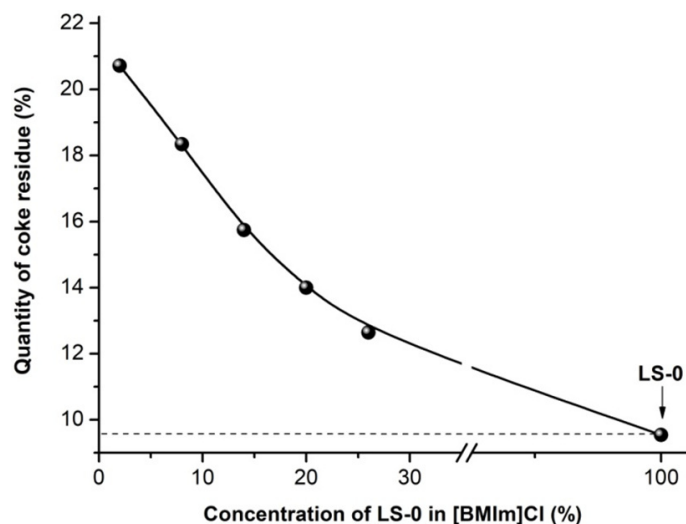


FIG. 6. Dependence of coke residue formation on the concentration of LS-0 in [BMIm]Cl

cellulose depends on the amorphous and an ordered region contained in its structure and is determined by the difference in the directions of thermochemical processes (Fig. 7).

As shown in Fig. 7, the initial stage of thermal destruction of cellulose includes the elimination of water molecules and the formation of unsaturated C=C bonds. However, further development of the process begins to depend on the morphological features of cellulose. Apparently, the ordering of the crystalline regions caused by hydrogen bonds in the glycoside unit (Fig. 1(A)) significantly reduces the mobility of cellulose chains. Therefore, stabilization of dehydroxylated hexoses of the cellobiose unit occurs due to the rupture of the glycoside bond (Fig. 7(A)). As a result, unstable structural fragments capable of forming low-molecular compounds are formed at the site of the rupture. After dissolution in the IL with subsequent regeneration, the morphology of cellulose changes (Fig. 1(B)), which is reflected in the process of its thermal destruction (Fig. 5(B, C) and Fig. 7(B)). In regenerated cellulose, especially at low concentrations in the IL, the hydrogen bonds that determine its spatial structure are destroyed. When cellulose is precipitated with water from an IL solution, new hydrogen bonds are chaotically formed between its macromolecules, the arrangement of which differs from the initial contacts. This leads to a change in the morphology of cellulose. In this case, as for the original LS-0, the initial act is the elimination of water. However, at a later stage, the thermochemical processes begin to differ. Since macromolecules in amorphous regions can have increased mobility, the stabilization of dehydroxylated hexoses can lead

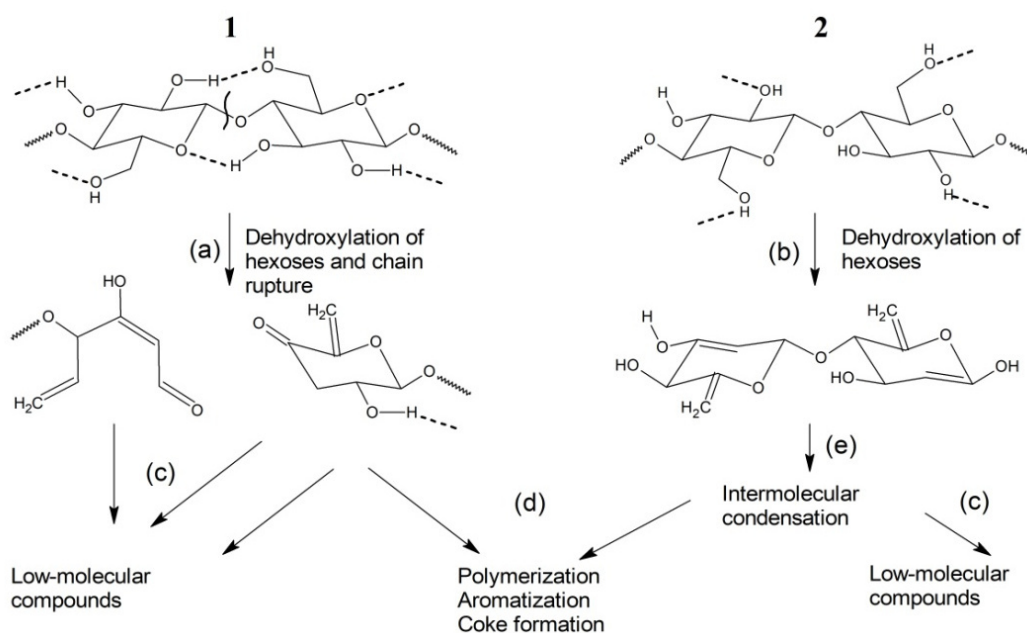


FIG. 7. Formal representation of thermal degradation of regenerated LS-0 cellulose before (1) and after dissolution in [BMIm]Cl (2)

to intermolecular reactions with the formation of polyene structures. In this case, the rupture of glycosidic bonds and the formation of low molecular weight pyrolysis products occur to a lesser extent, which leads to significant formation of coke residue (Fig. 5). As the LS-0 content in ILs increases, the crystallinity disorder decreases, which also affects the change in the directions of thermochemical processes. In this case, the process of formation of low molecular weight fragments accelerates, which, in turn, leads to a decrease in the amount of polyene structures and coke residue.

Figure 8 depicts the diffractograms of the regenerated cellulose samples. It can be observed that at concentrations of 2 and 8 %, the disappearance of characteristic reflections at  $2\theta$  (16.2 and 22.7) occurs, which may indicate the complete disappearance of the original ordering. This phenomenon is reflected in the thermochemical processes observed in the TGA curves (Fig. 5(B, C)).

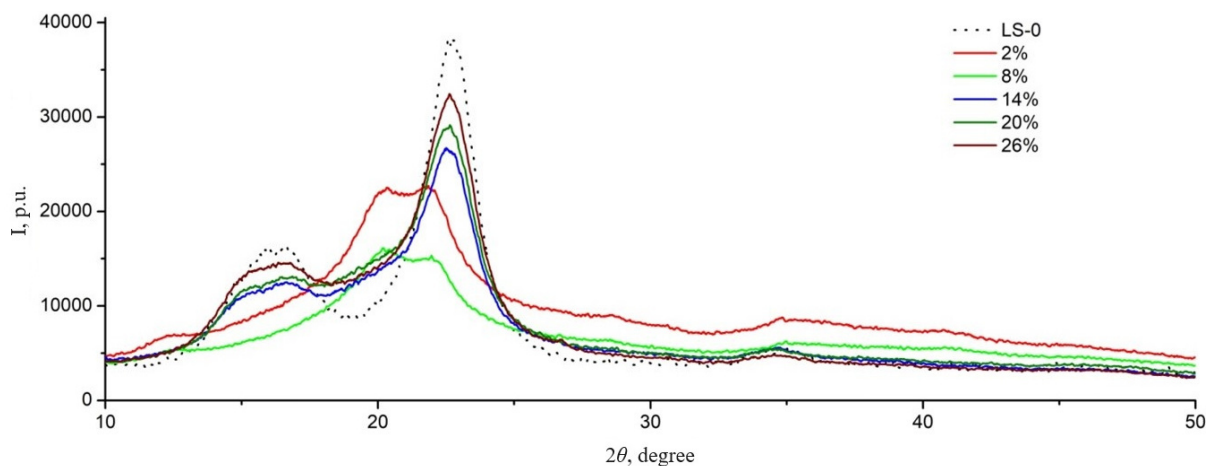


FIG. 8. Diffractograms of regenerated cellulose samples

As illustrated in Fig. 5(D), the thermal decomposition of cellulose regenerated from the solution containing 14 % is significantly different from the previous cases. The amount of carbon residue decreases, and two characteristic maxima appear in the DTG curve:  $T_{\text{mrd1}}$  (291.9 °C) and  $T_{\text{mrd2}}$  (358.7 °C). It is noteworthy that the DTG curve of the original LS-0 cellulose (Fig. 5(A)) also shows a weak peak in the range of 290 °C, which is difficult to distinguish from the primary peak of  $T_{\text{mrd2}}$ .

It can be assumed that this peak is also present in samples B and C (Fig. 5), although less distinct than that observed for  $T_{\text{mrd2}}$ . The same thermal degradation pattern is evident in the samples prepared from 20 and 26 % solutions (Fig. 5(E, F)). The maxima observed for  $T_{\text{mrd1}}$  and  $T_{\text{mrd2}}$  in the DTG curves can be explained by the presence of two structurally different phases contained in the samples. The presence of these peaks can be explained by the incomplete dissolution of the ordered regions present in the cellulose fibers.

Apparently, the initial dissolution of LS-0 cellulose involves the interaction of [BMIm]Cl with the most accessible amorphous regions, which leads to the consumption of most of the IL. The observation of crystalline formations with an ordered structure indicates a reduced susceptibility to dissolution, which suggests that their original structure is partially preserved. During precipitation of cellulose in an aqueous medium, a rapid regeneration of amorphous regions occurs, and the presence of partially ordered structures leads to the formation of pseudofibrils. In light of these observations, the first maximum observed in the range of  $290 \pm 7$  °C in the DTG curves can be attributed to the decomposition of the amorphous phase, and the second maximum to structural fragments with partial order.

The application of X-ray diffraction analysis (Fig. 8) to the examination of reduced cellulose samples enables the clear verification of structural alterations affecting the alteration of thermal stability. The graph illustrates the presence of ordered structures in the samples.

The degree of crystallinity was evaluated in accordance with the peak height method of the diffractogram, as previously described in the literature [42]. The following formula may be employed:

$$C = 100 \cdot \frac{I_{200} - I_{\text{non-cr}}}{I_{200}},$$

where  $C$  – degree of crystallinity [%], and  $I_{200}$  is the maximum peak intensity at the angle  $2\theta$  equal to 22 – 24 degrees. Additionally,  $I_{\text{non-cr}}$  represents the diffraction intensity of the non-crystalline part, which is taken at the angle  $2\theta$  equal to 18 degrees between the peaks. The results calculated using this formula are presented in Table 2.

Thus, the conducted studies of regenerated cellulose LS-0, obtained by precipitation from its solutions in [BMIm]Cl, show that there is a significant transformation of its structure. This is clearly observed during analysis using IR spectroscopy. These changes are fully observed in the results of TG analysis, which is expressed in a change of its thermal stability. Moreover, for high concentrations, this parameter increases.

TABLE 2. Degree of crystallinity of the regenerated cellulose under study

Sample	Degree of crystallinity C ( % )
Initial cellulose LS-0	81.3
LS-0 2 % after dissolution in [BMIm]Cl	41.8
LS-0 8 % after dissolution in [BMIm]Cl	43.7
LS-0 14 % after dissolution in [BMIm]Cl	59.7
LS-0 20 % after dissolution in [BMIm]Cl	59.3
LS-0 26 % after dissolution in [BMIm]Cl	62.7

#### 4. Conclusions

The study examined the physicochemical properties and morphological features of regenerated cellulose obtained by precipitation in water from its solutions in [BMIm]Cl with concentrations from 2 to 26 %. It was found that when the cellulose content in [BMIm]Cl was up to 8 %, significant morphological changes occurred, expressed in a significant change in its infrared spectra and a decrease in thermal stability. With increasing concentration, the spectral characteristics of the reconstituted cellulose approach the original LS-0. At the same time, the thermal stability increases significantly, and at LS-0 concentration of 26 %, the temperature of maximum decomposition rate exceeds this parameter for pure cellulose by more than 15 degrees. Thus, the study revealed significant changes in the structure of cellulose fibers that occur during their dissolution in ionic liquid [BMIm]Cl and determine the physicochemical properties of the reconstituted cellulose.

#### References

- [1] Szabó L., Milotskyi R., Sharma G., K. Takahashi. Cellulose processing in ionic liquids from a materials science perspective: turning a versatile biopolymer into the cornerstone of our sustainable future. *Green Chem.*, 2023, **25**, P. 5338-5389.
- [2] Gharekhani S., Sadeghinezhad E., Kazi S.N., Yarmand H., Badarudin A., Safaei M.R., Zubir M.N.M. Basic effects of pulp refining on fiber properties – a review. *Carbohydr. Polym.*, 2015, **115**, P. 785–803.
- [3] Stovbun S.V., Lomakin S.M., Shchegolikhin A.I., et al. Role of Structural Stresses in the Thermodestruction of Supercoiled Cellulose Macromolecules after Nitration. *Russ. J. Phys. Chem. B*, 2018, **12**, P. 36–45.
- [4] Stovbun S.V., Mikhaleva M.G., Skoblin A.A., Usachev S.V., Nikolsky S.N., Kharitonov V.A., Zlenko D.V., et al. Zhurkov's stress-driven fracture as a driving force of the microcrystalline cellulose formation. *Polymers*, 2020, **12** (12), 2952.
- [5] Cabiac A., Guillon E., Chambon F., Pinel C., Rataboul F., Essayem N. Cellulose reactivity and glycosidic bond cleavage in aqueous phase by catalytic and non catalytic transformations. *Appl. Catal. A*, 2011, **402**, P. 1–10.
- [6] Heinze T. Cellulose: Structure and Properties. In: Rojas, O. (eds) Cellulose Chemistry and Properties: Fibers, Nanocelluloses and Advanced Materials. *Advances in Polymer Science*, 2015, **271**, Springer, Cham.
- [7] Kondo T. Hydrogen bonds in cellulose and cellulose derivatives. In: Dumitriu S. (ed) *Polysaccharides: structural diversity and functional versatility*, 2nd edn. Marcel Dekker, New York, 2005, P. 69–98.
- [8] Stovbun S.V., Nikol'skii S.N., Mel'nikov V.P., et al. Chemical physics of cellulose nitration. *Russ. J. Phys. Chem. B*, 2016, **10**, P. 245–259.
- [9] Anpilova A.Y., Mastalygina E.E., Khrameeva N.P., et al. Methods for Cellulose Modification in the Development of Polymeric Composite Materials (Review). *Russ. J. Phys. Chem. B*, 2020, **14**, P. 176–182.
- [10] Morris E., Pulham C.R., Morrison C.A. Structure and properties of nitrocellulose: approaching 200 years of research. *RSC Adv.*, 2023, **13**, P. 32321–32333.
- [11] Sayyed A.J., Deshmukh N.A., Pinjari D.V. A critical review of manufacturing processes used in regenerated cellulosic fibres: viscose, cellulose acetate, cuprammonium, LiCl/DMAc, ionic liquids, and NMMO based lyocell. *Cellulose*, 2019, **26**, P. 2913–2940.
- [12] Burchard W., Habermann N., Klüfers P., Seger B., Wilhelm U. Cellulose in Schweizer's Reagent: A Stable, Polymeric Metal Complex with High Chain Stiffness. *Angew. Chem. Int. Ed.*, 1994, **33**, P. 884–887.
- [13] Dawsey T.R., McCormick C.L. The lithium chloride/dimethylacetamide solvent for cellulose: a literature review. *J. Macromol. Sci. Polymer. Rev.*, 1990, **30** (3-4), P. 405–440.
- [14] Xu A., Wang J., Wang H. Effects of anionic structure and lithium salts addition on the dissolution of cellulose in 1-butyl-3-methylimidazolium-based ionic liquid solvent systems. *Green Chem.*, 2010, **12**, P. 268–275.
- [15] Heinze T., Koschella A. Solvents applied in the field of cellulose chemistry – A mini review. *Polímeros: Ciência e Tecnologia*, 2005, **15**, P. 84–90.
- [16] Huang Y., Xin P., Li J., Shao Y., Huang C., Pan H. Room-temperature dissolution and mechanistic investigation of cellulose in a tetrabutylammonium acetate/dimethylsulfoxide system. *ACS Sustain. Chem. Eng.*, 2016, **4** (4), P. 2286–2294.
- [17] Kostag M., Jedvert K., Ahtel C., Heinze T., El Seoud O.A. Recent Advances in Solvents for the Dissolution, Shaping and Derivatization of Cellulose: Quaternary Ammonium Electrolytes and their Solutions in Water and Molecular Solvents. *Molecules*, 2018, **23**, 511.
- [18] El Seoud O.A., Kostag M., Jedvert K., Malek N.I. Cellulose in Ionic Liquids and Alkaline Solutions: Advances in the Mechanisms of Biopolymer Dissolution and Regeneration. *Polymers*, 2019, **11**, 1917.
- [19] Olsson C., Hedlund A., Idström A., Westman G. Effect of methylimidazole on cellulose/ionic liquid solutions and regenerated material therefrom. *J. Mater. Sci.*, 2014, **49**, P. 3423–3433.
- [20] Graenacher C. Cellulose solution. US Patent, 1934 (p. 1934176 A). Graenacher C., Sallmann R. Cellulose solution and process of making same. US Patent, 1939 (p. 2179181 A).
- [21] Ghandi K. A Review of Ionic Liquids, Their Limits and Applications. *Green and Sustainable Chemistry*, 2014, **4** (1), P. 44–53.

- [22] Swatloski R.P., Spear S.K., Holbrey J.D., Rogers R.D. Dissolution of Cellulose with Ionic Liquids. *J. Am. Chem. Soc.*, 2002, **124** (18), P. 4974–4975.
- [23] Fukaya Y., Sugimoto A., Ohno H. Superior solubility of polysaccharides in low viscosity, polar, and halogen-free 1,3-dialkylimidazolium formates. *Biomacromol.*, 2006, **7**, P. 3295–3297.
- [24] Xu A., Zhang Y., Lu W., Yao K., Xu H. Effect of alkyl chain length in anion on dissolution of cellulose in 1-butyl-3-methylimidazolium carboxylate ionic liquids. *J. Mol. Liq.*, 2014, **197**, P. 211–214.
- [25] Gupta K.M., Jiang J. Cellulose dissolution and regeneration in ionic liquids: A computational perspective. *Chemical Engineering Science*, 2015, **121**, P. 180–189.
- [26] Li X.J., Sun Y.S., Zhao Q. Experimental Research on the Solubility of Cellulose in Different Ionic Liquids. *Adv. Mat. Res.*, 2013, (**690-693**), P. 1568–1571.
- [27] Remsing R.C., Swatloski R.P., Rogers R.D., Moyna G. Mechanism of cellulose dissolution in the ionic liquid 1-n-butyl-3-methylimidazolium chloride: a <sup>13</sup>C and <sup>35/37</sup>Cl NMR relaxation study on model systems. *Chem. Commun. (Camb.)*, 2006, **12**, 1271–3.
- [28] Endo T., Hosomi S., Fujii S., Ninomiya K., Takahashi K. Nano-Structural Investigation on Cellulose Highly Dissolved in Ionic Liquid: A Small Angle X-ray Scattering Study. *Molecules*, 2017, **22**, 178.
- [29] Medronho B., Lindman B. Brief overview on cellulose dissolution/regeneration interactions and mechanisms. *Advances in colloid and interface science*, 2015, **222**, P. 502–508.
- [30] Usachev S.V., Zlenko D.V., Nagornova I.V., Koverzanova E.V., Mikhaleva M.G., Vedenkin A.S., Vtyurina D.N., Skoblin A.A., Nikolsky S.N., Politenkova G.G., Stovbun S.V. Structure and properties of helical fibers spun from cellulose solutions in (Bmim)Cl. *Carbohydr. Polym.*, 2020, **235**, 11586.
- [31] Pinkert A., Marsh K.N., Pang S., Staiger M.P. Ionic liquids and their interaction with cellulose. *Chem. Rev.*, 2009, **109** (12), P. 6712–6728.
- [32] Mikhaleva M., Vedenkin A., Usachev S., Levina I. Dissolution Efficiency of Wood Pulp in Ionic Liquids Based on 1-Butyl-3-Methylimidazolium with Different Anions. *Russ. J. Phys. Chem. B*, 2023, **17**, P. 996–1004.
- [33] Man Z., Muhammad N., Sarwono A., et al. Preparation of Cellulose Nanocrystals Using an Ionic Liquid. *J. Polym. Environ.*, 2011, **19**, P. 726–731.
- [34] Široký J., Blackburn R., Bechtold T., Taylor J., White P. Attenuated total reflectance Fourier-transform infrared spectroscopy analysis of crystallinity changes in lyocell following continuous treatment with sodium hydroxide. *Cellulose*, 2010, **17** (1), P. 103–115.
- [35] Haulea L.V., Carr C.M., Rigout M. Investigation into the supramolecular properties of fibres regenerated from cotton based waste garments. *Carbohydr. Polym.*, 2016, **144**, P. 131–139.
- [36] Wang J., Minami E., Kawamoto H. Thermal reactivity of hemicellulose and cellulose in cedar and beech wood cell walls. *J. Wood. Sci.*, 2020, **66**, 41.
- [37] Rebière J., Heuls M., Castignolles P., Violleau F., Durrieu V. Structural modifications of cellulose samples after dissolution into various solvent systems. *Anal. Bioanal. Chem.*, 2016, **408**, P. 8403–8414.
- [38] Im J., Lee S.H., Insol J., Won K.J., Kim K.S. Structural characteristics and thermal properties of regenerated cellulose, hemicellulose and lignin after being dissolved in ionic liquids. *J. Indus. Engin. Chem.*, 2022, **107**, P. 365–375.
- [39] Yang H., Jiang J., Zhang B., Zhang W., Xie W., Li J. Experimental study on pretreatment effects of [BMIM]HSO<sub>4</sub>/ethanol on the thermal behavior of cellulose. *RSC Adv.*, 2022, **12**, 10366.
- [40] Shen D.K., Gu S. The mechanism for thermal decomposition of cellulose and its main products. *Bioresource Technology*, 2009, **100**, P. 6496–6504.
- [41] Perova A.N., Brevnov P.N., Usachev S.V., et al. Comparative Analysis of Thermal and Physico-Mechanical Properties of Polyethylene Compositions Containing Microcrystalline and Nanofibrillary Cellulose. *Russ. J. Phys. Chem. B*, 2021, **15**, P. 716–723.
- [42] Terinte N., Ibbett R., Schuster K.C. Overview on native cellulose and microcrystalline cellulose I structure studied by X-ray diffraction (WAXD): Comparison between measurement techniques. *Lenzinger Berichte*, 2011, **89** (1), P. 118–131.

---

*Submitted 2025; revised 2025; accepted 2025*

#### *Information about the authors:*

*Mariya G. Mikhaleva* – Ph.D, senior researcher N.N. Semenov Federal Research Center for Chemical Physics Russian Academy of Sciences, 4 Kosygina Street, Moscow, Russian Federation 119991; ORCID 0000-0001-8192-69292; maria.mikhaleva@chph.ras.ru

*Sergey V. Usachev* – Ph.D, senior researcher N.N. Semenov Federal Research Center for Chemical Physics Russian Academy of Sciences, 4 Kosygina Street, Moscow, Russian Federation 119991; ORCID: 0000-0002-8971-9358; usachevsv@inbox.ru

*Alexander S. Vedenkin* – researcher N.N. Semenov Federal Research Center for Chemical Physics Russian Academy of Sciences, 4 Kosygina Street, Moscow, Russian Federation 119991; ORCID 0000-0001-9295-583X; alexander.vedenkin@chph.ras.ru

*Mariya I. Ikim M.* – Ph.D, senior researcher N.N. Semenov Federal Research Center for Chemical Physics Russian Academy of Sciences, 4 Kosygina Street, Moscow, Russian Federation 119991; ORCID 0000-0003-4411-1119; maria.ikim@chph.ras.ru

*Galina G. Politenkova* – researcher N.N. Semenov Federal Research Center for Chemical Physics Russian Academy of Sciences, 4 Kosygina Street, Moscow, Russian Federation 119991, +7(495)939-7225; galina.politenkova@chph.ras.ru

*Sergey M. Lomakin* – Ph.D, head of laboratory Emanuel Institute of Biochemical Physics of Russian Academy of Sciences, 4 Kosygina Street, Moscow, Russian Federation 119991; ORCID 0000-0003-3191-8415; lomakin@sky.chph.ras.ru

*Conflict of interest:* the authors declare no conflict of interest.

## Boron doped small fullerenes $C_{20}$ , $C_{24}$ , $C_{28}$ as a basis for the formation of heterostructures

Anton R. El Zanin<sup>a</sup>, Sergey V. Boroznin<sup>b</sup>, Irina V. Zaporotskova<sup>c</sup>

Volgograd State University, Volgograd, Russia

<sup>a</sup>aelzanin@volsu.ru, <sup>b</sup>boroznin@volsu.ru, <sup>c</sup>zaporotskova@volsu.ru

Corresponding author: A.R. El Zanin, aelzanin@volsu.ru

PACS 61.48.+c

**ABSTRACT** In this paper, the stability, geometric and electronic properties of boron doped small fullerenes  $C_{20}$ ,  $C_{24}$ ,  $C_{28}$  were investigated using density functional theory (DFT) methods. Average bonds lengths were calculated and the stability of optimized structures was estimated. An analysis of one-electron spectra and the density of states (DOS) allowed us to define the mechanisms for the change in the band gap and to determine the dependence of this parameter on the concentration of boron atoms. The established dependence of the band gap on the concentration of impurity atoms suggests the possibility of controlling the refractive index of the considered nanomaterials by doping with different concentrations of boron atoms, which indicates the applicability of such an approach to the construction of heterostructures in general and photonic crystals in particular. The obtained results can be useful for the fabrication of the novel optoelectronic devices which are used in infocommunication systems for the manipulating and transformation of optical signals.

**KEYWORDS** small fullerenes, DFT, band gap, DOS, heterostructures, photonic crystals

**ACKNOWLEDGEMENTS** The work was carried out within the government task of the Ministry of Science and Higher Education of the Russian Federation (subject “FZUU-2023-0001”).

**FOR CITATION** El Zanin A.R., Boroznin S.V., Zaporotskova I.V. Boron doped small fullerenes  $C_{20}$ ,  $C_{24}$ ,  $C_{28}$  as a basis for the formation of heterostructures. *Nanosystems: Phys. Chem. Math.*, 2025, **16** (3), 374–385.

### 1. Introduction

Improving the efficiency and reliability of information transmission systems is one of the most important vectors of the development of modern infocommunication technologies. Information transmission technologies using visible light as a signal carrier have become widespread. In this case, it is possible to implement a communication channel not only based on optical fiber, but also wirelessly, the so-called Li-Fi. Optical fiber technology, characterized by extremely high transmission capacity, the values of which can range from tens of Gbit/s to hundreds of Tbit/s [1–3], has now firmly entered the modern world. Li-Fi technology is only developing and is not so widespread yet, but it is high promising and is characterized by a sufficiently high transmission capacity and the possibility of application in air transport and medical facilities where Wi-Fi cannot be used cause of safety issues [4–6]. The above methods of information transmission, of course, require technical implementation using various optoelectronic devices. Heterostructures, and especially, photonic crystals, can be a basis for the construction of such devices, for example, optical switches [7,8], filters [9–14], logic adders and subtractors [15, 15–20], logic gates [21, 22].

Photonic crystals are structures characterized by a periodically (quasi-periodically) changing refractive index. The concept of a photonic band gap, analogous to the concept introduced to describe the behaviour of electrons in solids with a band gap, is used to describe the behaviour of photons in such structures. This corresponds to a certain range of wavelengths (frequencies), and photons with a wavelength (frequency) value within this range are unable to pass through a crystal [23–25]. The periodicity (or quasi-periodicity) of the refractive index changing determines the existence of such zones. The distinction between one-dimensional (1D), two-dimensional (2D) and three-dimensional (3D) photonic crystals is made on the basis of whether the refractive index changes along one, two or three orthogonal vectors (Fig. 1). It is also noteworthy that photonic crystals can be used to slow down optical pulses. Indeed, the speed of optical pulses can be reduced by more than 100 times [26, 27].

The selection of appropriate materials for heterostructures fabrication and the implementation of the technological process of its fabrication represent significant challenges. Carbon nanomaterials offer significant promise in this regard. Researchers have constructed different composites with the periodically changing properties using carbon nanotubes [28–34], graphene [35–41], and fullerenes [42–46]. These materials are advantageous, because structures with periodically changing physicochemical properties based on them can be obtained by doping different regions with impurity atoms. Boron atoms can act as an impurity, and this choice has a number of advantages: little distortion of the topology of the nanostructure due to a relatively small difference in the atomic radii of boron and carbon atoms, a significant effect of

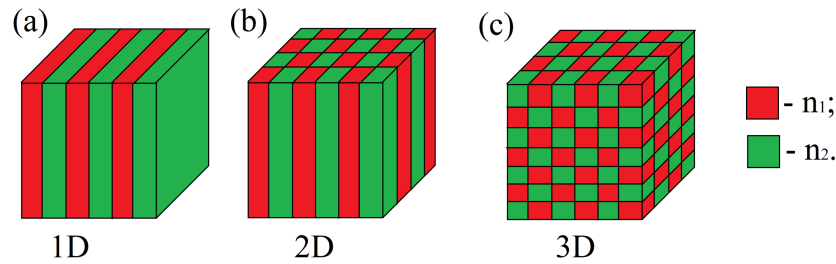


FIG. 1. Schematic illustration of one-dimensional (a), two-dimensional (b) and three-dimensional (c) photonic crystals consisting of two phases with different refractive indexes  $n_1$  and  $n_2$

even small amounts of impurity on the electronic properties of the material, and a well-established technology for doping carbon materials with boron atoms [47, 48].

In previous studies [49, 50], the concept of refractive index control was proposed. It is based on the relationship between the refractive index and the energy gap. By controlling the energy gap with the help of substituting boron atoms, it becomes possible to control the refractive index. The problem of the influence of substitution of carbon atoms by boron atoms in small fullerenes on electronic and optical properties is poorly studied. So, in the present work, we propose to consider the physicochemical properties of small fullerenes  $C_{20}$ ,  $C_{24}$ ,  $C_{28}$  doped with boron atoms in the context of heterostructures fabrication.

## 2. Materials and methods

### 2.1. Description of the investigation objects

The investigation objects were small fullerenes  $C_{20}$  with a point symmetry group  $I_h$ ,  $C_{24}$  with a point symmetry group  $D_{6d}$ ,  $C_{28}$  with a point symmetry group  $D_2$ . The concentrations of boron impurities were 15, 25 and 50 %. The structures corresponding to these concentrations were designated as  $BC_5$ ,  $BC_3$  and  $BC$ , respectively. The chosen concentrations are not arbitrary: a similar approach is widely used for planar and tubular carbon nanostructures [49–53].

It should be noted that the case under consideration is more specific in that neither graphene nor carbon nanotubes generally contain pentagons in their structure. The features of the structural characteristics of fullerenes lead to the deviation from the strictly defined structures  $BC_5$ ,  $BC_3$  and  $BC$  that are observed in boron-carbon nanolayers and nanotubes. It will be demonstrated subsequently that in  $BC_5$   $C_{20}$  each boron atom is surrounded by either five or six carbon atoms; in the  $BC_5$  nanotube, as indicated by the designation, there are precisely five carbon atoms around each boron atom. However, when defects (vacancies) are introduced into the graphene structure and pentagonal fragments are formed, it is possible to form fullerenes by convolution [54]. It is precisely due to this interconnectedness of various carbon nanostructures that it is possible to extend the approach previously used for graphene and carbon nanotubes to fullerenes. In certain instances, multiple variants of the mutual spatial arrangement of impurity atoms were contemplated, with the structures designated as Type A and Type B, respectively.

### 2.2. Details of the computer modeling

The study was carried out using the methods of DFT [55] at the level of theory B3LYP/6-31G. 6-31G basis set is widely used for computing structural and electronic properties of boron doped carbon nanostructures in modern studies [56,57]. The initial fullerenes were optimized, after which part of the carbon atoms were replaced by boron atoms, and reoptimization was carried out. The geometry of the obtained structures was characterized by the average bond lengths C–C  $d_{C-C}$ , B–C  $d_{B-C}$  and B–B  $d_{B-B}$ . It was also calculated the value of the relative elongation of the C–C bond  $\delta d_{C-C}$ :

$$\delta d_{C-C} = \frac{d_{C-C}(\text{doped}) - d_{C-C}(\text{pure})}{d_{C-C}(\text{doped})} \cdot 100\%, \quad (1)$$

where  $d_{C-C}(\text{doped})$  is an average length of the C–C bond in doped fullerene,  $d_{C-C}(\text{pure})$  is an average length of the C–C bond in pure one.

Important for possible practical applications is the determination of the stability of boron doped fullerenes. The stability of the considered structures was evaluated by the bond energy  $E_b$  calculated by the formula

$$E_b = nE(C) + mE(B) - E(C_nB_m), \quad (2)$$

where  $E(C)$  and  $E(B)$  are the energies of the isolated carbon and boron atoms,  $n$  and  $m$  are the numbers of the carbon and boron atoms,  $E(C_nB_m)$  is the energy of the fullerene.

The next step in the investigation is the evaluation of the possibility of refractive index control by doping selected small fullerenes with different concentrations of boron atoms. It should be noted here that the simplest way to change the refractive index  $n$  in the framework of this problem is to change the band gap. Thus

$$n^2 = \text{Re}\epsilon + k^2, \quad (3)$$

where  $\varepsilon$  is the permittivity,  $k$  is the imaginary component of the complex refractive index, which is responsible for absorption.

The absorption  $\alpha$  is determined by the conductivity of the sample  $\sigma$  according to the generally accepted formula:

$$\alpha = \sigma / cn\varepsilon_0, \quad (4)$$

where  $c$  is the speed of light and  $\varepsilon_0$  is a permittivity of a vacuum. The relationship between conductivity and the band gap  $\Delta E_g$  is well-known:

$$\sigma \sim \exp(-\Delta E_g / 2k_B T), \quad (5)$$

where  $k_B$  is the Boltzmann constant,  $T$  is a temperature. All above described allows to control the refractive index of the nanostructures under consideration.

The band gap  $\Delta E_g$  was estimated as the difference between energy of the lowest unoccupied molecular orbital  $E_{LUMO}$  (the bottom of the conduction zone) and the energy of the highest occupied molecular orbital  $E_{HOMO}$  (the maximum of the valence band):

$$\Delta E_g = E_{LUMO} - E_{HOMO}. \quad (6)$$

Such simple way of estimation of the band gap is suitable for heteroatom doped carbon nanostructures [58, 59].

In the case of spin degeneration of electronic states, the energy values of molecular orbitals corresponding to both the spin-up state (alpha orbitals) and the spin-down state (beta orbitals) were considered. The band gap is calculated separately for each type of orbital. The one-electron spectra and DOS were constructed using the GaussSum program [60]. The analysis of the charge distribution was carried out on the basis of calculations of the values of atomic partial charges according to Mulliken [61].

It should be noted that the values of some estimated parameters for different types of structures corresponding to the same concentration of impurity atoms were not considered separately, but rather, their average values were taken. Therefore, if no indication is given that a parameter value pertains to a specific structure type (e.g., A or B), the value in question represents the average.

### 3. Results and discussion

#### 3.1. Geometry and stability

Optimized geometries of the pure and doped small fullerenes  $C_{20}$ ,  $C_{24}$ ,  $C_{28}$  are represented in the Fig. 2.

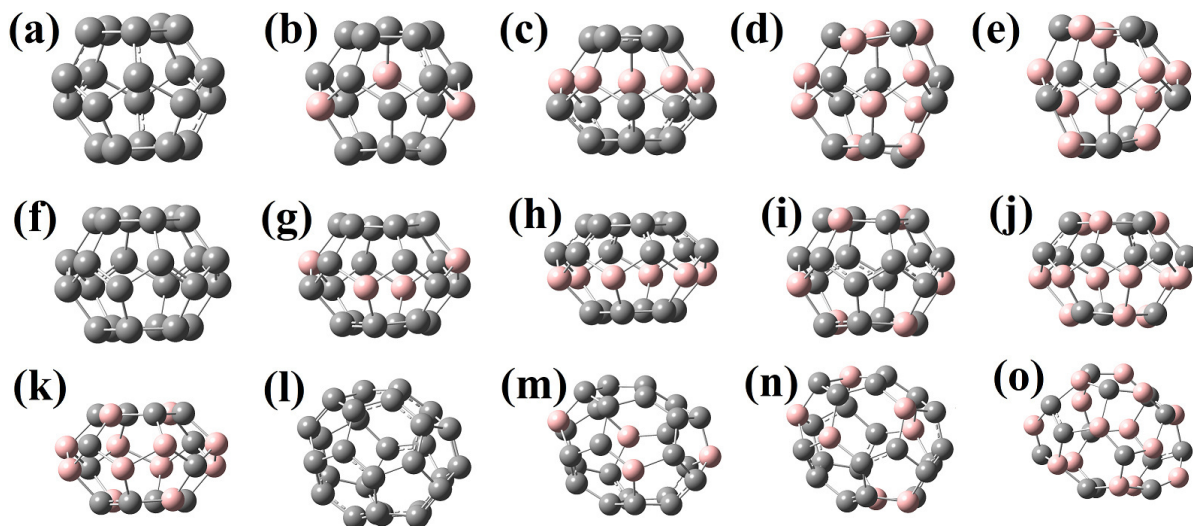


FIG. 2. Optimized geometries  $C_{20}$  (a),  $BC_5 C_{20}$  (b),  $BC_3 C_{20}$  (c),  $BC C_{20}$  type A (d),  $BC C_{20}$  type B (e),  $C_{24}$  (f),  $BC_5 C_{24}$  (g),  $BC_3 C_{24}$  type A (h),  $BC_3 C_{24}$  type B (i),  $BC C_{24}$  type A (j),  $BC C_{24}$  type B (k),  $C_{28}$  (l),  $BC_5 C_{28}$  (m),  $BC_3 C_{28}$  (n),  $BC C_{28}$  (o)

It was found that with the addition of 15 % of impurity atoms, the C–C bond length increases by 0.5 % in the case of fullerene  $C_{24}$ ; for the rest of the considered fullerenes, this value practically does not change and the absolute value of the elongation is several hundredths of a percent or less. An increase in the concentration of boron atoms leads to a decrease in the average C–C bond length for  $C_{20}$  and  $C_{28}$  fullerenes, as evidenced by the monotonously decreasing nature of the dependence of the elongation on concentration and negative values of this value over the entire concentration range from 15 to 50 % (Fig. 3a). In the case of fullerene  $C_{24}$ , the elongation value is observed to lie in the positive region of the graph between 15 % and approximately 20 % of the concentration of boron atoms. Upon further increase in the concentration

of the impurity, the observed dependence is found to be consistent with that observed in the case of the other fullerenes under consideration. Based on the dependence of the average length of the B–C bond on the concentration of boron atoms (Fig. 3b), an increase in this indicator is observed with increasing concentration, reaching a maximum in the concentration range from 30 to 40 % of the impurity and then decreasing. Neighboring boron atoms take place only in BC structures, and the  $d_{B-B}$  parameter is only applicable to these. For BC  $C_{20}$  and BC  $C_{24}$  fullerenes, the average B–B bond length is on the order of 1.70 – 1.75 Å, depending on the type of structure. This value is 0.10 – 0.15 Å longer than the average B–C bond length and approximately 0.20 Å longer than the average C–C bond length in BC  $C_{20}$  and BC  $C_{24}$ . In BC  $C_{28}$  fullerene, the value of the average bond length of B–B is more than 2.60 Å, which is 1.00 – 1.20 Å longer than the average bond length of B–C and C–C in it. This is manifested in the appearance of octagons in the structure (Fig. 4), which, hypothetically, could facilitate the intercalation process of this kind of material by atoms and molecules. This is due to the fact that the potential barrier overcome by the particle during the intercalation process is lower for an octagon than for a pentagon or hexagon.

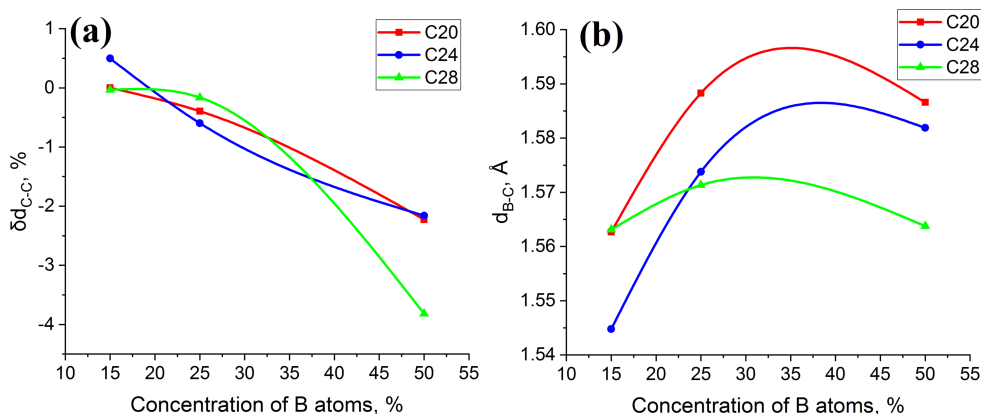


FIG. 3. The dependences of the relative elongation (a) and the average length of the B–C bond (b) on the concentration of boron atoms

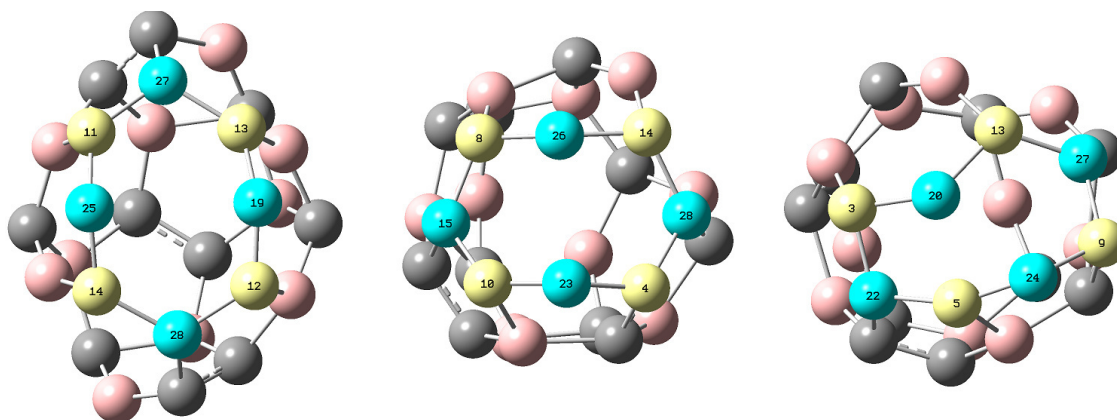


FIG. 4. Three octagons that take place in the BC  $C_{28}$  structure; atoms forming octagons are highlighted by yellow (carbon) and blue (boron) colors

Let us turn to the consideration of the stability of boron doped small fullerenes. The binding energy in such systems decreases monotonously with increasing impurity concentration (Fig. 5), respectively, pure fullerenes are more stable. However, the positive values of the binding energy over the entire concentration range under consideration indicate the possibility of their practical production, as well as the benefits of being in these states compared to being in the state of isolated carbon and boron atoms. Interestingly, the different spatial arrangement of boron atoms often has little effect on stability. The binding energies of different types corresponding to the same concentration differ by 0.22 – 0.43 %.

### 3.2. The influence of the concentration of the boron impurity on the band gap

Having considered the geometric and stability-related issues, we shall now turn our attention to the electronic properties of boron doped fullerenes. The following section will examine the relationship between the band gap of these nanostructures and the concentration of impurity atoms (Fig. 6).

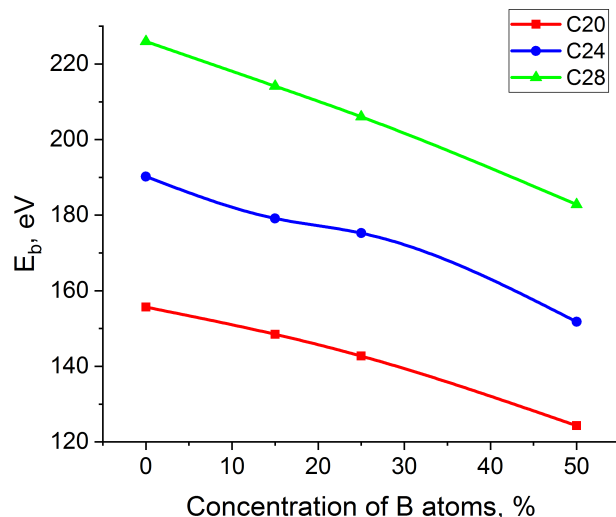


FIG. 5. The dependence of the binding energy on the concentration of boron atoms

In the case of fullerene  $C_{20}$ , the addition of 15 % of the impurity leads to an increase in the band gap to a value of 3.007 eV for the spin-up electronic states. For the spin-down states, an increase is also observed, but relatively small, by 0.126 eV compared to the initial structure. In the region of 15 % of the impurity concentration, the maximum value of the band gap is observed for both spin-up and spin-down states. In the range from 15 to 50 %, the function decreases monotonously. For the spin-up states, the band gap of the  $BC_3 C_{20}$  structure still has a greater value of the band gap compared to pure  $C_{20}$ ; for the spin-down states, a different situation is observed – the band gap is smaller compared to the original structure. In  $BC C_{20}$  fullerenes of both types, the electronic states are non-degenerate in spin, respectively, the band gaps for the spin-up and spin-down states are identical. The addition of 50 % of the impurity leads to a decrease in the band gap compared to the initial fullerene by 0.195 – 0.316 eV, depending on the spatial arrangement of the atoms.

Consider the case of fullerene  $C_{24}$ . For the pure variant, the band gap is 1.864 eV. It is noteworthy that the electronic states for all its derivatives considered are non-degenerate in spin. The addition of 15 and 25 % of impurity boron atoms increases the band gap; the addition of 50 %, as in the case of  $C_{20}$ , leads to its decrease to values of 1.801 eV (for type A) and 1.531 eV (for type B), i.e. up to 1.666 eV, if we take the average value.

For fullerene  $C_{28}$ , spin degeneracy is observed only in the case of the  $BC_3 C_{28}$  structure. The addition of 15 and 50 % impurities of boron atoms makes it possible to decrease the band gap to values of the order of 1.30 eV. The addition of 25 % of the impurity leads to an increase of the band gap. The values of this parameter for the spin-up and spin-down states differ by 3.6 %.

### 3.3. Analysis of the one-electron spectra, DOS and PDOS

Following an overview of the general patterns of change in the band gap during doping of small fullerenes, it is essential to examine the processes occurring with the electronic structure in greater detail. The objective of this analysis is to examine the single-electron spectra and DOS for each nanosystem in greater detail.

Consider the case of fullerene  $C_{20}$ . The comparison is made with a pure structure (Fig. 7a). An increase in the band gap for the  $BC_5 C_{20}$  case (Fig. 7b) for the spin-up states is associated with an increase in the bottom of the conduction band of 0.314 eV and a decrease in the top of the valence band of 0.860 eV. For the spin-down states there is a decrease in the top of the valence band by 1.070 eV, but at the same time there is a decrease in the bottom of the conduction band by 0.944 eV – these two processes have opposite effects on the band gap. Thus, in spin-down states, a decrease in the bottom of the conduction band partially compensates for a decrease in the top of the valence band, so the increase in the band gap is not as significant as in spin-up states.

We will now proceed to examine the  $BC_3 C_{20}$  structure (Fig. 7c). In this case, two processes are observed for both the spin-up and spin-down states: a decrease of the top of the valence band and a decrease of the bottom of the conduction band. The values of the top of the valence band are essentially identical for the various types of states under consideration, with a maximum difference of approximately 0.10 %. The value of the conduction band bottom for spin-up states is 0.979 eV higher than that for spin-down states. The decrease in the bottom of the conduction band for spin-down states is greater in absolute value than the decrease in the top of the valence band, which ensures a decrease in the band gap compared to the initial structure. In contrast, for spin-up states, the decrease in the bottom of the conduction band

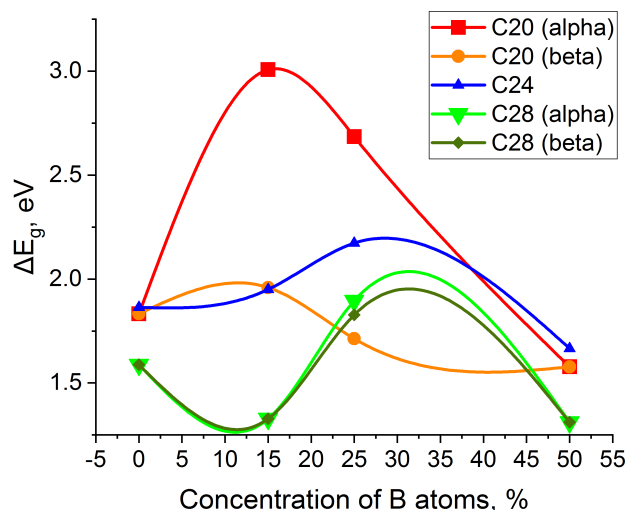


FIG. 6. The dependence of the band gap on the concentration of boron atoms; in the brackets it is the type of orbitals used for calculation of the band gap

is less significant in absolute value than the decrease in the top of the valence band, and therefore the band gap have the greater value than in pure  $C_{20}$ .

The qualitative mechanisms observed in the structures of fullerene  $C_{20}$  with a 50 % boron impurity (Fig. 7d,e) are analogous to those observed in the structures with a 25 % impurity. These include a decrease of the bottom of the conduction band and a decrease of the top of the valence band. However, in this case, the decrease in the bottom of the conduction band is fully compensated for by the decrease in the top of the valence band, resulting in a further narrowing of the band gap for both type A and type B structures. A comparison of the two structures reveals that the band gap of type A is 0.121 eV smaller than that of type B.

We now turn to materials based on fullerene  $C_{24}$  (Fig. 8). In the case of  $BC_5 C_{24}$  (Fig. 8b), there is an increase in the valence band top of 0.269 eV, while the bottom of the conduction band increases by 0.355 eV. Consequently, the band gap is observed to increase by 0.086 eV.

An increase in the impurity concentration to 25 % (Fig. 8c,d) results in an increase in the band gap to 2.130 eV for a type A structure and to 2.216 eV for a type B structure. In the case of a type A structure, there is an increase in the bottom of the conduction band and a relatively insignificant (approximately 0.30 %) decrease in the top of the valence band. It is evident that these processes are responsible for the observed increase in the band gap. In the case of a type B structure, a decrease is observed in both the bottom of the conduction band and the top of the valence band. A sufficiently large decrease in the top of the valence band by 0.511 eV results in an increase in the band gap. Conversely, a decrease in the conduction band bottom by 0.159 eV partially compensates for this.

The decrease in the band gap in  $BC C_{24}$  structures (Fig. 8e,f) is determined by a decrease in the bottom of the conduction band. The positions of the bottom of the conduction band in structures of type A and type B differ by 0.72 %, however, the band gaps differ by 17.6 %. This is due to a stronger decrease in the top of the valence band in the type A structure, while in the type B structure it is not so significant.

Further we will examine a number of different variants of boron doped fullerene  $C_{28}$  (Fig. 9). Upon doping  $C_{28}$  with 15 % of the impurity of boron atoms (Fig. 9b), the top of the valence band increases by 0.470 eV and the bottom of the conduction band increases by 0.210 eV. Therefore, the band gap is decreased by 0.260 eV. An increase in the band gap in the case of the  $BC_3 C_{28}$  structure (Fig. 9c) for both spin-up and spin-down states is associated with a more significant increase in the bottom of the conduction band relative to an increase in the top of the valence band. For the  $BC C_{28}$  structure (Fig. 9d), a decrease in the band gap is realized due to the same mechanisms as in the case of  $BC_5 C_{28}$ , i.e. due to a more significant increase in the top of the valence band relative to a smaller increase in the bottom of the conduction band. However, if in the case of  $BC_5 C_{28}$ , there was an increase in the bottom of the conduction band by 4.60 %, then here it was only by 0.62 %. At the same time, in the case of  $BC_5 C_{28}$ , there was an increase in the valence band top by 7.63 %, and in the case of  $BC C_{28}$  – by 4.95 %. As a result, the values of the band gap for structures with 15 and 50 % impurities differ slightly (by 1.28 %).

### 3.4. Charge distribution analysis

The analysis of the charge distribution showed that in all the considered cases, the electron density shifts from boron atoms to carbon atoms. A similar pattern also occurs for other carbon nanostructures: nanotubes [50] and nanolayers [51].

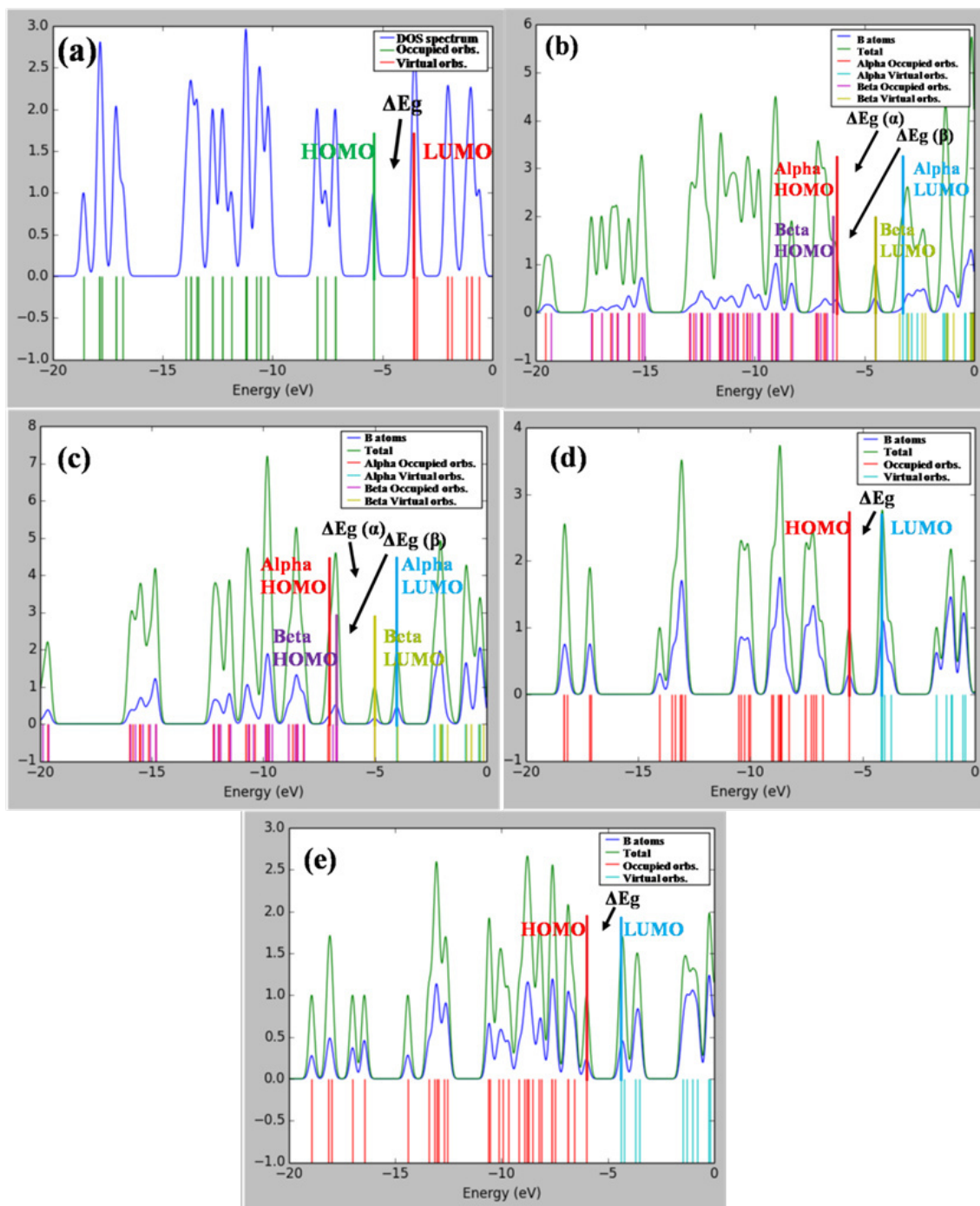


FIG. 7. One-electron spectra and total DOS of the  $C_{20}$  (a), total DOS (green curve) and partial DOS of boron atoms (blue curve) of the  $BC_5 C_{20}$  (b),  $BC_3 C_{20}$  (c),  $BC C_{20}$  type A (d),  $BC C_{20}$  type B (e)

We denoted the average charge on carbon atoms as  $Q(C)$ , on boron atoms  $-Q(B)$ . For the case of fullerene  $C_{20}$ , the maximum average charge on boron atoms is observed at an impurity concentration of 15 % and is 0.313; with increasing concentration, this indicator decreases monotonously. For  $BC C_{20}$  structures, the difference in the considered indicator for the two types is 1.7 %. The average charge on carbon atoms also decreases monotonously with increasing concentration, from  $-0.055$  for  $BC_5 C_{20}$  to  $-0.242$  for  $BC C_{20}$  type A and  $-0.238$  for type B. For boron doped fullerene  $C_{24}$ , the spatial arrangement of boron atoms is crucial. At an impurity concentration of 15 %, the average charge on boron atoms is 0.308. When switching to a concentration of 25 %, two options are possible: a decrease in this indicator by 19.8 % for type A and an increase by 6.4 % for type B. The difference in the value of the average charge on boron atoms for the two types of structures is 24.9 %. The average charge on carbon atoms decreases from  $-0.062$  for  $BC_5$  to  $-0.082$  for  $BC_3 C_{24}$  type A and  $-0.110$  for type B. In the case of a 50 % impurity concentration, the average charge on boron atoms is 0.243 for type A and 0.257 for type B; here, too, the minimum average charge on carbon atoms for all considered  $C_{24}$ -based structures

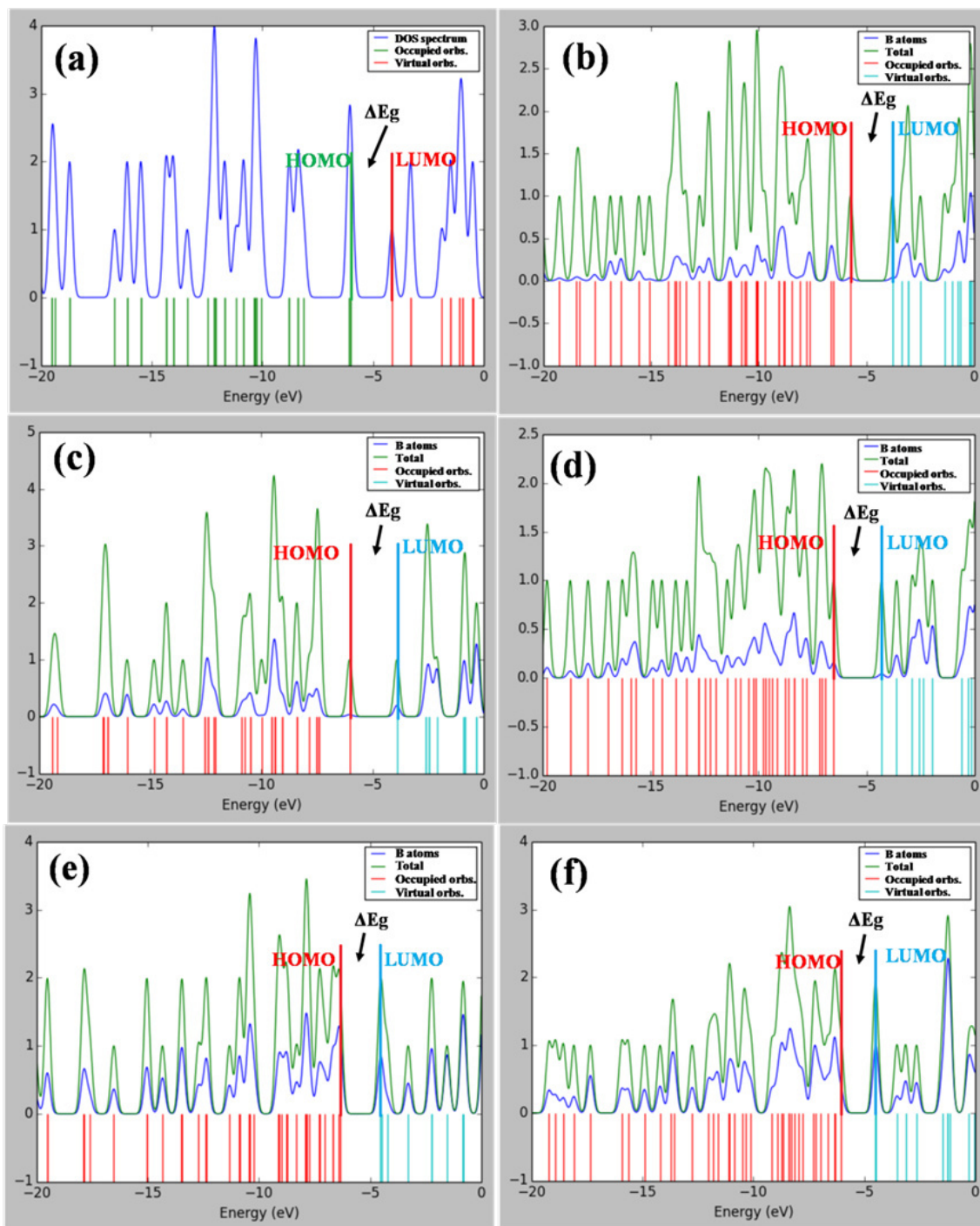


FIG. 8. One-electron spectra and total DOS of the  $C_{24}$  (a), total DOS (green curve) and partial DOS of boron atoms (blue curve) of the  $BC_5 C_{24}$  (b),  $BC_3 C_{24}$  type A (c),  $BC_3 C_{24}$  type B (d),  $BC C_{24}$  type A (e),  $BC C_{24}$  type B (f)

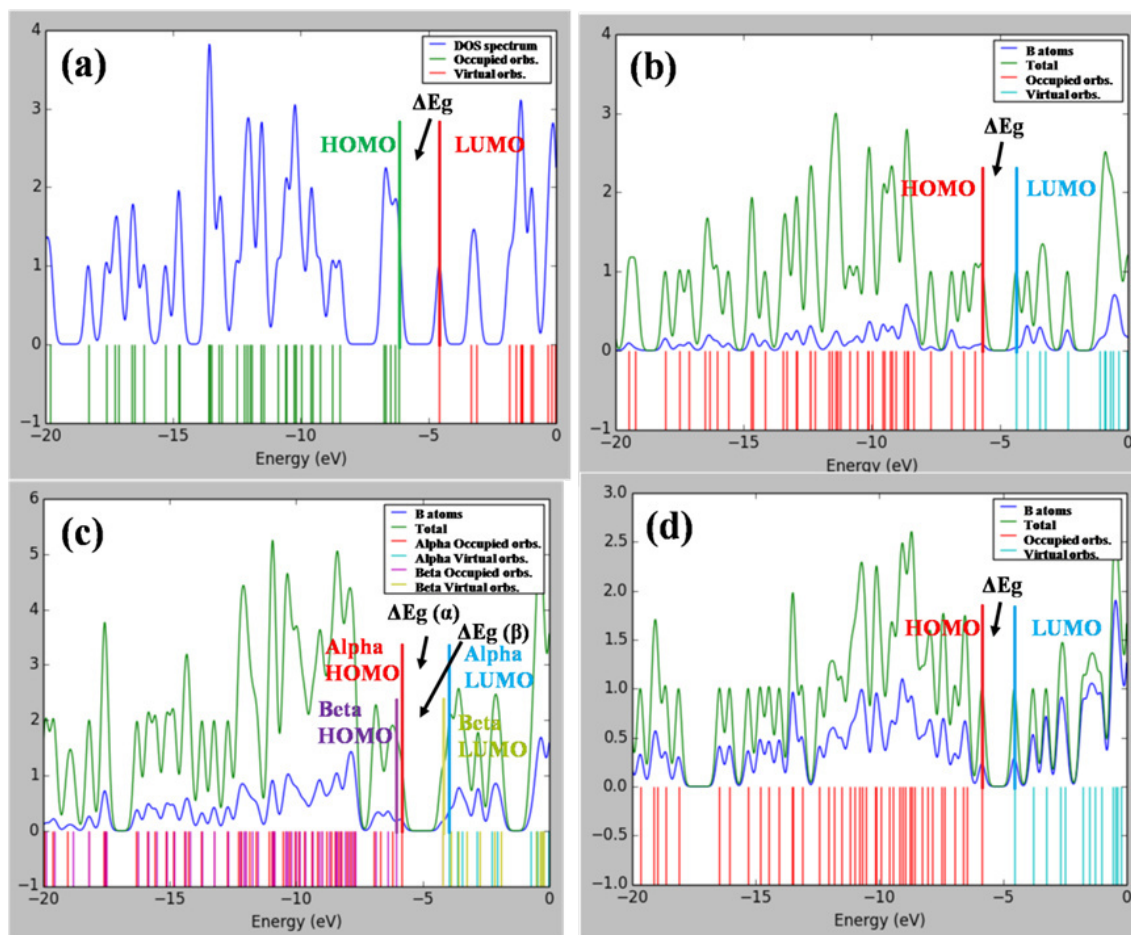


FIG. 9. One-electron spectra and total DOS of the C<sub>28</sub> (a), total DOS (green curve) and partial DOS of boron atoms (blue curve) of the BC<sub>5</sub> C<sub>28</sub> (b), BC<sub>3</sub> C<sub>28</sub> (c), BC C<sub>28</sub> (d)

is  $-0.243$  for type A and  $-0.257$  for type B. In the case of fullerene C<sub>28</sub>, the maximum average charge on boron atoms is for the BC<sub>3</sub> structure and is 0.337; for BC<sub>5</sub> and BC, the values of this parameter are 0.334 and 0.263, respectively. The average charge on carbon atoms decreases monotonously from  $-0.056$  for BC<sub>5</sub> to  $-0.263$  for BC.

Table 1 presents a compilation of the values of all the physical quantities discussed in the work.

#### 4. Conclusion

In the present work optimized structures of boron doped small fullerenes C<sub>20</sub>, C<sub>24</sub>, and C<sub>28</sub> with concentrations of the impurity of boron atoms of 15, 25, and 50 % were obtained. The study of their stability, geometric and electronic properties was carried out by calculations performed using methods of DFT. Single-electron spectra and DOS were also obtained for all the structures considered.

Thus, it was found that small fullerenes doped with boron atoms remain stable enough for their practical production. In the vast majority of cases, the substitution of carbon atoms with boron atoms leads to a decrease in the length of the C–C bond. At the same time, the B–C and B–B bonds formed have a longer length compared to C–C. The doping of the fullerene C<sub>28</sub> with 50 % of the boron atoms impurity leads to a sufficiently strong distortion of its geometric structure and the appearance of octagons in it.

The possibility of obtaining materials with different band gap widths from 1.311 to 3.007 eV by doping of the considered small fullerenes with different concentrations of boron atoms was established. The change in this parameter is associated with the restructuring of the electronic structure, the displacement of the bottom of the conduction band and the top of the valence band. If in fullerenes C<sub>20</sub> and C<sub>24</sub> the determining process leading to a decrease in the band gap was a decrease in the bottom of the conduction band, then in the case of fullerene C<sub>28</sub> this was determined by an increase in the top of the valence band. For all the considered nanostructures, it was established that the addition of 50 % of the impurity of boron atoms leads to a decrease in the band gap. This may be due to the fact that the average charge on carbon atoms and boron atoms in them is equal in modulus.

Ultimately, the present work demonstrated the possibility of controlling the refractive index of nanomaterials based on small fullerenes by changing the band gap by doping the material with boron atoms. Thus, it is possible to construct

TABLE 1. Geometric and electronic properties of boron doped small fullerenes C<sub>20</sub>, C<sub>24</sub>, C<sub>28</sub>.  $d_{C-C}$  – an average length of the C–C bond,  $d_{B-C}$  – an average length of the B–C bond,  $d_{B-B}$  – an average length of the B–B bond,  $E_b$  – binding energy,  $E_{LUMO}$  – energy of the lowest unoccupied molecular orbital,  $E_{HOMO}$  – energy of the highest occupied molecular orbital,  $\Delta E_g$  – band gap,  $Q(C)$  – an average charge on carbon atoms,  $Q(B)$  – an average charge on boron atoms

Structure	$d_{C-C}$ , Å	$d_{B-C}$ , Å	$d_{B-B}$ , Å	$E_b$ , eV	$E_{LUMO}$ , eV	$E_{HOMO}$ , eV	$\Delta E_g$ , eV	$Q(C)$	$Q(B)$
C <sub>20</sub>	1.4636	—	—	155.67	–3.568	–5.401	1.833	0.000	—
BC <sub>5</sub> C <sub>20</sub>	1.4636	1.5627	—	148.48	–3.254 ( $\alpha$ ) –4.512 ( $\beta$ )	–6.261 ( $\alpha$ ) –6.471 ( $\beta$ )	3.007 ( $\alpha$ ) 1.959 ( $\beta$ )	–0.055	0.313
BC <sub>3</sub> C <sub>20</sub>	1.4578	1.5883	—	142.71	–4.034 ( $\alpha$ ) –5.013 ( $\beta$ )	–6.719 ( $\alpha$ ) –6.726 ( $\beta$ )	2.685 ( $\alpha$ ) 1.713 ( $\beta$ )	–0.086	0.258
BC C <sub>20</sub> type A	1.4387	1.5851	1.7120	124.15	–4.208	–5.725	1.517	–0.242	0.242
BC C <sub>20</sub> type B	1.4247	1.5881	1.7056	124.43	–4.384	–6.022	1.638	–0.238	0.238
C <sub>24</sub>	1.4651	—	—	190.22	–4.146	–6.010	1.864	0.000	—
BC <sub>5</sub> C <sub>24</sub>	1.4725	1.5448	—	179.13	–3.791	–5.741	1.950	–0.062	0.308
BC <sub>3</sub> C <sub>24</sub> type A	1.4586	1.5703	—	175.07	–3.900	6.030	2.130	–0.082	0.247
BC <sub>3</sub> C <sub>24</sub> type B	1.4543	1.5773	—	175.46	–4.305	–6.521	2.216	–0.110	0.329
BC C <sub>24</sub> type A	1.4334	1.5778	1.7409	152.10	–4.555	–6.356	1.801	–0.243	0.243
BC C <sub>24</sub> type B	1.4349	1.5860	1.6942	151.45	–4.522	–6.053	1.531	–0.257	0.257
C <sub>28</sub>	1.4579	—	—	225.95	–4.569	–6.157	1.588	0.000	—
BC <sub>5</sub> C <sub>28</sub>	1.4575	1.5631	—	214.13	–4.359	–5.687	1.328	–0.056	0.334
BC <sub>3</sub> C <sub>28</sub>	1.4556	1.5713	—	206.03	–3.948 ( $\alpha$ ) –4.227 ( $\beta$ )	–5.844 ( $\alpha$ ) –6.054 ( $\beta$ )	1.896 ( $\alpha$ ) 1.827 ( $\beta$ )	–0.112	0.337
BC C <sub>28</sub>	1.4043	1.5638	2.6052	182.82	–4.541	–5.852	1.311	–0.263	0.263

heterostructures in general and photonic crystals in particular based on considered nanostructures. This opens up new opportunities for creating new and improving existing optoelectronic devices that can find their application in modern infocommunication systems.

## References

- [1] Essiambre R.J., Tkach R.W. Capacity trends and limits of optical communication networks. *Proceedings of the IEEE*, 2012, **100** (5), P. 1035–1055.
- [2] El-Hageen H.M., Alatwi A.M., Zaki Rashed A.N. High-speed signal processing and wide band optical semiconductor amplifier in the optical communication systems. *J. of Optical Communications*, 2024, **44** (s1), s1277–s1284.
- [3] Soma D., Beppu S., Wakayama Y., Sumita S., Takahashi H., Yoshikane N., Morita I., Fellow, Tsuritani T., Suzuki M. 50.47-Tbit/s standard cladding coupled 4-core fiber transmission over 9,150 km. *J. of Lightwave Technology*, 2021, **39** (22), P. 7099–7105.
- [4] Manral A., Singh R. Lifi technology. *Int. J. of Scientific Research in Science, Engineering and Technology*, 2016, **2**, P. 493–498.
- [5] Khaleel B.M., Alatba S.R., Hamdoun S.H., Terenchuk S. Exploring Li-Fi for IoT Advanced Audio Data Transfer. *Proceedings of the Conference "35th Conference of Open Innovations Association (FRUCT)"*, Tampere, Finland, 9 May 2024, P. 343–351.
- [6] Alfattani S. Review of LiFi technology and its future applications. *J. of Optical Communications*, 2021, **42** (1), P. 121–132.
- [7] Oton E., Cigl M., Morawiak P., Mironov S., Bubnov A., Piecek W. All-optical 3D blue phase photonic crystal switch with photosensitive dopants. *Scientific Reports*, 2024, **14** (1), 9910.
- [8] Masilamani S., Samundiswary P. Compact and efficient PC-based directional coupler all-optical switch. *J. of Optical Communications*, 2024, **44** (s1), s153–s160.
- [9] Kumar V., Suthar B. Unit cell independent optical filter using one-dimensional photonic crystal. *J. of Optics*, 2024, **53**, P. 5106–5109.
- [10] Banerjee A. Design of an optical buffer by using 1D quaternary photonic crystal. *J. of Optics*, 2024, **53** (2), P. 817–820.
- [11] Zhang A., Yang X., Wang J. Design of Channel Drop Filters Based on Photonic Crystal with a Dielectric Column with Large Radius inside Ring Resonator. *Photonics*, 2024, **11** (6), 554.

- [12] Liu M.D., Chen H.H., Wang Z., Zhang Y., Zhou X., Tang G.J., Ma F., He X.T., Chen X.D., Dong J.W. On-Chip Topological Photonic Crystal Nanobeam Filters. *Nano Letters*, 2024, **24** (5), P. 1635–1641.
- [13] Wang Y., Yao Y., Zhang H., Liu B., Duan S., Lin W. An electrically controlled tunable photonic crystal filter based on thin-film lithium niobate. *Optoelectronics Letters*, 2024, **20** (4), P. 200–204.
- [14] Ankita, Suthar B., Bissa S., Bhargava A. Dual-channel optical filter based on photonic crystal with double defect. *J. of Optics*, 2024, **53**, P. 3996–3999.
- [15] Hazra S., Mukhopadhyay S. Photonic crystal based integrated system for half adder and half subtractor operations. *Optical and Quantum Electronics*, 2024, **56** (5), 855.
- [16] Pathak P., Zafar R., Kanungo V., Vyas S. Photonic crystal-based all-optical half adder with high contrast ratio. *J. of Optical Communications*, 2024, **44** (s1), s119–s124.
- [17] Hazra S., Mukhopadhyay S. Implementation of photonic crystal based optical full adder using ring resonators. *Optics Communications*, 2024, 130828.
- [18] Goswami K., Mondal H., Sen M. Design of all optical logic half adder based on holes-in-slab photonic crystal. *Optical and Quantum Electronics*, 2024, **56** (2), 271.
- [19] Askarian A. All optical half subtractor based on linear photonic crystals and phase shift keying technique. *J. of Optical Communications*, 2024, **44** (s1), s449–s455.
- [20] Chen H., Chen H., Li A., Liu M., Chan E.H.W. Simple and reconfigurable photonics-based half adder and half subtractor. *Optics Communications*, 2024, **555**, 130206.
- [21] Elhachemi K., Rafah N. A novel proposal based on 2D linear resonant cavity photonic crystals for all-optical NOT, XOR and XNOR logic gates. *J. of Optical Communications*, 2024, **44** (s1), s283–s291.
- [22] He L., Liu D., Zhang H., Zhang F., Zhang W., Feng X., Huang Y., Cui K., Liu F., Zhang W., Zhang X. Topologically Protected Quantum Logic Gates with Valley-Hall Photonic Crystals. *Advanced Materials*, 2024, **36** (24), 2311611.
- [23] Mitin V.V., Kochelep V.A., Strosio M.A. *Quantum heterostructures: microelectronics and optoelectronics*. Cambridge: University Press, Cambridge, 1999, 642 p.
- [24] Yablonovitch E. Photonic band-gap structures. *JOSA B*, 1993, **10** (2), P. 283–295.
- [25] Yang Y., Wang L., Yang H., Li Q. 3D chiral photonic nanostructures based on blue-phase liquid crystals. *Small Science*, 2021, **1** (6), 2100007.
- [26] Vlasov Y.A., O’Boyle M., Hamann H.F., McNab S.J. Active control of slow light on a chip with photonic crystal waveguides. *Nature*, 2005, **438** (7064), P. 65–69.
- [27] Gersen H., Karle T.J., Engelen R.J.P., Bogaerts W., Korterik J.P., van Hulst N.F., Krauss T.F., Kuipers L. Real-space observation of ultraslow light in photonic crystal waveguides. *Physical Review Letters*, 2005, **94** (7), 073903.
- [28] Kempa K., Kimball B., Rybczynski J., Huang Z.P., Wu P.F., Steeves D., Sennett M., Giersig M., Rao D.V.G.L.N., Carnahan D.L., Wang D.Z., Lao J.Y., Li W.Z., Ren Z.F. Photonic crystals based on periodic arrays of aligned carbon nanotubes. *Nano Letters*, 2003, **3** (1), P. 13–18.
- [29] Cui K., Lemaire P., Zhao H., Savas T., Parsons G., Hart A.J. Tungsten–carbon nanotube composite photonic crystals as thermally stable spectral-selective absorbers and emitters for thermophotovoltaics. *Advanced Energy Materials*, 2018, **8** (27), 1801471.
- [30] Sun X., Zhang J., Lu X., Fang X., Peng H. Mechanochromic photonic-crystal fibers based on continuous sheets of aligned carbon nanotubes. *Angewandte Chemie Int. Ed.*, 2015, **54** (12), P. 3630–3634.
- [31] Tan Y.C., Tou Z.Q., Mamidala V., Chow K.K., Chan C.C. Continuous refractive index sensing based on carbon-nanotube-deposited photonic crystal fibers. *Sensors and Actuators B: Chemical*, 2014, **202**, P. 1097–1102.
- [32] Butt H., Dai Q., Wilkinson T.D., Amaratunga G.A.J. Negative index photonic crystal lenses based on carbon nanotube arrays. *Photonics and Nanostructures – Fundamentals and Applications*, 2012, **10** (4), P. 499–505.
- [33] Mahmoodi Y., Fathi D. High-performance refractive index sensor for oil derivatives based on MWCNT photonic crystal microcavity. *Optics & Laser Technology*, 2021, **138**, 106865.
- [34] Solookinejad G., Payravi M., Jabbari M., Nafar M., Sangachin E.A. Optical multistability in 1D photonic crystal doped with carbon-nanotube quantum dot nanostructures. *Laser Physics*, 2017, **27** (12), 125202.
- [35] Fernandes J.A., Feitosa F.A.O., Costa C.H.O., Vasconcelos M.S., Bezerra C.G., Anselmo D.H.A.L. Graphene-embedded planar and cylindrical Oldenburger–Kolakoski aperiodic photonic crystals. *Optical Materials*, 2024, **148**, 114832.
- [36] Hossain M.M., Talukder M.A. Tamm and surface plasmon hybrid modes in anisotropic graphene-photonic-crystal structure for hemoglobin detection. *Optics Express*, 2024, **32** (8), P. 14261–14275.
- [37] Xia B., Zeng X., Lan W., Zhang M., Huang W., Wang H., Liu C. Cellulose nanocrystal/graphene oxide one-dimensional photonic crystal film with excellent UV-blocking and transparency. *Carbohydrate Polymers*, 2024, **327**, 121646.
- [38] Kumar C., Raghuvanshi S.K., Kumar V. Graphene-based patch antenna array on photonic crystal substrate at terahertz frequency band. *J. of Electromagnetic Waves and Applications*, 2024, **38** (2), P. 250–263.
- [39] Liu W., Li G., Chen C., Liu J., Li Z.Y. Broadly tunable filter based on a graphene MEMS-photonic crystal composite structure and its application in single-pixel full-color displays. *J. of Materials Chemistry C*, 2024, **12** (18), P. 6588–6595.
- [40] Elblbeisi M., Taya S.A., Almawgani A.H., Hindi A.T., Alhamss D.N., Colak I., Patel S.K. Absorption Properties of a Defective Binary Photonic Crystal Consisting of a Metamaterial, SiO<sub>2</sub>, and Two Graphene Sheets. *Plasmonics*, 2024, **19** (3), P. 1431–1442.
- [41] Zhang C., Ota Y., Iwamoto S. Wide-mode-area slow light waveguides in valley photonic crystal heterostructures. *Optical Materials Express*, 2024, **14** (7), P. 1756–1766.
- [42] Kislyakov I.M., Ivanov P.V., Nunzi J.M., Vlasov A.Y., Ryzhov A.A., Venediktova A.V., Wang H., Wang Z., Zhang T., Dong N., Wang J. Nonlinear optical fullerene and graphene-based polymeric 1D photonic crystals: perspectives for slow and fast optical bistability. *JOSA B*, 2021, **38** (9), C198–C209.
- [43] Gaevski M.E., Kognovitskii S.O., Konnikov S.G., Nashchekin A.V., Nesterov S.I., Seisyan R.P., Zadiranov J.M. Two-dimensional photonic crystal fabrication using fullerene films. *Nanotechnology*, 2000, **11** (4), 270.
- [44] Xu B., Han P., Wang L., Li J., Liu X., Chen M., Hideki I. Optical properties in 2D photonic crystal structure using fullerene and azafullerene thin films. *Optics communications*, 2005, **250** (1–3), P. 120–125.
- [45] Srivastava S., Ojha S. Omnidirectional reflection bands in one-dimensional photonic crystal structure using fullerene films. *Progress In Electromagnetics Research*, 2007, **74**, P. 181–194.
- [46] Belousova I.M., Ryzhov A.A. Numerical simulation of nonlinear properties of fullerene-containing one-dimensional photonic crystal. *Optics and Spectroscopy*, 2012, **112**, P. 902–905.
- [47] Sawant S.V., Patwardhan A.W., Joshi J.B., Dasgupta K. Boron doped carbon nanotubes: Synthesis, characterization and emerging applications – A review. *Chemical Engineering J.*, 2022, **427**, 131616.

- [48] Zhang J.J., Ma J., Feng X. Precision Synthesis of Boron-Doped Graphene Nanoribbons: Recent Progress and Perspectives. *Macromolecular Chemistry and Physics*, 2023, **224** (1), 2200232.
- [49] Zaporotskova I.V., Boroznin S.V., Belonenko M.B., Drychkov E.S., Butenko Y.V. Graphene Nanotapes Modified with Impurity Boron Atoms as a Basis for Two-Dimensional Photonic Crystals. *Bulletin of The Russian Academy of Sciences: Physics*, 2022, **86**, P. 1450–1453.
- [50] Zaporotskova I.V., Boroznina N.P., Boroznin S.V., Drychkov E.S., Butenko Y.V., Belonenko M.B. Carbon Nanotubes Doped with Boron as a Basis for Two-Dimensional Photonic Crystals. *Bulletin of The Russian Academy of Sciences: Physics*, 2022, **86**, P. 673–677.
- [51] Boroznin S.V., Carbon nanolayers modified with boron atoms as a basis for devices with ionic conductivity: theoretical study. *J. of Advanced Materials and Technologies*, 2022, **7** (2), P. 97–103.
- [52] Fuentes G.G., Borowiak-Palen E., Knupfer M., Pichler T., Fink J., Wirtz L., Rubio A. Formation and electronic properties of  $BC_3$  single-wall nanotubes upon boron substitution of carbon nanotubes. *Physical Review B—Condensed Matter and Materials Physics*, 2004, **69** (24), 245403.
- [53] Yang N., Liu G., Chen T., Dong X., Li Y., Xu Z. Unveiling adsorption characteristics of  $BC_5$  monolayer: High electronic anisotropy and gas sensing performance. *Applied Surface Science*, 2023, **615**, 156226.
- [54] Chuvilin A., Kaiser U., Bichoutskaia E., Besley N.A., Khlobystov A.N. Direct transformation of graphene to fullerene. *Nature Chemistry*, 2010, **2** (6), P. 450–453.
- [55] Koch W., Holthausen M., *A Chemist's Guide to Density Functional Theory*, Wiley-VCH, Weinheim, 2002, 306 p.
- [56] Sakr M.A., Abdelsalam H., Teleb N.H., Abd-Elkader O.H., Zhang Q. Exploring the structural, electronic, and hydrogen storage properties of hexagonal boron nitride and carbon nanotubes: insights from single-walled to doped double-walled configurations. *Scientific Reports*, 2024, **14** (1), 4970.
- [57] Tomilin O.B., Rodionova E.V., Rodin E.A., Knyazev A.V. Emission properties of boron and nitrogen doped ultrashort carbon nanotubes. *Applied Surface Science*, 2024, **669**, 160443.
- [58] Pei S., Li J., Bai Z., Wang C., Lv X. Atomic insights of structural, electronic properties of B, N, P, S, Si-doped fullerenes and lithium ion migration with DFT-D method. *J. of Molecular Modeling*, 2024, **30** (12), 422.
- [59] Kurban M. Electronic structure, optical and structural properties of Si, Ni, B and N-doped a carbon nanotube: DFT study. *Optik*, 2018, **172**, P. 295–301.
- [60] O'boyle N.M., Tenderholt A.L., Langner K.M. Cclib: a library for package-independent computational chemistry algorithms. *J. of Computational Chemistry*, 2008, **29** (5), P. 839–845.
- [61] North S.C., Jorgensen K.R., Pricetolstoy J., Wilson A.K. Population analysis and the effects of Gaussian basis set quality and quantum mechanical approach: main group through heavy element species. *Frontiers in Chemistry*, 2023, **11**, 1152500.

---

Submitted 26 September 2024; revised 18 January 2025; accepted 5 May 2025

#### Information about the authors:

Anton R. El Zanin – Volgograd State University, Universitetskiy av., 100, Volgograd, 400062, Russia;  
ORCID 0009-0005-3897-9490; aelzanin@volsu.ru

Sergey V. Boroznin – Volgograd State University, Universitetskiy av., 100, Volgograd, 400062, Russia;  
ORCID 0000-0003-0110-2271; boroznin@volsu.ru

Irina V. Zaporotskova – Volgograd State University, Universitetskiy av., 100, Volgograd, 400062, Russia;  
ORCID 0000-0002-9486-2482; zaporotskova@volsu.ru

*Conflict of interest:* the authors declare no conflict of interest.

**Paper abstracts in Russian / Аннотации статей****Свободная энергия и энтропия конструктивных мер Гиббса для модели Изинга на дереве Кэли порядка три**

М.М. Рахматуллаев, З.А. Бурхонова

В этой статье мы изучаем нетрансляционно-инвариантные конструктивные меры Гиббса для модели Изинга на дереве Кэли третьего порядка, которые отличаются от известных мер Гиббса. Приведены условия для существования по крайней мере двух различных мер Гиббса, который определяют существование фазового перехода. Вычислены свободные энергии и энтропии для найденных мер. Полученные свободные энергии и энтропии сравниваются с известными результатами, и показано, что они отличаются от свободных энергии и энтропии для других мер Гиббса.

Ключевые слова: дерево Кэли, модель Изинга, мера Гиббса, свободная энергия, энтропия.

**Теоретическое исследование эффективного g-фактора квантовой проволоки Cd<sub>1-x</sub>MnxTe при комбинированном воздействии приложенного магнитного поля, спин-орбитальной связи и обменных эффектов**

Мохаммад Эльсаид, Диана Далиах, Айхам Шаер, Махмуд Али

В этой статье формула энергии для носителя заряда ( $e$ ), заключенного в квантовой яме разбавленного магнитного полупроводника (DMS) QW, изготовленной из Cd<sub>1-x</sub>MnxTe, получена и использована для расчета плотности состояний (DOS) и g-фактора Ланде. Исследуются уровни Ландау в квантовой проволоке, помещенной в однородное магнитное поле вдоль ее оси, с учетом наличия спин-орбитального взаимодействия Рашбы и обменного эффекта. Эти эффекты изменили DOS и уровни Ландау. Исследуется g-фактор электрона для самого низкого состояния. Наши результаты показывают, что g-фактор сильно зависит от комбинированных эффектов магнитного поля и величины спин-орбитального взаимодействия Рашбы. G-фактор может изменяться в широком диапазоне значений для объемного значения от 2 до 300, что делает его хорошим кандидатом для спинтронных приложений.

Ключевые слова: g-фактор Ланде; эффект Рашбы; магнитное поле, плотность состояний.

**Влияние конструкции SiC MOSFET на его сопротивление открытого канала и пробивное напряжение**

О.Б. Чуканова, К.А. Царик

Аннотация: Для повышения эффективности схем на основе SiC MOSFET необходимо увеличивать их удельные токи и надежность, соответственно, необходимо уменьшать сопротивление транзистора в открытом состоянии и увеличивать их пробивное напряжение. Для достижения этих целей исследованы зависимости электрофизических характеристик транзистора от его конструктивно-технологических особенностей при помощи Sentaurus TCAD. Показано, что для увеличения токов транзистора необходимо уменьшать длину канала, расстояние между р-базами истоков транзистора и создавать JFET область. Для увеличения пробивного напряжения прибора предложено увеличивать степень легирования области дрейфа, а также предложена новая конструкция транзистора, которая позволит получать приборы с пробивным напряжением различных номиналов до 2500 В.

Ключевые слова SiC MOSFET, TCAD, JFET легирование, пробивное напряжение

**Исследование усиления фемтосекундного лазера в кристаллах  $MgO:LiTaO_3$  с периодическими нелинейными свойствами**

О.И. Собиров, А.Э. Раджабов, А.Р. Матназаров,  
Б.Х. Эшчанов, Ш. Отажанов, У.К. Сапаев

В данной работе представлено теоретическое исследование процесса параметрического усиления оптического излучения в кристаллах с периодической модуляцией квадратичной нелинейной восприимчивости на примере  $MgO:LiTaO_3$ . Особое внимание уделено анализу влияния основных факторов, таких как линейное поглощение и дисперсия, на эффективность процесса. Установлено, что в инфракрасном спектральном диапазоне эффекты линейного поглощения и дисперсии существенно влияют на коэффициент усиления сигнальной волны, определяя динамику перераспределения энергии и спектральные характеристики получаемого излучения. В исследовании предложен новый подход к оптимизации длины домена относительно длины когерентности, что позволило достичь эффективности до 18% за счет точной настройки, превосходящей ранее опубликованные результаты для аналогичных материалов. Полученные результаты имеют важное значение для оптимизации параметров нелинейных кристаллов, разработки эффективных схем параметрического усиления и создания перспективных оптических устройств, работающих в инфракрасном диапазоне.

Ключевые слова: параметрическое усиление, нелинейный кристалл  $MgO:LiTaO_3$ , инфракрасный диапазон, лазерные технологии, нелинейная оптика, квазифазовое согласование.

**Быстрое развитие адиабатической квантовой динамики: применение к плоским системам Дирака**

И. Сетиаван, Р. Экавита, Р. Сугихаким, Б.Э. Гунара

Мы изучаем схему ускоренной адиабатической квантовой динамики (2+1) дираковской частицы. Эта схема была первоначально предложена Масудой и Накамурой. В этой схеме мы включаем адиабатический параметр, который поддерживает адиабатическое движение частицы, и ускоряем ее движение вперед, вводя параметр масштабирования времени. Ускоренное адиабатическое состояние вперед получается путем определения члена регуляризации и движущего потенциала. Мы вводим предлагаемый метод в систему с дираковской частицей, используя зависящее от размерности времени уравнение Дирака (2+1), и получаем член регуляризации, движущий скалярный потенциал и движущий векторный потенциал. Настраивая движущее электрическое поле, этот метод может ускорить адиабатическую динамику электрона как дираковской частицы, захваченной в основном состоянии в плоскости  $x$  и электрическом поле в направлении  $x$  и постоянном магнитном поле в направлении  $y$ . Это ускорение сохранит основное состояние волновой функции от начального до конечного момента времени.

Ключевые слова: ускоренное развитие, адиабатический, плоский Дирак

### **Эффект электрон-фононного взаимодействия на первом возбужденном уровне энергии гауссовой квантовой точки GaAs**

Сома Мукхопадхьяй, Ч. Видьюллата, Пуджа Саини, Захид Малик

Эффект электрон-фононного взаимодействия на первом возбужденном состоянии трехмерной полярной полупроводниковой квантовой точки с гауссовым ограничением изучается с использованием теории возмущений Рэлея-Шредингера второго порядка. Аналитическое выражение для поляронной поправки первого возбужденного состояния получено в правдоподобном приближении. Показано, что эта энергия зависит как от силы, так и от диапазона гауссова потенциала. Наконец, наша теория применяется к квантовой точке GaAs, и показано, что поляронный эффект на первом возбужденном уровне может быть значительно большим, если размер точки мал. Поскольку информация о возбужденных состояниях важна для изучения явлений декогеренции, наши результаты могут быть полезны для обработки квантовой информации.

Ключевые слова: электрон-фононное взаимодействие; первое возбужденное состояние; квантовая точка GaAs.

### **Свойства многомодовых фазово-усредненных когерентных состояний**

М.С. Гусельников, А.А. Гайдаш, Г.П. Мирошниченко, А.В. Козубов

Фазово-усредненные когерентные состояния широко используются в протоколах квантового распределения ключей с ложными состояниями и фазовым кодированием. С точки зрения развития архитектуры квантовых протоколов важно понимать, может ли фазовое усреднение осуществляться на произвольном этапе оптической схемы без влияния на информационные свойства квантовой системы. В настоящей работе с помощью формализма алгебры супероператоров показано, что фазовое усреднение двухмодового когерентного состояния коммутирует с линейными оптическими преобразованиями. Это означает, что фазовое усреднение может осуществляться практически на любом этапе оптической установки. Продемонстрировано, что граница Холево для такого состояния совпадает с границей Холево для обычных когерентных состояний, имея в виду, что граница Холево является количественной мерой максимального объема информации, доступного для злоумышленника. Полученные результаты указывают на то, что фазовое усреднение может быть напрямую применено к системам распределения квантовых ключей на боковых частотах.

Ключевые слова: когерентные состояния, фазовая рандомизация, фазово-усредненные когерентные состояния, квантовое распределение ключей, граница Холево, квантовое распределение ключей на боковых частотах

### **Оптимальность линейного вакансионного дефекта для нуклеации скирмионов**

М.Н. Поткина, И.С. Лобанов

Магнитные скирмионы открывают перспективу создания сверхплотных и энергоэффективных устройств памяти, однако их эффективная запись остается сложной задачей. Используя атомистическое спиновое моделирование и расчёты путей с минимальным перепадом энергии в пленке PdFe/Ir(111), мы показали, что нанесение линейных цепочек из четырёх атомных вакансий почти вдвое снижает барьер нуклеации скирмиона — до 44,7 мэВ при 3,75 Тл — по сравнению с 85 мэВ в образце без примесей. Линейные дефекты являются наилучшим решением за счёт того, что они исключают области с высокой энергией в ядре во время создания скирмиона, при этом минимально нарушая его

внешнее окружение с плотностью отрицательной энергии при депиннинге. Этот эффект, обусловленный геометрией, основан только на общих профилях плотности энергии, что делает его широко применимым ко всем материалам, способным поддерживать скирмионы.

Ключевые слова: теория переходного состояния, топологические магнитные солитоны, зарождение, беговая память

### **Магнитная структура доменных границ в напряженных цилиндрических проводах**

К.А. Чичай, И.С. Лобанов, В.М. Уздин

Мы исследуем внутреннюю структуру и динамику поперечных доменных границ в аморфных, напряженных ферромагнитных микропроводах, сравнивая две модели магнитоупругой анизотропии. В полной модели все три основные компоненты напряжений (осевая, радиальная, циркулярная), полученные из реалистичного профиля напряжений, преобразуются в пространственно изменяющиеся анизотропии; в редуцированной модели сохраняется только доминирующая компонента напряжения в каждой радиальной области. Микромагнитное моделирование показывает, что редуцированная модель создает преувеличенные периферические отклонения — более сильные радиальные проекции намагниченности и более глубокое проникновение возмущенного слоя — по сравнению с полной моделью. Энергетический анализ показывает, что исключение недоминантных анизотропий приводит к недооценке взаимодействий доменной границы с дефектами и резкому, похожему на оболочку радиальному упорядочению при более высоких значениях поверхностной анизотропии.

Кроме того, расчеты диссипации, основанные на подходе Тиля, показывают, что сокращенная модель переоценивает скорость доменной границы до 50%. Эти результаты демонстрируют, что включение полного тензора напряжений необходимо для точного прогнозирования как статических профилей доменных границ, так и их динамического отклика в напряженных микропроводах.

Ключевые слова: Доменная граница, цилиндрические системы, аморфные ферромагнитные микропровода, микромагнетизм, магнитоупругая анизотропия, внутренние механические напряжения.

### **Субпуассоновский свет в бозонных каналах с флуктуирующими тепловыми потерями**

И. Степанов, Р. Гончаров, А.Д. Киселев

Мы изучаем статистику фотонов одномодового субпуассоновского света, распространяющегося в тепловом бозонном канале с потерями и флуктуирующим пропусканием, который можно рассматривать как зависящую от температуры модель турбулентной атмосферы. Предполагая, что дисперсия пропускания может быть выражена через параметр силы флуктуации, мы показываем, что статистика фотонов света остается субпуассоновской при условии, что усредненный коэффициент пропускания превышает свое критическое значение. Критический коэффициент пропускания аналитически вычисляется как функция параметров входных состояний, температуры и силы флуктуации. Результаты применяются для изучения особых случаев одномодовых сжатых состояний и нечетных оптических состояний кота Шредингера.

Ключевые слова: субпуассоновский свет; флуктуации; бозонный канал.

**Эпоксид-индуцированный синтез аэрогелей германия в уксусной кислоте**

Ольга Гайтко, Светлана Голодухина, Сергей Котцов, Александра Сон,  
Таисия Козлова, Александр Баранчиков

Предложен новый метод золь-гель синтеза аэрогелей германия без участия алкоксидов. Метод основан на гидролизе  $\text{GeCl}_4$  пропиленоксидом в концентрированной уксусной кислоте, используемой в качестве растворителя. Предложенный способ позволяет получать монолитные аморфные аэрогели германия, состоящие из трехмерной сетки наноразмерных ( $\sim 20$  нм) частиц и обладающие удельной площадью поверхности около  $80 \text{ м}^2/\text{г}$ . Добавление соляной кислоты в реакционную смесь приводит к получению нанокристаллических аэрогелей  $\text{GeO}_2$  (гексагональная сингония). Синтезированные материалы были охарактеризованы методами рентгеновской дифракции, ИК-и КР-спектроскопии, сканирующей электронной микроскопии и низкотемпературной адсорбции азота.

Ключевые слова: золь-гель синтез, диоксид германия, оксид пропилена, сверхкритическая сушка

**Нанотрубки  $\text{TiO}_2$ , модифицированные оксидом кадмия, для фотоэлектрокаталитического окисления спиртов**

В.А.Гринберг, В.В.Емец, А.В.Шапагин, А.А.Аверин, А.А.Ширяев

Электроды из нанотрубок  $\text{TiO}_2$  (TNT) были изготовлены электрохимическим анодированием титана в электролите на основе этиленгликоля с добавлением  $\text{NH}_4\text{F}$  (0,5 мас. %) и воды (2 мас. %). Композит (TNT)–оксид кадмия ( $\text{CdO}$ ) был изготовлен с использованием потенциостатического катодного осаждения. Структурные свойства полученных покрытий были исследованы методами сканирующей электронной микроскопии и рентгеновской фотоэлектронной спектроскопии, спектроскопии комбинационного рассеяния, рентгеновской дифракции и просвечивающей электронной микроскопии. Электрод TNT- $\text{CdO}$  демонстрирует высокую эффективность в фотоэлектрохимической деградации метанола, этиленгликоля, глицерина и сорбитола в водных растворах 0.1 М  $\text{Na}_2\text{SO}_4$  при облучении эмитатором солнечного света. Наибольшие токи фотоокисления получены для сорбитола. Методом спектроскопии фототока с модуляцией интенсивности показано, что эффективность фотоэлектрокатализа обусловлена подавлением рекомбинации электронно-дырочных пар и увеличением скорости фотоиндуцированного переноса заряда. Таким образом, композит TNT- $\text{CdO}$  является эффективным фотоанодом для разработки технологии фотоэлектрохимической деградации сорбитола и других спиртов — побочных продуктов производства биотоплива.

Ключевые слова: Нанотрубки композита  $\text{TiO}_2$ – $\text{CdO}$ , метанол, этиленгликоль, глицерин, фотоэлектрокаталитическое окисление, сорбитол.

**Исследование морфологических особенностей и термической стабильности регенерированной древесной целлюлозы из ее растворов в  $[\text{BMIm}]\text{Cl}$** 

М.Г. Михалева, С.В. Усачев, А.С. Веденкин, М.И. Иким,  
Г.Г. Политенкова, С.М. Ломакин.

Проведены исследования морфологических особенностей регенерированной древесной целлюлозы ЛС-0, полученной из ее растворов в  $[\text{BMIm}]\text{Cl}$  в диапазоне концентраций от 2% до 26%. Обнаружено, что при концентрациях ЛС-0 до 8% в  $[\text{BMIm}]\text{Cl}$  на термограммах наблюдается снижение ее термической стабильности с одновременным

увеличением коксового остатка. В образцах регенерированной целлюлозы, полученной из растворов с содержанием ЛС-0 14% и более, на дифференциальных термогравиметрических кривых (DTG) наблюдаются два максимума. Это явление было объяснено присутствием двух фаз, образующихся в процессе растворения-регенерации. Методами ИК-спектроскопии и рентгеноструктурного анализа показано влияние [BMIm]Cl на морфологию регенерированной целлюлозы.

Ключевые слова: целлюлоза, ионные жидкости, термогравиметрия, ИК-спектроскопия, рентгеноструктурный анализ.

### **Допированные бором малые фуллерены C<sub>20</sub>, C<sub>24</sub>, C<sub>28</sub> как основа для формирования фотонных кристаллов**

А. Р. Эль Занин, С. В. Борознин, И. В. Запороцкова

В настоящей работе методами теории функционала плотности были исследованы стабильность, геометрические и электронно-энергетические свойства допированных бором малых фуллеренов C<sub>20</sub>, C<sub>24</sub>, C<sub>28</sub>. Были определены средние длины связей оптимизированных структур, содержащих различное количество примесных атомов бора, оценена их стабильность. По полученным одноэлектронным спектрам и плотности состояний удалось определить механизм изменения ширины запрещенной зоны для каждой структуры. Установленная зависимость ширины запрещенной зоны от концентрации атомов примеси позволяет говорить о возможности управления показателем преломления рассматриваемых наноматериалов путем допирования различными концентрациями атомов бора, что свидетельствует о применимости подобного подхода для конструирования фотонных кристаллов. Полученные результаты могут быть полезны для создания новых оптических и оптоэлектронных устройств, применяемых в инфокоммуникационных системах для регулирования и преобразования оптического сигнала.

Ключевые слова: малые фуллерены, теория функционала плотности, ширина запрещенной зоны, плотность состояний, фотонные кристаллы.



# NANOSYSTEMS:

**PHYSICS, CHEMISTRY, MATHEMATICS**

## INFORMATION FOR AUTHORS

The journal publishes research articles and reviews, and also short scientific papers (letters) which are unpublished and have not been accepted for publication in other magazines. Articles should be submitted in English. All articles are reviewed, then if necessary come back to the author to completion.

The journal is indexed in Web of Science Core Collection (Emerging Sources Citation Index), Chemical Abstract Service of the American Chemical Society, Zentralblatt MATH and in Russian Scientific Citation Index.

### Author should submit the following materials:

1. Article file in English, containing article title, the initials and the surname of the authors, Institute (University), postal address, the electronic address, the summary, keywords, MSC or PACS index, article text, the list of references.
2. Files with illustrations, files with tables.
3. The covering letter in English containing the article information (article name, MSC or PACS index, keywords, the summary, the literature) and about all authors (the surname, names, the full name of places of work, the mailing address with the postal code, contact phone number with a city code, the electronic address).
4. The expert judgement on possibility of publication of the article in open press (for authors from Russia).

Authors can submit a paper and the corresponding files to the following addresses: nanojournal.ifmo@gmail.com, popov1955@gmail.com.

### Text requirements

Articles should be prepared with using of text editors MS Word or LaTeX (preferable). It is necessary to submit source file (LaTeX) and a pdf copy. In the name of files the English alphabet is used. The recommended size of short communications (letters) is 4-6 pages, research articles– 6-15 pages, reviews – 30 pages.

#### Recommendations for text in MS Word:

Formulas should be written using Math Type. Figures and tables with captions should be inserted in the text. Additionally, authors present separate files for all figures and Word files of tables.

Recommendations for text in LaTeX:

Please, use standard Latex without macros and additional style files. The list of references should be included in the main LaTeX file. Source LaTeX file of the paper with the corresponding pdf file and files of figures should be submitted.

References in the article text are given in square brackets. The list of references should be prepared in accordance with the following samples:

- [1] Surname N. *Book Title*. Nauka Publishing House, Saint Petersburg, 2000, 281 pp.
- [2] Surname N., Surname N. Paper title. *Journal Name*, 2010, **1** (5), P. 17-23.
- [3] Surname N., Surname N. Lecture title. In: Abstracts/Proceedings of the Conference, Place and Date, 2000, P. 17-23.
- [4] Surname N., Surname N. Paper title, 2000, URL: <http://books.ifmo.ru/ntv>.
- [5] Surname N., Surname N. Patent Name. Patent No. 11111, 2010, Bul. No. 33, 5 pp.
- [6] Surname N., Surname N. Thesis Title. Thesis for full doctor degree in math. and physics, Saint Petersburg, 2000, 105 pp.

**Requirements to illustrations**

Illustrations should be submitted as separate black-and-white files. Formats of files – jpeg, eps, tiff.



# НАНОСИСТЕМЫ:

**ФИЗИКА, ХИМИЯ, МАТЕМАТИКА**

**Журнал зарегистрирован** Федеральной службой по надзору в сфере связи, информационных технологий и массовых коммуникаций (свидетельство ПИ № ФС 77–49048 от 22.03.2012 г.)

**ISSN 2220-8054**

**Учредитель:** федеральное государственное автономное образовательное учреждение высшего образования «Национальный исследовательский университет ИТМО»

**Издатель:** федеральное государственное автономное образовательное учреждение высшего образования «Национальный исследовательский университет ИТМО», 197101, Санкт-Петербург, Кронверкский пр., 49

**Главный редактор:** д.ф.-м.н., проф. Попов Игорь Юрьевич,  
iurorov@itmo.ru

**Адрес редакции:** 197101, Санкт-Петербург, Кронверкский пр., 49,  
<http://nanojournal.ifmo.ru/>,

**Отпечатано** в Учреждении «Университетские телекоммуникации»  
Адрес: 197101, Санкт-Петербург, Кронверкский пр., 49

## **Подписка на журнал НФХМ**

На второе полугодие 2025 года подписка осуществляется через  
ОАО «АРЗИ», подписной индекс **Э57385**

**Том 16, № 3, опубликовано 30.06.2025**

**Тираж** 100 экз., цена свободная